



Galloway, Ben Andrew (2017) *Properties of charmonium and bottomonium from lattice QCD with very fine lattices*. PhD thesis.

<http://theses.gla.ac.uk/8196/>

Copyright and moral rights for this work are retained by the author

A copy can be downloaded for personal non-commercial research or study, without prior permission or charge

This work cannot be reproduced or quoted extensively from without first obtaining permission in writing from the author

The content must not be changed in any way or sold commercially in any format or medium without the formal permission of the author

When referring to this work, full bibliographic details including the author, title, awarding institution and date of the thesis must be given

Enlighten:Theses  
<http://theses.gla.ac.uk/>  
theses@gla.ac.uk

# Properties of charmonium and bottomonium from lattice QCD with very fine lattices

Ben Andrew Galloway

Submitted in fulfilment of the requirements for the degree of  
Doctor of Philosophy



School of Physics and Astronomy  
College of Science and Engineering  
University of Glasgow  
September 2016



# Abstract

Lattice methods are essential theoretical tools for performing calculations in quantum chromodynamics (QCD). To make theoretical predictions (or postdictions) of properties of hadrons, we must solve the theory of QCD which describes their constituent quarks — and conversely, to further our knowledge of quarks, which are fundamental constituents of matter, we must examine the properties of their hadronic bound states, since free quarks are not observed due to the phenomenon known as quark confinement. It is not possible to solve QCD analytically, and so we must turn to numerical methods such as lattice QCD.

Despite being a well-established and mature formalism, lattice QCD has only really come into fruition over the last decade or so, developing in parallel with the advent of high-performance computing facilities. The available computing power is now sufficient to perform calculations on very fine lattices, with lattice spacings of about 0.06 fm or less. These are beneficial for two reasons: firstly, they are closer to the continuum limit, meaning that continuum extrapolations are better controlled; and secondly, it is only on finer and finer lattices that we are able to accurately simulate heavier and heavier quarks, such as charm and bottom.

We use very fine lattices from the MILC collaboration to determine multiple properties of heavyonium systems, in each case using the HISQ action for heavy valence quarks. Correlator fitting, and continuum and chiral extrapolations, are performed via Bayesian least-squares fitting methods.

The first calculation simulates charmonium via charm quarks at their physical mass, as well as bottomonium, via multiple intermediate heavy quark masses and an extrapolation in this heavy mass. Notably, this is a fully relativistic method of calculating the bottom quark, and is complementary to effective-action methods such as NRQCD. We perform this calculation on gauge configurations with 2+1 flavours of quarks in the sea, and are able to accurately determine properties of the ground-state pseudoscalar and vector mesons in each system, including their decay constants, the hyperfine mass splitting, and the temporal moments of the vector correlators — which we also make use of to renormalise the vector current. To fully investigate some small anomalies in some of the vector results, we also repeat a subset of these calculations using a one-link instead of a local vector current.

The second calculation represents an in-depth study of charmonium, including radial and orbital excitations as well as the ground states. We again simulate charm quarks at their physical mass, but this time on gauge configurations with 2+1+1 flavours of quarks in the sea, including those with light sea quarks at their physical masses. We also include a set of well-constructed smearing functions designed to increase the overlap of our correlators with the ground state, and therefore allow us to extract data on charmonium excited states more accurately.

Specifically, we concentrate on conventional low-lying excited states in the charmonium system, and accurately extract various mass splittings in the spectrum (including the 1S hyperfine splitting, and the spin-averaged 2S – 1S splitting) as well as temporal moments of the vector correlator (which we again utilise in a renormalisation procedure), and decay constants of the ground-state pseudoscalar and vector. We also use the calculated mass splittings to accurately reconstruct a selected portion of the charmonium spectrum.

This is the first time that we have used smeared operators with staggered quarks for this purpose, and so this calculation acts as a strong base upon which to build future work on excited states.

# Dedication

The dedication of this thesis is split, in no particular order or proportion, to my family and friends. In particular:

- to Mum, who finds it easy, and to Dad, to whom it looks like either Greek or double Dutch;
- to Yasmin and Colin, who expertly navigated asking if it was done;
- to Robyn, not a physicist but still a dork;
- to Grandma, beamingly proud;
- to Papa, an academic at heart;
- to Nonna, hero and matriarch;
- and to the Cecilians, who have sustained my sanity and encouraged my insanity better than they could ever know, and whose fault this really all is in the first place.

I love you all.

***How to Get There***

*Go to the end of the path until you get to the gate.*

*Go through the gate and head straight out towards the horizon.*

*Keep going towards the horizon.*

*Sit down and have a rest every now and again,*

*But keep on going, just keep on with it.*

*Keep on going as far as you can.*

*That's how you get there.*

— Michael Leunig

---

*Aequam memento rebus in arduis  
servare mentem*

— Horace

---

*What did the subatomic duck say?*

— Quark

# Acknowledgements

No man is an island, and this thesis was not completed in a vacuum, quantum or otherwise. There are a number of people who have supported, assisted, encouraged or guided me through the completion of this work, and it would be extremely remiss of me not to thank them here.

My supervisor, Professor Christine Davies, has provided me with help and guidance relating to physics, statistics and beyond; has always had a level-headed idea of what things I should and should not be stressed about; has always seemed to know where we want to be heading before we've even taken a step there; and has been the main reviewer of this thesis while I was writing it. It's been quite a journey, and without Christine's expertise both in lattice QCD and in supervising PhD students it would have undoubtedly been an even rockier one. She deserves my eternal thanks for putting up with my erratic thoughts, and for her patient guidance through the stresses inherent in this process.

Dr Jack Laiho deserves much gratitude too: as the supervisor for my Masters project, and for the beginning of my PhD, he introduced me properly to the world of academic research, and allowed me time to consider what I was really doing here. He also introduced me to the world of quantum gravity, which I still find a fascinating topic. There is an all-too-brief homage to it contained within my introductory chapter, which is down to his passion for the subject.

Other members of the PPT group (whether academics, postdocs or fellow PhD students), particularly those working on lattice QCD, and other members of the HPQCD collaboration, deserve a large chunk of gratitude. Their knowledge and willingness to share it was invaluable in all of the work that I did. Many people generated useful correlators before I even arrived, gave up time to help when code wasn't working, tweeted the silly punny jokes that I wrote on the whiteboard, and kept me updated on the number of retweets we got. I want to specifically thank Dr Brian Colquhoun and Dr Bipasha Chakraborty, with whom I have shared an office for several years now, and without whom I would have nowhere to turn for the answers to questions both inane and profound. Dr Jonna Koponen also deserves many thanks for patiently guiding me through the MILC code, the fitting code, and the underlying physics whenever I was in need.

Dr Andrew Davies was good enough, in my first year, to tutor me in quantum field theory, no matter how good a student I was. Drs Donald MacLaren, David Miller, and Craig Buttar had a part to play in getting me to where I am now, and helped me overcome what I saw at the time as an insurmountable obstacle. They all have my thanks.

For moral, financial, emotional, nutritional and alcoholic support — and probably everything else not directly related to physics — there are a long list of people who should have my gratitude. First and foremost, my parents, who have been supportive of everything I've done in my life, and this is no exception. There is no question that without you both, I would have fallen at the first and last hurdles, and many more in between. Thank you. My sister and her new husband (!) have been spectacular sources of motivation, even as they planned their wedding (and obtained any necessary technical support). I can't believe I've known you for the entire time it's taken me to write this thesis.

My life at university has been in many ways defined by my membership of the Cecilian Society, and I need to thank this wonderful group of people for providing me with a world completely removed from day-to-day activities in physics. Without you all, I would have gone stir-crazy long ago. With you all, I simply feel that I've been stir-crazy all along, and that that's how life actually works. In seriousness, I've found some of my best friends (and perhaps even more) here, and without your encouragement (and reminders of my advancing age) I am unlikely to have completed this endeavour at all. You continue to enrich my life in so many ways, whether we're naming a shoal of fish who will dance around a teenage nuclear zombie, or trying to save a sinking ship — metaphorical or otherwise.

Several notable mentions must be given to my colleagues at Glasgow Science Centre, who have provided entertainment as well as motivation over the past year in particular, and who were especially good at noticing when these things were required. I owe much, too, to the residents (and friends) of Flat Gay, for wine, cake, robots, and permitting me to have a second home. For his encouragement at the very start of my forays into physics in secondary school, Mr Bill Swiatek deserves much praise, and for his encouragement in the final stages of writing this thesis, Professor Tom Bryce deserves much acclaim. His words are most appropriate here: it is imperative that I finish!

## Specific Contributions

Much of this work makes extensive use of the MILC collaboration's various lattice gauge configurations, and also their excellent open-source lattice gauge theory code. More details on both of these aspects of MILC's work can be found in [1], and indeed throughout this thesis, but even in such a brief summary they deserve much gratitude.

Professor Carleton DeTar deserves to be thanked profusely for useful discussions in support of the work in Chapter 5 on excited states of charmonium, and its implementation with the MILC code. Peter Knecht's exploratory study of the methods we use here [2] was instrumental in paving the way for our larger study, and he also deserves thanks for the use of his correlators and his determination of appropriate smearings to use.

The lattice calculations described in this thesis were performed on the Darwin supercomputer as part of STFC's DiRAC facility jointly funded by STFC, BIS, and the Universities of Cambridge and Glasgow. The author has been supported by a College of Science and Engineering Scholarship 2011 from the University of Glasgow.



# Declaration

With the exception of chapters 1–3, which contain introductory material, the work presented in this thesis was carried out by the author unless noted otherwise. The composition of the material which makes up this thesis was carried out by the author.

A preliminary version of the work described in chapter 5 has appeared in the Proceedings of the 32nd International Symposium on Lattice Field Theory (Lattice 2014), held at Columbia University, New York, New York. This can be found in [3].

The copyright of this thesis rests with the author. No quotation from it should be published without the author’s prior written consent and information derived from it should be acknowledged.

## A Note on Pronouns

In academic writing, it is often customary to use ‘we’ to refer to a number of collaborators working on a scientific endeavour. Naturally, in many cases this is appropriate in this thesis, as it is in any academic work. On many occasions, however, the pronoun ‘I’ may seem more appropriate. Personally, when reading a paper, I find it jarring to come across the use of this pronoun, and try to use it as little as possible when writing.

In cases where work in this thesis has been carried out solely by the author, I often use ‘we’ when it does not distort clarity of meaning, in the hope that it is less jarring than a pronoun switch. Should this become a point of contention for you, dear reader, I invite you to understand ‘we’ as meaning me (the author) and you (the reader) which makes sense in almost all cases where it is used.

We may now embark on this journey together!



# Contents

<b>1</b>	<b>Lattice Quantum Chromodynamics</b>	<b>1</b>
1.1	The Standard Model . . . . .	1
1.2	Quantum Chromodynamics . . . . .	2
1.2.1	Quarkonium . . . . .	3
1.3	Path Integrals . . . . .	4
1.4	Discretising QCD . . . . .	5
1.4.1	Lattice Gluon Action . . . . .	6
1.4.2	Fermions on the Lattice . . . . .	7
1.5	Staggered Fermions . . . . .	9
1.5.1	Asqtad Improvement . . . . .	10
1.5.2	Highly Improved Staggered Quarks . . . . .	13
<b>2</b>	<b>Calculations on the Lattice</b>	<b>15</b>
2.1	Gauge Configurations . . . . .	16
2.1.1	Algorithms and Computing Power . . . . .	17
2.1.2	MILC Configurations . . . . .	19
2.1.3	Fixing the Lattice Scale . . . . .	21
2.2	Flavour Physics with the HISQ Formalism . . . . .	23
2.2.1	Staggered Operators . . . . .	24
2.2.2	Random Wall Sources . . . . .	29
2.2.3	Smearings . . . . .	31
2.2.4	MILC Code . . . . .	32
<b>3</b>	<b>Obtaining Physical Results</b>	<b>33</b>
3.1	Correlator Fitting . . . . .	33
3.1.1	Bayesian Methods . . . . .	36
3.1.2	Fitting Code . . . . .	38
3.1.3	EigenBasis Method . . . . .	39
3.2	Physical Extrapolation . . . . .	40
3.2.1	Continuum Limit . . . . .	40
3.2.2	Infinite Volume Limit . . . . .	41

3.2.3	Chiral Limit . . . . .	41
3.2.4	Operator Renormalisation . . . . .	42
3.3	Treatment of Heavy Quarks . . . . .	42
<b>4</b>	<b>Heavyonium Physics</b>	<b>45</b>
4.1	Details of Lattice Calculation . . . . .	47
4.1.1	Fitting Methodology . . . . .	49
4.2	Hyperfine Splitting . . . . .	50
4.2.1	Charmonium Cross-Check . . . . .	55
4.3	Moments of the Vector Correlator . . . . .	57
4.3.1	Current-Current Renormalisation . . . . .	62
4.3.2	Choice of $Z$ -Factor . . . . .	65
4.3.3	One-link Vector Operator . . . . .	65
4.3.4	Four-Flavour HISQ Ensembles . . . . .	78
4.4	Vector Decay Constant . . . . .	82
4.4.1	One-link Vector Operator . . . . .	85
4.4.2	Four-Flavour HISQ Ensembles . . . . .	87
4.5	Pseudoscalar Decay Constant . . . . .	88
4.6	Outstanding Discrepancies . . . . .	89
<b>5</b>	<b>Radial and Orbital Excitations of Charmonium</b>	<b>91</b>
5.1	Lattice Calculation . . . . .	93
5.1.1	Smearings . . . . .	95
5.1.2	Matrices of Correlators . . . . .	96
5.1.3	Correlator Fits . . . . .	98
5.2	Mass Splittings . . . . .	104
5.2.1	1S Hyperfine Splitting . . . . .	104
5.2.2	Spin-Averaged 2S – 1S Splitting . . . . .	109
5.2.3	2S Hyperfine Splitting . . . . .	112
5.2.4	Vector–Axial Vector Splitting . . . . .	114
5.3	Moments of the Vector Correlator . . . . .	116
5.3.1	Current-Current Renormalisation . . . . .	120
5.3.2	Previous Lattice Results . . . . .	121
5.4	Decay Constants . . . . .	126
5.4.1	Ratio of Vector Decay Constants . . . . .	129
5.4.2	Ratio of Pseudoscalar Decay Constants . . . . .	130
5.4.3	$\eta_c$ Decay Constant . . . . .	132
5.4.4	$J/\psi$ Decay Constant . . . . .	132
5.5	Consideration of Superfine Results . . . . .	135
5.5.1	Details of Superfine Calculations . . . . .	135

5.5.2	Effects of Different Fit Methods . . . . .	137
5.5.3	Possible Causes . . . . .	141
<b>6</b>	<b>Conclusions and Comparisons</b>	<b>147</b>
6.1	Bottomonium . . . . .	147
6.1.1	Hyperfine Splitting . . . . .	147
6.1.2	Decay Constants . . . . .	149
6.1.3	Vector Moments . . . . .	150
6.1.4	Outlook . . . . .	150
6.2	Charmonium . . . . .	150
6.2.1	Decay Constants . . . . .	151
6.2.2	Vector Moments . . . . .	151
6.2.3	Hyperfine Splitting . . . . .	154
6.2.4	Continuum Spectrum . . . . .	155
6.2.5	Outlook . . . . .	158



# List of Figures

1.1	Gauge-independent quantities on the lattice . . . . .	5
1.2	The smallest possible Wilson loop on the lattice, a $1 \times 1$ loop of gauge links known as a plaquette. . . . .	6
1.3	The six-link Wilson loop terms added by the Symanzik improvement procedure . . . . .	7
1.4	The gauge links used in applying the difference operator $\Delta_\mu$ to the field $\psi(x)$ . . . . .	7
1.5	A Feynman diagram of taste exchange. The quark entering on the lower left of the diagram emits a gluon with momentum $\pi/a$ , and thus changes taste. This gluon is highly virtual and is immediately reabsorbed by the quark entering on the top left, which also changes taste. . . . .	11
1.6	The smeared gauge links included in the asqtad action, which together constitute a fattened gauge link. The 5-link structure responsible for implementing the Lepage term is the rightmost one, labelled $5'$ . . . .	12
3.1	Plots of rescaled two-point charmonium correlators $\tilde{C}_{2\text{pt}}$ on the superfine 2+1 ensemble. These plots include statistical errors, which are smaller than the size of the points. The rescaling is performed by dividing the average correlator $\bar{C}_{2\text{pt}}$ by the ground state exponential, and the plateau of value $A_0^2$ is evident in each. Lines are drawn between the points, which clearly reveal the oscillating behaviour of the vector correlator. . . . .	35
3.2	A rescaled and cropped version of Figure 3.1b, showing the small ‘kink’ at the central $t$ -value. Although this is definitely present in the data here, the vertical axis has had to be scaled up significantly to show it — indeed it is not clear at all from the original plot that it even exists. This is another indication of the quality of the correlator data that we have obtained. . . . .	37

3.3	A plot demonstrating the convergence of a fit parameter as the number of exponentials in the fit function is increased. The specific parameter used in the example here is the energy of the $\psi(2S)$ charmonium meson, expressed as its difference to the energy of the ground-state $J/\psi(1S)$ . The fit has clearly converged once the sixth exponential is added, and shows no change as we continue to add more. The $\chi^2$ values for each fit are shown below the corresponding points, and these also stabilise as the fit converges. . . . .	37
4.1	The experimental heavyonium spectrum, with masses plotted relative to the spin-averages of the $\chi_b(1P)$ and $\chi_c(1P)$ states. Bottomonium states are plotted in red and charmonium states in blue, with the width of the lines corresponding to the uncertainty on their mass. This plot is based on a figure in [69] and has been updated with current experimental data from [4]. . . . .	45
4.2	The heavyonium hyperfine splitting as a function of the inverse heavyonium mass. Values are shown on the fine (magenta), superfine (green) and ultrafine (blue) lattices, using the local pseudoscalar and vector operators. The coloured dashed lines give the fitted result at each lattice spacing. The black points represent the experimental values and are shown at the physical masses of the $\eta_c$ and $\eta_b$ mesons. The grey band shows the combined fit to all the data, i.e. the extrapolation to the continuum. . . . .	52
4.3	The charmonium hyperfine splitting. The magenta point represents the experimental value. We plot against the squared lattice charm mass as a proxy for the lattice spacing. The grey band shows our calculated fit, although since the form of our fit function is so simple, this is equivalent to our calculated physical hyperfine splitting value inclusive of statistical errors only. The light magenta band shows our fitted continuum result with the addition of systematic errors, as described in the text. . . . .	56
4.4	Moments of the heavyonium vector correlator as a function of heavyonium mass, determined on the same lattices as in Figure 4.2. The black points are the results derived from experiment, and the grey band shows the fit as described in the text. . . . .	61
4.5	Moments of the heavyonium vector correlator as a function of heavyonium mass, as in Figure 4.4, but renormalised using $Z_4$ , the renormalisation factor obtained from the 4 <sup>th</sup> moment. . . . .	67

4.6	Moments of the heavyonium vector correlator as a function of heavyonium mass, as in Figure 4.4, but renormalised using $Z_6$ , the renormalisation factor obtained from the 6 <sup>th</sup> moment. . . . .	69
4.7	Moments of the heavyonium vector correlator as a function of heavyonium mass, determined on the same lattices as in Figure 4.4, but this time using the one-link vector operator. The black points are the results derived from experiment, and the grey band shows the fit as described in the text. In this case we renormalise using $Z_8$ . . . . .	73
4.8	Moments of the heavyonium vector correlator as a function of heavyonium mass determined using the one-link vector operator, as in Figure 4.7, but renormalised using $Z_4$ , the renormalisation factor obtained from the 4 <sup>th</sup> moment. . . . .	75
4.9	Moments of the heavyonium vector correlator as a function of heavyonium mass determined using the one-link vector operator, as in Figure 4.7, but renormalised using $Z_6$ , the renormalisation factor obtained from the 6 <sup>th</sup> moment. . . . .	77
4.10	Taste splittings between the local and one-link vector mesons calculated in this chapter, plotted against the inverse of the pseudoscalar meson mass. The magenta points are those on the fine lattice, the green, superfine, and the blue, ultrafine. Note the narrow range of the scale on the vertical axis in both cases. . . . .	79
4.11	Moments of the heavyonium vector correlator as a function of heavyonium mass, determined using the local vector operator, and renormalised with $Z_8$ , on two different ensembles. Results on the superfine 2+1-flavour lattices are displayed in green, with results from the superfine 2+1+1-flavour lattices displayed in red. . . . .	81
4.12	The decay constant of the heavy-heavy vector meson, as determined on the same lattices as in Figure 4.2 using the local vector operator. The colours represent the same lattices as they did in Figure 4.2. . . .	84
4.13	The decay constant of the heavyonium vector meson as determined for a subset of the bare quark masses on the same lattices as in Figure 4.12, but using the one-link vector operator. . . . .	86
4.14	The decay constant of the heavyonium vector meson as determined using the local vector operator. Results on the superfine 2+1-flavour lattices are displayed in green, with results from the superfine 2+1+1-flavour lattices displayed in red. . . . .	87

4.15	The decay constant of the heavy-heavy pseudoscalar meson as determined on the same lattices as in Figure 4.2, with the colours representing the same lattices as in that figure. The black points at the physical $\eta_b$ and $\eta_c$ masses represent determinations in the continuum limit from previous lattice calculations, in [74] and [45] respectively.	88
5.1	An overview of the current experimental understanding of the charmonium spectrum, as presented in [4]. Note the open charm threshold, labelled $D\bar{D}$ , just above 3700 MeV.	92
5.2	The Fermilab/MILC result for the spin-averaged 2S – 1S splitting in charmonium. Note the magenta burst at the lower left which represents the experimental value. This figure is reproduced from [84].	92
5.3	Plots of the effect of smearings on the convergence of correlators to a plateau. Here we show the effect of two different smearings applied to pseudoscalar charmonium correlators on the superfine 2+1+1 ensemble. The blue points are those obtained when no smearing is applied, and the red points show the results with the respective smearing applied to both the source and sink operators. It is clear that in both cases, the smearing causes the correlators to plateau more quickly than they otherwise would.	97
5.4	The spectrum of low-lying charmonium states as computed on each of the ensembles in Table 5.1. Individual determinations of each mass are plotted in order of decreasing lattice spacing from left to right, atop an indication of their experimental values. The lattice charm quark masses are tuned by fixing to the value of the $\eta_c(1S)$ , and it is clear from the plot how well-tuned they actually are — excepting, of course, the results on the ultrafine ensemble, which are discussed further in the text. Results for excited states on the superfine ensemble, particularly the 2S states, have an increased error in comparison to their coarser counterparts, and this is also discussed further in the text.	103

5.5	The hyperfine splitting of charmonium as determined on a range of ensembles. The groups of points from right to left indicate results on the very coarse, coarse, fine, superfine and ultrafine ensembles respectively, the ultrafine result having been corrected for mistuning with an appropriate uncertainty included. The grey band indicates the fitted curve at the physical light sea quark mass, and the magenta band shows our final result in the continuum limit, including both statistical and systematic errors. This is in excellent agreement with the experimental average [4], shown as the magenta point at zero lattice spacing. Note that the range of the vertical scale is just over 20 MeV, giving an indication of the accuracy of this entire set of results.	106
5.6	The spin-averaged 2S – 1S splitting in charmonium as determined on a range of ensembles — the groups of points from right to left indicate results on the coarse, fine and superfine ensembles respectively. The grey band indicates the fitted curve at the physical light sea quark mass, and the magenta band shows our final result in the continuum limit, including both statistical and systematic errors. This is in good agreement with the experimental average [4], shown as the magenta point at zero lattice spacing.	109
5.7	The 2S – 1S splitting in charmonium pseudoscalar and vector channels, fitted separately rather than being spin-averaged as in Figure 5.6.	111
5.8	The mass splitting between the radially-excited charmonium vector meson $\psi(2S)$ , and its corresponding pseudoscalar meson, the $\eta_c(2S)$ , as determined on a range of ensembles. The groups of points from right to left indicate results on the coarse, fine and superfine ensembles respectively. The grey band indicates the fitted curve at the physical light sea quark mass, and the magenta band shows our final result in the continuum limit, including both statistical and systematic errors. This is in good agreement with the experimental average [4], shown as the magenta point at zero lattice spacing.	113

5.9	The mass splitting between the ground-state charmonium vector meson $J/\psi(1S)$ , and its parity partner, the orbitally-excited axial vector meson $h_c(1P)$ , as determined on a range of ensembles. The groups of points from right to left indicate results on the coarse, fine and superfine ensembles respectively. The grey band indicates the fitted curve at the physical light sea quark mass, and the magenta band shows our final result in the continuum limit, including both statistical and systematic errors. This is in good agreement with the experimental average [4], shown as the magenta point at zero lattice spacing. . . . .	115
5.10	Moments of the charmonium vector correlator, determined on a range of lattice ensembles. From right to left, the groups of points indicate results on the very coarse, coarse, fine and superfine lattices. The magenta points are the results derived from experiment, and the grey bands show the fit as described in the text. . . . .	119
5.11	Moments of the charmonium vector correlator, as in Figure 5.10, but renormalised using $Z_4$ , the renormalisation factor obtained from the 4 <sup>th</sup> vector moment. . . . .	123
5.12	Moments of the charmonium vector correlator, as in Figure 5.10, but renormalised using $Z_6$ , the renormalisation factor obtained from the 6 <sup>th</sup> vector moment. . . . .	125
5.13	The 4 <sup>th</sup> moment of the charmonium vector correlator, as determined on a range of ensembles including the ultrafine, and renormalised with $Z_4$ , plotted on the same scale as Figure 5.10a. The groups of points from right to left indicate results on the very coarse, coarse, fine, superfine and ultrafine ensembles respectively. The grey band indicates the fitted curve at the physical light sea quark mass, and the magenta band shows our final result in the continuum limit. The magenta point is that derived from experimental results, and the grey point at zero lattice spacing is the continuum result from [56]. . . . .	127
5.14	The ratio of the decay constants of the vector mesons $J/\psi(1S)$ and $\psi(2S)$ , as determined on a range of ensembles. The groups of points from right to left indicate results on the coarse, fine and superfine ensembles respectively. The grey band indicates the fitted curve at the physical light sea quark mass, and the magenta band shows our final result in the continuum limit. The magenta point at zero lattice spacing is derived from experimental results [4] as described in the text.	129

- 5.15 The ratio of the decay constants of the pseudoscalar mesons  $\eta_c(1S)$  and  $\eta_c(2S)$ , as determined on a range of ensembles. The groups of points from right to left indicate results on the coarse, fine and superfine ensembles respectively. The grey band indicates the fitted curve at the physical light sea quark mass, and the magenta band shows our final result in the continuum limit. The magenta point at zero lattice spacing is the equivalent ratio of vector decay constants derived from experimental results [4], and the overlapping grey point is our fitted result to the vector ratio from Figure 5.14. . . . . 131
- 5.16 The decay constant of the ground-state charmonium pseudoscalar meson  $\eta_c(1S)$ , as determined on a range of ensembles. The groups of points from right to left indicate results on the very coarse, coarse, fine and superfine ensembles respectively. The grey band indicates the fitted curve at the physical light sea quark mass, and the magenta band shows our final result in the continuum limit. This is in very good agreement with the continuum result obtained by the HPQCD collaboration in [45] using HISQ valence quarks on the asqtad configurations, shown as the magenta point at zero lattice spacing. 133
- 5.17 The decay constant of the ground-state charmonium vector meson  $J/\psi(1S)$ , as determined on a range of ensembles. The groups of points from right to left indicate results on the very coarse, coarse, fine and superfine ensembles respectively, and the results have been renormalised using  $Z_8$ , determined from the 8<sup>th</sup> moment of the vector correlators. The grey band indicates the fitted curve at the physical light sea quark mass, and the magenta band shows our final result in the continuum limit. This is in good agreement with the experimental result derived from [4], shown as the magenta point at zero lattice spacing. . . . . 134
- 5.18 Vector channel 2S – 1S mass splitting with varying degrees of forced priors for the associated amplitudes  $A_0$  and  $A_1$ . No thinning of the data is performed on any of the fits above the dotted line. For comparison, the priors used in the bottom two cases are  $A_0 = A_1 = 0.01(1.00)$  and  $A_0 = A_1 = 0.10(20)$ , from the bottom up. As the priors are widened and made less precise, there is a clear drift away from the experimental value [4] (shown as the magenta dotted line) and an accompanying increase in statistical error. . . . . 138

5.19	The vector channel 2S – 1S splitting from various different traditional ( <i>trad</i> ) and EigenBasis ( <i>gevp</i> ) fits to data from the superfine $m_\ell/m_s = 1/5$ ensemble. Thinning of the correlator data is denoted by the <i>thin</i> parameter, and the applied SVD cut by <i>svd</i> . The experimental value [4] is again plotted as the magenta dotted line. . . . .	140
5.20	The vector channel 2S – 1S splitting from different traditional ( <i>trad</i> ) and EigenBasis ( <i>gevp</i> ) fits to data from the coarse $m_\ell/m_s = \text{phys}$ ensemble. Thinning of the correlator data is denoted by the <i>thin</i> parameter, and the applied SVD cut by <i>svd</i> . The experimental value [4] is again plotted as the magenta dotted line. This does not display the same erratic behaviour as the corresponding data from the superfine ensemble, displayed in Figure 5.19. We also note here that we do not necessarily expect agreement with the experimental result due to larger discretisation effects on the coarse lattices, and indeed this seems to be the case. . . . .	142
5.21	The vector channel 2S – 1S splitting from different traditional ( <i>trad</i> ) and EigenBasis ( <i>gevp</i> ) fits to data from the fine $m_\ell/m_s = \text{phys}$ ensemble. Thinning of the correlator data is denoted by the <i>thin</i> parameter, and the applied SVD cut by <i>svd</i> . The experimental value [4] is again plotted as the magenta dotted line. This does not display the same erratic behaviour as the corresponding data from the superfine ensemble, displayed in Figure 5.19. . . . .	143
5.22	The pseudoscalar channel 2S – 1S splitting from various different traditional ( <i>trad</i> ) and EigenBasis ( <i>gevp</i> ) fits to data from the superfine $m_\ell/m_s = 1/5$ ensemble. Thinning of the correlator data is denoted by the <i>thin</i> parameter, and the applied SVD cut by <i>svd</i> . The parameter <i>diag</i> here represents the pair of <i>t</i> -values used to diagonalise the matrix of correlators, and as expected for the EigenBasis method [64], this choice has almost no effect on the result. The magenta dotted lines again represent the range of the experimental determination in [4]. . . . .	144

6.1	A comparison of our continuum-extrapolated result for the bottomonium hyperfine splitting, in red, with two values from experiment, and another three lattice results. In magenta is the world average result from [4], and in blue, the result from the Belle Collaboration [76]. In black are the Fermilab Lattice and MILC Collaborations' Clover result [88], Stefan Meinel's NRQCD result [89], and the HPQCD Collaboration's NRQCD result [73], which each agree well with our value. Although our determination is not incompatible with the experimental average, it clearly favours the recent Belle result. . . . .	148
6.2	A comparison of results for the decay constant of the $\eta_c(1S)$ . The lower section plots a previous determination by the HPQCD collaboration on 2+1-flavour lattices in [45]. The middle section contains the continuum result on 2+1-flavour lattices from chapter 4 of this thesis, and the top section the continuum result on 2+1+1-flavour lattices from chapter 5 of this thesis. . . . .	152
6.3	A comparison of results for the decay constant of the $J/\psi(1S)$ . The lower section plots a previous determination by the HPQCD collaboration on 2+1-flavour lattices in [56], and the two continuum results on 2+1-flavour lattices from chapter 4 of this thesis, determined using local and one-link vector currents. The middle section plots the continuum result on 2+1+1-flavour lattices from chapter 5 of this thesis, and the top section contains the result derived from experimental world averages in [4]. . . . .	153
6.4	A comparison of results for the charmonium hyperfine splitting, as determined in this work and in others. The lower section contains results computed on 2+1-flavour lattices, in blue: two in chapter 4 of this thesis via different continuum fits, and previous determinations by several lattice collaborations [56, 83, 88]. The middle section contains the continuum result on 2+1+1-flavour lattices from chapter 5 of this thesis, in red. In magenta in the top section is the current experimental average from [4]. . . . .	156

6.5	The spectrum of low-lying charmonium states computed from the continuum results of fits to the hyperfine splitting, pseudoscalar and vector $2S - 1S$ splittings, and the vector–axial-vector splitting. The black lines indicate the experimental averages from [4], and the line widths correspond to the (generally very small) uncertainties on these results. The magenta boxes indicate the range of our results from the continuum fits. The baseline here which all the splittings are added to is the mass of the $\eta_c(1S)$ , which we fix to for tuning our bare lattice charm quark masses, and for which we do not therefore compute a continuum determination. . . . .	157
-----	--	-----

# List of Tables

1.1	The three generations of fermions in the Standard Model, with the world average determinations of their masses from [4]. The first column lists their electric charges in units of the elementary charge $e$ . . . . .	2
2.1	Ensembles of MILC configurations which include the effects of 2+1 flavours of quarks in the sea ( $u$ , $d$ and $s$ ). The inverse lattice spacing values are given here in units of $r_1$ [15] (defined in section 2.1.3). This can be converted to an inverse lattice spacing in GeV as also explained in section 2.1.3. The $\delta$ values represent the difference between the sea quark mass and its physical value as a fraction of the $s$ quark mass, and $\beta$ is the gauge coupling used in generating the ensembles as discussed in section 1.4.1. . . . .	19
2.2	Details of the 2+1+1-flavour MILC configurations [16]. We label each according to its approximate lattice spacing, and can then refer uniquely to each ensemble with a combination of its label and the mass of the light quarks in the sea (expressed as a fraction of the sea strange quark mass). The lattice spacing $a$ is listed in units of $w_0$ (defined in section 2.1.3), as determined in [46] and, in some cases, updated in [47]. . . . .	20
2.3	Phases and spins for local staggered currents . . . . .	26
4.1	Parameters used on the different ensembles of 2+1-flavour MILC configurations in this calculation. Specifically, we list the lattice charm mass on each ensemble, the Naik parameter $\varepsilon$ associated with each $am_c$ , the number of configurations $N_{\text{cfg}}$ from each ensemble, and the number of time sources $N_t$ on each configuration, used in the calculation. . . . .	48
4.2	Parameters used to tune the Naik coefficients for each heavy valence quark mass. These are dependent only on the value of $am_h$ and so remain the same across different ensembles for the same $am_h$ values (in lattice units). . . . .	48

4.3	Results in lattice units for the masses of the $\eta_h$ and $\phi_h$ mesons, and their difference, for each bare quark mass used on each of the ensembles listed in Table 2.1. . . . .	51
4.4	Time moments of the heavyonium vector correlator for each heavy-quark mass on each ensemble, raised to the appropriate power, in lattice units. As displayed here, these results are unrenormalised; to do this, we use the renormalisation factor $Z_8$ obtained from the 8 <sup>th</sup> moment of the correlator as detailed in section 4.3.1. . . . .	58
4.5	Time moments of the charmonium and bottomonium vectors. In the left-hand columns, we list the physical results from our continuum fits and their associated index $n$ . In the right-hand columns, we list the comparable results extracted from experiment in [79] and [80], indexed by $k$ and appropriately normalised for comparison to our results. . . . .	62
4.6	Agreement of the calculated time moments of the charmonium and bottomonium vectors from our continuum fits with the corresponding values extracted from experiment, as listed in Table 4.5. We define this as the difference between the calculated lattice value and the experimentally-extracted value, $(G_n^V)^{\frac{1}{n-2}} - \mathcal{M}_k^{\text{norm}}$ , divided by the error estimate on the lattice value. . . . .	62
4.7	Renormalisation factors determined from the current-current correlator method, for each heavy quark mass on each ensemble. $Z_n$ is the renormalisation factor obtained by matching the $n^{\text{th}}$ lattice moment to its equivalent continuum value, derived from experimental results. . . . .	64
4.8	$\chi^2$ and statistical $Q$ values for continuum fits to the $n^{\text{th}}$ moments of the vector correlator, when renormalised using the listed $Z$ -factors. It is clear that using $Z_8$ results in the minimal $\chi^2$ and maximal $Q$ values. . . . .	65
4.9	Time moments of the heavyonium vector correlator for each heavy-quark mass on each ensemble, calculated using the one-link vector operator. These results are again displayed in lattice units, raised to the appropriate power — that being, for the $n^{\text{th}}$ moment, $1/(n-2)$ . . . . .	70
4.10	$\chi^2$ and statistical $Q$ values for continuum fits to the $n^{\text{th}}$ moments of the one-link vector correlator, when renormalised using the listed $Z$ -factors. We use $Z_8$ again for minimal $\chi^2$ and maximal $Q$ values. . . . .	71

4.11	Time moments of the charmonium and bottomonium one-link vectors. In the left-hand columns, we list the physical results from our continuum fits and their associated index $n$ . In the right-hand columns, we list the comparable results extracted from experiment in [79] and [80], indexed by $k$ and appropriately normalised for comparison to our results. . . . .	71
4.12	Results in lattice units for the decay constants of the $\eta_h$ and $\phi_h$ mesons for each bare quark mass on the ensembles listed in Table 2.1. $Z_8$ is the renormalization factor obtained from the 8 <sup>th</sup> moment of the correlator as described in the text. This is used to renormalise the vector decay constant by setting the above $Z = Z_8$ and then multiplying to cancel it out. The equivalent renormalization factor for the $\eta_h$ is unity, so no change is necessary there. These results were obtained using the local vector operator. . . . .	83
4.13	Results in lattice units for the mass and decay constant of the $\phi_h$ meson for a subset of the heavy quark masses used before, but using the one-link vector operator. Results are obtained on each of the ensembles listed in Table 2.1. We also list the renormalisation factors $Z_8$ calculated for this data, again using the current-current renormalisation method. . . . .	85
5.1	Parameters used on the different ensembles of 2+1+1-flavour MILC configurations in the calculations in this chapter. We list the bare lattice charm mass $am_c$ and the Naik parameter $\varepsilon$ on each ensemble, the number of configurations $N_{\text{cfg}}$ from each ensemble, and the number of time sources $N_t$ on each configuration that are utilised. The rightmost four columns list the parameters used to define the Gaussian covariant smearings applied to the source and sink operators, as described by equation 2.37. No smearings are used on the very coarse ensembles, and only one smearing is used in the ultrafine case. . . . .	94

5.2	Results in lattice units for the rest masses of the $\eta_c(1S)$ , $J/\psi(1S)$ , $\eta_c(2S)$ , $\psi(2S)$ and $h_c(1P)$ charmonium mesons as determined on each of the ensembles listed in Table 5.1. The presence of a symbol in the rightmost column indicates that values in that row have been taken from a traditional fit; else, they have been determined via an EigenBasis fit. Rows with a * had no EigenBasis fit performed to the data, and in the ultrafine row denoted by ‡, the traditional fit was chosen over the EigenBasis fit for all correlators. The ultrafine case is the only one where the traditional fit is better, most likely because the of relatively small data sample on this ensemble. . . . .	100
5.3	Results in lattice units for the local amplitudes of the $\eta_c(1S)$ , $J/\psi(1S)$ , $\eta_c(2S)$ , $\psi(2S)$ and $h_c(1P)$ charmonium mesons as determined on each of the ensembles listed in Table 5.1. The ‡ and * symbols mean the same as in Table 5.2. . . . .	101
5.4	Results in lattice units for selected mass splittings in the charmonium system, as determined on each of the ensembles listed in Table 5.1. The splitting between the vector and pseudoscalar 1S states is known as the 1S hyperfine splitting, and is labelled as $\Delta M_{\text{hyp}(1S)}$ . Similarly for the vector and pseudoscalar 2S states, we list the 2S hyperfine splitting $\Delta M_{\text{hyp}(2S)}$ . The spin-averaged 2S – 1S splitting is denoted by $\Delta M_{2S-1S}$ . The splitting between the axial vector $h_c(1P)$ and ground-state vector $J/\psi(1S)$ states is referred to as $\Delta M_{1P-1S}$ . . . . .	105
5.5	Time moments of the charmonium vector correlator on each ensemble, in lattice units and as yet unrenormalised. The $n^{\text{th}}$ moment is raised to the power $1/(n-2)$ — this reduces all of the moments to the same dimension. . . . .	116
5.6	Time moments of the charmonium vector correlators. In the left-hand columns, we list the physical results from our continuum fits and their associated index $n$ . In the right-hand columns, we list the comparable results extracted from experiment in [79] and [80], indexed by $k$ and appropriately normalised for comparison to our results. . . . .	117
5.7	Renormalisation factors determined from the current-current correlator method, for each ensemble listed in Table 5.1. $Z_n$ is the renormalisation factor obtained by matching the $n^{\text{th}}$ lattice moment to its equivalent continuum value, derived from experimental results. . . . .	120
5.8	$\chi^2$ and statistical $Q$ values for continuum fits to the $n^{\text{th}}$ moments of the vector correlator, when renormalised using the listed $Z$ -factors. It is clear that using $Z_8$ results in the minimal $\chi^2$ and maximal $Q$ values. . . . .	121

5.9	Results for selected decay constants (or their ratios) in the charmonium system, as determined on each of the ensembles listed in Table 5.1. The ground-state pseudoscalar decay constant $f_{\eta_c(1S)}$ is absolutely normalised, so we quote a value for it here in lattice units. The decay constants of the vector mesons $J/\psi(1S)$ and $\psi(2S)$ require a renormalisation factor to be matched to continuum results (indeed, we quote the ground-state vector decay constant $f_{J/\psi(1S)}/Z$ before this renormalisation is performed) but this is the same for both mesons on each ensemble, so we can take their ratio to cancel it out. We also determine the ratio of the decay constants of the $\eta_c(1S)$ and $\eta_c(2S)$ as a cross-check, since this should be of the same order as the equivalent quantity for the vectors. . . . .	128
5.10	Results of fits to correlators using the EigenBasis fit method, for three different lattice calculations on the superfine ensemble. We denote pseudoscalar results with $ps$ and vector results with $vec$ . Various input and output parameters of the fits are also listed — in particular, the final column lists the $2S - 1S$ splitting that is discussed in the text.	136



# Chapter 1

## Lattice Quantum Chromodynamics

### 1.1 The Standard Model

The Standard Model of particle physics describes our current understanding of fundamental particles and their interactions. Mathematically, it is represented as a gauge quantum field theory with the symmetries of the unitary product group  $SU(3) \times SU(2) \times U(1)$ .

The particle content of the Standard Model is divided into two classes: fermions, with spin  $\frac{1}{2}$ , and bosons, with spin 1 (or spin 0 in the case of the recently-discovered Higgs boson). Fermions obey the Pauli exclusion principle, meaning that any two fermions are forbidden from occupying the same quantum state, and they interact via the exchange of spin-1 gauge bosons. These bosons are the photon,  $\gamma$ , which mediates the electromagnetic force, the gluon,  $g$ , which mediates the strong force, and the  $Z$  and  $W^\pm$  bosons which mediate the weak force.

The fermions in the Standard Model are further divided into quarks and leptons. There are six flavours of quark (up, down, strange, charm, bottom and top), and six leptons: three which are electrically charged (electron, muon and tau) and three corresponding uncharged neutrinos. These fermions can be arranged in three generations according to their mass and electric charge, as shown in Table 1.1.

The six quarks vary greatly in their masses, and can be arranged in a mass hierarchy which correlates with the three generations. Current world averages for the masses of the quarks in the  $\overline{MS}$  scheme, from [4], are also listed in Table 1.1, and we note the increased magnitude of the masses with each generation. In particular, the mass of the top quark is far greater than any of the others — there is no clear explanation of why this should be the case, and research into this issue may reveal new insights into the origin of quark masses.

For each particle, there also exists a corresponding antiparticle with opposite electric charge. Photons, gluons, and the  $Z$  boson are their own antiparticles; it is

$+\frac{2}{3}e$	up $m_u = 2.3^{+0.7}_{-0.5} \text{ MeV}$	charm $m_c = 1.275 \pm 0.025 \text{ GeV}$	top $m_t = 173.21 \pm 0.51 \pm 0.71 \text{ GeV}$
$-\frac{1}{3}e$	down $m_d = 4.8^{+0.5}_{-0.3} \text{ MeV}$	strange $m_s = 95 \pm 5 \text{ MeV}$	bottom $m_b = 4.18 \pm 0.03 \text{ GeV}$
$-1e$	electron $m_e = 0.510998928(11) \text{ MeV}$	muon $m_\mu = 105.6583715(35) \text{ MeV}$	tau $m_\tau = 1776.82(16) \text{ MeV}$
0	electron neutrino $m_{\nu_e} < 225 \text{ eV}$	muon neutrino $m_{\nu_\mu} < 0.19 \text{ MeV}$	tau neutrino $m_{\nu_\tau} < 18.2 \text{ MeV}$

Table 1.1: The three generations of fermions in the Standard Model, with the world average determinations of their masses from [4]. The first column lists their electric charges in units of the elementary charge  $e$ .

currently an open question as to whether neutrinos exhibit this behaviour [5]. If they do, they would be the only fermions to do so.

The fourth fundamental force, gravity, is not included in the Standard Model for two reasons. Firstly, it is far weaker than any of the three other forces at the scales of fundamental particles (with a relative strength of  $10^{-41}$  for two up quarks in comparison to their electromagnetic interaction) and so is frequently negligible in calculations of processes in elementary particle physics. The second reason is that we do not yet have a consistently renormalizable quantum theory of gravity. This is necessary to accurately describe conditions where enough mass is present for spacetime to be appreciably curved following the axioms of general relativity, and yet in a small enough region of space that quantum effects are also important. Such conditions arise within the event horizon of a black hole, for example, or in the very early universe following the Big Bang.

## 1.2 Quantum Chromodynamics

The SU(3) sector of the Standard Model, which deals with interactions of the strong force, is known as quantum chromodynamics (QCD). The QCD Lagrangian is [6]

$$\mathcal{L}_{\text{QCD}} = \sum_f \bar{\psi}_f (i\gamma_\mu D_\mu - m_f) \psi_f - \frac{1}{4} F_{\mu\nu}^a F^{\mu\nu a} \quad (1.1)$$

where the sum is over quark flavour  $f$ .  $\psi$  is the quark field,  $m_f$  is the mass of the quark, and  $\gamma_\mu$  are the Dirac gamma matrices:

$$\gamma_t = \begin{pmatrix} \mathbb{1} & 0 \\ 0 & -\mathbb{1} \end{pmatrix} \quad \gamma_i = \begin{pmatrix} 0 & \sigma_i \\ \sigma_i & 0 \end{pmatrix} \quad (1.2)$$

where  $\sigma_i$  are the Pauli matrices:

$$\sigma_x = \begin{pmatrix} 0 & 1 \\ 1 & 0 \end{pmatrix} \quad \sigma_y = \begin{pmatrix} 0 & -i \\ i & 0 \end{pmatrix} \quad \sigma_z = \begin{pmatrix} 1 & 0 \\ 0 & -1 \end{pmatrix}. \quad (1.3)$$

We also define  $\gamma_5 = \gamma_x \gamma_y \gamma_z \gamma_t$ , and note that  $\gamma_\mu^2 = \mathbb{1}$ . It follows that  $\gamma_5^2 = \mathbb{1}$  also.

$F_{\mu\nu}^a$  is the gluon field strength tensor, defined as

$$F_{\mu\nu}^a = \partial_\mu A_\nu^a - \partial_\nu A_\mu^a - g_s f^{abc} A_\mu^b A_\nu^c \quad (1.4)$$

with  $A_\mu$  the gluon field and  $f^{abc}$  the structure constants of the SU(3) group.  $g_s$  defines the strength of the strong coupling, and is related to the strong coupling constant  $\alpha_s$  through  $\alpha_s = g_s^2/4\pi$ .

The interactions between the quark and gluon fields are contained within the covariant derivative  $D_\mu$ :

$$D_\mu = \partial_\mu + ig_s A_\mu^a \frac{\lambda_a}{2} \quad (1.5)$$

where  $\lambda_a$  is a Gell-Mann matrix. The Gell-Mann matrices are a representation of the generators of SU(3).

QCD is a non-Abelian gauge theory in which the gauge bosons, the gluons, self-interact according to the last term in equation 1.4. The QCD vacuum therefore consists of strongly-interacting background gluons as well as virtual quark-antiquark pairs, referred to as sea quarks.

Quarks and gluons carry an SU(3) ‘colour’ charge, but coloured states are never observed. Instead, they are confined within colourless objects called hadrons, and the constituent quarks bound inside a hadron are known as valence quarks. Hadrons containing three quarks are known as baryons — the familiar proton and neutron are examples of these — and hadrons containing one quark and one antiquark are known as mesons.

A further important feature of QCD is that the theory is asymptotically free [7, 8], meaning that the strength of the interaction between quarks and gluons decreases with increasing energy. Consequently, at low energies such as those for valence quarks bound inside hadrons, calculations using perturbative methods will not be applicable, since  $g_s$  is too large to perform an expansion in. For such cases, we require a non-perturbative formulation such as lattice QCD.

### 1.2.1 Quarkonium

Before we delve into formulating lattice QCD, we briefly outline different meson states that will be relevant to the work presented in this thesis.

As mentioned, mesons are hadrons consisting of one quark and one antiquark. The name ‘quarkonium’ refers to a flavourless meson state which consists of a quark

and its own antiquark, and usually refers to either charmonium ( $c\bar{c}$ ) or bottomonium ( $b\bar{b}$ ). The top quark has such a high mass that it will undergo electroweak decay before it forms a bound state, and the lighter quarks (up, down and strange) form admixtures such as the  $\eta$  and  $\pi$  mesons rather than pure  $q\bar{q}$  states.

We will use ‘heavyonium’ to refer specifically to quarkonium states formed by heavy quarks — that is, charmonium or bottomonium, or analogous states formed on the lattice by quarks with masses between those of the  $c$  and  $b$  quarks. The results presented in this thesis will primarily concern properties of charmonium or bottomonium states, and these will be detailed further in the relevant chapters.

### 1.3 Path Integrals

To construct a formulation of QCD on the lattice it is instructive to consider the path integral formulation of quantum field theory [9]. Firstly we note that the action  $\mathcal{S}$  for a quantum field theory is given by the integral of the Lagrangian, viz.

$$\mathcal{S}_{\text{QCD}} = \int d^4x \mathcal{L}_{\text{QCD}}. \quad (1.6)$$

The path integral approach allows us to express the amplitude for some event as a quantum superposition of all possible paths between the initial and final states of the system, with each path weighted by the action. The expectation value for some operator  $\Gamma$  in QCD can then be written as

$$\langle \Gamma \rangle = \frac{\int \mathcal{D}\phi \Gamma e^{i\mathcal{S}_{\text{QCD}}}}{\int \mathcal{D}\phi e^{i\mathcal{S}_{\text{QCD}}}} \quad (1.7)$$

where the denominator is simply for normalisation.

It is useful in a lattice formulation to Wick rotate the fields into Euclidean space, by applying the transformation  $t \rightarrow it$  in the time direction. The action then transforms as  $\mathcal{S}_{\text{QCD}} \rightarrow i\mathcal{S}_{\text{QCD}}$ . This simplifies the contribution of the action to the path integral since the oscillating complex exponential is transformed to a decaying exponential,  $e^{i\mathcal{S}_{\text{QCD}}} \rightarrow e^{-\mathcal{S}_{\text{QCD}}}$ , and is then easier to integrate [10]. Explicitly, after the Wick rotation we now have

$$\langle \Gamma \rangle = \frac{\int \mathcal{D}\phi \Gamma e^{-\mathcal{S}_{\text{QCD}}}}{\int \mathcal{D}\phi e^{-\mathcal{S}_{\text{QCD}}}}. \quad (1.8)$$

The integration measure  $\mathcal{D}\phi$  denotes that the path integral is over all possible values of each field in the Lagrangian. In continuum QCD, the quark and gluon fields in the Lagrangian have values at all points in spacetime. In a numerical simulation, we would therefore require an infinite number of integrations over this infinite number of points, which is of course not feasible. To proceed, we must somehow regularise the spacetime.

## 1.4 Discretising QCD

In 1974, Kenneth Wilson showed that it was possible to reduce the infinite number of integrations required in the QCD path integral by discretising the theory onto a 4-dimensional hypercubic lattice with a finite volume [11]. Quark fields are then defined only on the lattice sites and are represented as 3-component colour vectors.

Gluon fields are defined as  $3 \times 3$  matrices on the gauge links between the lattice sites. A gauge link connecting site  $x$  to the next site in the forward  $\mu$  direction,  $(x + \hat{\mu})$ , is defined as

$$U_\mu(x) = e^{ig_s A_\mu(x)} \quad (1.9)$$

with  $A_\mu(x)$  the gluon field. The conjugate  $U_\mu^\dagger(x)$  represents the reverse link from  $(x + \hat{\mu})$  to  $x$ , since the gauge links are unitary. This construction preserves gauge invariance when parallel-transporting colour across the links. Any closed loop of gluon fields or any connected path of gauge links terminated by quark fields, as shown in Figure 1.1, will be gauge-independent.

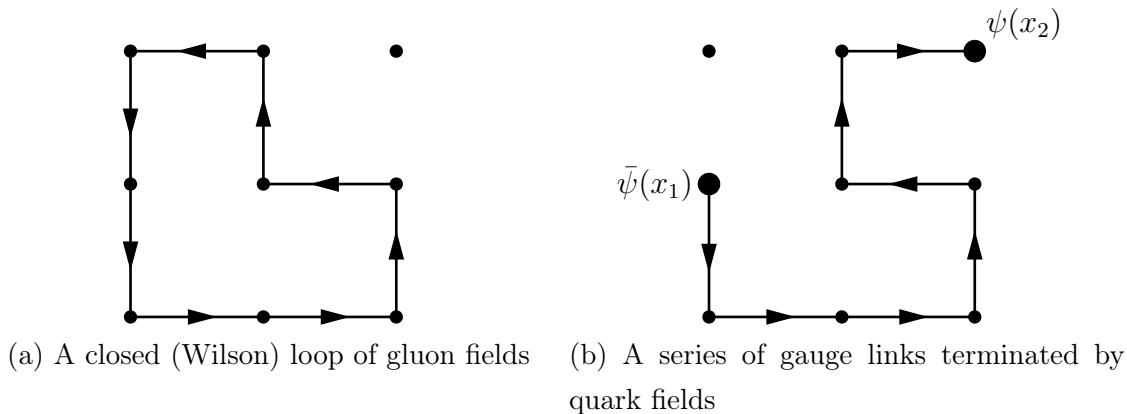


Figure 1.1: Gauge-independent quantities on the lattice

The distance between lattice points is referred to as  $a$ , the lattice spacing. For all of the lattices used for calculations in this thesis,  $a$  is the same in each of the 4 lattice directions. It is also possible to use anisotropic lattices, where  $a$  is smaller in the time direction than in the three spatial directions, to produce a better signal for some classes of calculation [12].

Now that we have discretised our spacetime, there are methods available to us for the calculation of quantities on the lattice. The practicalities of these methods will be described in more detail in the next chapter, once we have defined discretised actions for the quark and gluon fields. For now, though, we should note that in translating continuum QCD to the lattice, discretisation errors are unavoidably introduced, and must be kept under control in order to obtain accurate physical values. In analysing lattice results, we may choose to either perform a continuum extrapolation  $a \rightarrow 0$  (provided we have results at multiple lattice spacings), or

simply include discretisation effects as a systematic error. It is clear that in both cases, discretisation errors will have a significant negative impact on the final result if they are not reduced to an acceptable level.

### 1.4.1 Lattice Gluon Action

The simplest discretisation of the gluonic part of the QCD action is known as the Wilson action, and is given by [12]

$$\mathcal{S}_W = \beta \sum_{\text{plaq}} \left( 1 - \frac{1}{n_c} \text{Re} [\text{Tr}(U_{\text{plaq}})] \right) \quad (1.10)$$

where  $\beta$  is the gauge coupling, equal to  $2n_c/g_s^2 \equiv 6/g_s^2$ .  $n_c$  is the number of colour charges in the theory, which is 3 for QCD. The sum is over  $1 \times 1$  loops of gauge links known as plaquettes, defined by

$$U_{\text{plaq}} = U_\mu(x) U_\nu(x + \hat{\mu}) U_\mu^\dagger(x + \hat{\nu}) U_\nu^\dagger(x) \quad (1.11)$$

and shown in Figure 1.2.

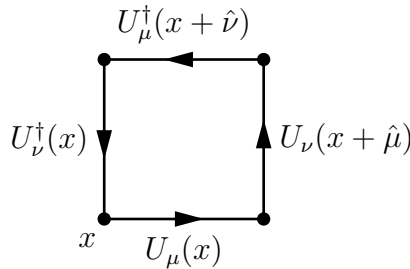


Figure 1.2: The smallest possible Wilson loop on the lattice, a  $1 \times 1$  loop of gauge links known as a plaquette.

In the continuum limit, the Wilson gluon action reduces to the purely gluonic part of the QCD Lagrangian. We are free to use any lattice action with this property in our simulations. This is a useful tool in combatting discretisation errors which appear at finite lattice spacing:

$$\mathcal{S}_W^{\text{lattice}} = \mathcal{S}_W^{\text{continuum}} + \mathcal{O}(a^2) + \dots \quad (1.12)$$

Symanzik proposed a programme of improvement in [13, 14], improving the Wilson action by adding counterterms that vanish in the continuum limit. For example, two six-link Wilson loop terms — a rectangle  $U_r$  and a ‘parallelogram’  $U_p$  — can be added to the Wilson action viz.

$$\begin{aligned} \mathcal{S}_W = \beta \sum_{\text{plaq}} \left( 1 - \frac{1}{3} \text{Re} [\text{Tr}(U_{\text{plaq}})] \right) \\ + \beta_r \sum_r \left( 1 - \frac{1}{3} \text{Re} [\text{Tr}(U_r)] \right) \\ + \beta_p \sum_p \left( 1 - \frac{1}{3} \text{Re} [\text{Tr}(U_p)] \right) \end{aligned} \quad (1.13)$$

where  $\beta_r$  and  $\beta_p$  are determined such that they cancel the discretisation errors arising from the plaquettes in the first term. These loops are depicted in Figure 1.3.

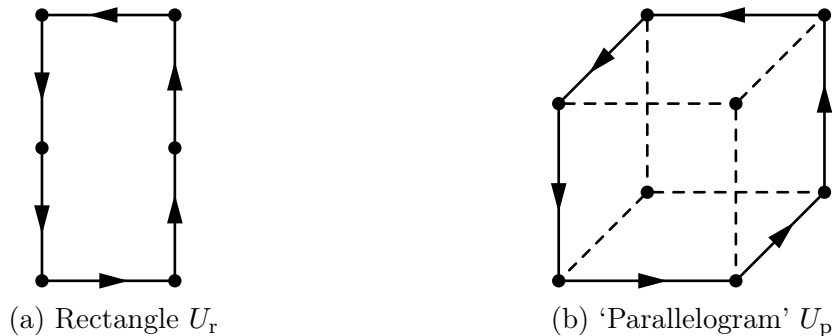


Figure 1.3: The six-link Wilson loop terms added by the Symanzik improvement procedure

The original  $\beta$  parameter requires retuning for improved gauge actions to ensure that we accurately match the continuum action, and for the MILC ensembles that we describe in chapter 2 [15, 16],  $\beta$  is set to be  $10/g_s^2$ .

## 1.4.2 Fermions on the Lattice

The fermionic part of the continuum QCD action is naively discretised by replacing the covariant derivative  $D_\mu$  with a finite difference operator  $\Delta_\mu$ , to obtain

$$\mathcal{S}_f = \sum_x \bar{\psi}(x) (\gamma_\mu \Delta_\mu + m) \psi(x) \quad (1.14)$$

for a quark of mass  $m$ . The simplest difference operator is that which is averaged over the forward and backward gauge links, namely

$$\Delta_\mu \psi(x) = \frac{1}{2} (U_\mu(x) \psi(x + \hat{\mu}) - U_\mu^\dagger(x - \hat{\mu}) \psi(x - \hat{\mu})) . \quad (1.15)$$

These links are visualised in Figure 1.4.

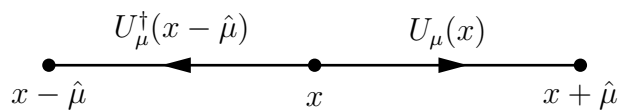


Figure 1.4: The gauge links used in applying the difference operator  $\Delta_\mu$  to the field  $\psi(x)$ .

## The Doubling Problem

The naive quark discretisation suffers from a problem known as doubling, for reasons which will become clear. To identify the source of this problem, it is instructive

to examine the fermion propagator in momentum space. By applying a Fourier transform to the continuum fermion fields, we can obtain the continuum action in momentum space, which is

$$\frac{1}{(2\pi)^4} \int dp \bar{\Psi}(p)(i\gamma^\mu p_\mu + m)\Psi(p) \quad (1.16)$$

with  $p_\mu$  the momentum operator and  $\Psi(p)$  the fermion fields in momentum space. The propagator in momentum space is then the inverse of  $(i\gamma^\mu p_\mu + m)$ .

On the lattice, our Fourier transform gives a different result since we have a finite difference operator instead of the derivative. In addition, due to the finite lattice spacing  $a$ , the lattice momentum is constrained to be between  $p = \pm\frac{\pi}{a}$ . The lattice action in momentum space is then

$$\frac{1}{(2\pi)^4} \int_{-\frac{\pi}{a}}^{+\frac{\pi}{a}} dp \bar{\Psi}(p)(i\gamma^\mu \frac{\sin p_\mu a}{a} + m)\Psi(p) \quad (1.17)$$

and so the inverse propagator on the lattice is  $(i\gamma^\mu \frac{\sin p_\mu a}{a} + m)$ .

The lattice propagator behaves like the continuum propagator for  $\sin p_\mu a = 0$ , and this occurs whenever each component of  $p_\mu$  is either 0 or  $\frac{\pi}{a}$ . Therefore, a  $d$ -dimensional propagator represents  $2^d$  identical fermions on the lattice, which must reduce to a single physical fermion in the continuum limit. In the work presented in this thesis, we use 4-dimensional lattices, and so in using the naive quark discretisation we would obtain 15 extra copies of the same quark flavour for each quark we attempted to simulate.

## Wilson Action

Kenneth Wilson determined that the doubling problem could be addressed by including an additional two-link term in the fermion action [17]:

$$\mathcal{S}_f^W = \mathcal{S}_f - \sum_x \bar{\psi}(x) \frac{r}{2} \Delta_\mu^2 \psi(x) \quad (1.18)$$

with Wilson parameter  $r$  which is usually set to 1, and the two-link finite difference operator  $\Delta_\mu^2$  defined as

$$\Delta_\mu^2 \psi(x) = U_\mu(x) \psi(x + \hat{\mu}) + U_\mu^\dagger(x - \hat{\mu}) \psi(x - \hat{\mu}) - 2\psi(x). \quad (1.19)$$

This gives the doublers a mass in the continuum limit and thus decouples them from the theory. To see this, consider the inverse lattice propagator in this case:

$$\left( i\gamma^\mu \frac{\sin p_\mu a}{a} + m + \frac{2r}{a} (\cos p_\mu a - 1) \right). \quad (1.20)$$

It is clear that the new third term vanishes only for the quark with  $p_\mu = 0$ , and so prevents the doublers from behaving like continuum quarks.

Unfortunately the Wilson action explicitly breaks chiral symmetry [17]. There are other methods which address the doubling problem — for example, we can add counterterms in a programme of Symanzik improvement, much like for the gluon action, to obtain what is known as the Wilson clover action [18] — but the method we focus on in this thesis is known as *staggering*.

## 1.5 Staggered Fermions

Staggering addresses the doubling problem by reducing the total number of quarks of a given flavour from 16 to 4. This is achieved through the use of a staggering transformation [17, 19, 20] given by

$$\psi(x) \rightarrow \Omega(x)\chi(x) \quad (1.21)$$

$$\bar{\psi}(x) \rightarrow \bar{\chi}(x)\Omega^\dagger(x) \quad (1.22)$$

where we define

$$\Omega(x) = \prod_{\mu} (\gamma_{\mu})^{x_{\mu}}. \quad (1.23)$$

Note that, since  $\gamma_{\mu}^2 = \mathbb{1}$ , the staggering matrix  $\Omega(x)$  depends only on whether the coordinates of site  $x$  are even or odd, and therefore, in four spacetime dimensions, there are only  $2^4 = 16$  different  $\Omega$  matrices. It follows that

$$\Omega(x + n\hat{\mu}) = \begin{cases} \Omega(x) & \text{for } n \text{ even} \\ \Omega(x + \hat{\mu}) & \text{for } n \text{ odd} \end{cases} \quad (1.24)$$

and similarly, for neighbouring lattice sites,

$$\Omega(x + \hat{\mu}) = \pm \gamma_{\mu} \Omega(x) \quad (1.25)$$

with the phase factor ( $\pm$ ) dependent on  $x$  and the direction  $\mu$  in which we travel to its neighbour.

It follows readily from the above definitions that

$$\Omega^\dagger(x)\Omega(x) = \mathbb{1} \quad (1.26)$$

and also that

$$\Omega^\dagger(x)\gamma_{\mu}\Omega(x \pm \hat{\mu}) = (-1)^{x_{\mu}^<} \quad (1.27)$$

where we have used the notation

$$x_{\mu}^< = \sum_{\nu < \mu} x_{\nu}. \quad (1.28)$$

Therefore, applying the staggering transformation to the naive fermion action will absorb the Dirac  $\gamma$  matrix to give the staggered action:

$$\mathcal{S}_{\text{stag}} = \sum_x \bar{\chi}(x) \left( (-1)^{x_\mu^<} \Delta_\mu + m \right) \chi(x). \quad (1.29)$$

The staggered action is diagonal in spin space, meaning that the four components of the spinor  $\chi(x)$  are equal. Thus we may discard three of them, which reduces the number of doublers by a factor of 4. The 4 remaining doublers in the staggered formulation are usually referred to as tastes, and must be accounted for in staggered simulations. However, we are now simulating a one-component spinor instead of a four-component spinor, which will be less computationally intensive. In addition, we still have an exact symmetry in our Lagrangian, unlike in the case of Wilson fermions.

Note that the Dirac  $\gamma$  matrices have been replaced in the action by position-dependent phases. This will also be helpful in implementing computer simulations, and we will return to this point in the next chapter.

### 1.5.1 Asqtad Improvement

To attempt to improve our naive staggered discretisation, we consider the main sources of discretisation errors. The first of these is in the replacement of our derivatives with finite-difference operators. This can be improved by introducing a 3-link term referred to as the Naik term [21]:

$$\Delta_\mu \rightarrow \Delta_\mu - \frac{1}{6} \Delta_\mu^3. \quad (1.30)$$

Thanks to the identity in equation 1.24, the Naik term has no adverse effect on the staggered phase factor since it acts across an odd number of links and so behaves exactly like a 1-link term.

The second major source of error is taste-exchange interactions. As a consequence of the doubling symmetry, a low-energy quark which absorbs momentum  $\pi/a$  is not driven off-shell, but instead changes into a low-energy quark of a different taste. The simplest process by which this occurs is the emission of a single gluon with any components of its four-momentum equal to  $\pi/a$  — recall that this is the highest possible momentum on the lattice, and that this is the point where the doublers live. The emitting quark will then, therefore, change taste. Since this gluon is highly virtual (with momentum scale  $q^2 \approx (\pi/a)^2$ ), it must immediately be reabsorbed by another quark, which also changes taste. This process is illustrated in Figure 1.5.

Taste-exchange interactions are unphysical and so it is desirable to remove their effects by reducing the coupling between quarks and high-momentum gluons to zero

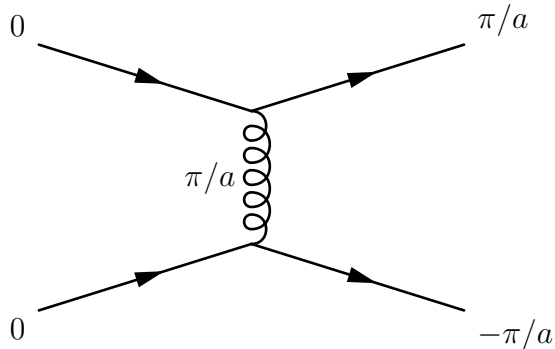


Figure 1.5: A Feynman diagram of taste exchange. The quark entering on the lower left of the diagram emits a gluon with momentum  $\pi/a$ , and thus changes taste. This gluon is highly virtual and is immediately reabsorbed by the quark entering on the top left, which also changes taste.

[22, 23, 24]. This can be implemented by introducing a form factor to the gluon-quark vertex which vanishes for taste-changing gluons, and this is done by smearing the link operator in the action:

$$U_\mu(x) \rightarrow \mathcal{F}_\mu U_\mu(x) \quad (1.31)$$

where the smearing operator  $\mathcal{F}_\mu$  is [20]

$$\mathcal{F}_\mu = \prod_{\rho \neq \mu} \left( 1 + \frac{a^2 \delta_\rho^{(2)}}{4} \right) \quad (1.32)$$

and  $\delta_\rho^{(2)}$  approximates a covariant second derivative:

$$\begin{aligned} \delta_\rho^{(2)} U_\mu(x) &= \frac{1}{a^2} (U_\rho(x) U_\mu(x + \hat{\rho}) U_\rho^\dagger(x + \hat{\mu}) \\ &\quad - 2 U_\mu(x) \\ &\quad + U_\rho^\dagger(x - \hat{\rho}) U_\mu(x - \hat{\rho}) U_\rho(x - \hat{\rho} + \hat{\mu})) . \end{aligned} \quad (1.33)$$

The smeared operator  $\mathcal{F}_\mu U_\mu(x)$  is then identical to the unsmeared link operator  $U_\mu(x)$  (up to  $\mathcal{O}(a^2)$  errors, which we shall deal with momentarily) for gluons with low momentum. However, when acting on a gluon field that has any component of its momentum other than  $q_\mu$  equal to  $\pi/a$ , the smeared operator  $\mathcal{F}_\mu$  will vanish [24]. For gluons with  $q_\mu = \pi/a$ , the corresponding quark-gluon vertex is approximately zero even with the naive quark action, so no correction is necessary [24].

Smearing with  $\mathcal{F}_\mu$  removes the leading-order taste-exchange interactions, but introduces new discretisation errors of order  $a^2$ . It is possible to remove these by adding a new term known as the Lepage term [24] to obtain

$$\mathcal{F}_\mu^{\text{asqtad}} = \mathcal{F}_\mu - \sum_{\rho \neq \mu} \frac{a^2 (\delta_\rho)^2}{4} \quad (1.34)$$

where  $\delta_\rho$  approximates a covariant first derivative:

$$\begin{aligned} \delta_\rho U_\mu(x) = \frac{1}{a} & \left( U_\rho(x) U_\mu(x + \hat{\rho}) U_\rho^\dagger(x + \hat{\mu}) \right. \\ & \left. - U_\rho^\dagger(x - \hat{\rho}) U_\mu(x - \hat{\rho}) U_\rho(x - \hat{\rho} + \hat{\mu}) \right) . \end{aligned} \quad (1.35)$$

The Lepage term does not affect taste exchange but clearly counteracts the errors introduced by  $\mathcal{F}_\mu$ .

Smearing with  $\mathcal{F}_\mu^{\text{asqtad}}$  is implemented in practice by introducing fattened gauge links, consisting of a combination of 1-link, 3-link, 5-link and 7-link paths between lattice sites [25]. The Lepage term is introduced via the addition of a second 5-link term. These smeared gauge links are illustrated in Figure 1.6 below.

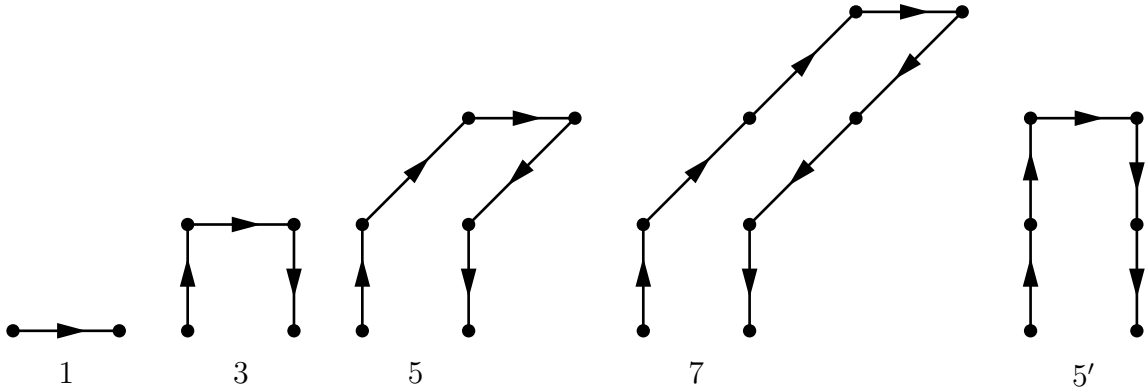


Figure 1.6: The smeared gauge links included in the asqtad action, which together constitute a fattened gauge link. The 5-link structure responsible for implementing the Lepage term is the rightmost one, labelled 5'.

Starting from the naive staggered action of equation 1.29, if we include the Naik term in the derivative and smear the gauge links with  $\mathcal{F}_\mu^{\text{asqtad}}$ , we have removed all tree-level  $\mathcal{O}(\alpha_s a^2)$  errors arising from taste-exchange interactions. The resulting action is known as the asqtad ( $a^2$  tadpole improved) action, and is given by

$$\mathcal{S}_{\text{asqtad}} = \sum_x \bar{\chi}(x) \left[ \sum_\mu \gamma_\mu \left( \Delta_\mu(V) - \frac{1}{6} \Delta_\mu^3(U) \right) + m \right] \chi(x) \quad (1.36)$$

where  $V$  is the smeared link operator defined by

$$V_\mu(x) = \mathcal{F}_\mu^{\text{asqtad}} U_\mu(x) . \quad (1.37)$$

The ‘tadpole’ improvement portion of the asqtad name refers to a procedure whereby each link operator  $U_\mu$  in the action is divided by  $u_0$ , the scalar mean value of the link [26, 27]. The mean link can be nonperturbatively defined in terms of the value of the plaquette  $U_{\text{plaq}}$  measured on the lattice [26]:

$$u_0 \equiv \left\langle \frac{1}{3} \text{Tr}(U_{\text{plaq}}) \right\rangle^{1/4} . \quad (1.38)$$

This has the effect of reducing the large perturbative contributions of the so-called ‘tadpole’ diagrams of QCD. However, it is also prudent to note that tadpole improvement is not required when the gauge links are smeared and reunitarised [28, 10] — just like those which we will shortly describe.

## 1.5.2 Highly Improved Staggered Quarks

The remaining discretisation errors in the asqtad action are dominated by taste-exchange interactions within quark loops, i.e. at one-loop order rather than at tree level. These effects can be suppressed by repeated smearings of the gauge links, as discussed in detail in [20].

Multiple iterations of the smearing process can introduce further problems. It is immediately apparent that we must take care not to introduce further  $\mathcal{O}(a^2)$  errors, which would only be compounded by multiple smearings. This can be avoided by using an  $a^2$ -improved smearing operator such as  $\mathcal{F}_\mu^{\text{asqtad}}$  above:

$$\mathcal{F}_\mu^{\text{asqtad}} \rightarrow \mathcal{F}_\mu^{\text{asqtad}} \mathcal{F}_\mu^{\text{asqtad}} \quad (1.39)$$

Another problem with multiple smearings is that diagrams with two-gluon vertices are unphysically enhanced. This is due to the replacement of single gauge links in the action with a sum of large numbers of products of links. Thankfully we can eliminate this problem by reunitarising the link operator after smearing:

$$\mathcal{F}_\mu^{\text{asqtad}} \rightarrow \mathcal{F}_\mu^{\text{asqtad}} \mathcal{U} \mathcal{F}_\mu^{\text{asqtad}} \quad (1.40)$$

where  $\mathcal{U}$  is an SU(3) projection operator<sup>1</sup>. This has no effect on single-gluon vertices, and so no additional  $\mathcal{O}(a^2)$  errors are introduced.

We may simplify our double-smearing operator by moving both Lepage terms (contained within  $\mathcal{F}_\mu^{\text{asqtad}}$  as per equation 1.34) to be applied in the outermost smearing step. We therefore define the double-smearing operator as

$$\mathcal{F}_\mu^{\text{HISQ}} = \left( \mathcal{F}_\mu - \sum_{\rho \neq \mu} \frac{a^2 (\delta_\rho)^2}{2} \right) \mathcal{U} \mathcal{F}_\mu \quad (1.41)$$

with  $\mathcal{F}_\mu$  as defined in equation 1.32, and the new Lepage correction term twice that defined in equation 1.34.

Returning briefly to examine tree-level diagrams once again, we note that the largest remaining discretisation errors are of order  $(ap_\mu)^4$ . These will be negligibly

---

<sup>1</sup>In fact it is valid and advantageous to reunitarise the link operator by projecting onto U(3), not necessarily SU(3), since the key requirement we wish to fulfil here is that the gluons are unitary. This is how the HPQCD collaboration currently defines the HISQ action, making it slightly simpler to compute. See [29] for some further detail.

small for light (up, down and strange) quarks, but larger for the more massive charm quarks — on the order of  $(am_c)^4$ , since the  $c$  quarks in typical mesons can be considered to be nonrelativistic. These errors will appear, for example, in the relativistic dispersion relation for the charm quark, and can be removed by adjusting the coefficient of the Naik term in the derivative:

$$\Delta_\mu \rightarrow \Delta_\mu - \frac{1}{6}(1 + \varepsilon)\Delta_\mu^3. \quad (1.42)$$

Our choice of  $\varepsilon$  is dependent on the lattice quark mass  $am$  and is determined by a perturbative expansion in this parameter, stated explicitly in [20]:

$$\varepsilon = -\frac{27}{40}(am)^2 + \frac{327}{1120}(am)^4 - \frac{5843}{53760}(am)^6 + \frac{153607}{3942400}(am)^8 - \dots. \quad (1.43)$$

The particular values we use in our calculations are noted alongside the relevant quark masses in chapters 4 and 5.

With an appropriate choice for  $\varepsilon$ , discretisation errors through order  $(am)^4$  are removed, and the tree-level dispersion relation for the charm quark becomes  $c^2 = 1 + \mathcal{O}((am_c)^{12})$  at leading order in  $v/c$  [20], with  $v$  the quark's velocity. It is clear that the action we are currently constructing will be capable of simulating charm quarks very accurately.

Applying  $\mathcal{F}_\mu^{\text{HISQ}}$  to the gauge links, and retuning the coefficient of the Naik term, the resulting action is

$$\mathcal{S}_{\text{HISQ}} = \sum_x \bar{\chi}(x) (\gamma_\mu \mathcal{D}_\mu^{\text{HISQ}} + m) \chi(x) \quad (1.44)$$

where we define the difference operator  $\mathcal{D}_\mu^{\text{HISQ}}$  as

$$\mathcal{D}_\mu^{\text{HISQ}} = \Delta_\mu(W) - \frac{1}{6}(1 + \varepsilon)\Delta_\mu^3(X) \quad (1.45)$$

with the smeared gauge links

$$W_\mu(x) = \mathcal{F}_\mu^{\text{HISQ}} U_\mu(x) \quad (1.46)$$

and

$$X_\mu(x) = \mathcal{U} \mathcal{F}_\mu U_\mu(x). \quad (1.47)$$

This action is known as the Highly Improved Staggered Quark (HISQ) action [20], and is the action used for valence quarks in all the simulations presented in this thesis.

# Chapter 2

## Calculations on the Lattice

In the previous chapter we discretised both fermionic and gluonic parts of the QCD action onto a regularised spacetime lattice. We now wish to proceed with calculating expectation values for QCD quantities using the path integral formulation set forth in section 1.3, viz.

$$\langle \Gamma \rangle = \frac{\int \mathcal{D}\phi \Gamma e^{-\mathcal{S}_{\text{QCD}}}}{\int \mathcal{D}\phi e^{-\mathcal{S}_{\text{QCD}}}} \quad (2.1)$$

for some operator  $\Gamma$ .

Now that we have our lattice action, we can describe this path integral in a form suitable for simulation. For gauge links  $U_\mu$ , and anticommuting quark and antiquark fields represented by Grassmann numbers  $\psi$  and  $\bar{\psi}$ , we have:

$$\langle \Gamma \rangle = \frac{1}{Z} \int \mathcal{D}U_\mu \mathcal{D}\psi \mathcal{D}\bar{\psi} \Gamma e^{-\mathcal{S}_g + \bar{\psi}(\not{D} + m)\psi} \quad (2.2)$$

with  $\mathcal{S}_g$  our chosen gauge action,  $\mathcal{D}\psi$  the integration measure, and  $m$  the quark mass.  $\not{D}$  is the difference operator corresponding to our chosen action from the previous chapter (inclusive of the relevant gamma matrices), making  $(\not{D} + m)$  the corresponding Dirac matrix.  $Z$  is simply for normalisation:

$$Z = \int \mathcal{D}U_\mu \mathcal{D}\psi \mathcal{D}\bar{\psi} e^{-\mathcal{S}_g + \bar{\psi}(\not{D} + m)\psi} . \quad (2.3)$$

The quark and antiquark fields must be integrated out to obtain a path integral of the form

$$\langle \Gamma \rangle = \frac{1}{Z} \int \mathcal{D}U_\mu \Gamma e^{-\mathcal{S}_g} \det(\not{D} + m) \quad (2.4)$$

which can be calculated on the lattice, as we will detail in the following sections. If the operator  $\Gamma$  has any dependence on the fermion fields, integrating these out means that we must also include a quark propagator  $(\not{D} + m)^{-1}$  connecting the positions of the fields, as well as the fermionic determinant above [30].

We note that by integrating out the quark and antiquark fields, this formulation has separated the valence quarks — those which appear in the propagator — from

the sea quarks, which are accounted for by the determinant in equation 2.4. This means that we are now free to choose different masses for the sea quarks and valence quarks in our simulations, a point that will be useful when generating gauge configurations.

## 2.1 Gauge Configurations

By virtue of the lattice and of our discretised actions, we no longer need to perform our path integration over an infinite spacetime. However, we must still integrate over all possible configurations of the gluon field in equation 2.4, and this makes the number of integration variables so large as to be impractical.

To overcome this problem, we note that the path integral is effectively a weighted average over paths with weight  $e^{-S_g + \ln \det(\mathcal{D} + m)}$ . This means that instead of performing the integration directly, it is possible to use Monte Carlo importance sampling, whereby a representative ensemble of gauge configurations is generated. A configuration is simply a set of field values on all gauge links of the lattice, and these are generated in a Markov chain such that the probability of a single configuration being present in the ensemble is proportional to  $e^{-S_g + \ln \det(\mathcal{D} + m)}$ . We may then estimate the expectation value of  $\Gamma$  by computing its value on each configuration and performing a simple unweighted average over these results.

This method has a further advantage in that configurations need only be generated once, and can then be used repeatedly for a variety of different lattice calculations. The downside is that the Monte Carlo estimate of an expectation value will never be exact — statistical errors are inherent in the procedure which vanish only as infinitely many configurations are included in the ensemble. However, it is possible to keep these errors under control by using enough configurations: as  $N$ , the number of configurations, increases, the statistical error decreases as  $1/\sqrt{N}$  [31].

Generating gauge configurations which facilitate accurate calculations presents a number of challenges. The most important of these is including the effects of sea quarks. Early calculations in lattice QCD were forced to neglect sea quarks entirely, by setting  $\det(\mathcal{D} + m) = 1$  in equation 2.4, due to limitations in raw computational power. This is known as the quenched approximation, and it leads to large systematic errors of order 10% [32, 33]. It is only relatively recently that enough computing power has become available to make unquenched simulations possible [33].

The principal difficulty here is that direct evaluation of the determinant  $\det(\mathcal{D} + m)$  is not viable. By rewriting it in terms of so-called ‘pseudofermion’ fields, we can exchange the determinant for the inverse of the Dirac operator,  $(\mathcal{D} + m)^{-1}$  [30]. This is more feasible than computing the determinant, but presents its own

issues — we must now invert the large sparse matrix  $(\not{D} + m)$ . The computational cost of this inversion is proportional to the ratio of the matrix's maximum and minimum eigenvalues, and since its minimum eigenvalue is approximately  $m$  [30], more computation time is required for smaller sea quark masses.

As a compromise, configurations are frequently generated with heavier-than-physical up and down quark masses in the sea, requiring the results of calculations to be extrapolated to the physical point. Additional extrapolations will of course introduce additional errors into the calculation, but these can be controlled by simulating at a variety of light sea quark masses. State-of-the-art configurations are now available with up and down quarks in the sea at their approximate physical masses, and some of these will be detailed in the next section.

Up and down quarks are nearly degenerate in their masses, and their degree of non-degeneracy is quantified by the breaking of a symmetry known as isospin. Generally, isospin breaking effects are too small to affect the results of lattice calculations, and so sea quarks are simulated in the isospin-symmetric limit with  $m_u = m_d \equiv m_\ell = (m_u^{\text{phys}} + m_d^{\text{phys}})/2$ . However, the precision of lattice calculations is beginning to reach the point where isospin breaking effects should be included, and research is underway into simulations with  $m_u \neq m_d$ .

An additional issue is encountered when simulating sea quarks with staggered actions, namely that we must somehow deal with the extra tastes that these actions introduce. Traditionally this has been done by replacing the determinant  $\det(\not{D} + m)$  in the path integral with its fourth root, which then represents only a single taste (per quark flavour). This procedure, known as *rooting*, has been controversial, and its validity has been discussed and tested extensively in the lattice literature [15, 34, 35, 36, 37, 38, and references therein]. While there is no rigorous mathematical proof of its validity, it suffices to note for our purposes that a number of criticisms of the rooting procedure have been comprehensively addressed in the previous references, and, while there are still open questions to be resolved, the numerical and theoretical evidence in favour of its validity remains strong.

### 2.1.1 Algorithms and Computing Power

Ensembles of gauge configurations are generated using the Hybrid Monte Carlo algorithm [39], or more modern variants thereof which include the effects of sea quarks [40, 41, 42]. Starting from some randomly-chosen initial values, the algorithm performs a molecular dynamics (MD) evolution of the configuration in a fictitious time dimension. A Metropolis step is included which decides whether to accept or reject the updates based on the variation of the action that they induce. A certain number of configurations are discarded at the beginning of this procedure to allow

the values to thermalise.

Modern algorithms spend most of their computer time inverting the Dirac matrix  $(\not{D} + m)$  in order to include the effects of sea quarks. These inversions are typically performed using variants of the conjugate gradient algorithm, which is discussed in more detail in section 2.2.2 with respect to valence quarks.

Due to the way the Monte Carlo algorithm evolves the configurations, it is clear that configurations at adjacent MD times will be strongly correlated with one another. The extent of this correlation is statistically quantified by an autocorrelation length in the MD time. Performing calculations on configurations which are closer together in MD time than this autocorrelation length can lead to underestimates of statistical errors. In an attempt to avoid this, the algorithm also generally discards a certain number of intermediate configurations before saving one for inclusion in the final ensemble. This will clearly reduce the statistical correlations between neighbouring configurations, although they may still be present to such an extent that we must perform statistical binning on meson correlation functions calculated using the configurations.

The computational cost of generating lattice gauge configurations is substantial, and in most cases much larger than the cost of calculations performed on them. The largest contribution to this cost comes from the lattice size  $V$ , with the computational cost varying as  $V^{1+\delta}$  [30]. This limits the size of lattices that can be generated within a reasonable time, especially since one requires  $\mathcal{O}(10^3)$  statistically independent configurations to generate results with small statistical errors. For the Hybrid Monte Carlo algorithm,  $\delta = \frac{1}{4}$  [43, 44].

The computational cost of a calculation performed on the lattice is roughly proportional to:

$$\left(\frac{L}{a}\right)^3 \left(\frac{T}{a}\right) \frac{1}{a} \frac{1}{am_\pi^2} \quad (2.5)$$

where  $L/a$  is the number of lattice points in each of the three spatial directions, and  $T/a$  the number of points in the temporal direction. The first two factors simply give the number of lattice sites, and the other two account for a so-called ‘critical slowing-down’ of the algorithms used to evaluate the path integral [10]. Since the lattice spacing  $a$  appears in all four factors, it is clear that it is the most important element in determining computer time: computational cost is roughly proportional to  $a^{-6}$ .

Performing calculations on configurations with larger lattice spacings is therefore faster, but discretisation errors become smaller with smaller lattice spacings as we approach the continuum limit more closely. Lattice calculations have traditionally had to balance these factors very carefully, but we are now in an era where computing power has grown to the extent that generating large lattices with small lattice

spacings, and performing calculations on them, can be done in a feasible amount of time. This will form a large part of the focus of calculations in this thesis.

## 2.1.2 MILC Configurations

The results presented in this thesis have been calculated using two different sets of gauge configurations generated (and made freely available) by the MILC Collaboration [1]. Here we detail some of their properties for reference in the following chapters.

### Asqtad Configurations

The first set of configurations [15] are generated using a tree-level improved gluon action, and include the effect of  $u$ ,  $d$  and  $s$  quarks in the sea, generated using the asqtad formalism. These ensembles are listed in Table 2.1 along with relevant parameters. The  $u$  and  $d$  quarks in the sea are degenerate and are denoted by the subscript  $\ell$ . We will refer to these as the 2+1-flavour configurations, or the (three-flavour) asqtad configurations.

Label	$a$ / fm (approx.)	Lattice size ( $L^3 \times T$ )	$\beta$	$\delta x_\ell$	$\delta x_s$	$r_1/a$
fine	0.09	$28^3 \times 96$	7.09	0.20	0.19	3.699(3)
superfine	0.06	$48^3 \times 144$	7.47	0.16	-0.03	5.296(7)
ultrafine	0.045	$64^3 \times 192$	7.81	0.17	0.04	7.115(20)

Table 2.1: Ensembles of MILC configurations which include the effects of 2+1 flavours of quarks in the sea ( $u$ ,  $d$  and  $s$ ). The inverse lattice spacing values are given here in units of  $r_1$  [15] (defined in section 2.1.3). This can be converted to an inverse lattice spacing in GeV as also explained in section 2.1.3. The  $\delta$  values represent the difference between the sea quark mass and its physical value as a fraction of the  $s$  quark mass, and  $\beta$  is the gauge coupling used in generating the ensembles as discussed in section 1.4.1.

The parameters  $\delta x_\ell$  and  $\delta x_s$  quantify the mistuning of the sea quark masses on each ensemble, and are defined as

$$\delta x_q = \frac{m_{q,\text{sea}} - m_{q,\text{phys}}}{m_{s,\text{phys}}}. \quad (2.6)$$

Values for these parameters were determined in [45] and are also listed in Table 2.1.

## HISQ Configurations

The second set of configurations [16] also includes the effect of  $c$  quarks in the sea, and all four flavours of sea quark are generated with the HISQ action. The gluon action here is improved to order  $\alpha_s a^2$ . These configurations are listed in Table 2.2, and will be referred to as the 2+1+1-flavour configurations, or the (four-flavour) HISQ configurations.

Label	$a$ / fm (approx.)	$m_\ell/m_s$	Lattice size ( $L^3 \times T$ )	$\beta$	$\delta_m$	$w_0/a$
very coarse	0.15	1/5	$16^3 \times 48$	5.80	0.228	1.1119(10)
		1/10	$24^3 \times 48$	5.80	0.046	1.1272(7)
		phys.	$32^3 \times 48$	5.80	-0.048	1.1367(5)
coarse	0.12	1/5	$24^3 \times 64$	6.00	0.237	1.3826(11)
		1/10	$32^3 \times 64$	6.00	0.068	1.4029(9)
		phys.	$48^3 \times 64$	6.00	-0.040	1.4149(6)
fine	0.09	1/5	$32^3 \times 96$	6.30	0.291	1.9006(20)
		1/10	$48^3 \times 96$	6.30	0.104	1.9330(20)
		phys.	$64^3 \times 96$	6.30	-0.010	1.9518(7)
superfine	0.06	1/5	$48^3 \times 144$	6.72	0.366	2.8960(60)
ultrafine	0.045	1/5	$64^3 \times 192$	7.00	0.276	3.892(11)

Table 2.2: Details of the 2+1+1-flavour MILC configurations [16]. We label each according to its approximate lattice spacing, and can then refer uniquely to each ensemble with a combination of its label and the mass of the light quarks in the sea (expressed as a fraction of the sea strange quark mass). The lattice spacing  $a$  is listed in units of  $w_0$  (defined in section 2.1.3), as determined in [46] and, in some cases, updated in [47].

The up and down quarks here are once again degenerate. In contrast to the three-flavour configurations, however, this set includes ensembles where the  $u/d$  sea quark masses are set to their physical average value. As we have discussed, such configurations are far more computationally intensive to generate than those with heavier light quarks, but they allow us to obtain results which require little to no chiral extrapolation.

Here we quantify the mistuning of the sea masses with the parameter

$$\delta_m = 2\delta x_\ell + \delta x_s \quad (2.7)$$

with  $\delta x_q$  defined as in equation 2.6. Many of these values have been determined in [47], although some are calculated by hand using the tuned lattice charm quark

masses from chapter 5. Multiplying the tuned charm mass by the world-average ratio of charm-to-strange-quark masses from [4] gives the physical strange mass  $m_{s,\text{phys}}$  in lattice units, and likewise multiplying this by the world-average ratio of strange-to-light-quark masses [4] allows us to determine the physical light quark mass  $m_{\ell,\text{phys}}$ . These values can then be used in equation 2.6 to obtain the required  $\delta x_q$  on each ensemble.

The primary contribution to  $\delta_m$  for these ensembles is that from the light quarks: on each of these configurations, the sea strange quark mass has been tuned to close to its physical value<sup>1</sup>, as has the charm. The sea charm quark masses on these ensembles are in fact mistuned to a much smaller degree than the light and strange sea quarks. This is quantified in [47]. We therefore safely neglect any consideration of sea charm mistunings on fits performed to results obtained on these ensembles.

Note that the  $w_0/a$  values listed in Table 2.2 are mostly published in [46] or [47], but there is an important exception: the value on the ultrafine ensemble was determined by Craig McNeile for the HPQCD collaboration, and does not yet appear in any published works.

### 2.1.3 Fixing the Lattice Scale

When generating gauge configurations, the lattice spacing  $a$  is not known *a priori*, and must be determined via quantities with a known physical value that can be calculated on the lattice — or, equivalently, through some interpolating quantity whose value can be both determined accurately on the lattice and derived accurately from experimental measurements [16]. By comparing the value derived from experiment with that calculated on the lattice, we can determine  $a$  in fm for each ensemble, or equivalently,  $a^{-1}$  in GeV which is needed to convert lattice results to physical units. Clearly the accuracy with which such a parameter can be determined is crucial in setting the overall accuracy of any dimensionful quantity derived from lattice calculations. Numerous different parameters have been used to set the lattice scale over time, and here we will briefly review those which we use for the MILC configurations in the previous subsection.

#### Sommer Parameter

The Sommer parameter  $r_0$  was introduced in 1992 [48], and is based on the potential between two static quarks. More recently, the MILC collaboration has used a slightly modified version of this parameter, known as  $r_1$  [49]. On the lattice, this is calculated

---

<sup>1</sup>The MILC collaboration has also produced a separate set of ensembles with unphysical strange quark masses in the sea [16], should a study of effects arising from this be required — we will not use these in this work.

by fitting large Wilson loops as a function of lattice time [46] to extract the potential between two infinitely heavy quarks separated by a distance  $r/a$  (in lattice units).  $r_1$  is then defined as the point where the force  $F(r)$  calculated from the derivative of this potential satisfies [50]

$$r^2 F(r) = 1 \tag{2.8}$$

which requires a further fit to the potential to be performed. The original Sommer parameter  $r_0$  is defined by setting the same expression equal to 1.65 [48].

The actual calculation here is advantageous in that it requires no evaluation of quark propagators, since Wilson loops are simply products of gauge links, but the subsequent analysis is a complicated one to perform. In addition, it is challenging to calculate large Wilson loops with good signal-to-noise ratios, and this may be a contributing factor to tensions between different determinations of the Sommer scale [51].

The physical value of  $r_1$  that we will use has been accurately determined on 2+1-flavour lattices<sup>2</sup> by the HPQCD collaboration in [52] as  $r_1 = 0.3133(23)$  fm, by comparing the PDG value of  $f_\pi$ , the decay constant of the pion, with a lattice calculation of  $r_1 f_\pi$ . The MILC collaboration has calculated  $r_1/a$  on each of its generated ensembles [15] as listed in Table 2.1.

### Wilson Flow Parameter

The Wilson flow parameter  $w_0$  was introduced in [51] to attempt to remedy some of the problems encountered with  $r_1$ . It keeps the advantages of the Sommer parameter in that it also requires no quark propagators to calculate, but is easier to compute with high precision because, unlike  $r_1$ , it does not require the asymptotic-time fitting of Wilson loops, and does not suffer from the same signal-to-noise issues. Its evaluation is simpler, and the analysis required to compute it from lattice data is less cumbersome, and correspondingly more precise.

Measurement of the Wilson flow parameter is performed by smoothing the gluon field using a series of infinitesimal smearing steps [51]. The field then becomes smooth and renormalised, and gauge-invariant functions of the field therefore become physical quantities. Different parameters suitable for fixing the lattice scale can then be defined from the flow-time dependence of these quantities [46]. Specifically,  $w_0$  is defined by:

$$t \frac{d}{dt} (t^2 \langle E \rangle) \Big|_{t=w_0^2} = 0.3 \tag{2.9}$$

---

<sup>2</sup>The HPQCD collaboration has also determined  $r_1$  on the 2+1+1-flavour lattices, in [46], as  $r_1 = 0.3112(30)$  fm, using the same method. We will not use this number, preferring to fix the lattice spacing on the four-flavour ensembles using the Wilson flow parameter, but note it here for posterity.

where  $t$  is the flow time, and  $\langle E \rangle$  is the expectation value of the gluon action density, a gauge-invariant function of the gluon field [46].

The physical value of the Wilson flow parameter has again been determined accurately by HPQCD, using the decay constant of the pion  $f_\pi$  [46], as  $w_0 = 0.1715(9)$  fm, and similarly, the  $w_0/a$  value as determined on each ensemble is listed in Table 2.2.

Perhaps the single disadvantage of using the  $w_0$  parameter is that, due to the use of pure gluon fields in its computation, its value can be somewhat affected by the masses of quarks in the sea [47], and so can introduce such a dependence into quantities calculated using it. However, it is relatively straightforward to deal with this when fitting the overall results in a chiral and continuum extrapolation, by including some terms in the fit function to account for it.

## 2.2 Flavour Physics with the HISQ Formalism

The properties of a stable meson  $M$  can be determined on the lattice by calculating two-point correlation functions  $\langle \Gamma_{\text{sk}}(y) \Gamma_{\text{sc}}^\dagger(x) \rangle$ . Here sc and sk stand for ‘source’ and ‘sink’ respectively, which we shall define momentarily.  $\Gamma_{\text{sc,sk}}(x)$  are operators which have non-zero overlap with the mesonic state  $|M\rangle$  we wish to investigate; in other words,

$$\langle 0 | \Gamma_{\text{sc,sk}}(x) | M \rangle \neq 0. \quad (2.10)$$

Consider a meson with quantum numbers  $J^{PC}$  created at lattice site  $\mathbf{0}$  at time 0, allowed to propagate, and destroyed at site  $\mathbf{x}$  at time  $t$ . The site  $(\mathbf{0}, 0)$  is then labelled the source of the meson, and the site  $(\mathbf{x}, t)$  the sink<sup>3</sup>. Performing a discrete Fourier transform in the spatial directions allows us to express the two-point correlator as a function of Euclidean time [30]:

$$C_{2\text{pt}}(t; \mathbf{p}) = \sum_{\mathbf{x}} \langle J(\mathbf{x}, t) J^\dagger(\mathbf{0}, 0) \rangle e^{-i\mathbf{p}\cdot\mathbf{x}} \quad (2.11)$$

with the current,  $J$ , defined by

$$J(\mathbf{x}, t) = \bar{\psi}(\mathbf{x}, t) \Gamma \psi(\mathbf{x}, t) \quad (2.12)$$

where  $\Gamma$  is some combination of Dirac  $\gamma$  matrices, chosen appropriately at the source (and sink) to create (and destroy) a meson with the desired quantum numbers. In all of the calculations in this thesis, we will consider only correlators with zero momentum, and can therefore reduce the above expression to:

$$C_{2\text{pt}}(t) = \sum_{\mathbf{x}} \langle J(\mathbf{x}, t) J^\dagger(\mathbf{0}, 0) \rangle. \quad (2.13)$$

---

<sup>3</sup>Note that we have switched to a three-vector notation for the spatial components of the lattice sites, to explicitly show the time-dependence of the correlation function.

In cases where the current  $J$  couples to the same point  $(\mathbf{x}, t)$  for both quark and antiquark fields, as we have illustrated here, the operator is said to be *local*. If  $\Gamma_A$  and  $\Gamma_B$  are our chosen  $\gamma$  matrix combinations at the source and sink respectively, this imposes a restriction on the correlator that  $\Gamma_A = \Gamma_B$ . This restriction may be avoided by using a non-local current  $J(\mathbf{x}, t) = \bar{\psi}(\mathbf{x}, t)\Gamma\psi(\mathbf{x}', t')$ , with the lattice sites  $(\mathbf{x}, t)$  and  $(\mathbf{x}', t')$  in the same hypercube.

Explicitly writing the correlator in terms of the quark fields, we obtain [12]

$$C_{2\text{pt}}(t) = \sum_{\mathbf{x}} \langle \bar{\psi}(\mathbf{x}, t) \Gamma_B \psi(\mathbf{x}, t) \bar{\psi}(\mathbf{0}, 0) \Gamma_A \psi(\mathbf{0}, 0) \rangle \quad (2.14)$$

and noting that our creation and annihilation operators can be combined into quark propagators by Wick contracting the quark and antiquark fields, we can rewrite the expression for the correlator in terms of these propagators. We can calculate valence quark propagators on the lattice (the procedure for which we examine in more detail in section 2.2.2), and may therefore compute our correlation functions by combining them:

$$C_{2\text{pt}}(t) = \sum_{\mathbf{x}} \text{Tr} [\Gamma_B G(\mathbf{x}, t; \mathbf{0}, 0) \Gamma_A G(\mathbf{0}, 0; \mathbf{x}, t)] \quad (2.15)$$

where  $G(\mathbf{x}, t; \mathbf{0}, 0)$  is the propagator from site  $(\mathbf{0}, 0)$  to site  $(\mathbf{x}, t)$ , and the trace is over (implicit) colour and spin indices.

We view the path-reversed propagator  $G(\mathbf{0}, 0; \mathbf{x}, t)$  as describing the antiquark in our meson pair. This can be simply computed from the identity  $G(\mathbf{0}, 0; \mathbf{x}, t) = \gamma_5 G^\dagger(\mathbf{x}, t; \mathbf{0}, 0) \gamma_5$  and does not require a separate matrix inversion to calculate.

### 2.2.1 Staggered Operators

The choice of operators  $\Gamma_{A,B}$  in the correlation function is what will determine the quantum numbers of the meson that we create from the vacuum. For staggered mesons, the spin  $\gamma_n$  of the operator fixes what  $J^{PC}$  it couples to, and the taste of the operator,  $\gamma_s$ , is its total Dirac  $\gamma$  matrix content after staggering. Staggered operators are defined by their spin and taste, and are generally denoted  $\gamma_n \otimes \gamma_s$ .

Staggered operators with the same spin  $\gamma_n$  but different taste content  $\gamma_s$  will, appropriately, create different tastes of meson, with slightly different masses on the lattice. However, as outlined in the previous chapter, taste splittings are inherently a discretisation effect, and so each taste of meson must have the same mass in the continuum limit. With the HISQ action, taste splittings are generally very small [20, 53], and so we are free to choose different tastes of operator if one is more suitable for the calculation being performed.

An appropriate choice of operators is now all that we need in order to determine the masses of a system of stable mesons. For example, if we were to choose

$\Gamma_{sc} = \Gamma_{sk} = \bar{d}\gamma_\mu\gamma_5u$ , we could determine the mass of the  $\pi^+$  from the rate of exponential fall-off of the correlator, and also its decay constant from the exponential's coefficient. These useful properties of the correlator are exactly what we utilise to fit lattice data, and this is dealt with fully in section 3.1.

As noted in section 1.5, four different quark tastes remain in staggered quark propagators, which can be combined to produce 16 different tastes of meson. This can be accounted for by normalising each quark loop for one staggered taste [34]. Two-point correlators by definition contain a single quark loop, and so we should divide two-point functions by 4 to cover this.

### Point Splitting

We can rewrite equation 2.15 for the two-point lattice correlator in terms of staggered quark propagators  $g(\mathbf{x}, t; \mathbf{0}, 0)$  by applying the relevant staggering transformations  $\Omega(\mathbf{x}, t)$  and Wick contracting the quark fields:

$$C_{2\text{pt}}(t) = \sum_{\mathbf{x}} \text{Tr} \left[ \Gamma_B \Omega(\mathbf{x}, t) g(\mathbf{x}, t; \mathbf{0}, 0) \Omega^\dagger(\mathbf{0}, 0) \Gamma_A \Omega(\mathbf{0}, 0) g(\mathbf{0}, 0; \mathbf{x}, t) \Omega^\dagger(\mathbf{x}, t) \right]. \quad (2.16)$$

The trace here is over spin, and this rewriting is only possible when the correlator written in terms of naive quarks is spin-diagonal. In other words, the only spin-dependence is in the  $\Omega$  matrices, so we can factor out the propagators from the above expression in a separate trace over colour. We may then perform the spin trace and cancel out the taste  $\gamma$  matrices to generate staggered phase factors, which we will compute shortly.

The staggering matrix for neighbouring lattice sites follows the relation set out in equation 1.25. It follows from this that the use of a non-local operator will change the  $\gamma$  matrix content of a correlator once the staggering transformation is applied. For example, an operator with one link of point splitting in the  $\mu$  direction will gain one extra  $\gamma_\mu$  after staggering. When point splitting is included, the general staggered operator  $\gamma_n \otimes \gamma_s$  therefore looks like<sup>4</sup>

$$\bar{\chi}(x) \Omega^\dagger(x) \gamma_n \Omega(x + n + s) \chi(x + n + s). \quad (2.17)$$

### Staggered Operator Phases

In addition to being spin-diagonal, a staggered correlation function must be a taste singlet, i.e. the product of all the tastes must be  $\mathbb{1}$ . When the taste  $\gamma$  matrices are anticommutated so that they can be cancelled out, an overall phase factor arises in the correlator, and this can be determined analytically by performing the spin trace

---

<sup>4</sup>Note again a change in notation here: we have switched back to labelling the lattice sites as four-vectors for simplicity.

described above. If our correlation function is not a taste singlet, this trace will yield a result of zero.

To perform the spin trace and obtain an expression for the overall phase factor, consider the general staggered operator in equation 2.17 above. First, let us find the phase factor which arises from writing the point-split staggering matrix  $\Omega(x+n+s)$  as  $\gamma_{n+s}\Omega(x)$ . This results in a factor of  $(-1)^{x_\mu^<}$  for each component of  $(n+s)_\mu = 1$ , of which there are 4. Here we have used the notation

$$x_\mu^< = \sum_{\nu < \mu} x_\nu \quad (2.18)$$

which we introduced in equation 1.28. We can now write our general staggered operator as

$$\left( \prod_{(n+s)_\mu=1} (-1)^{x_\mu^<} \right) \bar{\chi}(x)\Omega^\dagger(x)\gamma_n\gamma_{n+s}\Omega(x)\chi(x+n+s) \quad (2.19)$$

or, since  $\gamma_n\gamma_{n+s} = \pm\gamma_s$ ,

$$\pm \left( \prod_{(n+s)_\mu=1} (-1)^{x_\mu^<} \right) \bar{\chi}(x)\Omega^\dagger(x)\gamma_s\Omega(x)\chi(x+n+s). \quad (2.20)$$

Our next step is now clearly to anticommute  $\gamma_s$  with  $\Omega(x)$  so that the staggering matrices will cancel each other. This results in a factor of  $(-1)^{\bar{x}_\mu}$  for each  $\mu$  with  $s_\mu = 1$ . Here we have introduced another convenient shorthand:

$$\bar{x}_\mu = \sum_{\nu \neq \mu} x_\nu. \quad (2.21)$$

The overall factor appearing in our taste-singlet operator is then

$$\left( \prod_{(n+s)_\mu=1} (-1)^{x_\mu^<} \right) \left( \prod_{s_\mu=1} (-1)^{\bar{x}_\mu} \right). \quad (2.22)$$

Phases for a selection of local staggered currents are detailed in Table 2.3.

Operator	$J^{PC}$	Partner	Phase
$\gamma_5 \otimes \gamma_5$	$0^{-+}$	$0^{+-}$	1
$\gamma_0\gamma_5 \otimes \gamma_0\gamma_5$	$0^{-+}$	$0^{++}$	$(-1)^{(x+y+z+t)}$
$\gamma_i \otimes \gamma_i$	$1^{--}$	$1^{+-}$	$(-1)^i$
$\gamma_i\gamma_0 \otimes \gamma_i\gamma_0$	$1^{--}$	$1^{++}$	$(-1)^{(x+y+z+t+i)}$

Table 2.3: Phases and spins for local staggered currents

Finally, we determine a relationship between quark and antiquark propagators for staggered quarks. Much like the naive-quark equivalent

$$G(y, x) = \gamma_5 G^\dagger(x, y) \gamma_5 \quad (2.23)$$

where  $G(x, y)$  describes a propagator from site  $x$  to site  $y$ , we view the path-reversed propagator as describing an antiquark propagating from  $x$  to  $y$ . The anticommutation relation for the staggering matrix with  $\gamma_5$  is

$$\Omega(x) \gamma_5 = \varepsilon(x) \gamma_5 \Omega(x) \quad (2.24)$$

where we define

$$\varepsilon(x) = (-1)^{\sum_\mu x_\mu}. \quad (2.25)$$

Therefore, in applying the staggering transformation and anticommuting the  $\gamma$  matrices appropriately, we find that

$$g(y, x) = g^\dagger(x, y) \varepsilon(x) \varepsilon(y). \quad (2.26)$$

for staggered propagators.

## Oscillations

The naive quark action of equation 1.14 is invariant under the doubling transformation

$$\begin{aligned} \psi(x) &\rightarrow i\gamma_5 \gamma_\mu (-1)^{x_\mu} \psi(x) \\ &= i\gamma_5 \gamma_\mu e^{i\pi x_\mu} \psi(x) \end{aligned} \quad (2.27)$$

and this gives rise to the doubling problem discussed in chapter 1. Recall that, since this transformation is applicable in each of the 4 spacetime directions, a naive quark field will describe 16 different quarks of a given flavour instead of just one. The staggering transformation reduces the total number of quarks of each flavour to 4, and we refer to them as tastes.

In calculating a two-point correlation function as described above, a sum over space is carried out to give zero three-momentum, and (for staggered quarks) this cancels out the three spatial doublers. The doubler in the time direction remains, however, and so the staggered quark may have low energy  $E \approx 0$  or high energy  $E \approx \pi$  (in lattice units).

To quantify the effect this has on our correlator, we will follow a similar example to that given in [54], and closely emulate the treatment used there. First we note that the high-energy staggered quark field may be transformed back into a low-energy field by reapplying the time component of the doubling transformation, viz.

$$\psi(x)|_{E \approx \pi} \rightarrow i\gamma_5 \gamma_0 (-1)^t \psi(x). \quad (2.28)$$

Now consider the case of a pseudoscalar current

$$J_5(x) = \bar{\Psi}(x)\gamma_5\psi(x) \quad (2.29)$$

which will, in the continuum limit, couple to pseudoscalar  $J^P = 0^-$  mesons. Here  $\Psi$  denotes a quark field which may also be staggered, but which describes a quark of different mass to the field  $\psi$ . Substituting the transformed high-energy field into this current, we obtain

$$\begin{aligned} J_5(x)|_{E \approx \pi} &\rightarrow \bar{\Psi}(x)\gamma_5(i\gamma_5\gamma_0)(-1)^t\psi(x) \\ &= (-1)^t\bar{\Psi}(x)i\gamma_0\psi(x) \end{aligned} \quad (2.30)$$

which implies that the current  $J_5$  also couples to  $J^P = 0^+$  mesons: those with opposite parity to the pseudoscalar<sup>5</sup>.

In constructing a correlator from the pseudoscalar current, we will therefore obtain an expression of the form

$$C_{2\text{pt}}(t) = |\langle 0|\bar{\Psi}\gamma_5\psi|0\rangle|^2 e^{-E^-t} + (-1)^t |\langle 0|\bar{\Psi}i\gamma_0\psi|0\rangle|^2 e^{-E^+t} \quad (2.31)$$

where  $E^-$  and  $E^+$  are the energies of the  $J^P = 0^-$  and  $J^P = 0^+$  mesons respectively. It is clear that the second component oscillates in sign from one time step to the next.

In staggered simulations, oscillating components of meson correlators are a frequent occurrence. In addition to their appearance in flavoured mesons as explained here, they will also appear in flavourless mesons where both quarks are staggered. Oscillations must therefore be properly accounted for when fitting correlation functions, and more details on how this is done are discussed in section 3.1.

The exception to this is in local pseudoscalar currents at zero momentum with a quark and antiquark of equal mass, where the oscillating components cancel out. This is important for our purposes, since it makes staggered lattice calculations of pseudoscalars very accurate. Indeed, several of the calculations in the following chapters will compute exactly these types of currents.

It should be noted that since oscillating components will, in general, couple to the parity partner of the intended current, they can in fact be very useful, allowing us to extract the properties of two different mesons from a single correlator (given sufficient accuracy). Indeed this is exactly the method used in chapter 5 of this thesis when calculating the spectrum of excited charmonium states. For example, the  $h_c$  axial-vector meson ( $J^{PC} = 1^{+-}$ ) is the parity partner of the ground-state  $J/\psi$  vector meson ( $J^{PC} = 1^{--}$ ) and so we can extract information on both of them from the same correlation function. Partners for selected local currents are also listed in Table 2.3 above.

<sup>5</sup>We can explicitly see this by noting: 1. that there is no three-vector index, so  $J = 0$ , and 2. that  $P\gamma_0P = \gamma_0$ , where  $P \equiv \gamma_0$  is the parity operator, so  $P = +$ .

## 2.2.2 Random Wall Sources

Staggered quark propagators  $g(x, y)$  are calculated as the inverse of the appropriate Dirac matrix: for HISQ quarks, we have the relation

$$g(x, y) = \left( [\mathcal{D}^{\text{HISQ}} + m](x, y) \right)^{-1}. \quad (2.32)$$

This inversion is performed using an iterative procedure based on the conjugate gradient algorithm [55], which, for a square matrix  $A$  and vector  $\eta$ , solves  $Ab = \eta$  for  $b$ . In the case of the propagator inversion we have here,  $A$  is the Dirac matrix  $[\mathcal{D}^{\text{HISQ}} + m](x, y)$ , and  $\eta(x)$  is known as the source vector. Since we have defined the propagator  $g(x, y)$  as the inverse of the Dirac matrix, the solution to this problem is

$$b = g(y) = \sum_x g(x, y)\eta(x) \quad (2.33)$$

which describes a quark propagating from all sites  $x$  to site  $y$ . The complex conjugate  $g^\dagger(y)$  describes the corresponding antiquark.

We can take advantage of this fact to increase the statistics in our simulations by using what is known as a random wall source [52]. On a single source timeslice  $t = t_0$  of the lattice, the source vector  $\eta(x)$  is defined as a colour 3-vector of  $U(1)$  random numbers with unit norm. On all other timeslices  $\eta(x)$  is set to zero.

We can obtain an expression for the contraction of quark and antiquark propagators  $g(y)$  and  $g^\dagger(y)$  made from these random wall sources:

$$g^\dagger(y)g(y) = \sum_{x, x'} g^\dagger(x', y)g(x, y)\eta^\dagger(x')\eta(x) \quad (2.34)$$

and, noting that when  $x' \neq x$  the random source vectors will cancel on the average and only contribute a small amount of noise, this can, to a good approximation, be simplified to:

$$g^\dagger(y)g(y) = \sum_{x, x'} g^\dagger(x', y)g(x, y)\delta_{x, x'} = \sum_x g^\dagger(x, y)g(x, y) \quad (2.35)$$

which describes a separate meson correlator originating at each spatial point  $x$  on the source timeslice. We are now, in effect, simulating  $L^3$  correlators rather than just one. This represents a significant increase in statistics<sup>6</sup> with no increase in computational cost, and is clearly much faster than attempting to simulate all these correlators individually.

This ‘embedding’ of the source timeslice into  $g(y)$  is extended to include the source operator when using staggered quarks: the relevant staggered phase and

---

<sup>6</sup>Of course there exist statistical correlations between the spatial points on a single timeslice, so the net statistical gain is less than  $L^3$ . Qualitatively, there is still a significant increase, since the gain in signal overcomes the increase in noise for all the calculations which we perform.

point-splitting must be applied to  $\eta(x)$  before computing the staggered propagator  $g(y)$ . For example, to produce a correlator for a local vector meson polarised in the  $x$ -direction (i.e. using the  $\gamma_x \otimes \gamma_x$  operator), we require a phase of  $(-1)^x$  embedded in the source, and must insert a phase of  $(-1)^x$  when combining the propagators at the sink. The correlator is therefore made by combining a quark propagator  $g_\eta(y)$  made from a random wall source  $\eta(x)$  with an antiquark propagator  $g_\rho^\dagger(y)$  made from the same random wall but patterned with the appropriate staggered phases:  $\rho(x) = (-1)^x \eta(x)$ .

This patterning of the source is slightly different if the source operator includes any point splitting. Taking a similar example of the  $x$ -polarised one-link vector meson  $\gamma_x \otimes \mathbb{1}$ , the same quark propagator  $g_\eta(y)$  is combined with an antiquark propagator  $g_\sigma^\dagger(y)$  made from a source vector  $\sigma(x)$  with point splitting averaged symmetrically over the forward and backward directions — explicitly:

$$\sigma(x) = \frac{1}{2} [\eta(x + \hat{x}) + \eta(x - \hat{x})] . \quad (2.36)$$

To further improve statistical precision, in all of the simulations presented in this thesis we calculate propagators from several different time sources  $t_0$  on each gauge configuration, which are then averaged over.

### Subset Corner Mask

In the case of vector mesons we can use a method to allow us to obtain correlators in each of the three orthogonal spatial directions from a single random wall source. This method is referred to in what follows as the subset corner mask.

After the random wall source is constructed, we set its values on all lattice sites to be zero except on the corners of each  $2^4$  hypercube. This means that the appropriate phases we need to insert to produce a vector correlator are all simply set to 1, which allows us to obtain correlators for different vector polarisations from the same source.

If this were not implemented, we would require three different sources patterned with phases of  $(-1)^x$ ,  $(-1)^y$  and  $(-1)^z$ . The computational cost of the calculation is therefore significantly decreased, at the expense of slightly reducing our statistics.

Quantitatively, the HPQCD collaboration has found that using three differently-patterned sources gains us a factor of  $\sqrt{3}$  in statistics, compared to using a single source with the subset corner mask. This is often a worthwhile sacrifice to make to gain a factor of 3 in computer time. In cases where it is not possible to use the subset corner mask (such as alongside the smearings detailed below), but where we still wish to reduce our computational costs, the simplest solution is often to study just a single vector polarisation, albeit with the corresponding reduction in statistics

this entails<sup>7</sup>.

### 2.2.3 Smearings

We have discussed how the choice of operators used in calculating a correlator will determine what  $J^{PC}$  it couples to, and how this can be used to determine the properties of a meson with these quantum numbers by fitting to a decaying exponential. In fact, the chosen operators will couple to any meson with the same quantum numbers, and so in principle we can also determine the properties of excited meson states by fitting to a sum of decaying exponential functions.

It is difficult to obtain a reasonable signal for radially excited states unless the chosen operator  $\Gamma$  has a very large overlap with the corresponding state. Thankfully there are steps we can take to improve this overlap via the use of smeared operators — these are simply the standard staggered operators we have already discussed, with smearing functions applied to them. Ideally we would use smearings which improve overlap with the excited states we wish to study, but in practice these are very difficult to find.

Instead, we use smearings which have a large overlap with the ground state. Finding these is a much more feasible task, and also improves determinations of excited states since it allows us to precisely extract the ground state at small  $t$ -values. We are therefore able to more accurately determine the corresponding excited-state contributions to the correlator, which manifest themselves most strongly at the same small  $t$ -values.

In many of our calculations of excited charmonium states in chapter 5, we apply Gaussian covariant smearings to both source and sink operators to improve their overlap with the ground state as described. The use of covariant smearings is a deliberate choice, as it means that we do not have to take the extra step of gauge-fixing the lattice configurations we wish to use. These smearings are of the form

$$\left[1 + \frac{r^2 \cdot \mathcal{D}^2}{4 \cdot n}\right]^n \xrightarrow{n \rightarrow \infty} \exp\left(\frac{r^2 \cdot \mathcal{D}^2}{4}\right) \quad (2.37)$$

where  $n$  is the number of iterations applied, and the parameter  $r$  determines the width of the Gaussian — effectively setting the size of the smearing. Values used for these parameters are given in chapter 5. Note that  $\mathcal{D}$  here is, specifically, the stride-2 covariant difference operator (in spatial directions only), which is necessary to preserve the taste of the staggered mesons we are studying.

---

<sup>7</sup>This is, in fact, probably a smaller reduction in statistics than one might expect. Vector correlators with different polarisations but created from the same source (patterned with appropriate phases) will exhibit a significant degree of statistical correlation, and so averaging them for analysis does not gain us a huge amount in the way of statistics.

Several different smearings can be applied in otherwise identical calculations to increase statistics. This also allows for the comparison of different smearings to determine if one results in a better overlap.

Smearing the operators in this way results in a matrix of different correlation functions being obtained, and these can be fit simultaneously to take account of correlations between them. Methods for performing such a fit are also discussed in section 3.1.

## 2.2.4 MILC Code

The procedures described in the preceding sections for calculating staggered-quark correlators on various gluon ensembles are implemented in this thesis through the use of the MILC collaboration's open-source lattice gauge theory code [1]. The utilities within this code are written with lattice QCD in mind, and indeed there are several designed for working with HISQ quarks.

The code allows us to script the reading in of gauge configurations; the calculation of an appropriate Dirac matrix  $[\mathcal{D}^{\text{HISQ}} + m]$ , including specifying an appropriate coefficient  $\varepsilon$  for the Naik term in the derivative (see equation 1.42) which depends on the quark mass; the calculation of appropriate source vectors on a specific timeslice of the lattice, and the application of the appropriate phase patterns; the inversion of the Dirac matrix, using a version of the conjugate gradient algorithm, to calculate staggered propagators; and the combination of these propagators with appropriate phases at the sink to produce correlation functions.

In other words, we can compute correlation functions on pre-existing gauge configurations simply by specifying certain input parameters, and the procedures to be carried out. The ability to use the MILC code in such a way makes performing calculations on many different gauge configurations, with multiple time sources on each configuration, much more efficient. This is crucial in allowing us to obtain correlators with high statistical precision.

# Chapter 3

## Obtaining Physical Results

### 3.1 Correlator Fitting

Two-point lattice correlators are functions of  $t$ , the time separation between the source and the sink, and, as we have already mentioned, can be expressed as a series of decaying exponentials. Staggered correlation functions will, in general, also contain oscillating states as discussed in section 2.2.1. Combining all this information, we arrive at a suitable fit function for our correlators:

$$C_{2\text{pt}}(t) = \sum_{n=0}^{n_{\text{exp}}} \left[ A_n^2 e^{-E_n t} - (-1)^t A_{o,n}^2 e^{-E_{o,n} t} \right] \quad (3.1)$$

where the subscript  $o$  denotes a parameter belonging to the oscillating part of the correlator. Terms with  $n = 0$  represent the ground states, and larger values correspond to excited states with the same quantum numbers.  $E_n$  denotes the energy of a particular state  $n$  (which, at rest, is equal to its mass). We constrain the energies in a hierarchy such that  $E_n < E_{n+1}$ .  $A_n$  is the state's amplitude and is related to the matrix element  $\langle 0|\Gamma|n\rangle$ , from which we can extract properties of the meson's decays.

Before fitting, we average each set of correlators for the same meson over time sources and configurations, and, in the vector case, also over the three different polarisations. The fit is performed to the average correlator  $\overline{C}_{2\text{pt}}(t)$ , and takes account of statistical correlations between neighbouring lattice times  $t$ . In some cases we bin the correlators in Monte Carlo time to remove statistical correlations between data from neighbouring configurations, and thus obtain a more realistic estimate of statistical errors from the fit.

In all of the calculations in this thesis, we use periodic boundary conditions on our lattices, which means that we must also account for mesons propagating in the opposite direction. To extract physical quantities, we therefore fit the resulting average correlators  $\overline{C}_{2\text{pt}}(t)$  to an augmented form of our fit function, which includes

some additional terms to account for this periodic nature:

$$C_{2\text{pt}}(t) = \sum_{n=0}^{n_{\text{exp}}} \left[ A_n^2 \text{fn}(E_n, t) - A_{o,n}^2 \text{fo}(E_{o,n}, t) \right] \quad (3.2)$$

where

$$\text{fn}(E, t) = e^{-Et} + e^{-E(T-t)} \quad (3.3)$$

$$\text{fo}(E, t) = (-1)^{t/a} \text{fn}(E, t) \quad (3.4)$$

with  $T$  the time extent of the lattice [56].

In principle there can be an infinite number of terms included in the fit function, but correlation functions are, generally, dominated by contributions from the ground state, especially at large  $t$  values, and so higher-order terms describing the excited states become negligibly small in this region. This is evident in examining a rescaled version  $\tilde{C}_{2\text{pt}}$  of the average correlators  $\bar{C}_{2\text{pt}}$ , calculated by dividing out the ground state exponential:

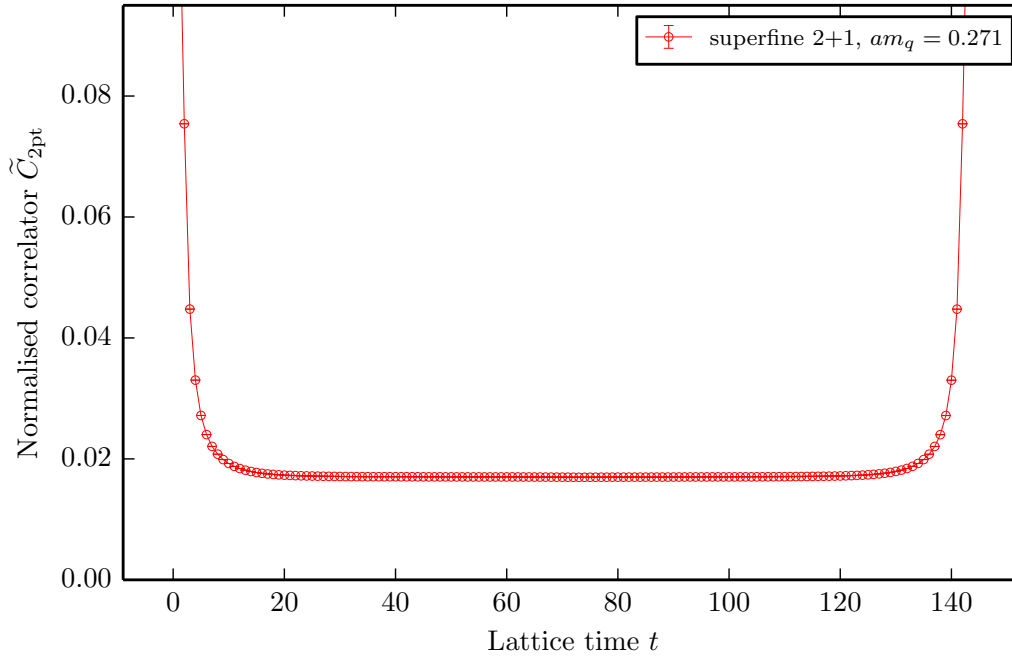
$$\tilde{C}_{2\text{pt}} = \frac{\bar{C}_{2\text{pt}}}{e^{-Et} + e^{-E(T-t)}} \quad (3.5)$$

where  $T$  is the time extent of the lattice.  $E$  is the energy of the ground state, obtained either from the full fit to the correlator or from an effective mass calculation as detailed later in this section.  $\tilde{C}_{2\text{pt}}$  will then exhibit a central plateau of value  $A_0^2$ , the square of the ground state amplitude, rather than following the continuous exponential decay of the raw average correlator.

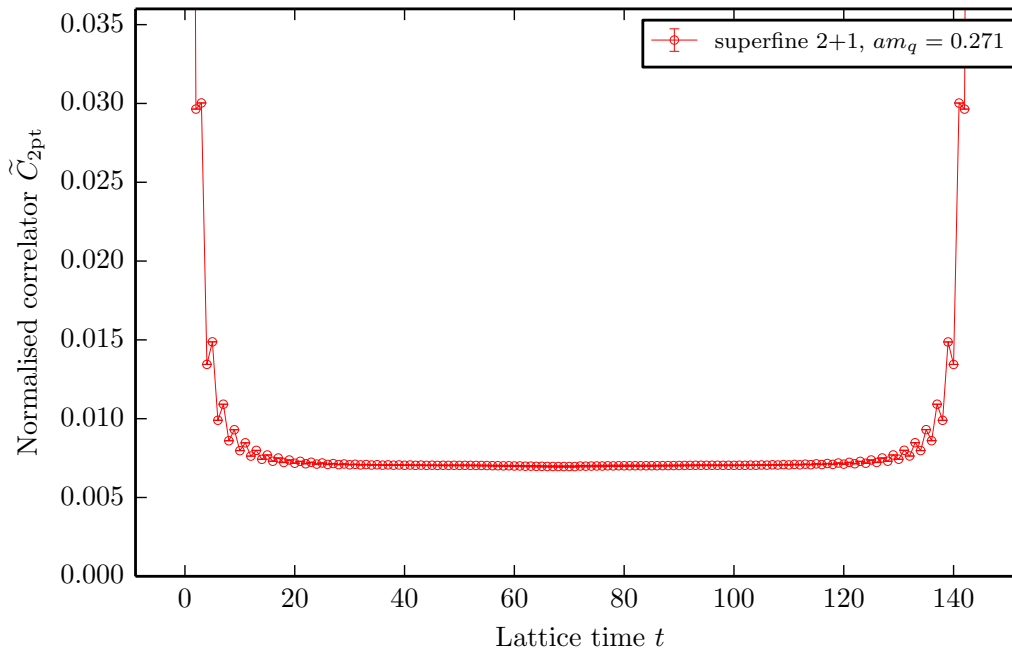
Two examples of such rescaled correlators are shown in Figure 3.1 — one  $J^P = 0^-$  pseudoscalar and one  $J^P = 1^-$  vector. These were calculated on the superfine 2+1 ensemble as listed in Table 2.1 for charmonium mesons, and form part of the data that we focus on in chapter 4. The oscillatory behaviour of the vector correlator is clearly demonstrated.

The mid-point of the correlator — where the time separation  $t$  reaches half of the time extent of the lattice — is the furthest point from the random wall source. Values of the correlator at and around this point are a good test of the convergence of the matrix inversions required to calculate our propagators, and we often monitor them for this purpose. A magnified version of the correlator data in Figure 3.1b centred on the mid-point is presented in Figure 3.2.

It is clear that there is a bump present in the data, but this appears to be a very small effect. This justifies the way in which we allow the fit code to treat correlators as periodic, and fold them about the midpoint in  $t$  before averaging and fitting. This folding is another way of increasing our statistics, and any additional uncertainty it introduces will clearly be very small, since values either side of the midpoint agree very well.



(a) Pseudoscalar



(b) Vector

Figure 3.1: Plots of rescaled two-point charmonium correlators  $\tilde{C}_{2\text{pt}}$  on the superfine 2+1 ensemble. These plots include statistical errors, which are smaller than the size of the points. The rescaling is performed by dividing the average correlator  $\overline{C}_{2\text{pt}}$  by the ground state exponential, and the plateau of value  $A_0^2$  is evident in each. Lines are drawn between the points, which clearly reveal the oscillating behaviour of the vector correlator.

Typically, we therefore only need include somewhere in the region of  $n_{\text{exp}} = 6\text{--}10$  exponentials to obtain a good fit, depending on how many correlators are included, and on the time range of the fit. Practically, we carry out successive fits while increasing the number of exponentials included. This allows us to determine when the fit has converged by observing that the parameters we are interested in have stabilised once a certain number of exponentials have been added. An example of this convergence is shown in Figure 3.3.

Strictly speaking, because all four tastes of meson remain in staggered propagators, we should normalise our correlators for one taste by dividing by 4, as noted in section 2.2.1. In practice, when using the MILC code to calculate two-point correlators this is not necessary, because the lattice derivative defined in the code omits the factor of  $\frac{1}{2}$  shown in equation 1.15. Each propagator it calculates (by inverting the Dirac matrix including this derivative) is therefore already smaller by a factor of 2, and in combining two propagators to make a two-point correlator, we obtain the required normalisation without further manipulation.

### 3.1.1 Bayesian Methods

Traditionally, a multi-exponential fit to the function in equation 3.2 would be performed by minimising a  $\chi^2$  parameter, defined as the difference between the data and the values of the fit function, taking into account the statistical correlations between successive data points through the use of a correlation matrix. This method becomes unsuitable with more than a few exponentials in the fit, because the parameters related to the high-energy terms are poorly constrained. This means that they wander off from their true value in the multi-dimensional parameter space, and hence affect the error estimates for the (better-constrained) low-energy parameters.

We address this through the use of Bayesian constrained curve fitting [57], in which we augment the traditional  $\chi^2$  parameter with a Bayesian prior:

$$\chi_{\text{aug}}^2 = \chi^2 + \chi_{\text{prior}}^2 \quad (3.6)$$

where

$$\chi_{\text{prior}}^2 = \sum_n \frac{(A_n - \tilde{A}_n)^2}{\tilde{\sigma}_{A_n}^2} + \sum_n \frac{(E_n - \tilde{E}_n)^2}{\tilde{\sigma}_{E_n}^2}. \quad (3.7)$$

The  $\chi_{\text{prior}}^2$  terms discourage the fit from venturing outside the region  $[\tilde{A}_n - \tilde{\sigma}_{A_n}, \tilde{A}_n + \tilde{\sigma}_{A_n}]$  for each amplitude, and the region  $[\tilde{E}_n - \tilde{\sigma}_{E_n}, \tilde{E}_n + \tilde{\sigma}_{E_n}]$  for each energy. The Bayesian priors  $\tilde{A}_n \pm \tilde{\sigma}_{A_n}$  and  $\tilde{E}_n \pm \tilde{\sigma}_{E_n}$  are inputs to the fit which must be chosen with physical motivation, and perhaps based on previous knowledge. Since we must define a prior for each parameter included in the fit, we can include as many exponentials as we wish without worrying about how many data points we have — the fit will

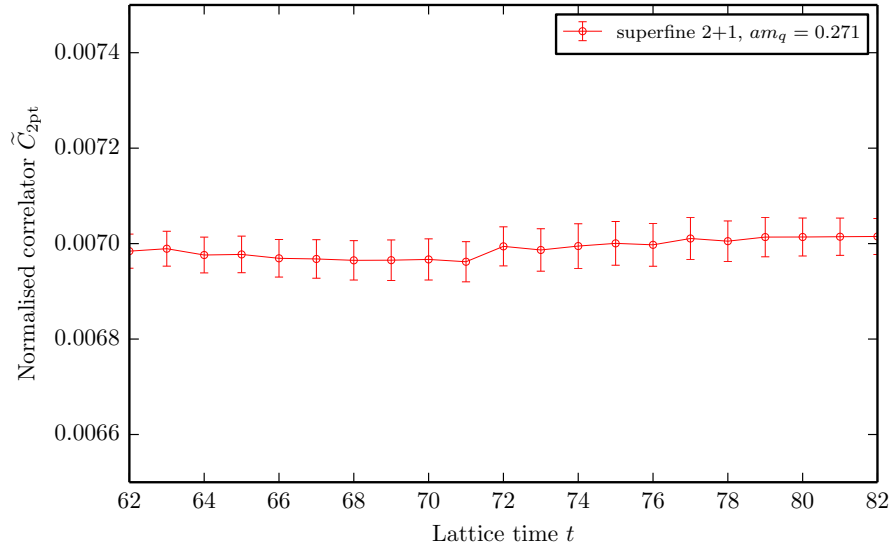


Figure 3.2: A rescaled and cropped version of Figure 3.1b, showing the small ‘kink’ at the central  $t$ -value. Although this is definitely present in the data here, the vertical axis has had to be scaled up significantly to show it — indeed it is not clear at all from the original plot that it even exists. This is another indication of the quality of the correlator data that we have obtained.

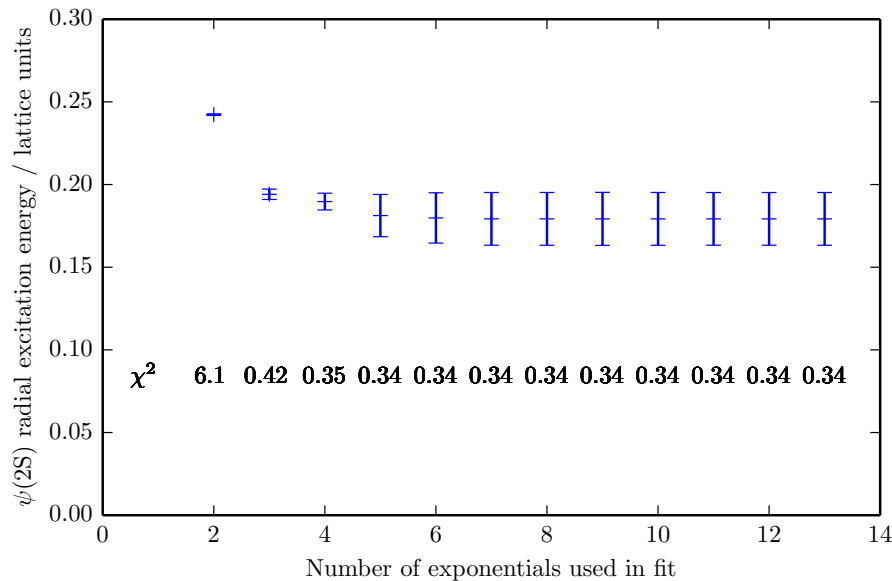


Figure 3.3: A plot demonstrating the convergence of a fit parameter as the number of exponentials in the fit function is increased. The specific parameter used in the example here is the energy of the  $\psi(2S)$  charmonium meson, expressed as its difference to the energy of the ground-state  $J/\psi(1S)$ . The fit has clearly converged once the sixth exponential is added, and shows no change as we continue to add more. The  $\chi^2$  values for each fit are shown below the corresponding points, and these also stabilise as the fit converges.

simply not constrain higher-order parameters more tightly than their prior value if it cannot extract any further information about them from the data.

Typically, we can take quite wide priors on most of the parameters. Amplitudes are typically taken to be  $0.01 \pm 1.0$  with our normalisation of the correlators, and the energy splittings in the hierarchy of states as approximately  $600 \pm 300$  MeV expressed in lattice units. The prior for the energy of the ground state can be determined from an effective mass calculation on the correlator. The effective mass  $m_{\text{eff}}$  of a correlator is defined as

$$m_{\text{eff}}(t) = -\ln \left[ \frac{C_{2\text{pt}}(t+1)}{C_{2\text{pt}}(t)} \right] \quad (3.8)$$

and will provide a good approximation to the ground state mass at large  $t$  values. Note that we will shortly describe a number of methods which will automatically generate more precise priors for us from the data at hand, so the prior values quoted here are in fact rarely entered manually in the fits we describe in the following chapters.

### 3.1.2 Fitting Code

We perform the fitting procedure using code developed by G. P. Lepage [57], which performs Bayesian least-squares fits to given data. For our fit function, we take equation 3.2 with a number of exponentials  $n_{\text{exp}}$ . Our fit parameters are the amplitudes  $A_n$  and  $A_{o,n}$  along with, perhaps counterintuitively, the logarithm of the ground-state energy and (for excited states) the logarithms of the energy differences to the next-lowest state. This keeps the values of the energies positive and correctly ordered — a key problem faced by previous fit methods.

To obtain good fits, we also remove values in the correlator at time separations below  $t_{\text{min}}/a$  and above  $(T - t_{\text{min}})/a$ . This reduces adverse effects from higher excitations, which manifest themselves most strongly at extremal  $t$  values, although we must be careful not to be too harsh in our choice of  $t_{\text{min}}$  if we are also attempting to determine the parameters of some of these excited states.

It is also sometimes useful to introduce a singular value decomposition (SVD) [58], removing small eigenvalues of the statistical correlation matrix to regulate its singularity. Values derived from the inverse of this matrix are used in the calculation of the  $\chi^2$  value to be minimised, and it is impossible to compute this inverse accurately if the matrix is singular, or nearly so. An SVD cut regulates the singularity of the matrix by effectively replacing its smallest eigenvalues by a larger minimum eigenvalue, at the cost of some precision in the data being input to the fit. However, this cost is often worth the gain in numerical stability [59].

In the standard Bayesian fit, priors for energy and amplitude values can be determined by an initial ‘fast fit’ which removes all terms from the data other than

those with  $n = 0$ , via statistical marginalisation [60]. Inputting even very wide priors of 1(100) to this fast fit allows it to return a good estimate of the ground state amplitude and energy in the correlator under consideration, and these are then used as more precise priors in the full fit. The fit code keeps track of statistical correlations between the ‘fast fit’ results and the data, and this ensures that the statistical errors in the full fit are estimated correctly.

From the fit to each average correlator, we can extract the amplitude and energy of the ground state and (ideally) some excited states. From these, it is possible to compute a number of physical quantities of interest, and this is exactly what we will do in the following chapters.

### 3.1.3 EigenBasis Method

When applying smearings to source and sink operators in a lattice calculation, we will end up with a matrix of correlation functions containing each combination of different smearings applied. We use this method in chapter 5 to improve the overlap of operators with the ground state meson, with the aim of making more accurate determinations of the parameters of excited states.

It is often the case when looking at excited states that the fit code can find plausible solutions to the fit which incorporate spurious, non-physical states with vanishing amplitudes. This is due to a lack of prior knowledge about excited states in the fit, the existence of which can be tricky to establish definitively due to their contributions to the correlator rapidly reducing as  $t$  increases.

A fit method based on the generalised eigenvalue approach to lattice spectroscopy [61, 62, 63] has also been developed by G. P. Lepage [64] as part of the same fit code mentioned above, and is known as the EigenBasis method. Given  $N$  different smearings (including no smearing) and an  $N \times N$  matrix of correlators formed from every combination of these smearings applied at the source and sink, a new basis can be defined which makes the matrix of correlators approximately diagonal at a given value of  $t$ .

The diagonal elements then overlap strongly with the lowest-lying states [64] and there is an obvious choice of priors for the amplitudes: approximately 1 on the diagonal elements and approximately 0 elsewhere. In the EigenBasis fits described in this thesis, we define these priors more precisely as 1.0(3) and 0.0(1) respectively. Such a prior is optimised for this type of fit, as by construction it encodes information about the excited states present, and so stabilises the fit against the spurious states mentioned previously.

Note that the EigenBasis fit method does not take oscillating states into account, as it derives its fundamental quantity — the optimised prior — from just

two  $t$ -values. It is possible, however, to fit oscillating states using the standard Bayesian fit method above at the same time as using the EigenBasis method to fit the non-oscillating states, simply by defining additional priors for the oscillating contributions. This is exactly the method used in many of the fits in chapter 5.

On a related note, when fitting correlators with different smearings applied, we must make a slight modification to our fit function in equation 3.2, as the amplitudes for each state will differ depending on which smearing is used:

$$C_{2\text{pt}}(t) = \sum_n^{n_{\text{exp}}} \left[ A_{n,\text{sc}} A_{n,\text{sk}} \text{fn}(E_n, t) - A_{o,n,\text{sc}} A_{o,n,\text{sk}} \text{fo}(E_{o,n}, t) \right] \quad (3.9)$$

with  $\text{fn}(E, t)$  and  $\text{fo}(E, t)$  having the same meanings as before. We now have a different amplitude  $A_n$  for each smearing used at the source (sc) and sink (sk) of the correlator. For correlators on the diagonal of the matrix, where the same smearing is applied to the source and sink, this simplifies to the same form as before, since  $A_{n,\text{sc}} A_{n,\text{sk}} = A_{n,\text{sc}}^2 = A_{n,\text{sk}}^2$ .

## 3.2 Physical Extrapolation

We noted in section 1.4 that to obtain physical results from lattice QCD calculations, we must extrapolate our lattice results to the physical world, and this requires calculations to be performed at multiple lattice spacings. The extrapolation necessarily introduces some systematic errors which we must understand in order to be able to quantify them and keep them under control.

More generally, we note that statistical errors in lattice calculations are due to Monte Carlo evaluation of the path integral, but these can easily be kept under control if we have sufficient statistics — using several time sources on large numbers of configurations, for instance. Systematic errors, on the other hand, are inherent in lattice calculations, due to the ultraviolet cutoff imposed by the lattice, and the need to use discretised derivatives [31]. These are the errors which will manifest themselves during the following extrapolations.

### 3.2.1 Continuum Limit

Results from lattice calculations depend on the finite lattice spacing  $a$ , and must be extrapolated to  $a = 0$  to be compared with physical results. A controlled extrapolation is only possible by fitting to results from multiple lattice spacings. The fit function used to carry out this extrapolation can vary in its details, but generally it will take the form

$$P(a) = P(0) \left( 1 + \sum_i c_i (\Lambda a)^i \right) \quad (3.10)$$

with  $P(0)$  the physical result, and  $c_i$  some coefficients of the powers of  $\Lambda a$ .  $\Lambda$  here is some factor modelling the scale of the discretisation errors. The HISQ action, being improved to better than  $\mathcal{O}(a^2)$ , contains only even powers of  $a$ , and so we will only require even powers of  $a$  to describe its discretisation errors. In fact we will see that the functional dependence on  $a$  is often at an even higher order than this.

Smaller lattice spacings are, clearly, closer to the continuum limit, and so the use of very fine lattices in our calculations is expected to improve the accuracy of the continuum extrapolations we perform.

### 3.2.2 Infinite Volume Limit

Lattices necessarily only represent finite boxes of spacetime: the MILC configurations we use are asymmetric, with  $L$  points in each of the spatial directions and  $T$  points in the Euclidean time direction. The temporal length is longer ( $T > L$ ), which allows more time for the contributions of excited states in a correlator to decay. In addition, for the mesons that we consider in this work, the spatial lengths are long enough that the volume of the box greatly exceeds the size of the particle.

The largest finite-volume effect, then, is that which arises due to virtual pions crossing the periodic spatial boundaries of the lattice. As the spatial volume increases, this effect is suppressed in approximate proportion to  $e^{-m_\pi L}$  [30]. It has been estimated [65, 66] that the errors arising from this effect are less than 1% when  $m_\pi L \gtrsim 4$ , and the MILC collaboration have taken care to ensure that the lattices they generate fulfil this condition [15, 16].

This does depend, to some extent, on the quantities that we are calculating. However, the HPQCD collaboration has previously performed tests on several different lattice volumes, and found that finite-volume errors are negligible in calculations of strangeonium. Given that charmonium and bottomonium states are both smaller than strangeonium (and far smaller than pions), finite size effects should therefore be negligibly small for all of the calculations described in this thesis.

### 3.2.3 Chiral Limit

As explained in section 2.1, it is more computationally demanding to generate lighter quarks in the sea. This means it is often the case that configurations will be generated with up and down quarks in the sea which are unphysically heavy, and if we perform calculations on these lattices, we should perform a chiral extrapolation to remove the dependence of lattice quantities on the sea quark masses.

It is not feasible to address this using the 2+1 ensembles in chapter 4, since the ensembles we use there all have the same relative light sea quark masses. However, there are sets of the 2+1+1 ensembles where all of the quarks in the sea are set at

their physical mass (except that the up and down quarks are still isospin-symmetric,  $m_u = m_d$ ) and using these in conjunction with the heavier-mass ensembles enables us to perform a chiral extrapolation with very well-controlled errors.

Due to the effect of virtual pions as discussed above, lattices with physical pions must have a large volume, which makes them even more computationally intensive to generate. However, their inclusion in simulations is invaluable in controlling discretisation errors, and were they numerous enough that we could discard all other gauge configurations, we would eliminate the need for chiral extrapolation altogether.

### 3.2.4 Operator Renormalisation

Meson operators on the lattice are defined in a different regularisation scheme to their equivalents in the continuum. A finite lattice spacing is all the regularisation required on the lattice, since it removes high-energy states with momentum  $p > \pi/a$ . In the continuum, operators are frequently defined in the  $\overline{\text{MS}}$  scheme, for example, and so a renormalisation factor  $Z$  is required to match the two currents:

$$J_{\text{continuum}} = Z J_{\text{lattice}}. \quad (3.11)$$

This is not required for absolutely every lattice quantity. For example, the local pseudoscalar operator  $P = \bar{\chi}(\gamma_5 \otimes \gamma_5)\chi$  needs no renormalisation thanks to the partially-conserved axial current relation for staggered quarks:

$$\partial_\mu A^\mu = (m_1 + m_2)P \quad (3.12)$$

where  $m_1$  and  $m_2$  are the masses of the valence quarks in the pseudoscalar meson. It is clear from this relation that  $m_q P$  is conserved, and so the renormalisation factors for the operators  $m_q$  and  $P$  must cancel.

There are many different methods available to calculate these  $Z$ -factors, and we will delve into more details as and when we require them.

## 3.3 Treatment of Heavy Quarks

Heavy quark dynamics are not easily simulated with most quark actions on the lattice [28]. The introduction of the HISQ action made this possible for  $c$  quarks with errors at the few-percent level, as demonstrated in [20] and noted in section 1.5.2. This was a significant step forward [67] since effective field theories like nonrelativistic QCD (NRQCD) work very well for the heavy  $b$  quark, but are less successful for the much lighter (and thus less nonrelativistic)  $c$  quark.

The difficulty with heavy quarks stems from the ultraviolet cutoff that we introduce by discretising our spacetime onto a lattice. On a lattice with lattice spacing  $a$ , the shortest wavelength oscillation that can be simulated is that with wavelength  $\lambda_{\min} = 2a$  [10]. Therefore, energies and momenta larger than  $\pi/a$  are not resolved by the lattice. This implies that lattice quark actions will result in large discretisation errors for quarks with rest mass on the order of the cutoff  $\pi/a$  or above, or, equivalently, where the quark mass in lattice units  $am$  does not satisfy  $am \ll 1$  [12].

Consider what this means for charmonium. The charm quark mass is approximately 1.275 GeV [4], and so simulating charmonium mesons with small discretisation errors requires a lattice spacing of less than  $1/1.275 \text{ GeV} \approx 0.15 \text{ fm}$ . State-of-the-art gauge configurations have been produced by the MILC collaboration with lattice spacings of this order and below [15, 16]. Hence, we can set out to perform a fully relativistic simulation of charmonium on these lattices using HISQ valence quarks — indeed this is exactly the technique used in [56], and is the method we will follow in this thesis.

The situation for bottomonium is not so straightforward. Analogously to the rough calculation for charmonium, the bottom quark has a mass of approximately 4.18 GeV [4], and so it would only be accurately resolved by a lattice spacing of significantly less than  $1/4.18 \text{ GeV} \approx 0.05 \text{ fm}$ . This is below the bound of current computational ability, and so we must resort to different techniques to those used for charmonium.

Alternative methods have been developed to deal with this problem, for example NRQCD [68, 50], where advantage is taken of the fact that relativistic effects are very small for heavy quarks. The theory then discretises a nonrelativistic Lagrangian to describe the heavy quarks, which avoids the above problem by allowing the lattice spacing to be matched to the size, rather than the mass, of the relevant hadron.

We will not consider NRQCD in any detail here as we wish to determine the robustness of fully relativistic simulations. As mentioned, the MILC collaboration have produced a recent generation of gauge field ensembles with lattice spacings as low as approx. 0.045–0.06 fm [15, 16], and this allows for an alternative treatment. Accurate, fully relativistic calculations of mesons containing valence  $b$  quarks are still out of reach directly on these lattices, but it is possible to perform calculations at the charm quark mass  $m_c$  and a number of heavier intermediate masses  $m_h$ , where  $m_c < m_h < m_b$ .

The behaviour of bottomonium states can then be determined by extrapolating to  $m_b$  from these intermediate masses, meaning that all relativistic effects are included. The extrapolation inherently introduces extra errors into the final result, and so care must be taken to control other sources of error — in particular, discretisation errors, which would obviously have a detrimental effect on the extrapolation.

Very fine lattices allow us to attain heavy quark masses  $m_h$  close to the physical  $m_b$  — because the inverse lattice spacing is larger, and so the mass of the  $b$  quark in lattice units is reduced — and thus increase the accuracy of our extrapolations.

In this thesis, we will perform relativistic calculations at heavy intermediate masses, and attempt to extrapolate to the bottom quark mass. We will also perform fully relativistic simulations at the charm quark mass directly, and attempt to investigate some of the excited states of charmonium. We now turn to these matters as the subject of the following chapters.

# Chapter 4

## Heavyonium Physics

The mass spectra of charmonium and bottomonium are well-determined experimentally, and exhibit a number of similar features. We will briefly examine these here, as a background to our calculations, with reference to the plot in Figure 4.1. This is an updated version of a similar figure in [69], with values revised and added according to the current Particle Data Group estimates [4], and it shows the different states in the charmonium and bottomonium spectra as determined by experimental measurements.

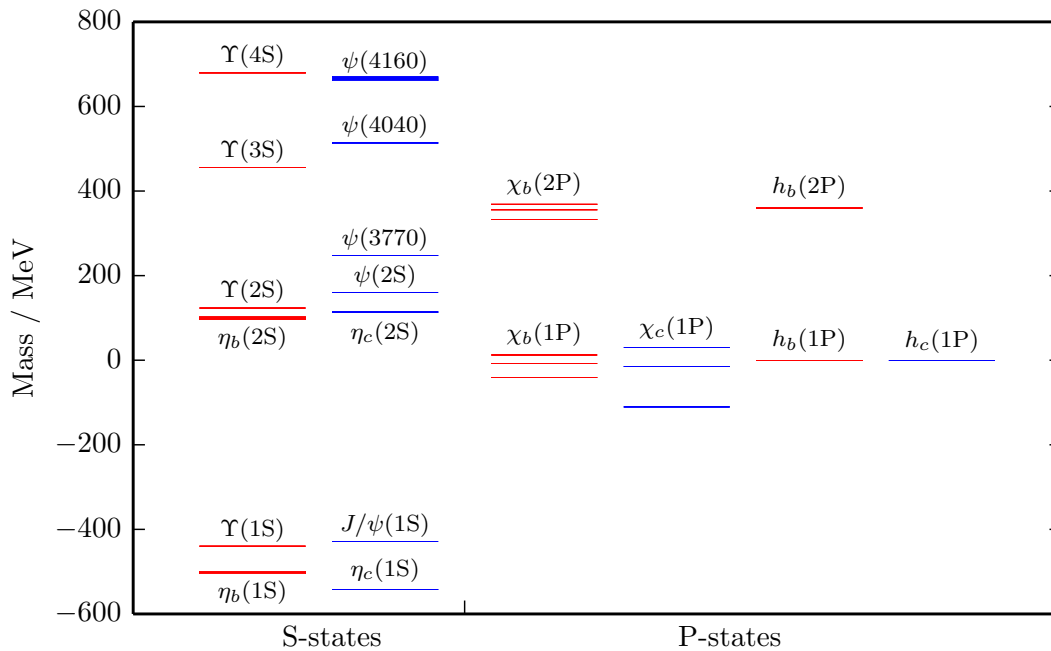


Figure 4.1: The experimental heavyonium spectrum, with masses plotted relative to the spin-averages of the  $\chi_b(1P)$  and  $\chi_c(1P)$  states. Bottomonium states are plotted in red and charmonium states in blue, with the width of the lines corresponding to the uncertainty on their mass. This plot is based on a figure in [69] and has been updated with current experimental data from [4].

Since the bottom quark is significantly heavier than the charm quark, the absolute scale of bottomonium meson masses is much larger than for charmonium, but here we fit both spectra onto the same plot by defining the masses relative to the spin-average of the respective  $\chi(1P)$  states. It is clear from this plot that radial excitations match very closely between the two systems<sup>1</sup>, and this matching is even better if we consider just the spin-averaged S-states [69].

The lowest-energy states in each system, the  $\eta(1S)$  mesons, have masses of approximately 2984 MeV and 9398 MeV for charmonium and bottomonium respectively. Comparing this to the scale of the vertical axis in Figure 4.1, we see that the splittings between states in both systems are significantly smaller than the absolute masses of the mesons. Therefore, dynamical scales such as the kinetic energies of the heavy valence quarks are also much smaller than the meson masses, meaning that the velocities of these quarks are non-relativistic [69].

The momenta of the valence quarks are of the same order as the momenta of typical gluons in the system, meaning that the energies of these gluons will be large [68], and strong interactions between heavy quarks will be almost instantaneous. This interaction can therefore be well-described by a potential model. The heavy quark potential is reviewed fully in [72], and we will not discuss it in detail here, save to say that the spin-averaged values of energy splittings can be accurately predicted with this model [69]. Mass splittings between excited states can therefore be thought of as consequences of a spin-independent non-relativistic potential. On the other hand, splittings between states with the same excitation require a spin-dependent potential to be modelled successfully [69], and we therefore often refer to them as spin splittings.

An important example of such a spin-dependent splitting is the hyperfine mass splitting between 1S states, in both charmonium and bottomonium. In this chapter and the following chapter, we will calculate values for these hyperfine splittings as well as referring back to them for several other purposes.

## Heavyonium on the Lattice

Precision studies of heavyonium in lattice QCD are important tests of QCD as a theory, in that they can provide pre- or postdictions of experimentally determined quantities. In this chapter, we will focus on the ground-state pseudoscalar ( $J^{PC} = 0^{-+}$ ) and vector ( $J^{PC} = 1^{--}$ ) mesons in the charmonium and bottomonium systems.

---

<sup>1</sup>Radial excitations of the  $\psi$  system match so closely to those of the  $\Upsilon$  that they provide evidence in favour of the suggestion that the  $\psi(3770)$ , with quantum numbers  $J^{PC} = 1^{--}$ , is not in fact an S-wave state but a D-wave state [70]. Thanks to measurements of its leptonic decay width, the current hypothesis is in fact that the  $\psi(3770)$  is an admixture of D-wave, S-wave and  $D\bar{D}$  states [71].

The charmonium ground-state pseudoscalar is referred to as the  $\eta_c$ , and that for bottomonium is, analogously, denoted  $\eta_b$ . The vector states are known as the  $J/\psi$  for charmonium, and the  $\Upsilon$  for bottomonium.

The energies of all four of these states are experimentally well-determined [4], as are the hyperfine splittings between the vector and pseudoscalar states. In addition, we have knowledge of their behaviour on the lattice from previous lattice calculations [56, 73, 74] and the determination of the 1S hyperfine splitting in both charmonium and bottomonium is regarded as a sensitive test of the precision of our lattice formalism [67, 20].

In this chapter we report on attempts to precisely determine the hyperfine splitting on state-of-the-art gauge configurations. We will also determine the decay constants of the vector states, and renormalise these by calculating moments of current-current correlators and comparing them to values derived from experiment. Finally, we will calculate the decay constants of the pseudoscalar states, and compare these to previous lattice determinations.

Charm and bottom are both heavy quarks, and so simulating them on the lattice requires some extra considerations. We will perform fully relativistic calculations at the physical charm quark mass, relying on our use of the HISQ action to keep discretisation errors small even on the coarser lattices. The bottom quark is too heavy for this to be a viable method, and so we will calculate at several intermediate heavy masses  $m_h$  and extrapolate to the physical bottom quark mass.

## 4.1 Details of Lattice Calculation

We perform our lattice calculation using the MILC code [1], on the fine, superfine and ultrafine 2+1-flavour ensembles listed in Table 2.1. The lattice spacing  $a$  is determined from the MILC collaboration's values for the modified Sommer parameter  $r_1/a$  on each ensemble (also in Table 2.1), and the physical value of  $r_1 = 0.3133(23)$  fm determined in [52].

On each of these ensembles, we calculate HISQ propagators for quarks of mass  $am_c$  and several heavier masses  $am_h$ . The lattice  $c$  quark mass  $am_c$  is tuned on each ensemble by fixing to the mass of the  $\eta_c$  meson, and has been determined on the ensembles that we are using in [45]. These are listed in Table 4.1 for each ensemble.

The Naik parameter  $\varepsilon$  for each lattice quark mass is calculated by an expansion in powers of the quark mass given explicitly in [20], and its value is also listed in Table 4.1 for the charm quarks. The heavier intermediate masses are chosen to run in discrete steps from just above the lattice charm mass up to about  $am_h = 0.8$ , and the specific heavy masses used across all three ensembles are listed in Table 4.2 along with their corresponding values of  $\varepsilon$ .

Label	$a$ / fm (approx.)	$am_c$	Naik $\varepsilon$	$N_{\text{cfg}} \times N_t$
fine	0.09	0.413	-0.107	$1355 \times 4$
superfine	0.06	0.271	-0.0480	$519 \times 4$
ultrafine	0.045	0.193	-0.0247	$708 \times 4$

Table 4.1: Parameters used on the different ensembles of 2+1-flavour MILC configurations in this calculation. Specifically, we list the lattice charm mass on each ensemble, the Naik parameter  $\varepsilon$  associated with each  $am_c$ , the number of configurations  $N_{\text{cfg}}$  from each ensemble, and the number of time sources  $N_t$  on each configuration, used in the calculation.

$am_h$	Naik $\varepsilon$
0.3	-0.0584
0.4	-0.101
0.5	-0.151
0.6	-0.208
0.7	-0.268
0.8	-0.329
0.85	-0.359

Table 4.2: Parameters used to tune the Naik coefficients for each heavy valence quark mass. These are dependent only on the value of  $am_h$  and so remain the same across different ensembles for the same  $am_h$  values (in lattice units).

The propagators are made from a random wall source on a given timeslice of the lattice, and the calculation is repeated for multiple different timeslices  $N_t$ , on multiple configurations  $N_{\text{cfg}}$  in each ensemble. The numbers of configurations and time sources that we use on each ensemble are also listed in Table 4.1.

The propagators are then combined with appropriate operators to produce the desired correlators. The most accurate meson correlators are those from local or one-link separated sources and sinks, and so we choose the local  $\gamma_5 \otimes \gamma_5$  operator to produce pseudoscalar correlators, and the local  $\gamma_\mu \otimes \gamma_\mu$  operator for the vectors. In the vector case, we utilise a subset corner mask to allow us to obtain correlators for three different vector polarisations from a single random wall source (in fact the same source as that used for the pseudoscalar, with appropriate vector phases applied).

All of the correlators are normalised by dividing by a factor of 3 to account for the random colour 3-vectors in the source, and also by the spatial volume of the lattice  $L^3$ , since we are using a random wall source. We average each set of correlators over time sources and configurations, and for the vector, also over the three different polarisations. In the cases where we use the subset corner mask, we also scale the resulting correlators up by a factor of 8, to account for the smaller effective spatial lattice volume resulting from using only the corners of each hypercube.

It should be noted that correlators as described above had previously been generated by members of the HPQCD collaboration on the fine ensemble, for masses  $am_c = 0.413$  and  $am_h = 0.7$  and  $0.85$ . These correlators are included in the fits described in the next section, along with those generated by the author on the superfine and ultrafine ensembles.

### 4.1.1 Fitting Methodology

Once we have averaged sets of two-point meson correlators for a range of heavyonium pseudoscalar and vector states on several different ensembles, we fit the average correlators  $\overline{C}_{2\text{pt}}$  to extract physical quantities. This fit is performed to the function given in equation 3.2, using the fit code described in section 3.1.2. No oscillating terms are necessary in the analysis of zero-momentum heavy-heavy pseudoscalar correlators (such as we have here) as this current does not couple to an additional opposite-parity meson. These terms are necessary in the analysis of heavy-charm or heavy-strange mesons, and, importantly, for the heavy-heavy vector mesons that we have generated here.

We use the amplitudes  $A_n$  and logarithms of the energies  $E_n$  as fit parameters. Priors for energy and amplitude values are determined by an initial ‘fast fit’ as described in section 3.1.2. For each of the correlator fits considered here we use

$t_{\min} = 8$  to reduce unwanted effects from higher excitations in the correlator. This is determined by trial and error, comparing the  $\chi^2$  and statistical  $Q$ -values for a sample of possible fits as  $t_{\min}$  is altered. We find that the use of an SVD cut larger than the fit code's very small default of  $10^{-15}$  is not necessary in any of these correlator fits, probably due to the use of fast fits to determine accurate priors.

Taking 10 exponentials in the fit function gives a  $\chi^2$  per degree of freedom  $< 1$  for each correlator fit, and when this happens we see the parameters for the ground state stabilise, meaning that we can determine these as accurately as possible while still accounting for the systematic effects of higher excitations in the correlator. The pseudoscalar and vector correlators for each bare quark mass are fitted simultaneously to take account of the correlations between them. All but one of the fits have a  $\chi^2$  value per degree of freedom less than 0.7, with some as low as about 0.14.

From the fit to each average correlator, we can extract the amplitude and mass of the ground state for both the pseudoscalar and vector mesons. From these, we compute a number of physical quantities of interest which will be described in detail in the following sections. In what follows, we will generically refer to the pseudoscalar heavyonium ground-state meson as the  $\eta_h$ , and the vector as the  $\phi_h$ .

## 4.2 Hyperfine Splitting

The hyperfine splitting — the difference between the  $\phi_h$  and the  $\eta_h$  masses — can be determined from each of our fits. The results we obtain, in lattice units, for these masses and their differences are given in Table 4.3.

The calculated values of  $a^{-1}$  on each ensemble (as derived from the  $r_1/a$  values in Table 2.1) are used to translate these results into physical units, and we can then plot the results from different ensembles together. In plotting, we must use a proxy for the quark mass  $am_h$  since the same bare quark mass in lattice units corresponds to different physical quark masses at different lattice spacings — in other words, the mass ‘runs’ with the QCD scale set by the lattice spacing. Here we use the mass of the  $\eta_h$  as a proxy. A plot of the hyperfine splitting results against the inverse of the  $\eta_h$  mass (since we expect the hyperfine splitting to be roughly inversely proportional to the quark mass) is shown in Figure 4.2.

When converting the lattice hyperfine splittings to physical units, we take double the error on the values of  $r_1/a$  in Table 2.1, due to this approximate inverse relationship between hyperfine splitting and quark mass [56]. To understand the origin of this factor of two, suppose the inverse lattice spacing is increased by some small value  $\delta$ . The mass of a heavyonium meson is then shifted upwards by the same proportion, which therefore affects the hyperfine splitting. However, we must then retune the heavy quark mass to correct the mass of the meson — this means

Label	$am_h$	$aM_{\eta_h}$	$aM_{\phi_h}$	$a(M_{\phi_h} - M_{\eta_h})$
fine	0.413	1.28053(7)	1.32901(13)	0.04848(11)
	0.7	1.86535(5)	1.90242(9)	0.03706(6)
	0.85	2.14982(5)	2.18500(8)	0.03519(5)
superfine	0.271	0.89512(4)	0.92926(13)	0.03415(11)
	0.4	1.18141(3)	1.20886(9)	0.02745(7)
	0.5	1.39346(3)	1.41783(7)	0.02437(6)
	0.6	1.59907(3)	1.62136(6)	0.02229(5)
	0.7	1.79893(3)	1.81986(5)	0.02093(4)
	0.8	1.99303(3)	2.01315(5)	0.02013(3)
ultrafine	0.193	0.66635(3)	0.69186(7)	0.02552(6)
	0.3	0.91365(2)	0.93359(5)	0.01995(4)
	0.4	1.13305(2)	1.15010(4)	0.01705(3)
	0.5	1.34512(2)	1.36033(3)	0.01521(2)
	0.6	1.551350(15)	1.56534(3)	0.013993(19)
	0.7	1.752240(14)	1.76544(3)	0.013201(16)
	0.8	1.947690(13)	1.96043(2)	0.012738(14)

Table 4.3: Results in lattice units for the masses of the  $\eta_h$  and  $\phi_h$  mesons, and their difference, for each bare quark mass used on each of the ensembles listed in Table 2.1.

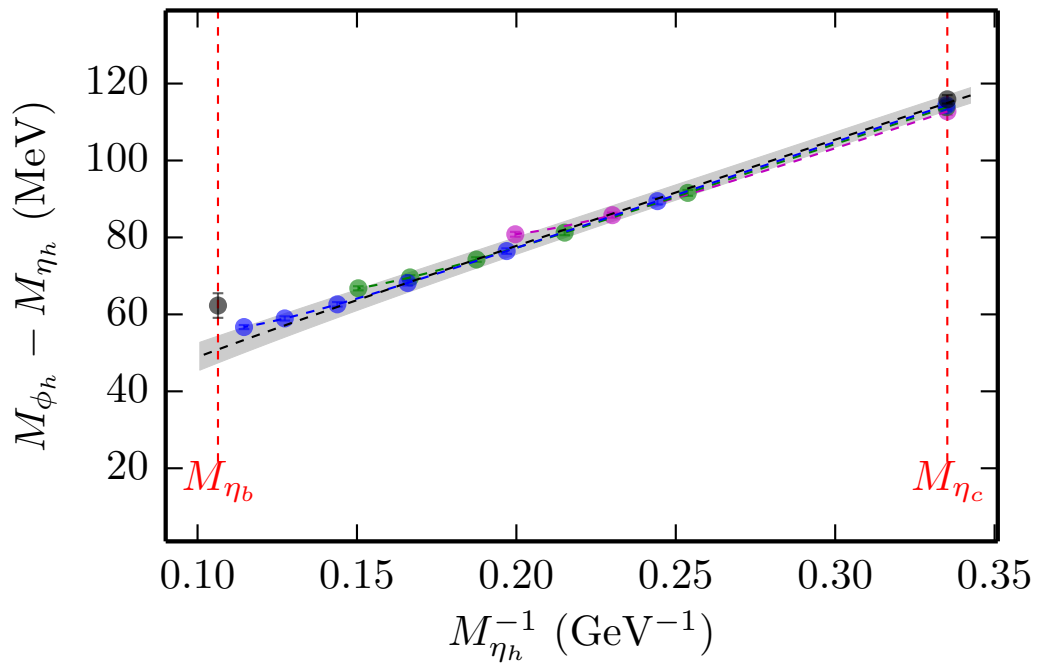


Figure 4.2: The heavyonium hyperfine splitting as a function of the inverse heavyonium mass. Values are shown on the fine (magenta), superfine (green) and ultrafine (blue) lattices, using the local pseudoscalar and vector operators. The coloured dashed lines give the fitted result at each lattice spacing. The black points represent the experimental values and are shown at the physical masses of the  $\eta_c$  and  $\eta_b$  mesons. The grey band shows the combined fit to all the data, i.e. the extrapolation to the continuum.

a decrease in the quark mass of the same proportion  $\delta$ . Because of the inverse relationship mentioned, the hyperfine splitting is then increased by a further factor of  $\delta$ . Overall, then, the uncertainty in the hyperfine splitting value is  $2\delta$ , twice that of the original change in the inverse lattice spacing.

We attempt a fit to these data points using the same fitting codebase as for the individual correlator fits. To obtain a result at the  $\eta_c$  mass we must extrapolate to the continuum limit by taking account of the results at different lattice spacings. To obtain a result at the  $\eta_b$  mass we must also extrapolate in  $M_{\eta_h}$  as described previously. Discretisation errors are well controlled since we have results at several different lattice spacings.

Our fit function takes care of these requirements simultaneously — following [74] we set it up as:

$$F(M, a) = A \left( \frac{M}{M_0} \right)^b \sum_{i=0}^6 \sum_{j=0}^4 c_{ij} \left( \frac{M_0}{M} \right)^i (am)^{2j} \quad (4.1)$$

where  $M$  is the pseudoscalar meson mass and  $am$  the quark mass in lattice units. For the hyperfine splitting we take priors on  $A$  of 0.5(5) and on  $b$  of 0(1). Priors on the coefficients  $c_{ij}$  are generally taken as 0(1), and we take  $M_0 = 1 \text{ GeV}$  for simplicity — this is simply a fixed point for scaling.

It is worth pointing out here that we do not include any terms to model for dependence on the masses of the sea quarks. The reasons for this are two-fold: firstly, on each of the lattices we use here, the light quark mass is identical in relation to the strange quark mass; and secondly, previous HPQCD calculations have determined that there is no significant sea quark mass dependence when using  $r_1/a$  to fix the lattice spacing [75]. Sea-quark mass dependence will be included in the fits in the next chapter, where we use the four-flavour ensembles and set the lattice scale using the Wilson flow parameter  $w_0/a$ .

The fit we obtain in the continuum limit is represented as the grey band in Figure 4.2. Note that our lattice calculations do not include the effects of electromagnetism or  $q\bar{q}$  annihilation, and so far we have not attempted to include these in the fit or on the plot. The fit is excellent, with a  $\chi^2$  value per degree of freedom of 0.11 and a statistical  $Q$ -value of 1.0, and gives continuum results at the physical  $b$  and  $c$  masses of:

$$M_{\Upsilon} - M_{\eta_b} = 50.9(3.5) \text{ MeV} \quad (4.2)$$

$$M_{J/\psi} - M_{\eta_c} = 115.0(2.0) \text{ MeV} \quad (4.3)$$

where the errors quoted are purely statistical.

### Accounting for Annihilation Effects

Both pseudoscalar and vector heavyonium mesons have zero electric charge, and thus there are no electromagnetic effects which contribute to the hyperfine splitting. However, it is true for both charmonium and bottomonium that the vector state has negligible width compared to the pseudoscalar, and so annihilation effects will be larger for the  $\eta_b$  and  $\eta_c$  than they are, respectively, for the  $\Upsilon$  and  $J/\psi$ .

To account for this, we make an estimate of how large these annihilation effects will be. A perturbative calculation in [20] estimates the shift  $\Delta M_{\eta_c}$  that annihilation produces in the mass of the  $\eta_c$ , by relating it to the total decay width  $\Gamma$  via:

$$\Delta M_{\eta_c} = \Gamma(\eta_c \rightarrow \text{hadrons}) \left( \frac{\ln(2) - 1}{\pi} + \mathcal{O}(\alpha_s) \right) \quad (4.4)$$

and we can reasonably assume that the same relationship will hold for the  $\eta_b$ .

Looking at bottomonium first, the total decay width has been experimentally determined as  $10.8_{-4.2}^{+6.0}$  MeV [4, 76]. Substituting this into the expression above gives us  $\Delta M_{\eta_b} = -1.1_{-0.6}^{+0.4}$  MeV. Since this has a significant uncertainty attached to it, we account for the full range of possibilities by shifting our result for the bottomonium hyperfine splitting upwards by  $2(2)$  MeV.

The situation is slightly more complicated for charmonium. The original calculation in [20] obtains a value of  $\Delta M_{\eta_c} = -2.4$  MeV, but the experimental average for the total  $\eta_c$  decay width has increased to  $31.8(8)$  MeV [4] since its publication. Using this new value, we obtain a shift of  $\Delta M_{\eta_c} = -3.1$  MeV.

However, nonperturbative calculations of disconnected diagrams in [77], while agreeing on a value of a few MeV for  $\Delta M_{\eta_c}$ , obtain the opposite sign. The discussion in [56] suggests that this could be due to the gluons produced by  $c\bar{c}$  annihilation forming either a resonance such as a glueball that is lighter than the  $\eta_c$ , or a lighter hadron, which disrupts the perturbative result.

To account for both of these possibilities, we do not apply a shift to the charmonium hyperfine splitting, but instead take an additional systematic error of  $\pm 3.0$  MeV. It makes sense to pursue a different course of action here, given that the perturbative result will be more reliable in the (less relativistic) bottomonium case than for the lighter charmonium.

Our final results are then:

$$M_{\Upsilon} - M_{\eta_b} = 52.9(4.0) \text{ MeV} \quad (4.5)$$

$$M_{J/\psi} - M_{\eta_c} = 115.0(3.6) \text{ MeV} \quad (4.6)$$

where we have applied the shift to the bottomonium value, and combined the statistical and systematic errors for charmonium to facilitate comparisons.

The differences of the current experimental averages for the masses of these mesons are [4]:

$$M_{\Upsilon} - M_{\eta_b} = 62.3(3.2) \text{ MeV} \quad (4.7)$$

$$M_{J/\psi} - M_{\eta_c} = 113.3(7) \text{ MeV}. \quad (4.8)$$

The charmonium value is in good agreement with the experimental average, and also with the value obtained from the lattice in [56] (which implemented a very similar method to this calculation) of  $116.5(2.1)(2.4) \text{ MeV}$ .

The bottomonium value is not incompatible with the experimental average — the two results agree at the  $2\sigma$  level once we have accounted for annihilation effects — but clearly favours the most recent result included in this average, that from the Belle collaboration of  $57.9(2.3) \text{ MeV}$  [76]. Our bottomonium result is also in agreement with the value obtained on  $2+1+1$ -flavour lattices but using NRQCD to simulate the  $b$  quark, which is  $60.0(6.4) \text{ MeV}$  [73].

More extensive comparisons of various charmonium and bottomonium hyperfine splitting results, including those determined here, are made in chapter 6. We defer further discussion on them until then.

### 4.2.1 Charmonium Cross-Check

As a test of the stability of our charmonium result, we can perform a separate fit to only the charmonium points. This means that we have no heavy quark mass dependence to take account of, since all of our charmonium correlators were generated using a well-tuned physical  $c$  quark mass, and we need only concern ourselves with continuum extrapolation.

We are able to obtain a good fit with the simplest possible form of the fit function: that to a single physical value  $p$ . We do not require any terms which model dependence on discretisation errors, and this suggests that the discretisation errors are very small. Indeed this can be seen on the plot. Taking a Bayesian prior of  $100(50) \text{ MeV}$  on  $p$  produces a fit with a  $\chi^2$  of 0.44 and a  $Q$ -value of 0.72.

A plot of the charmonium results is shown in Figure 4.3. Here we plot against the square of the lattice charm quark mass as a proxy for the lattice spacing. The fit we obtain is displayed as the grey band on the plot, and gives a physical value for the charmonium hyperfine splitting of  $113.69(53) \text{ MeV}$ . The error here is purely statistical, and to account for annihilation effects as described above, we again include a systematic error of  $\pm 3.0 \text{ MeV}$ .

We also take an additional systematic error of  $\pm(2 \times 0.73\%)$ . This is twice the relative error on the physical value of  $r_1 = 0.3133(23) \text{ fm}$  used to determine the lattice spacing, which — unlike in the heavyonium fits — is not included when

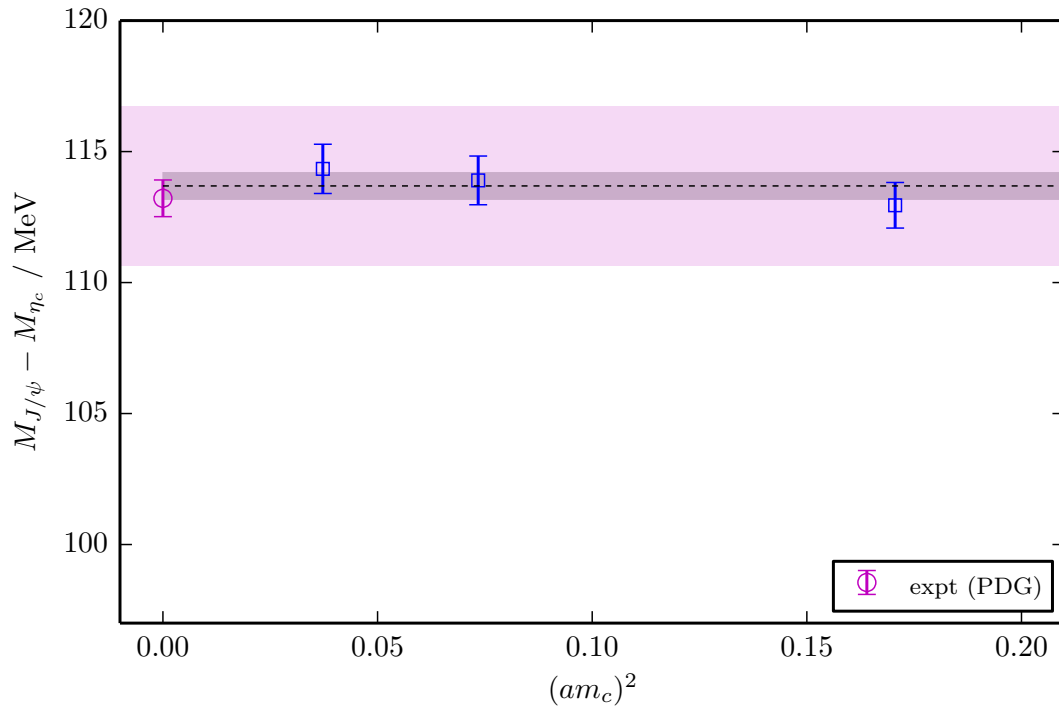


Figure 4.3: The charmonium hyperfine splitting. The magenta point represents the experimental value. We plot against the squared lattice charm mass as a proxy for the lattice spacing. The grey band shows our calculated fit, although since the form of our fit function is so simple, this is equivalent to our calculated physical hyperfine splitting value inclusive of statistical errors only. The light magenta band shows our fitted continuum result with the addition of systematic errors, as described in the text.

converting the lattice results to physical units, and is therefore not included on the plotted points. As in the previous section, we also take double the error on the values of  $r_1/a$  in Table 2.1 when converting our lattice results to physical units. The reason for doubling both of these errors is also explained in detail in the previous section, relating to our use of the  $\eta_c$  mass to tune the bare charm quark mass.

Combining these errors for ease of comparison we obtain a final result of:

$$M_{J/\psi} - M_{\eta_c} = 113.9(3.5) \text{ MeV} \quad (4.9)$$

which is in agreement with the result from our full fit as well as the experimental average. We therefore conclude that the charmonium hyperfine splitting is mainly unaffected by inclusion in the heavy-quark extrapolation.

### 4.3 Moments of the Vector Correlator

Time moments  $G_n^V$  of the vector heavyonium correlator are defined as:

$$G_n^V = Z^2 C_n^V = Z^2 \sum_{\tilde{t}} \tilde{t}^n \overline{C}_{\phi_h}(\tilde{t}) \quad (4.10)$$

where  $\overline{C}$  is the average correlator, and  $\tilde{t}$  is lattice time symmetrised<sup>2</sup> around the centre of the lattice. Going forward in lattice time  $t$ ,  $\tilde{t}$  runs from 0 to  $(T/2 - 1)$ , is 0 again at the midpoint in  $t$ , and then runs from  $(-T/2 + 1)$  to  $-1$ .  $Z$  is a renormalisation factor which matches the vector current on the lattice to that in the continuum, and is different for each heavy mass at each lattice spacing. We determine  $Z$  using the current-current correlator method, which is explained in more detail in section 4.3.1, and use the value obtained from the 8<sup>th</sup> moment,  $Z_8$ , to renormalise the rest.

Lattice results for the 4<sup>th</sup>, 6<sup>th</sup>, 8<sup>th</sup> and 10<sup>th</sup> moments at each bare heavy quark mass are given in Table 4.4. Multiplying the lattice results by  $Z_8^2$  performs the renormalisation as described, and we take each moment  $G_n^V$  to the power  $1/(n - 2)$  to reduce them all to the same dimension. Finally, we divide by  $a^{-1}$  (determined, as before, from the  $r_1/a$  values in Table 2.1) to obtain the correct physical dimensions of  $\text{GeV}^{-1}$ .

We perform a continuum fit to the same functional form as in equation 4.1, and this again allows for extrapolation to the physical bottom quark mass. Here, however, we strongly constrain the leading power  $b$  to be  $-1.000000(1)$ , since we expect the moments (with appropriate roots as defined above) to be inversely proportional

<sup>2</sup>More precisely, as we will define it,  $\tilde{t}$  is actually antisymmetric around the centre of the lattice. Since we will only ever calculate even moments in this work, meaning that  $n$  is always even in equation 4.10, the sign of  $\tilde{t}$  has no bearing on our results.

Label	$am_h$	$\left(\frac{G_4^V}{Z^2 a^2}\right)^{1/2}$	$\left(\frac{G_6^V}{Z^2 a^4}\right)^{1/4}$	$\left(\frac{G_8^V}{Z^2 a^6}\right)^{1/6}$	$\left(\frac{G_{10}^V}{Z^2 a^8}\right)^{1/8}$
fine	0.413	0.758630(73)	1.63514(12)	2.38869(15)	3.09524(18)
	0.7	0.491872(24)	1.135643(38)	1.669306(48)	2.153072(58)
	0.85	0.409219(15)	0.987658(24)	1.466719(30)	1.893197(36)
superfine	0.271	1.07379(16)	2.28194(26)	3.36231(32)	4.38204(37)
	0.4	0.795125(76)	1.72128(12)	2.53238(16)	3.30000(19)
	0.5	0.663350(48)	1.462713(79)	2.14895(10)	2.79403(12)
	0.6	0.568088(32)	1.280873(53)	1.882604(69)	2.441009(83)
	0.7	0.494791(22)	1.144570(37)	1.687259(48)	2.183120(59)
	0.8	0.435875(16)	1.037224(27)	1.537373(35)	1.987749(43)
ultrafine	0.193	1.43172(20)	3.03834(32)	4.49688(41)	5.87100(47)
	0.3	1.017444(84)	2.18429(14)	3.23559(18)	4.23450(21)
	0.4	0.806782(46)	1.754420(78)	2.59278(10)	3.39039(12)
	0.5	0.669669(29)	1.481237(48)	2.184022(64)	2.848464(78)
	0.6	0.571624(19)	1.291509(32)	1.903425(42)	2.474582(52)
	0.7	0.496786(13)	1.150697(22)	1.699636(29)	2.203839(36)
	0.8	0.4369835(94)	1.040678(16)	1.544610(21)	2.000320(26)

Table 4.4: Time moments of the heavyonium vector correlator for each heavy-quark mass on each ensemble, raised to the appropriate power, in lattice units. As displayed here, these results are unrenormalised; to do this, we use the renormalisation factor  $Z_8$  obtained from the 8<sup>th</sup> moment of the correlator as detailed in section 4.3.1.

to the quark mass. Since the moments are not as sensitive to short-distance effects as the hyperfine splitting [56], we reduce the prior on the overall factor  $A$  to be  $x \pm x$  and the prior on the coefficients  $c_{ij}$  of the lattice spacing-dependent terms to be  $0 \pm y$ , where  $x = 0.15n - 0.3$  and  $y = 4/n$ . This dependence on  $n$  means that the fit function has an appropriate normalisation for each different moment, both in terms of its overall factor  $A$  (dependent on  $x$ ) and the scale of the discretisation errors (modelled by  $y$ , and decreasing with increasing  $n$ ).

We fit to the 4<sup>th</sup>, 6<sup>th</sup>, 8<sup>th</sup> and 10<sup>th</sup> moments separately and obtain fits with  $\chi^2$  values per degree of freedom of 0.25, 0.22, 1.94 and 1.18, and  $Q$ -values of 1.0, 1.0, 0.013 and 0.27 respectively. These fits are good, with the exception of that to the 8<sup>th</sup> moment. While this fit is not unacceptable, it is significantly worse than its counterparts. However, as we will see in Table 4.8 in the next section, it is the best possible fit to these data, far better than the other fits obtained using different  $Z$ -factors for renormalisation. The physical results derived from Table 4.4, along with our fits, are plotted in Figure 4.4 as a function of the heavyonium mass.

The fitted continuum results at the physical  $\eta_h$  masses can be compared to the  $q^2$ -derivative moments  $\mathcal{M}_k$  of the heavy quark vacuum polarisation  $\Pi_h(q^2)$  [78]:

$$\mathcal{M}_k = \frac{12\pi^2 e_h^2}{k!} \left( \frac{d}{dq^2} \right)^k \Pi_h(q^2) \Big|_{q^2=0} \quad (4.11)$$

where  $n = 2k + 2$  and  $e_h$  is the electric charge of the heavy quark under consideration. Values for  $\mathcal{M}_k$  can be extracted very accurately [79, 80] from experimental results in the  $c$  and  $b$  regions for the normalised heavy-quark cross-section

$$R_h(s) = \frac{\sigma_{e^+e^- \rightarrow h\bar{h}+X}(s)}{\sigma_{e^+e^- \rightarrow \mu^+\mu^-}(s)} \quad (4.12)$$

with  $h$  denoting a charm or bottom quark, since we can define [78, 79, 80]

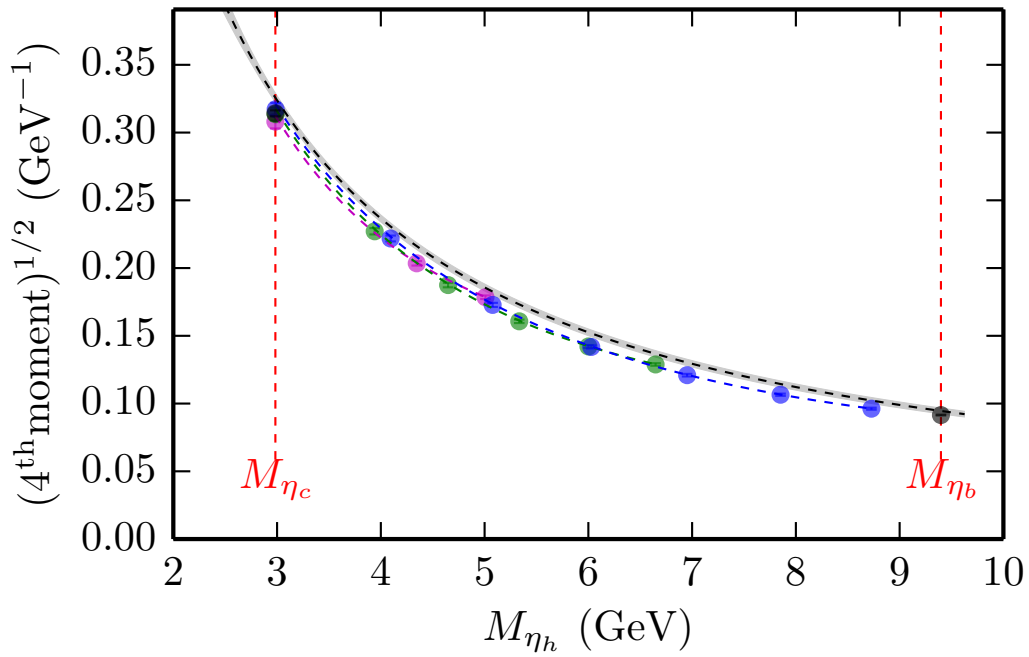
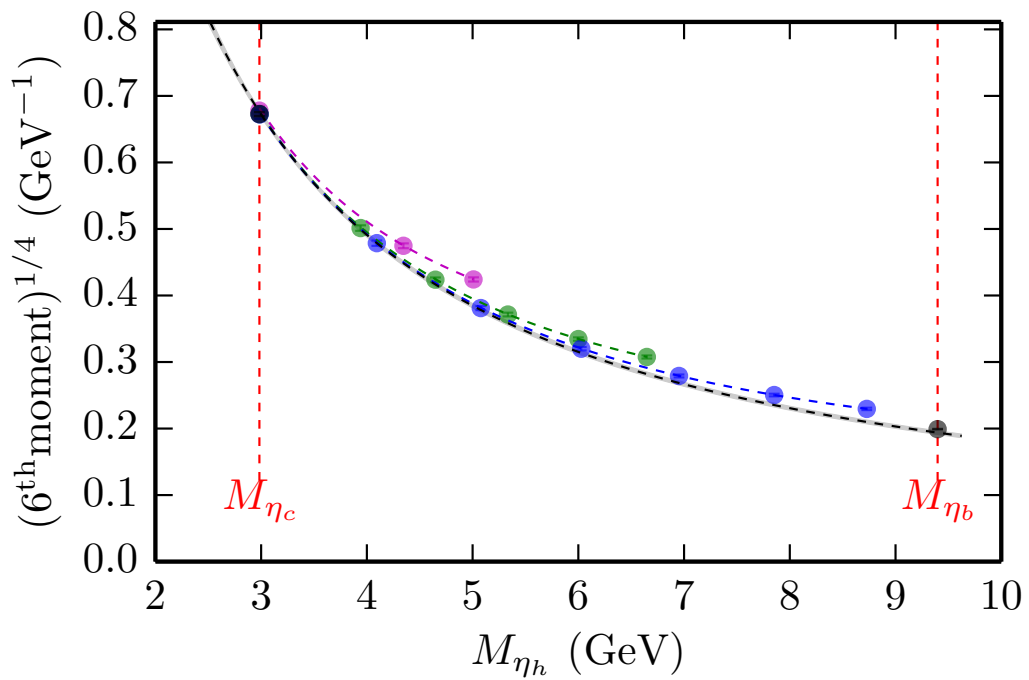
$$\mathcal{M}_k \equiv \int \frac{ds}{s^{k+1}} R_h(s). \quad (4.13)$$

We must then normalise these moments and reduce them to the same dimension before comparing to our lattice results, viz.

$$\mathcal{M}_k^{\text{norm}} = \left( \frac{(2k+2)! \mathcal{M}_k}{12\pi^2 e_h^2} \right)^{1/2k}. \quad (4.14)$$

The extracted values from [79] and [80], appropriately normalised for comparison, are listed alongside our physical results in the continuum limit in Table 4.5, and are also plotted in Figure 4.4 at the physical  $\eta_c$  and  $\eta_b$  masses.

The agreement of our physical results with those derived from experiment is variable, as we show in Table 4.6, although none of the agreements are unreasonable.

(a) 4<sup>th</sup> moment(b) 6<sup>th</sup> moment

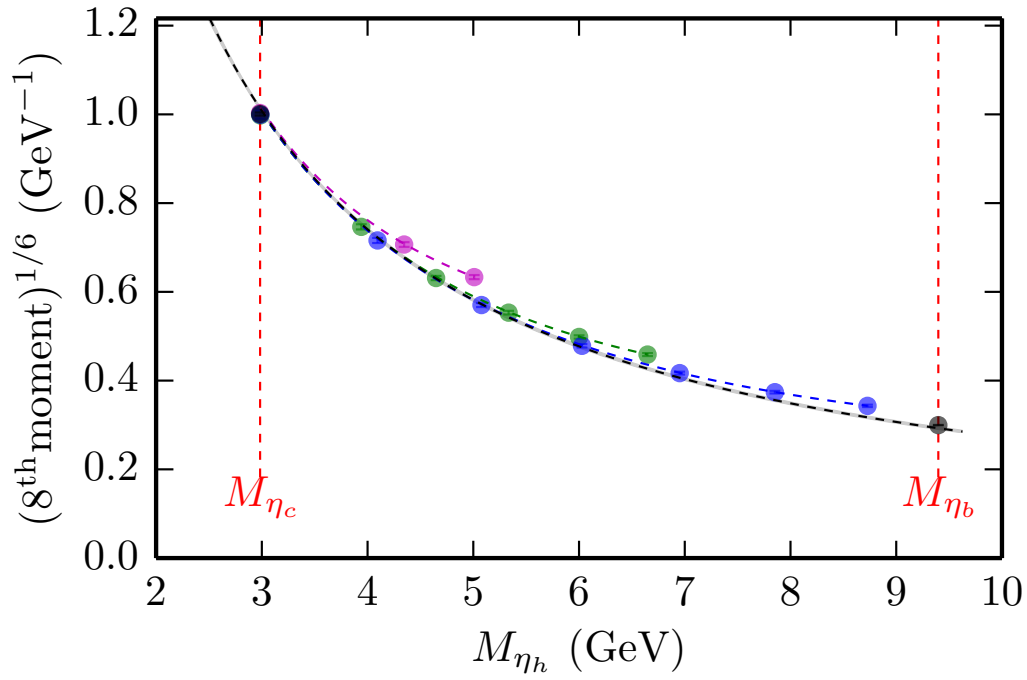
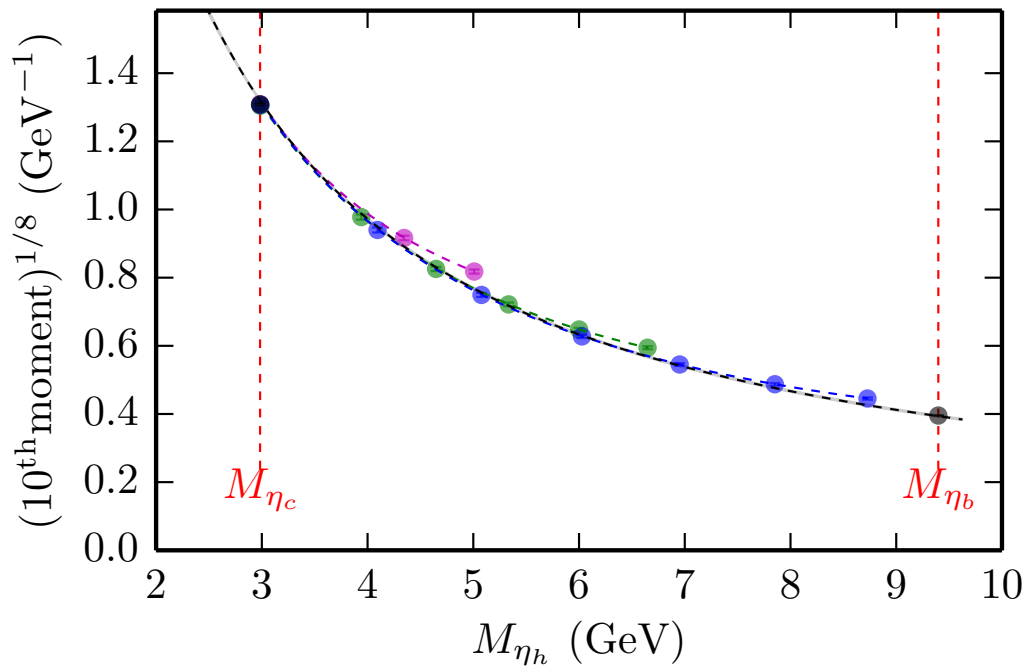
(c) 8<sup>th</sup> moment(d) 10<sup>th</sup> moment

Figure 4.4: Moments of the heavyonium vector correlator as a function of heavyonium mass, determined on the same lattices as in Figure 4.2. The black points are the results derived from experiment, and the grey band shows the fit as described in the text.

$n$	$k$	Charmonium		Bottomonium	
		$(G_n^V)^{\frac{1}{n-2}}/\text{GeV}^{-1}$	$\mathcal{M}_k^{\text{norm}}/\text{GeV}^{-1}$	$(G_n^V)^{\frac{1}{n-2}}/\text{GeV}^{-1}$	$\mathcal{M}_k^{\text{norm}}/\text{GeV}^{-1}$
4	1	0.3257(34)	0.3142(22)	0.0946(22)	0.09151(31)
6	2	0.6760(40)	0.6727(30)	0.1939(28)	0.19910(49)
8	3	1.0136(42)	1.0008(34)	0.2927(31)	0.29964(55)
10	4	1.3196(44)	1.3088(35)	0.3937(35)	0.39548(59)

Table 4.5: Time moments of the charmonium and bottomonium vectors. In the left-hand columns, we list the physical results from our continuum fits and their associated index  $n$ . In the right-hand columns, we list the comparable results extracted from experiment in [79] and [80], indexed by  $k$  and appropriately normalised for comparison to our results.

Most of the continuum values are within  $3\sigma$  of their experimental counterparts, with only one value — the 4<sup>th</sup> charmonium moment — exhibiting a greater discrepancy than this, at the  $3.4\sigma$  level, and a further two agreeing to better than  $1\sigma$ . Our lattice results have small statistical errors, of similar size to their experimental counterparts in the charmonium case, and it may be the case that we are underestimating the discretisation errors present in these results.

$n$	$k$	Charmonium agreement	Bottomonium agreement
4	1	+3.4 $\sigma$	+1.4 $\sigma$
6	2	+0.8 $\sigma$	-1.9 $\sigma$
8	3	+3.0 $\sigma$	-2.2 $\sigma$
10	4	+2.5 $\sigma$	-0.5 $\sigma$

Table 4.6: Agreement of the calculated time moments of the charmonium and bottomonium vectors from our continuum fits with the corresponding values extracted from experiment, as listed in Table 4.5. We define this as the difference between the calculated lattice value and the experimentally-extracted value,  $(G_n^V)^{\frac{1}{n-2}} - \mathcal{M}_k^{\text{norm}}$ , divided by the error estimate on the lattice value.

There are other possible causes of this discrepancy, and we will investigate some of these in considerable detail in later subsections. For now, let us explain the process of calculating the renormalisation factors that have been used in this section, as mentioned earlier.

### 4.3.1 Current-Current Renormalisation

To determine the renormalisation factors  $Z$  used in this chapter, we follow the current-current renormalisation method detailed in Appendix B of [56]. An overview

of the procedure is given here.

We define lattice time moments for our vector correlators as in equation 4.10:

$$Z^2 C_n^V = Z^2 \sum_{\tilde{t}} \tilde{t}^n \overline{C}_{\phi_h}(\tilde{t}) \quad (4.15)$$

and for our pseudoscalar correlators as:

$$C_n^P = \sum_{\tilde{t}} \tilde{t}^n (am_h)^2 \overline{C}_{\eta_h}(\tilde{t}) \quad (4.16)$$

with an extra factor of  $(am_h)^2$  to ensure that  $C_n^P$  is finite as  $a \rightarrow 0$ .

The pseudoscalar correlator is absolutely normalised due to the partially-conserved axial current relation for HISQ quarks [20, 81], but the vector current on the lattice must be renormalised by a factor  $Z$  as included above. We can match the lattice moments to results derived from perturbation theory in the continuum [78, 79] and thus obtain values for  $Z$  on each ensemble for each heavy-quark mass used.

In the continuum we define for the pseudoscalar:

$$c_n^P = \frac{g_n^P(\alpha_{\overline{\text{MS}}}(\mu), \mu/m_h)}{(am_h(\mu))^{n-4}} + \mathcal{O}((am_h)^m) \quad (4.17)$$

and for the vector:

$$c_n^V = \frac{g_n^V(\alpha_{\overline{\text{MS}}}(\mu), \mu/m_h)}{(am_h(\mu))^{n-2}} + \mathcal{O}((am_h)^m) \quad (4.18)$$

where  $m$  generically denotes some higher power of  $am_h$ , and  $g_n^{P,V}$  is the perturbative series for continuum QCD in the  $\overline{\text{MS}}$  scheme, for the pseudoscalar ( $P$ ) and vector ( $V$ ) respectively. These series have been calculated to four loops in [78, 79], and we use the coefficients determined there to determine  $g_n^{P,V}$  to this order. We take  $\mu/m_h = 1$ ; however, the values we obtain depend only very weakly on  $\mu$  since we also allow for higher-order terms in the series up to 20<sup>th</sup> order. Priors of 0.0(0.5) are taken on the coefficients of these higher-order terms.

The dominant subleading term in the perturbative series is that arising from the gluon condensate, viz.

$$g_n^{P,V} = \mathcal{O}(\alpha_{\overline{\text{MS}}}(\mu), \mu/m_h) + \Delta \mathcal{M}_n^{(G^2)} + \dots \quad (4.19)$$

and an analytic expression for this term is constructed in [78] which contains a correction factor of  $\langle \alpha_s G^2 / \pi \rangle$ . An upper bound for the value of this factor has been determined in [82], as  $0.006 \pm 0.012 \text{ GeV}^4$ . We therefore also include such a term to correct for contributions from the gluon condensate, allowing for  $\langle \alpha_s G^2 / \pi \rangle = 0 \pm 0.012 \text{ GeV}^4$  in the correction factor.

We define both pseudoscalar and vector moments since this will allow us to eliminate the terms in  $(am_h)^m$  from the continuum expressions in (4.17) and (4.18).

Taking the ratio of the appropriate pseudoscalar and vector moments, these terms will cancel and eliminate any error from not including their contribution<sup>3</sup>. We can then match the moments on the lattice to those in the continuum, and determine  $Z$  via:

$$Z_n = \sqrt{\frac{C_{n+2}^P/C_n^V}{c_{n+2}^P/c_n^V}}. \quad (4.20)$$

Since the continuum moments are functions of  $\alpha_{\overline{\text{MS}}}(\mu)$  and  $am_h$ ,  $Z$  will be different for each bare quark mass and at each lattice spacing. Therefore, we must perform this matching separately for each heavy-quark mass on each of our ensembles. The  $Z$ -factors obtained from this procedure are listed in Table 4.7 for  $n = 4, 6$  and  $8$ .

Label	$am_h$	$Z_4$	$Z_6$	$Z_8$
fine	0.413	0.994(14)	0.929(12)	0.932(14)
	0.7	1.1105(31)	0.9768(27)	0.9488(34)
	0.85	1.20938(62)	1.04776(80)	0.9998(20)
superfine	0.271	0.982(12)	0.959(12)	0.967(13)
	0.4	0.9927(70)	0.9407(64)	0.9458(66)
	0.5	1.0174(50)	0.9376(45)	0.9357(46)
	0.6	1.0563(33)	0.9497(29)	0.9367(29)
	0.7	1.1083(17)	0.9776(15)	0.9513(16)
	0.8	1.17095(62)	1.01949(56)	0.97884(71)
ultrafine	0.193	0.986(11)	0.978(11)	0.984(12)
	0.3	0.9833(57)	0.9605(55)	0.9679(56)
	0.4	0.9930(42)	0.9455(39)	0.9512(39)
	0.5	1.0170(32)	0.9410(29)	0.9402(29)
	0.6	1.0553(22)	0.9514(19)	0.9398(19)
	0.7	1.1066(12)	0.9777(10)	0.9523(10)
	0.8	1.16854(40)	1.01787(35)	0.97757(37)

Table 4.7: Renormalisation factors determined from the current-current correlator method, for each heavy quark mass on each ensemble.  $Z_n$  is the renormalisation factor obtained by matching the  $n^{\text{th}}$  lattice moment to its equivalent continuum value, derived from experimental results.

<sup>3</sup>There is a slightly subtle point related to taking this ratio that is worth making here. One may be surprised to find that, despite using  $Z_8$  to fix the normalisation — meaning that we have, in essence, set the values of the  $8^{\text{th}}$  moment equal to those derived from perturbation theory — these values (as plotted in Figure 4.4c) still exhibit some discretisation errors, albeit small. The reason for this is likely to be that we are in fact setting the value of the ratio of pseudoscalar to vector moments equal to its perturbative partner, and not the vector moment directly.

### 4.3.2 Choice of $Z$ -Factor

We must choose which  $Z$ -factor to use to renormalise the moments in the previous section, and also the vector decay constants in the following section. To do so, we consider two points related to the renormalisation of the moments.

The first point is illustrated in Table 4.8, which lists the  $\chi^2$  and statistical  $Q$  values of the continuum fit performed to each calculated moment  $(G_n^V)^{1/(n-2)}$  for each choice of  $Z$ . It is clear from the values in the table that using the renormalisation factors  $Z_8$  obtained from the 8<sup>th</sup> moment results in the best continuum fits to the data, evidenced by the minimal  $\chi^2$  and maximal  $Q$  values this produces. This is our first reason to select  $Z_8$  for use in our renormalisations.

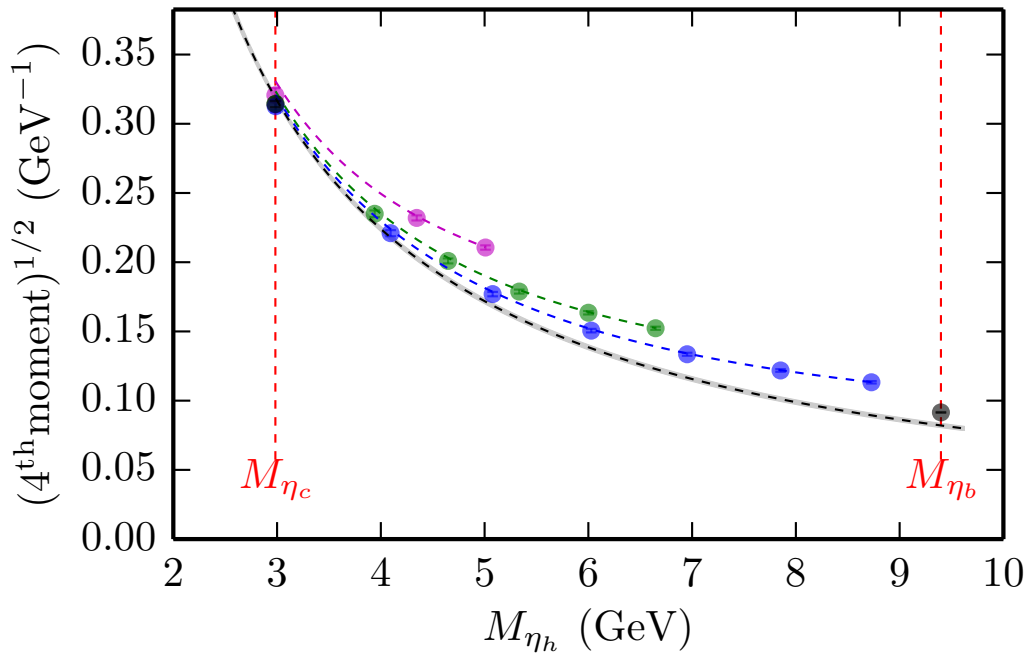
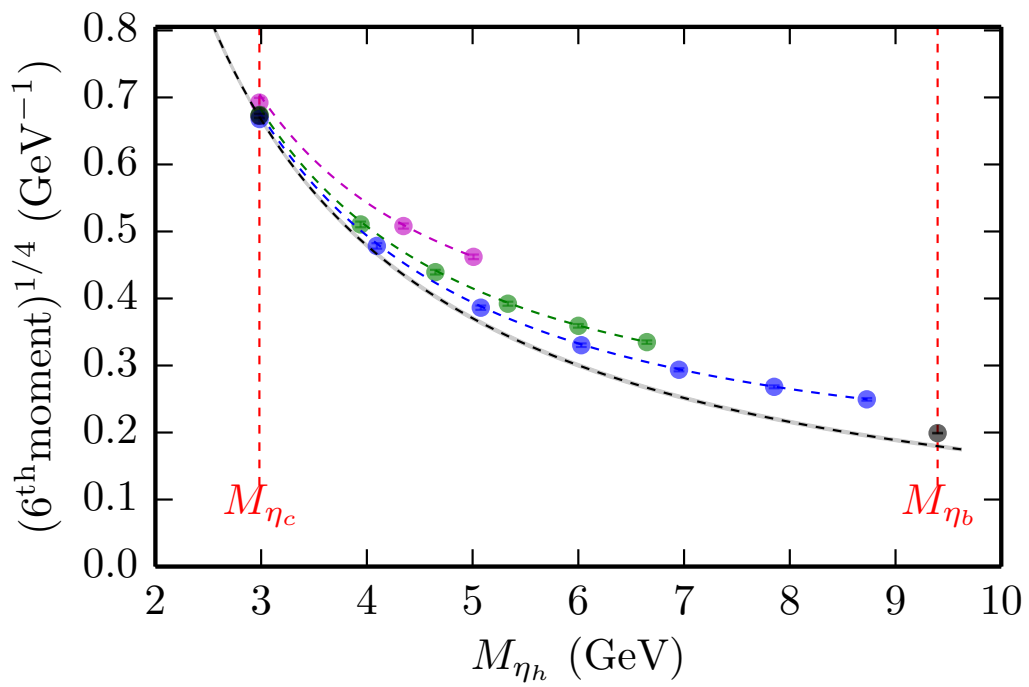
$n$	$Z_4$		$Z_6$		$Z_8$	
	$\chi^2$	$Q$	$\chi^2$	$Q$	$\chi^2$	$Q$
4	0.8	0.69	3.7	$5.6 \times 10^{-7}$	0.25	1.0
6	1.3	0.16	3.0	$6.1 \times 10^{-5}$	0.22	1.0
8	3.4	$5.1 \times 10^{-6}$	6.8	$7.5 \times 10^{-16}$	1.9	0.013
10	1.8	0.024	4.5	$3.4 \times 10^{-9}$	1.2	0.27
Sum	7.3	0.8740	18.0	$6.156 \times 10^{-5}$	3.57	2.283

Table 4.8:  $\chi^2$  and statistical  $Q$  values for continuum fits to the  $n^{\text{th}}$  moments of the vector correlator, when renormalised using the listed  $Z$ -factors. It is clear that using  $Z_8$  results in the minimal  $\chi^2$  and maximal  $Q$  values.

The second point is most simply understood by considering plots of the moments  $(G_n^V)^{1/(n-2)}$  when using different renormalisation factors. The previous Figure 4.4 showed the plots obtained when renormalising with  $Z_8$ . We now plot the same quantities, but instead using  $Z_4$  and  $Z_6$  for renormalisation, in Figures 4.5 and 4.6 respectively. In comparing the results from different ensembles in each case, it is clear that the calculated moments exhibit the smallest discretisation errors when renormalised by  $Z_8$ . This is unsurprising, since in general, the lower moments contain larger momenta and are hence more relativistic, and we therefore expect larger discretisation errors there. Choosing  $Z_4$  or  $Z_6$ , then, pushes these discretisation errors onto the results for each of the moments. Predictability notwithstanding, this is our second reason for selecting  $Z_8$ , and it is therefore the factor which we use to renormalise the local vector current whenever it is required in this chapter.

### 4.3.3 One-link Vector Operator

To further investigate the differences in our fitted continuum moments from their experimentally-determined values, we repeat a subset of our lattice calculation using

(a) 4<sup>th</sup> moment(b) 6<sup>th</sup> moment

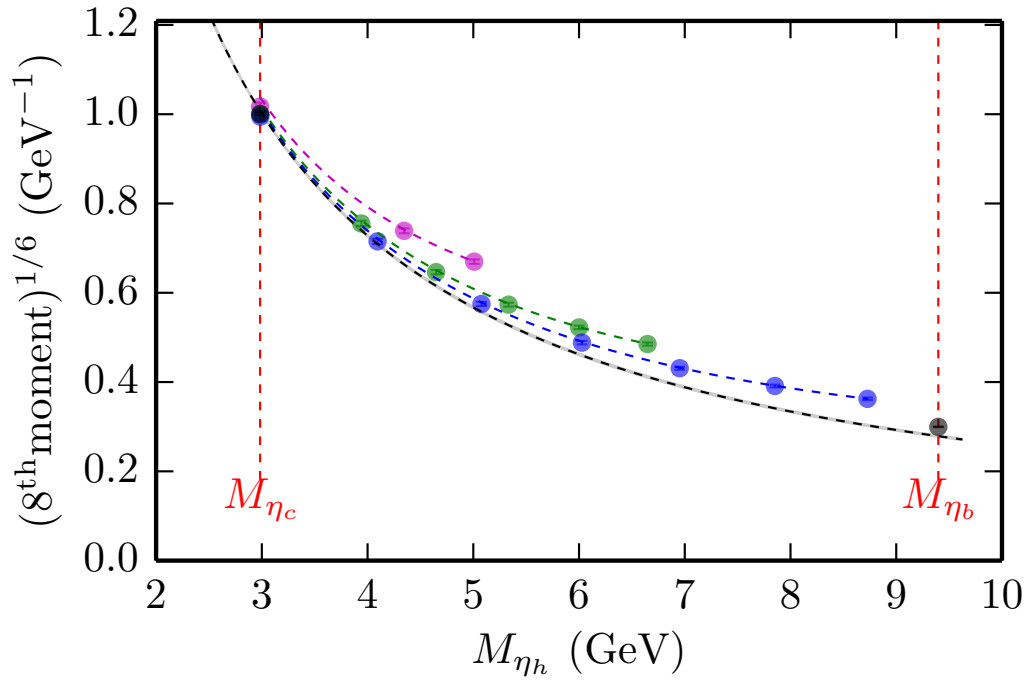
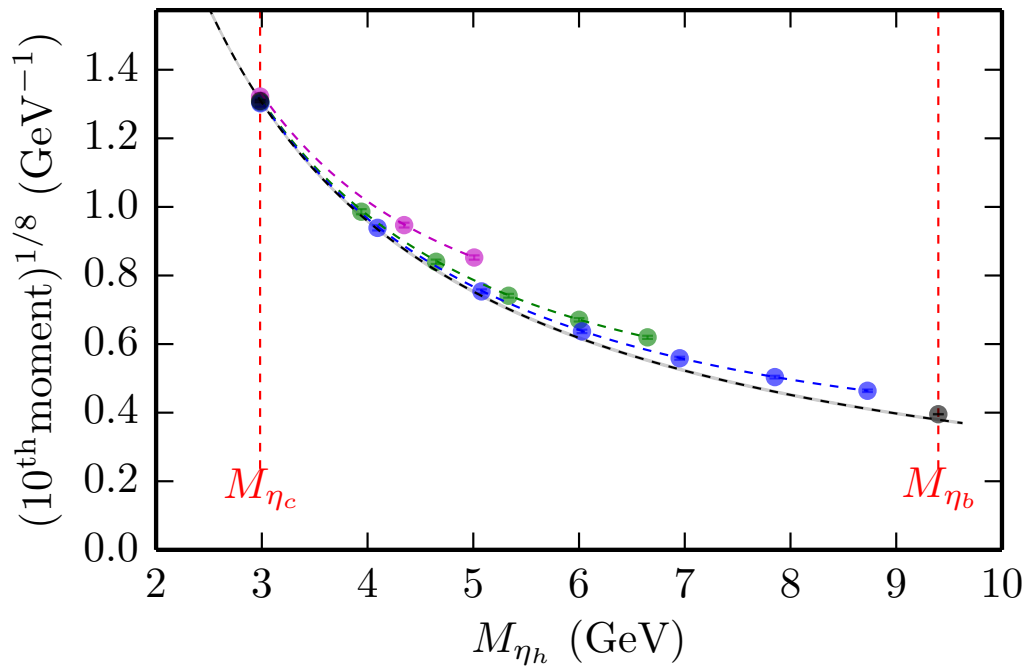
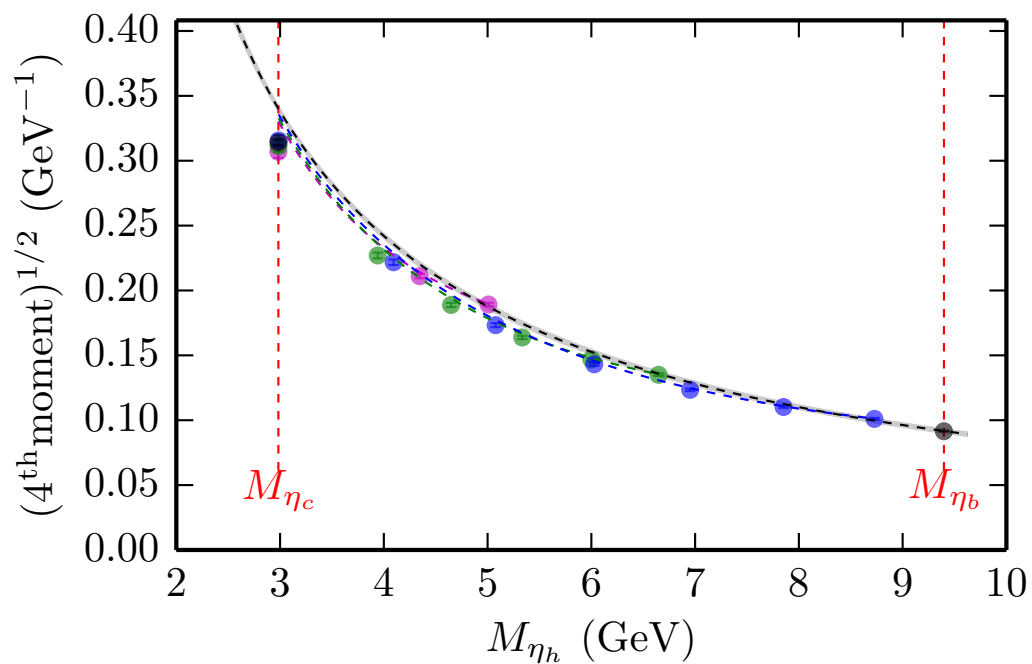
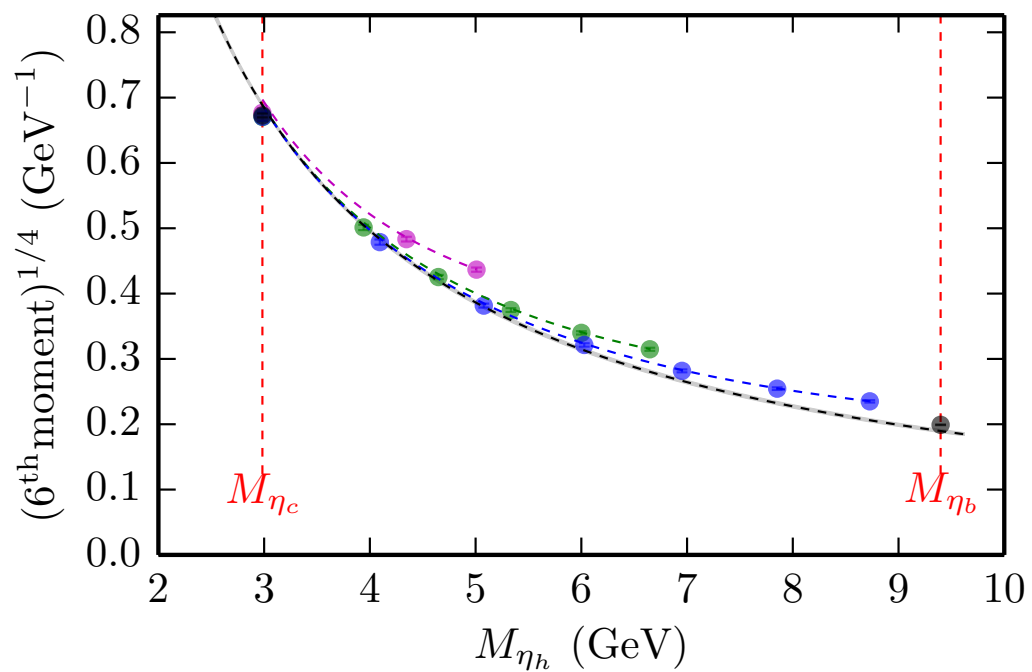
(c) 8<sup>th</sup> moment(d) 10<sup>th</sup> moment

Figure 4.5: Moments of the heavyonium vector correlator as a function of heavyonium mass, as in Figure 4.4, but renormalised using  $Z_4$ , the renormalisation factor obtained from the 4<sup>th</sup> moment.

(a) 4<sup>th</sup> moment(b) 6<sup>th</sup> moment

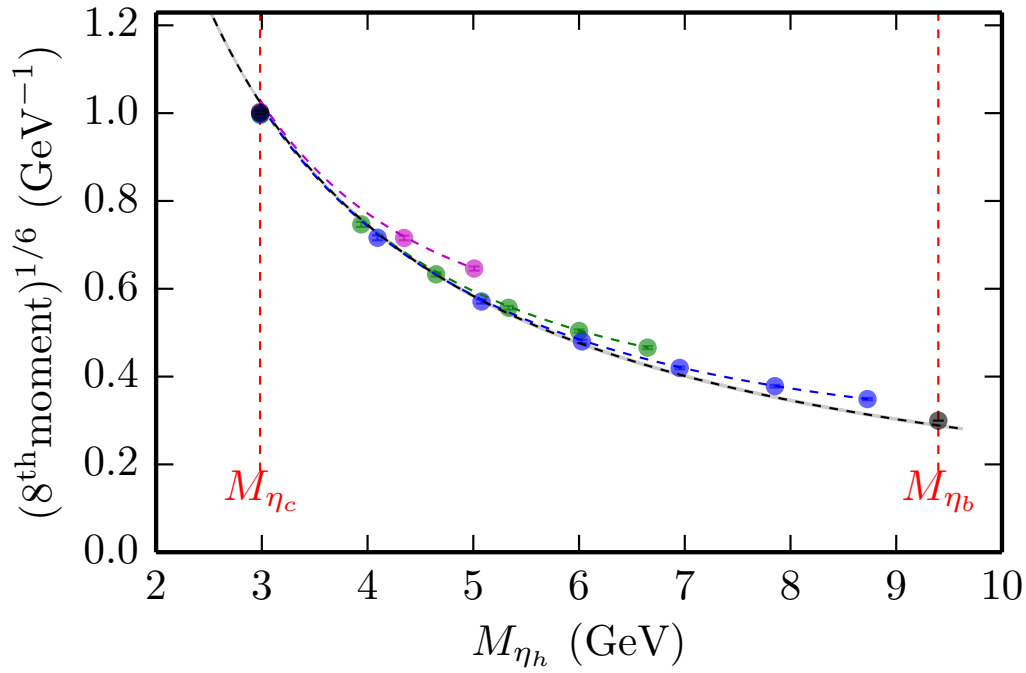
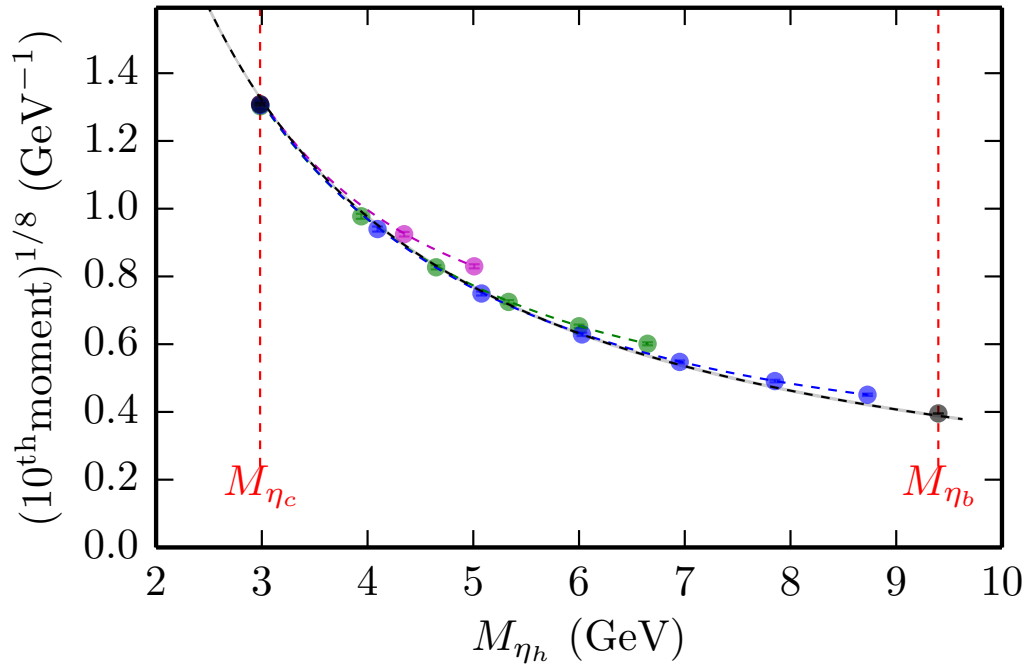
(c) 8<sup>th</sup> moment(d) 10<sup>th</sup> moment

Figure 4.6: Moments of the heavyonium vector correlator as a function of heavyonium mass, as in Figure 4.4, but renormalised using  $Z_6$ , the renormalisation factor obtained from the 6<sup>th</sup> moment.

a different vector operator. Whereas before we used the local  $\gamma_i \otimes \gamma_i$  operator, we now use the one-link  $\gamma_i \otimes \mathbb{1}$  operator. Since we are using staggered quarks, this will project on to a different taste of meson, although we recall from section 1.5.2 that different tastes should have identical properties in the continuum limit. This new calculation then acts as a probe of taste-dependent effects which may be affecting our results.

We repeat the calculation and analysis performed above, now using the one-link operator, for a subset of the bare quark masses listed in Table 4.4. Results of fits to these new correlators are shown in Table 4.9.

Label	$am_h$	$\left(\frac{G_4^V}{Z^2 a^2}\right)^{1/2}$	$\left(\frac{G_6^V}{Z^2 a^4}\right)^{1/4}$	$\left(\frac{G_8^V}{Z^2 a^6}\right)^{1/6}$	$\left(\frac{G_{10}^V}{Z^2 a^8}\right)^{1/8}$
fine	0.413	0.594170(45)	1.460396(82)	2.22450(11)	2.93953(14)
	0.7	0.362690(15)	0.980100(28)	1.517808(37)	2.010432(45)
	0.8	0.314406(11)	0.881246(21)	1.376697(27)	1.826937(33)
superfine	0.271	0.890235(58)	2.09808(11)	3.18783(14)	4.21373(17)
	0.4	0.640559(27)	1.561972(49)	2.384145(67)	3.159609(83)
	0.7	0.3740909(80)	1.003207(15)	1.552352(20)	2.058225(25)
	0.8	0.3234130(59)	0.899214(11)	1.402675(15)	1.862044(18)
ultrafine	0.193	1.225552(66)	2.83312(12)	4.29848(16)	5.67769(20)
	0.7	0.3817612(44)	1.0185031(82)	1.575144(11)	2.089763(14)
	0.8	0.3294951(33)	0.9111399(60)	1.4198339(81)	1.885236(10)

Table 4.9: Time moments of the heavyonium vector correlator for each heavy-quark mass on each ensemble, calculated using the one-link vector operator. These results are again displayed in lattice units, raised to the appropriate power — that being, for the  $n^{\text{th}}$  moment,  $1/(n - 2)$ .

Renormalisation is once again performed using  $Z_8$ , the renormalisation factor obtained from the 8<sup>th</sup> moment. This allows for a closer comparison to the results obtained using the local vector operator, but is also the most appropriate choice in this calculation for the same reasons as before. This was verified by carrying out continuum fits to the data renormalised using each of  $Z_4$ ,  $Z_6$ , and  $Z_8$ , and examining the  $\chi^2$  and statistical  $Q$ -values of the fits. These are listed in Table 4.10.

In this case, the fits resulting from renormalisation with  $Z_8$  and  $Z_4$  have equal total  $\chi^2$  and  $Q$  values. However, the data renormalised with  $Z_4$  still exhibits larger discretisation errors. This can be clearly seen in comparing Figure 4.7, which plots each of the moments renormalised using  $Z_8$ , to Figure 4.8, which plots the same quantities renormalised using  $Z_4$ . For posterity, Figure 4.9 plots the moments renormalised using  $Z_6$ .

$n$	$Z_4$		$Z_6$		$Z_8$	
	$\chi^2$	$Q$	$\chi^2$	$Q$	$\chi^2$	$Q$
4	0.74	0.69	1.2	0.27	1.0	0.42
6	0.94	0.49	0.99	0.45	0.78	0.65
8	1.2	0.29	1.3	0.22	1.1	0.36
10	1.2	0.27	1.3	0.20	1.2	0.31
Sum	4.08	1.74	4.79	1.14	4.08	1.74

Table 4.10:  $\chi^2$  and statistical  $Q$  values for continuum fits to the  $n^{\text{th}}$  moments of the one-link vector correlator, when renormalised using the listed  $Z$ -factors. We use  $Z_8$  again for minimal  $\chi^2$  and maximal  $Q$  values.

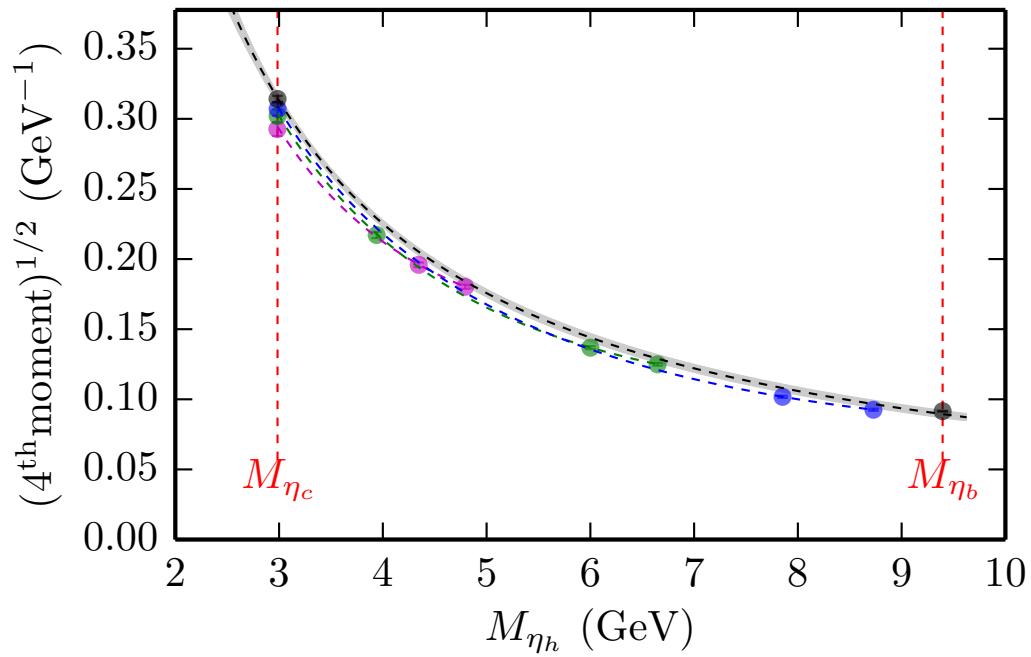
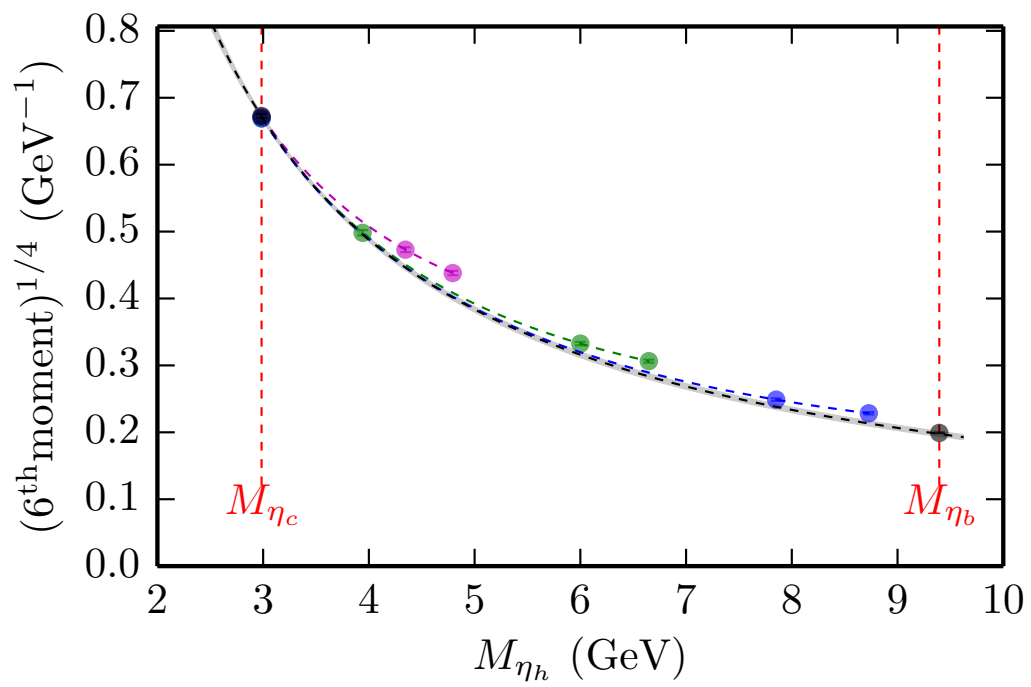
Our continuum fits are carried out in exactly the same manner as those using the local data. Using  $Z_8$  for renormalisation, the fits we obtain are good, with  $\chi^2$  values per degree of freedom of 1.0, 0.78, 1.1 and 1.2, and  $Q$ -values of 0.42, 0.65, 0.36 and 0.31, for the 4<sup>th</sup>, 6<sup>th</sup>, 8<sup>th</sup> and 10<sup>th</sup> moments respectively. We do not generally expect these fits to be as good as those to the local data, since we are now only working with just over half as many data points, although in some cases they are in fact even better. These fits are also plotted in Figure 4.7.

Our physical results for each moment in the continuum limit, along with purely statistical errors, are listed in Table 4.11, alongside the appropriately-normalised continuum moments  $\mathcal{M}_k^{\text{norm}}$  derived from experimental results, as described previously.

$n$	$k$	Charmonium		Bottomonium	
		$(G_n^V)^{\frac{1}{n-2}}/\text{GeV}^{-1}$	$\mathcal{M}_k^{\text{norm}}/\text{GeV}^{-1}$	$(G_n^V)^{\frac{1}{n-2}}/\text{GeV}^{-1}$	$\mathcal{M}_k^{\text{norm}}/\text{GeV}^{-1}$
4	1	0.3147(37)	0.3142(22)	0.0894(27)	0.09151(31)
6	2	0.6721(42)	0.6727(30)	0.1976(40)	0.19910(49)
8	3	0.9990(43)	1.0008(34)	0.2975(45)	0.29964(55)
10	4	1.3069(44)	1.3088(35)	0.3942(48)	0.39548(59)

Table 4.11: Time moments of the charmonium and bottomonium one-link vectors. In the left-hand columns, we list the physical results from our continuum fits and their associated index  $n$ . In the right-hand columns, we list the comparable results extracted from experiment in [79] and [80], indexed by  $k$  and appropriately normalised for comparison to our results.

The agreement between the calculated values from our fits and the values derived from experiment is now less than  $1\sigma$  in every case for both the charmonium and bottomonium moments. This suggests that there are significant taste effects present

(a) 4<sup>th</sup> moment(b) 6<sup>th</sup> moment

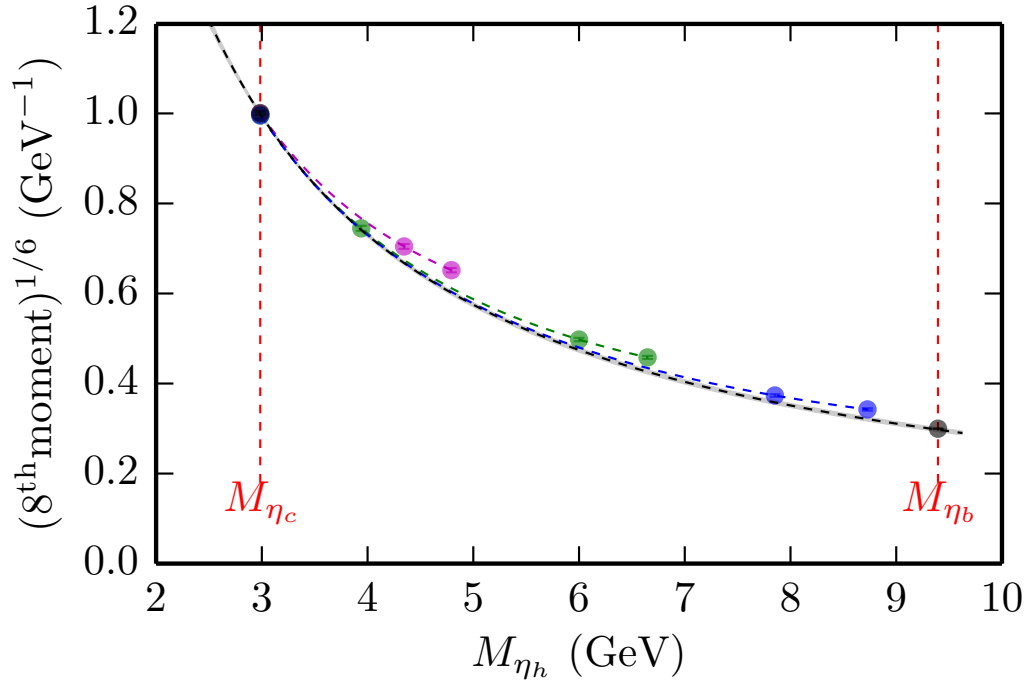
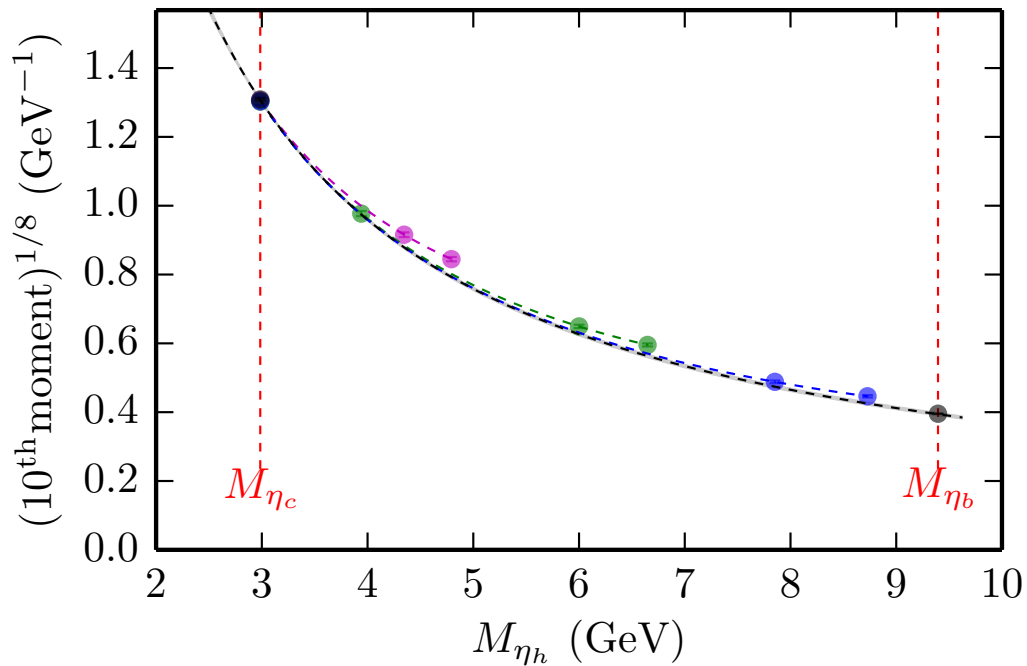
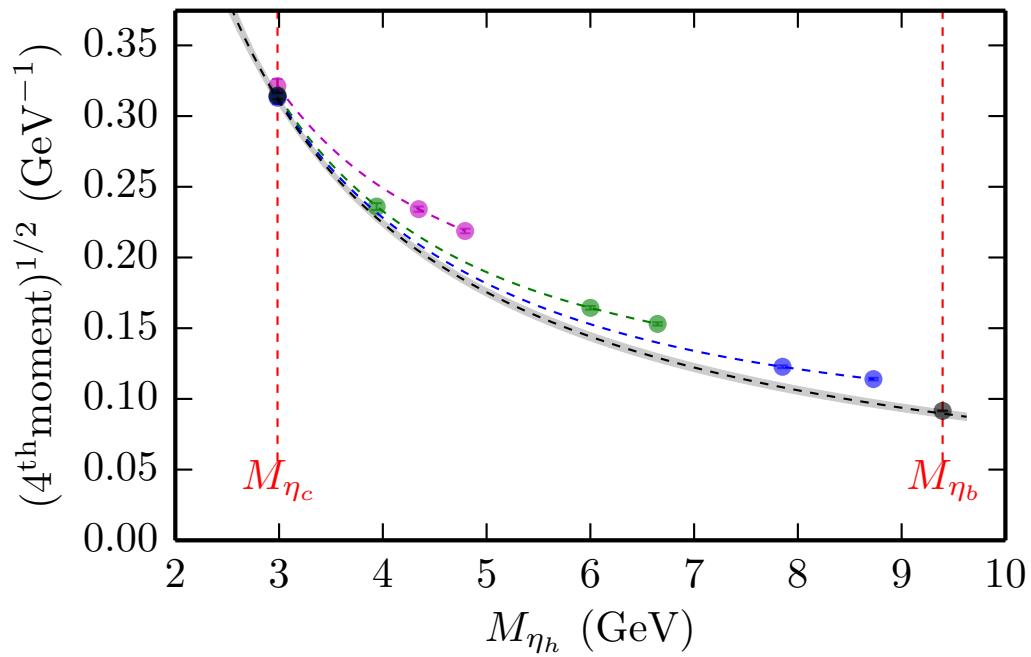
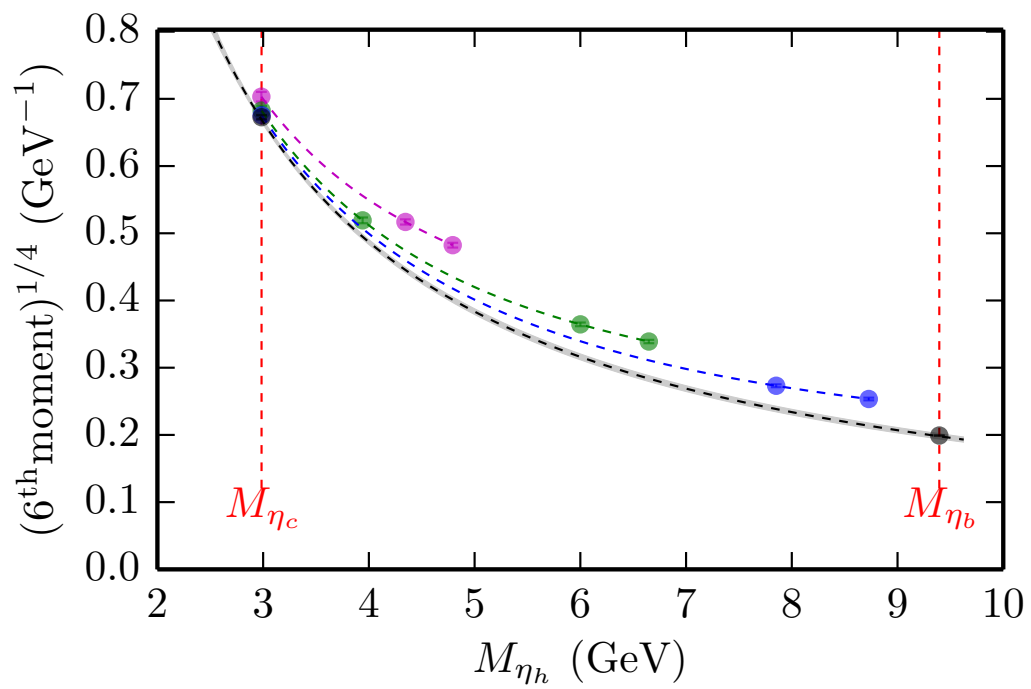
(c) 8<sup>th</sup> moment(d) 10<sup>th</sup> moment

Figure 4.7: Moments of the heavyonium vector correlator as a function of heavyonium mass, determined on the same lattices as in Figure 4.4, but this time using the one-link vector operator. The black points are the results derived from experiment, and the grey band shows the fit as described in the text. In this case we renormalise using  $Z_8$ .

(a) 4<sup>th</sup> moment(b) 6<sup>th</sup> moment

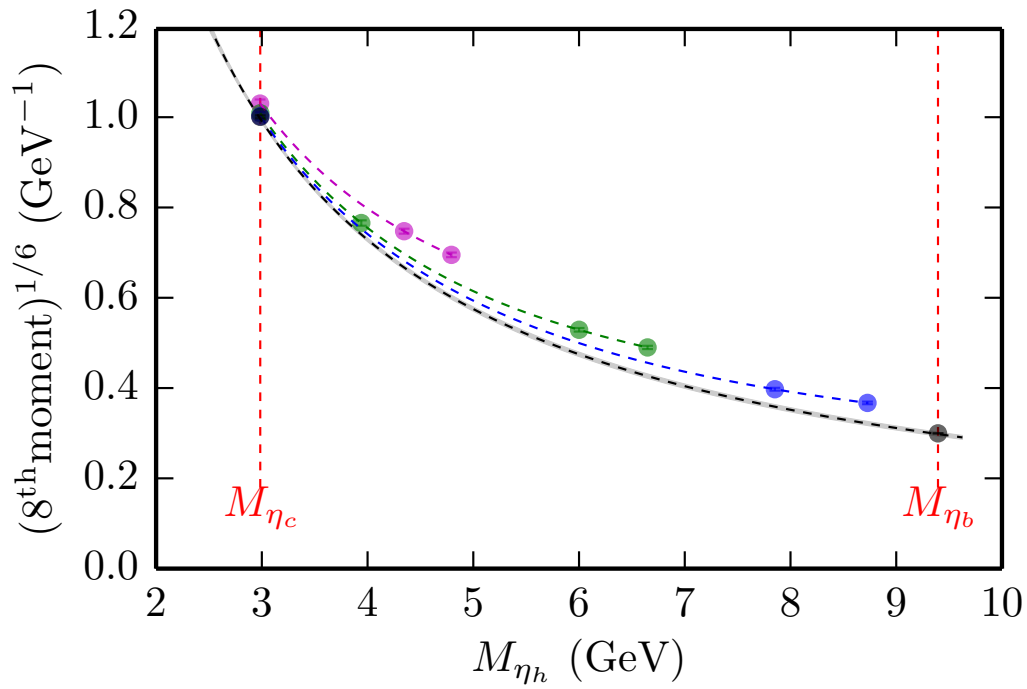
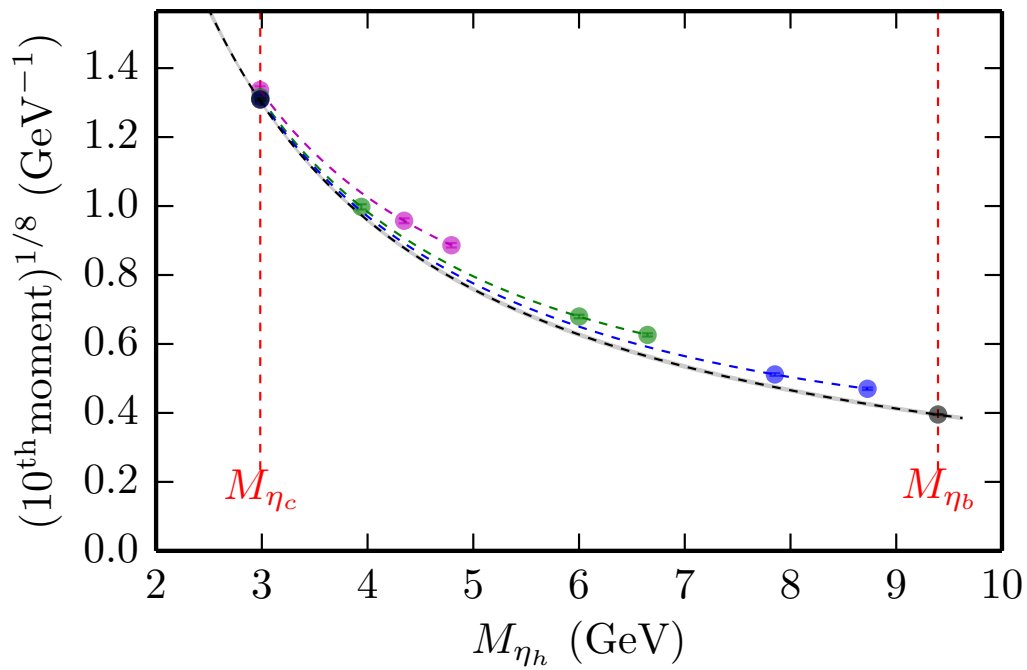
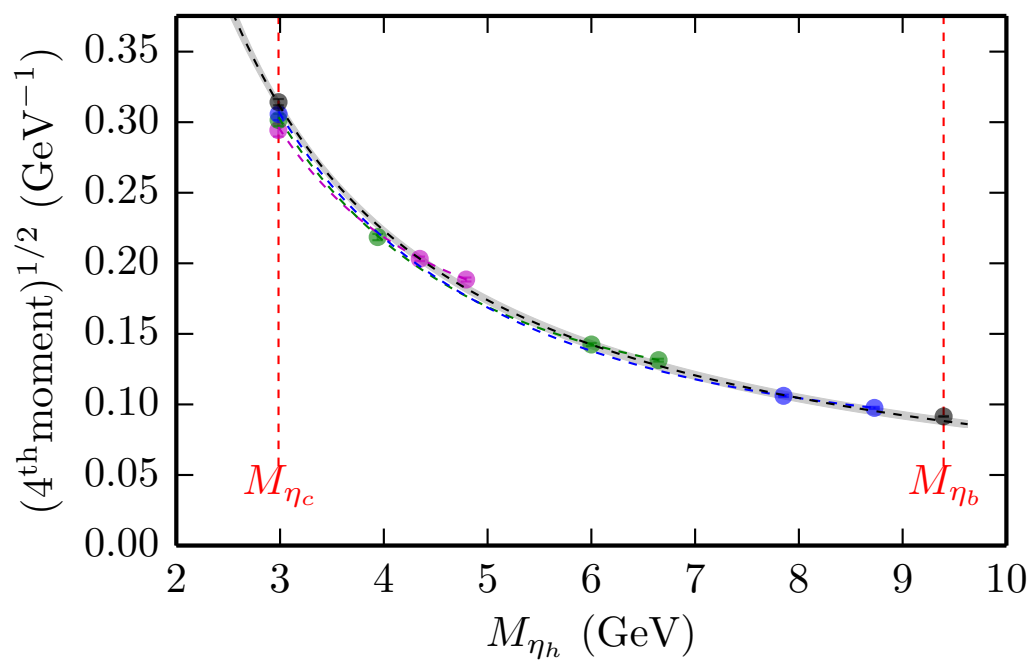
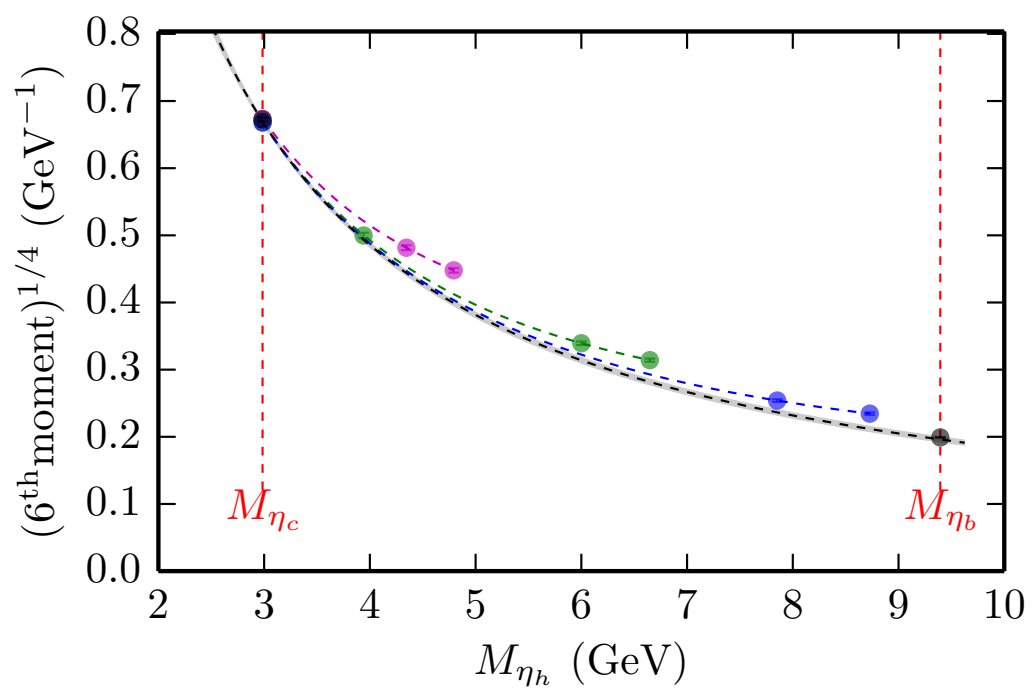
(c) 8<sup>th</sup> moment(d) 10<sup>th</sup> moment

Figure 4.8: Moments of the heavyonium vector correlator as a function of heavyonium mass determined using the one-link vector operator, as in Figure 4.7, but renormalised using  $Z_4$ , the renormalisation factor obtained from the 4<sup>th</sup> moment.

(a) 4<sup>th</sup> moment(b) 6<sup>th</sup> moment

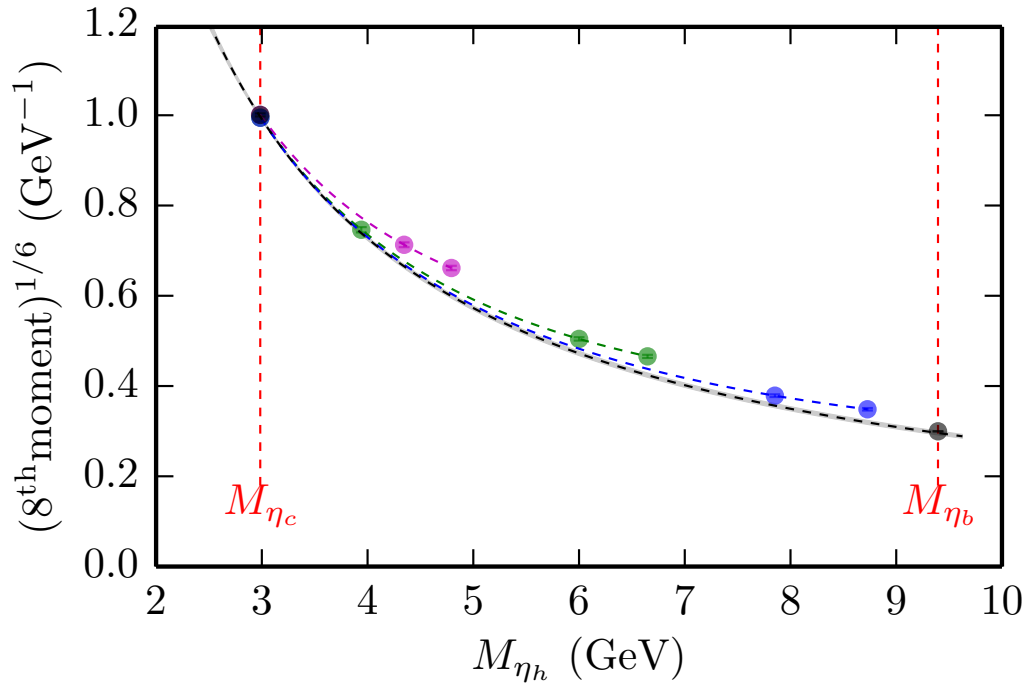
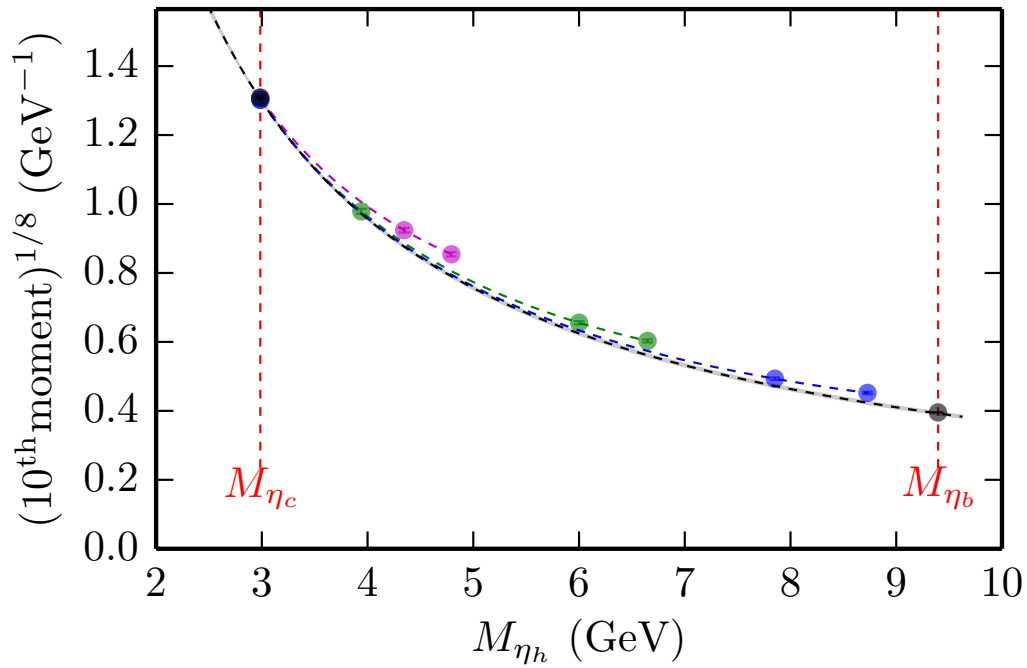
(c) 8<sup>th</sup> moment(d) 10<sup>th</sup> moment

Figure 4.9: Moments of the heavyonium vector correlator as a function of heavyonium mass determined using the one-link vector operator, as in Figure 4.7, but renormalised using  $Z_6$ , the renormalisation factor obtained from the 6<sup>th</sup> moment.

in this quantity which we have not fully understood. As a rudimentary first check with the data we already have, we can plot the mass splitting between the tastes of each vector meson to ensure it is, as expected, small. This is shown in Figure 4.10, and clearly indicates that taste splittings are on the order of a few MeV — less than 0.1% in all cases. Thankfully, this is too small a difference to be appreciably affecting our results directly, as we would expect with the HISQ action, and it seems likely that a more subtle effect is at play.

It would be worthwhile investigating this effect further with a complete set of one-link results — that is, adding to the present calculation until we have data for as many heavy quark masses as we do in the local case, to allow for an even fuller comparison. We note also that statistical errors for the calculated bottomonium moments are slightly increased in comparison to their local counterparts. This is probably due to simply having fewer data points available with which to perform the heavy-mass extrapolation, and so would presumably also be solved by introducing further data at other heavy quark masses.

#### 4.3.4 Four-Flavour HISQ Ensembles

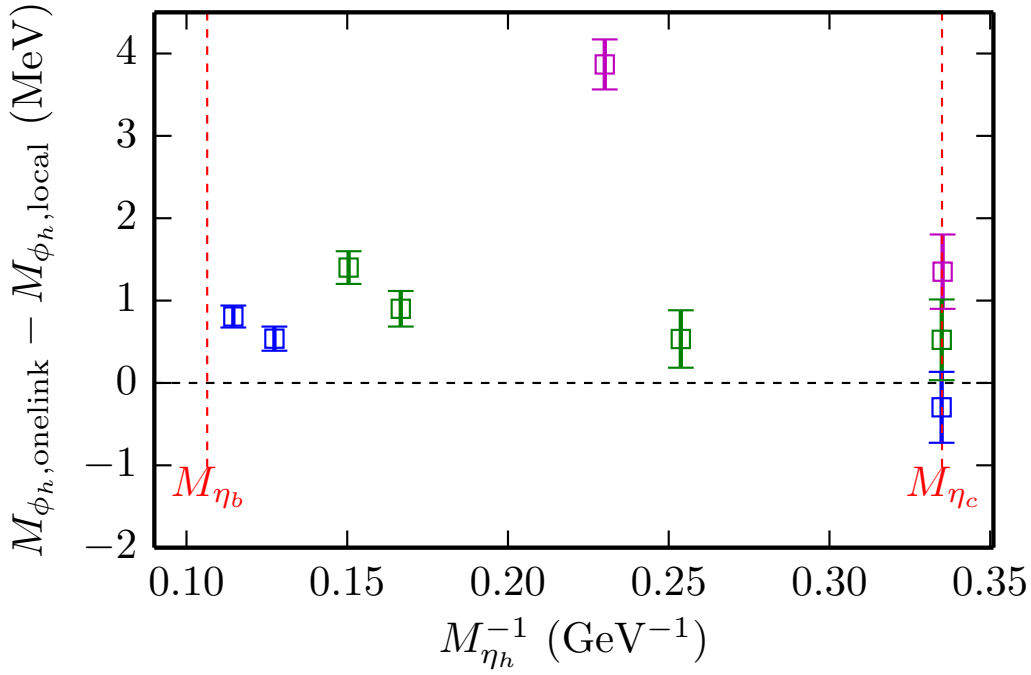
Another effect that our original calculation is missing is that of *c*-in-the-sea: the gluon field ensembles from the MILC collaboration that we have been using include the effect of *u*, *d* and *s* quarks in the sea — generated using the asqtad action — but not charm. MILC have also generated a set of configurations that utilise an improved gluon action and include four flavours of HISQ sea quarks [16], so we repeat part of our calculation on one of these ensembles to determine how large an effect this may have. These 2+1+1-flavour configurations are used extensively in the next chapter, and have been described in detail in section 2.1.2.

We choose the superfine 2+1+1-flavour lattice with parameters closest to the superfine 2+1-flavour lattice we have been using, and once again repeat the above calculation, reverting to the use of the local vector operator since we have more local data for comparison. A full range of heavy quark masses is used, from a charm of 0.269 (in lattice units) to heavier intermediate masses of 0.5, 0.6, 0.7 and 0.8. This charm mass was subsequently found to be slightly too low<sup>4</sup>, but we are still able to compare with the 2+1 results. In the 2+1 case we also have a heavy mass of 0.4, which is omitted on the 2+1+1 ensemble for speed.

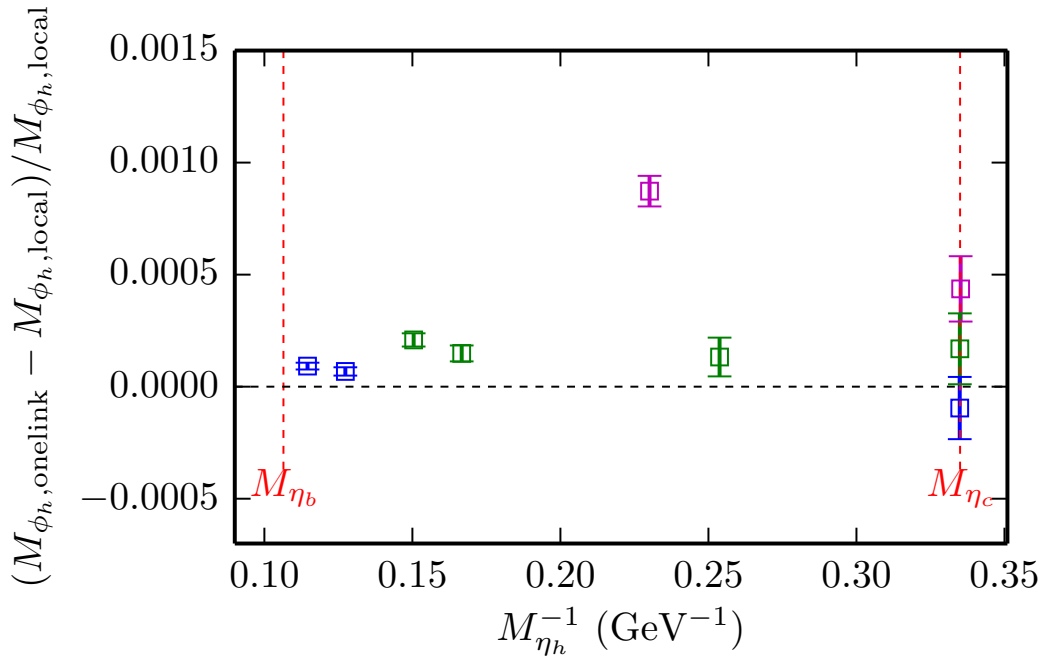
The results from the 2+1+1-flavour ensemble are converted to physical units by using the  $w_0/a$  value listed in Table 2.2, and then plotted alongside the results from

---

<sup>4</sup>The correctly-tuned charm mass on this ensemble is 0.274, which is the value we use for the calculations in chapter 5. The difference between the two values is less than 2%, which justifies our claim that a comparison is still valid in this case.

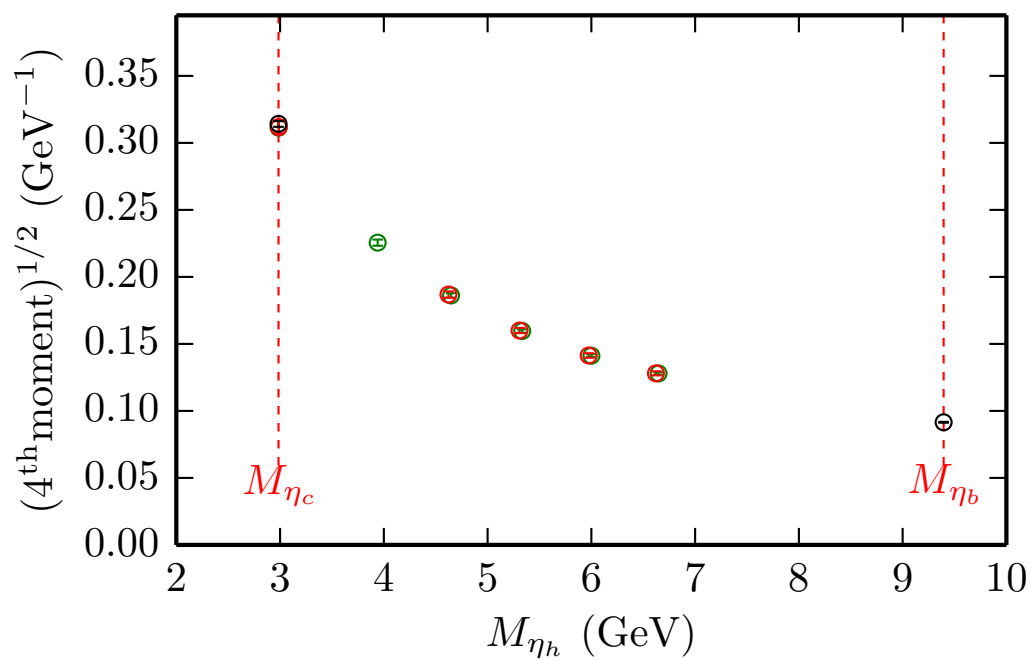
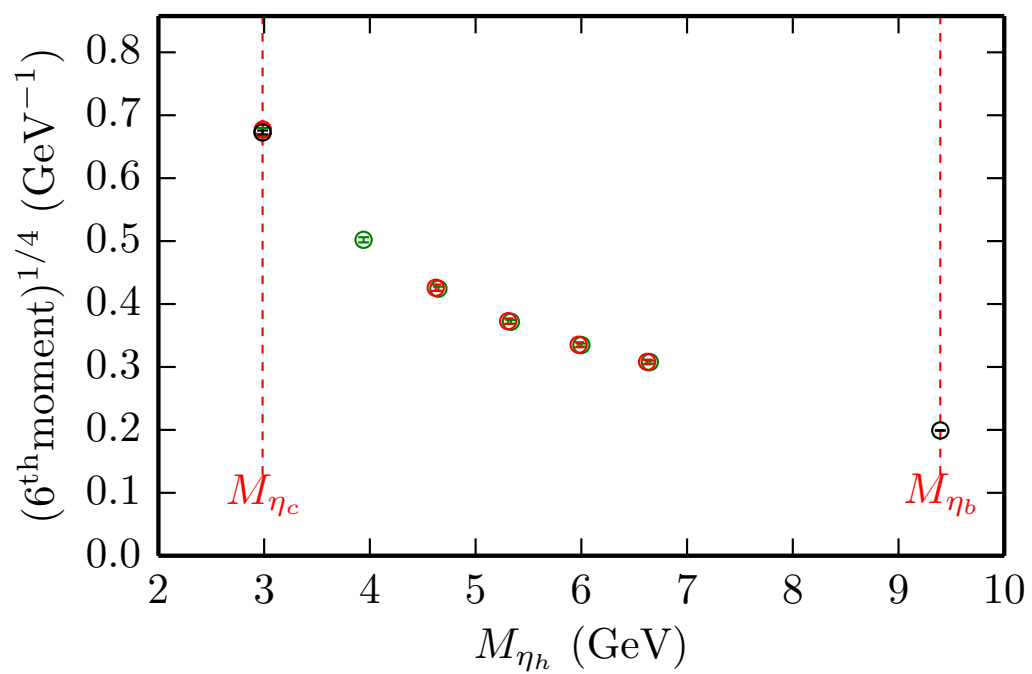


(a) Taste splittings expressed as an absolute value in MeV



(b) Taste splittings expressed as a fraction of the local vector meson mass

Figure 4.10: Taste splittings between the local and one-link vector mesons calculated in this chapter, plotted against the inverse of the pseudoscalar meson mass. The magenta points are those on the fine lattice, the green, superfine, and the blue, ultrafine. Note the narrow range of the scale on the vertical axis in both cases.

(a) 4<sup>th</sup> moment(b) 6<sup>th</sup> moment

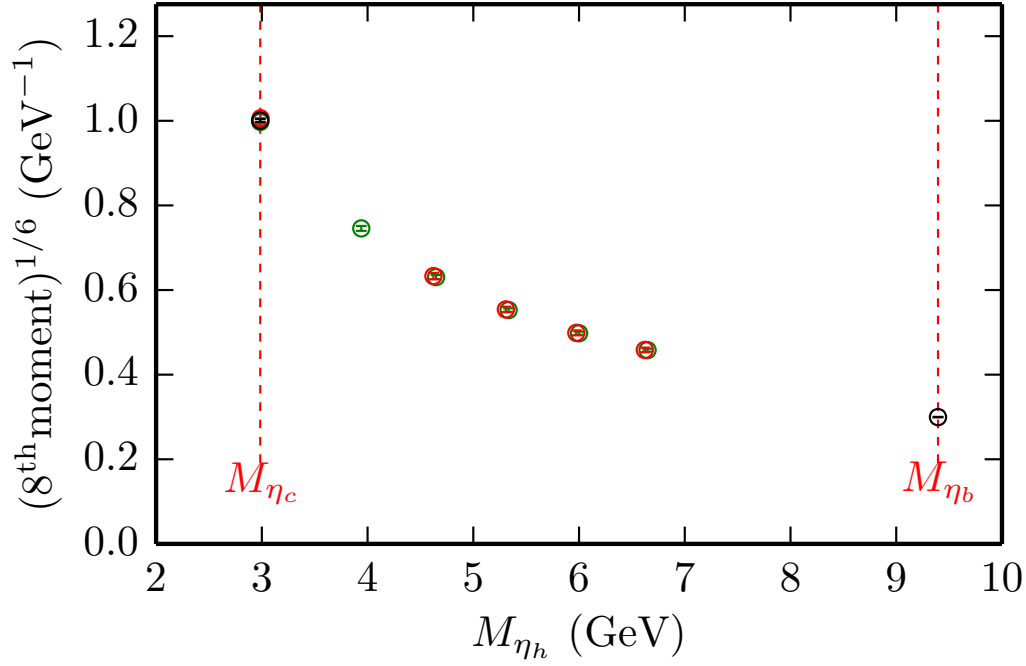
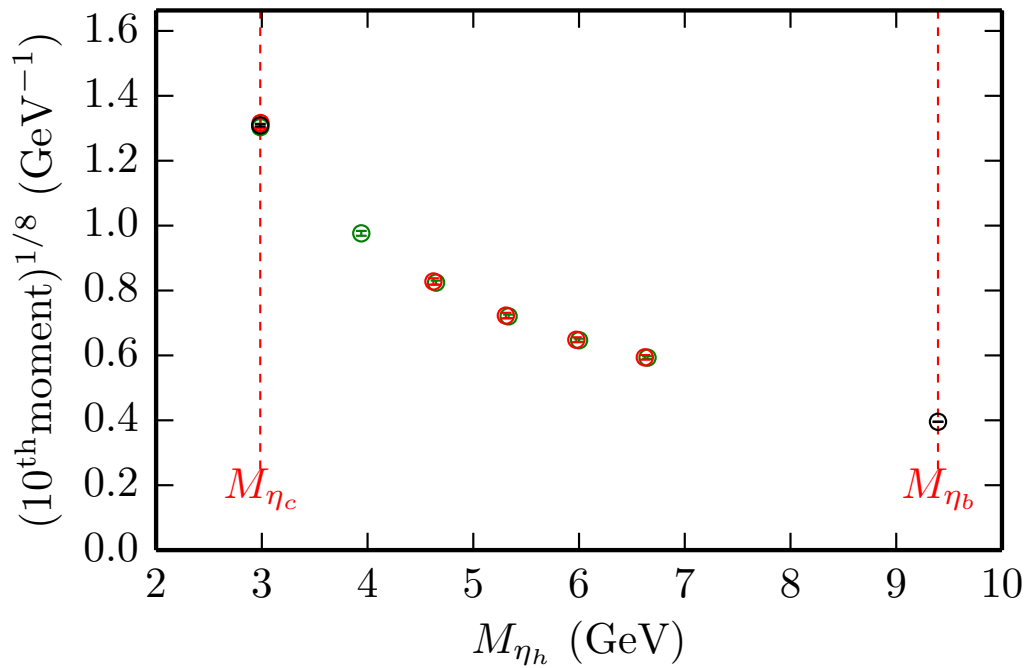
(c) 8<sup>th</sup> moment(d) 10<sup>th</sup> moment

Figure 4.11: Moments of the heavyonium vector correlator as a function of heavyonium mass, determined using the local vector operator, and renormalised with  $Z_8$ , on two different ensembles. Results on the superfine 2+1-flavour lattices are displayed in green, with results from the superfine 2+1+1-flavour lattices displayed in red.

the 2+1-flavour ensemble. For simplicity we again renormalise using  $Z_8$ , although of course this is recalculated for the results from the four-flavour ensemble. A plot for each moment is shown in Figure 4.11.

Clearly we do not expect these two sets of results to agree exactly — only one has charm quarks in the sea, and the sea quark actions are different in each case. We also use different quantities to fix the lattice spacing. Nevertheless, they agree very closely, within errors at each lattice heavy quark mass. This suggests that our results have very little dependence on sea charm effects, and also on what quantity we use to fix the lattice scale.

The discrepancies we have examined here will be discussed further in section 4.6.

## 4.4 Vector Decay Constant

The ground-state amplitude  $A_0$  that we obtain from our vector correlator fits is directly related to the matrix element for the vector operator we use to create the meson from (and annihilate it to) the vacuum. The definition of the decay constant  $f_{\phi_h}$  for the local vector operator is:

$$\langle 0 | \bar{\psi} \gamma^i \psi | \phi_h \rangle = f_{\phi_h} M_{\phi_h} \epsilon^i \quad (4.21)$$

where  $\epsilon^i$  is the polarisation of the meson. The decay constant is therefore a measure of the internal structure of a meson, and is related to the leptonic width  $\Gamma$  measured by experiment via:

$$\Gamma(\phi_h \rightarrow e^+ e^-) = \frac{4\pi}{3} \alpha_{\text{QED}}^2 e_h^2 \frac{f_{\phi_h}^2}{M_{\phi_h}} \quad (4.22)$$

where  $\alpha_{\text{QED}}$  is the electromagnetic coupling constant, and  $e_h$  is the electrical charge of the heavy quark in units of the electron's charge; this is  $+\frac{2}{3}$  for charm and  $-\frac{1}{3}$  for bottom.

On the lattice, we can calculate decay constants from the ground-state masses and amplitudes obtained from our correlator fits, viz.

$$f_{\phi_h} = Z \cdot A_{0,\phi_h} \sqrt{\frac{2}{M_{\phi_h}}} \quad (4.23)$$

where  $Z$  is a renormalisation factor which matches the lattice QCD vector current to the same current in the continuum. We determine  $Z$  via the current-current correlator method as described in section 4.3.1 above, using the same correlators as are fitted to determine  $A_{0,\phi_h}$  and  $M_{\phi_h}$ . This provides the advantage of cancelling some discretisation errors which appear in the unrenormalised decay constant. Our calculated (and as yet unrenormalised) decay constants are listed in Table 4.12, along with the  $Z$ -factor determined from the 8<sup>th</sup> time-moment of the vector correlator in section 4.3.1.

Label	$am_h$	$af_{\eta_h}$	$af_{\phi_h}/Z$	$Z_8$
fine	0.413	0.17211(11)	0.18289(29)	0.932(14)
	0.7	0.22337(11)	0.22989(23)	0.9488(34)
	0.85	0.25661(11)	0.26108(22)	0.9998(20)
superfine	0.271	0.11844(7)	0.12383(34)	0.967(13)
	0.4	0.13755(8)	0.14030(27)	0.9458(66)
	0.5	0.15121(8)	0.15257(24)	0.9357(46)
	0.6	0.16503(9)	0.16515(21)	0.9367(29)
	0.7	0.17985(9)	0.17863(20)	0.9513(16)
	0.8	0.19646(9)	0.19364(19)	0.97884(71)
	0.8	0.19646(9)	0.19364(19)	0.97884(71)
ultrafine	0.193	0.08813(4)	0.09156(16)	0.984(12)
	0.3	0.10361(4)	0.10444(13)	0.9679(56)
	0.4	0.11580(4)	0.11512(12)	0.9512(39)
	0.5	0.12720(5)	0.12540(11)	0.9402(29)
	0.6	0.13867(5)	0.13587(11)	0.9398(19)
	0.7	0.15088(5)	0.14698(10)	0.9523(10)
	0.8	0.16447(5)	0.15918(10)	0.97757(37)

Table 4.12: Results in lattice units for the decay constants of the  $\eta_h$  and  $\phi_h$  mesons for each bare quark mass on the ensembles listed in Table 2.1.  $Z_8$  is the renormalization factor obtained from the 8<sup>th</sup> moment of the correlator as described in the text. This is used to renormalise the vector decay constant by setting the above  $Z = Z_8$  and then multiplying to cancel it out. The equivalent renormalization factor for the  $\eta_h$  is unity, so no change is necessary there. These results were obtained using the local vector operator.

We renormalise the calculated vector decay constants by multiplying by  $Z_8$ , and translate to physical units by multiplying by the inverse lattice spacing  $a^{-1}$  — determined, as before, from the  $r_1/a$  values in Table 2.1. These values are then plotted against the inverse of the  $\eta_h$  mass, in Figure 4.12.

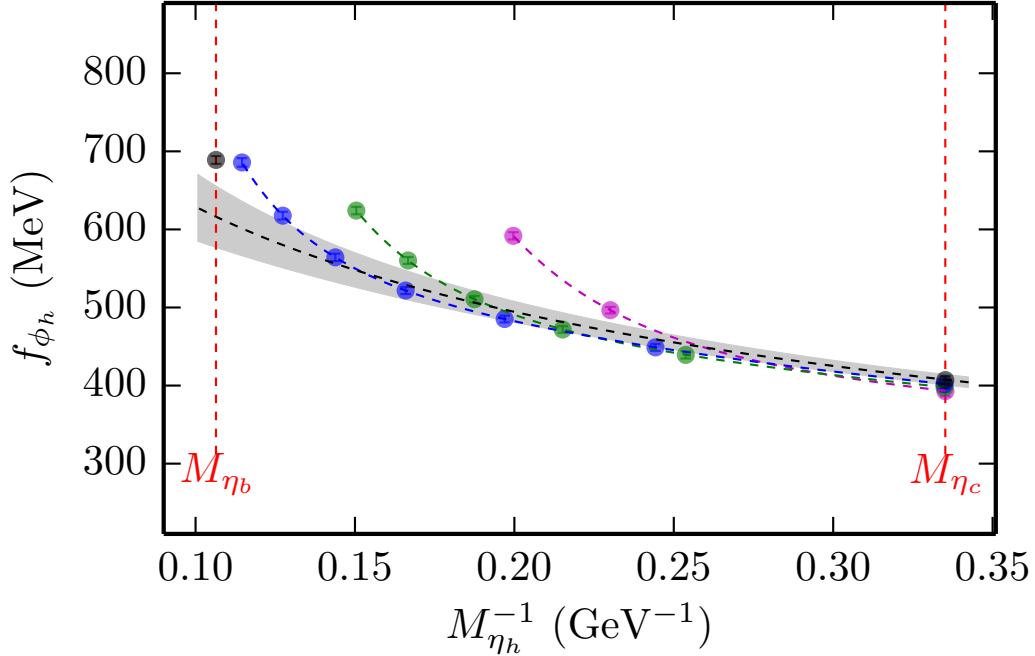


Figure 4.12: The decay constant of the heavy-heavy vector meson, as determined on the same lattices as in Figure 4.2 using the local vector operator. The colours represent the same lattices as they did in Figure 4.2.

We attempt a continuum fit to these points using the same method as for the hyperfine splitting, and with the same fit function and broad priors given in equation 4.1. The fit is excellent, with a  $\chi^2$  per degree of freedom of 0.088 and a  $Q$ -value of 1.0. Our continuum and heavy-quark extrapolation then gives results at the physical  $b$  and  $c$  masses of:

$$f_{\Upsilon} = 616(39) \text{ MeV} \quad (4.24)$$

$$f_{J/\psi} = 407.5(6.8) \text{ MeV}. \quad (4.25)$$

The errors here are statistical only, and, for bottomonium, are dominated by errors in the continuum extrapolation.

We can compare these results to experimentally-determined values by making use of equation 4.22. Experimental averages for the leptonic widths  $\Gamma$  of both the  $\Upsilon$  and  $J/\psi$  can be used [4], along with their experimentally-determined masses, to extract values for comparison:

$$f_{\Upsilon} = 689(5) \text{ MeV} \quad (4.26)$$

$$f_{J/\psi} = 407(5) \text{ MeV}. \quad (4.27)$$

These values are also plotted in Figure 4.12 as the black points at the physical  $\eta_b$  and  $\eta_c$  masses.

Our determined charmonium value agrees very well with the experimental result, and is of comparable accuracy. This provides further evidence of the ability of the HISQ action to simulate charm quarks very accurately.

Our bottomonium value exhibits a discrepancy with the experimental value at the  $2\sigma$  level, and also has a notably increased error compared to the charmonium value — although the latter is not surprising, given the large discretisation errors evident in the plot. A number of further investigations into the source of this discrepancy were carried out, and we now recount the details of these investigations.

#### 4.4.1 One-link Vector Operator

We further investigate the difference in our fitted result for  $f_\Upsilon$  from its value determined by experiment by examining the same quantity when calculated using the one-link vector operator, much as we did for the moments in the previous section. Using the correlators from the one-link calculation carried out for the moments, we repeat the analysis performed above. Results of fits to these new correlators are shown in Table 4.13, along with the renormalisation factor  $Z_8$  determined from the one-link moments in the previous section.

Label	$am_h$	$aM_{\phi_h}$	$af_{\phi_h}/Z$	$Z_8$
fine	0.413	1.32959(14)	0.15037(24)	1.154(17)
	0.7	1.90408(10)	0.18114(18)	1.2623(46)
	0.8	2.09431(9)	0.19330(18)	1.3367(30)
superfine	0.271	0.92942(7)	0.10658(12)	1.134(15)
	0.4	1.20902(5)	0.11923(11)	1.1334(80)
	0.7	1.82013(4)	0.14640(8)	1.2215(20)
	0.8	2.01357(3)	0.15643(8)	1.28878(94)
ultrafine	0.193	0.69180(6)	0.08012(10)	1.126(14)
	0.7	1.76556(2)	0.12331(6)	1.1964(13)
	0.8	1.96061(2)	0.13197(6)	1.25862(48)

Table 4.13: Results in lattice units for the mass and decay constant of the  $\phi_h$  meson for a subset of the heavy quark masses used before, but using the one-link vector operator. Results are obtained on each of the ensembles listed in Table 2.1. We also list the renormalisation factors  $Z_8$  calculated for this data, again using the current-current renormalisation method.

We plot these results and carry out a continuum fit in exactly the same manner

as we did for the results using the local operator. This fit is very good, with a  $\chi^2$  value per degree of freedom of 0.84 and a  $Q$ -value of 0.58. We do not expect the fit to be as good as before since we are now only working with just over half as many data points. These results and the fit to them are plotted in Figure 4.13.

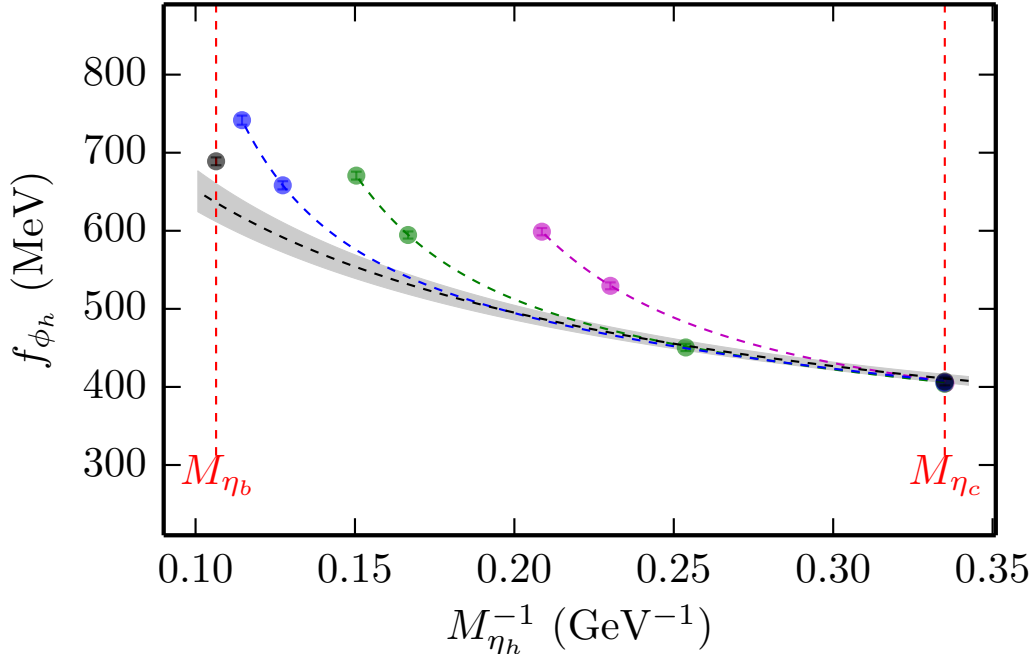


Figure 4.13: The decay constant of the heavyonium vector meson as determined for a subset of the bare quark masses on the same lattices as in Figure 4.12, but using the one-link vector operator.

This fit gives results at the physical  $b$  and  $c$  masses of:

$$f_{\Upsilon} = 636(24) \text{ MeV} \quad (4.28)$$

$$f_{J/\psi} = 410.8(5.4) \text{ MeV} \quad (4.29)$$

where the errors are once again purely statistical.

Both of these results are consistent with the results obtained using the local vector operator, and the charmonium result is once again in good agreement with experiment. We verified in Figure 4.10 that taste splittings were small for the mesons in this calculation, and these results suggest that taste effects are small for this quantity more generally.

The bottomonium result, although slightly increased, still exhibits a  $2\sigma$  discrepancy in comparison to experiment, indicating that our observed discrepancy is not caused by taste effects in this case. The plot of results suggests that discretisation errors on  $f_{\phi_h}$  are apparently even larger in this formalism.

### 4.4.2 Four-Flavour HISQ Ensembles

We also investigate the effect of missing charm quarks in the sea for the vector decay constant, like we did for the moments. Again we use the same correlators that were calculated in that case, using the superfine 2+1+1-flavour ensemble and reverting to the use of the local vector operator. The full range of heavy quark masses is identical: a slightly-mistuned charm of 0.269 plus heavier intermediate masses of 0.5, 0.6, 0.7 and 0.8, with the heavy mass of 0.4 omitted for speed.

The results from the 2+1+1-flavour ensemble are once again converted to physical units by using the  $w_0/a$  value listed in Table 2.2, and then plotted alongside the results from the 2+1-flavour ensemble. This plot is shown in Figure 4.14.

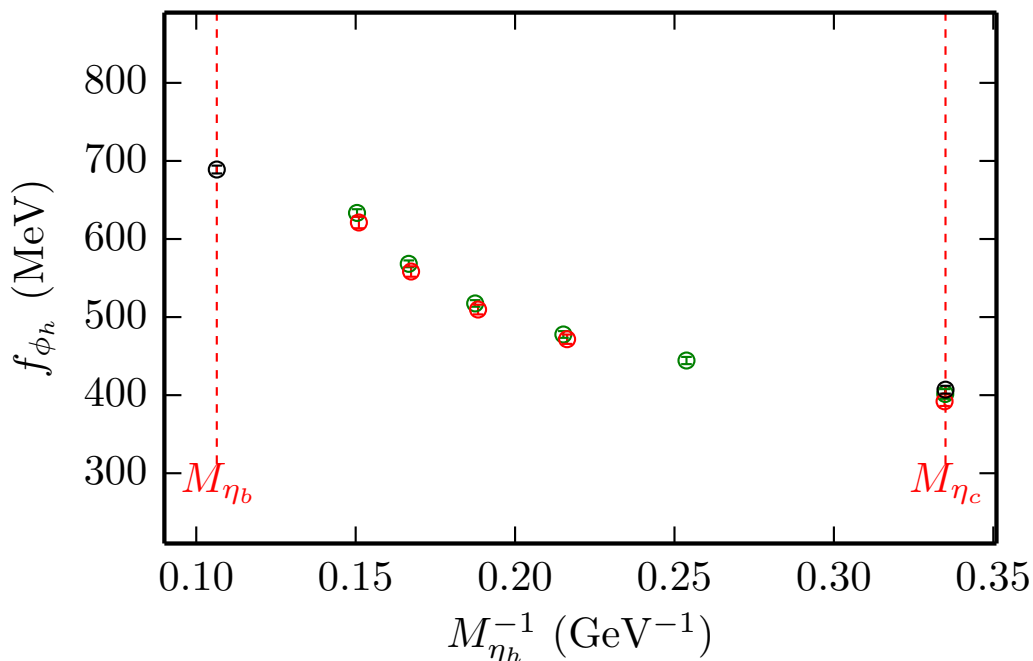


Figure 4.14: The decay constant of the heavyonium vector meson as determined using the local vector operator. Results on the superfine 2+1-flavour lattices are displayed in green, with results from the superfine 2+1+1-flavour lattices displayed in red.

As in the case of the moments, we do not expect these two sets of results to agree exactly — only one has charm quarks in the sea, and the sea quark actions are different in each case. We also use different quantities to fix the lattice spacing. Nevertheless, they agree very closely, within errors at each lattice heavy quark mass. This suggests that the heavyonium decay constant has negligible dependence on sea charm effects, and also on what quantity we use to fix the lattice scale.

## 4.5 Pseudoscalar Decay Constant

In Table 4.12, we also list the decay constants determined from the ground-state amplitude  $A_0$  of our fits to the pseudoscalar correlators, viz.

$$f_{\eta_c} = 2m_c A_{0,\eta_c} \sqrt{\frac{2}{M_{\eta_c}^3}} \quad (4.30)$$

where  $m_c$  is the charm quark mass. Thanks to the PCAC relation for HISQ quarks, no renormalisation of this quantity is required. We can therefore simply translate these results to physical units by multiplying by the inverse lattice spacing as before. The physical results are again plotted, in Figure 4.15, against the inverse of the  $\eta_h$  mass.

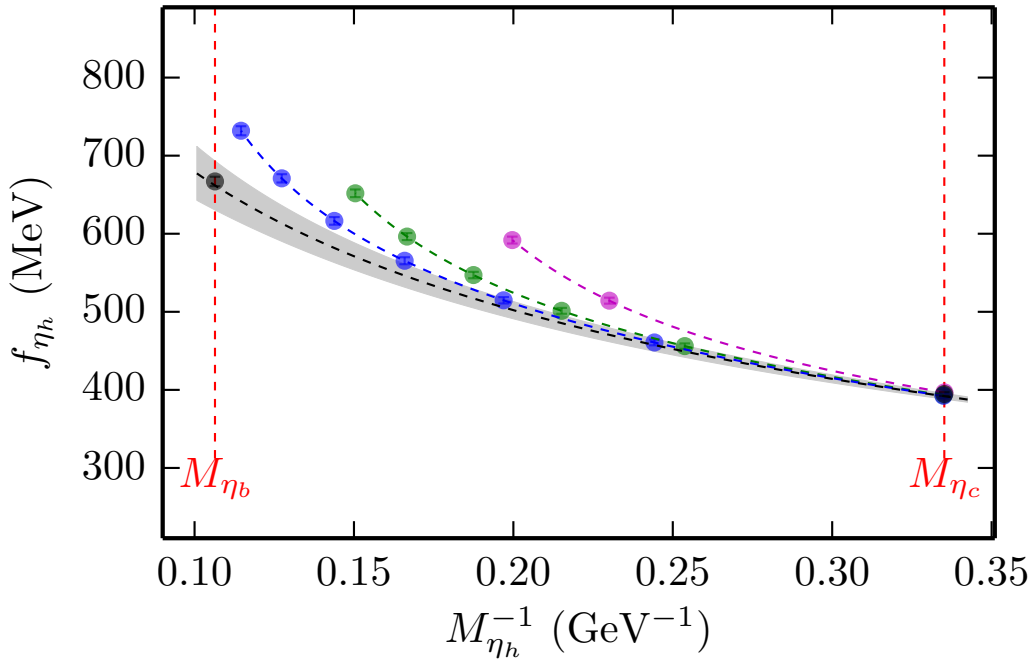


Figure 4.15: The decay constant of the heavy-heavy pseudoscalar meson as determined on the same lattices as in Figure 4.2, with the colours representing the same lattices as in that figure. The black points at the physical  $\eta_b$  and  $\eta_c$  masses represent determinations in the continuum limit from previous lattice calculations, in [74] and [45] respectively.

We perform a continuum fit to these points using the same method and fit function as we have used previously for the hyperfine splitting and the vector decay constant. Once again we are able to use the same broad priors thanks to the ‘fast fit’ carried out prior to the full fit. The fit that we obtain is excellent, with a  $\chi^2$  value per degree of freedom of 0.028 for 16 degrees of freedom, and a  $Q$ -value of 1.0.

Results from the extrapolation to the physical  $b$  and  $c$  masses are:

$$f_{\eta_b} = 662(31) \text{ MeV} \quad (4.31)$$

$$f_{\eta_c} = 391.8(3.7) \text{ MeV} \quad (4.32)$$

where the errors are purely statistical.

Unfortunately, there is no meaningful experimental comparison for this quantity, for either charmonium or bottomonium. There are, however, previous lattice results at the physical  $b$  and  $c$  masses of:

$$f_{\eta_b} = 667(6) \text{ MeV} \quad (4.33)$$

$$f_{\eta_c} = 394.7(2.4) \text{ MeV} \quad (4.34)$$

from [74] and [45] respectively. These are also plotted in Figure 4.15 as the black points at the physical  $\eta_b$  and  $\eta_c$  masses.

Our result for  $f_{\eta_b}$  is in agreement with the determination in [74], but has a significantly larger statistical error. The method used in [74] was very similar to that used in this calculation (in fact it is another of the precursors to this work). This means that the act of performing a heavy-mass extrapolation is not the root cause here. It may well be the case that the previous work was able to achieve a smaller error since they had results at further different lattice spacings to those used here. This is therefore another way in which this calculation could possibly be extended.

Our result for  $f_{\eta_c}$  agrees well with the previous lattice determination, and has a comparable error. A further comparison of results for the decay constant of the  $\eta_c$  is delayed until chapter 6, as this quantity will also be determined in the next chapter.

## 4.6 Outstanding Discrepancies

In this chapter, we have successfully extended the methods used for the lattice calculations in [56] and [74] to include heavyonium as well as charmonium states, and to investigate vector heavyonium correlators as well as pseudoscalars. Our choice of  $Z$ -factor for renormalising these vectors, and the corresponding justification for that choice, are not the same as those in [56]. It is therefore non-trivial that our charmonium results, in the main, agree with those determined in that work. We have already mentioned that our result for the  $\eta_b$  decay constant is in agreement with that obtained in [74], but could be improved in accuracy by the addition of results at even more different lattice spacings.

Our investigations into possible reasons for the discrepancy between our calculated value of  $f_{\Upsilon}$  and the experimental result have proven inconclusive, although we

have demonstrated that it is not a simple taste-splitting effect. There are also still some unresolved questions surrounding certain of our calculated moments and their values derived from experiment in both the bottomonium and charmonium cases. There is excellent agreement between these values when we calculate the moments using the one-link vector operator, but this is not the case when we do so using the local vector operator. The discrepancy between the one-link and the local moments, albeit small, is likely to require some additional calculations to fully understand. This seems especially prudent when we consider that this study includes fewer data sets than that in [56], which calculated continuum vector charmonium moments that were in good agreement with the experimental results.

In fact, many of the calculations described in this chapter would undoubtedly benefit from some further work, to either resolve or solidify the discrepancies that we have found. It is possible that performing a full calculation on 2+1+1-flavour lattices would resolve things. The preliminary calculation outlined above — for the moments and the vector decay constant on the 2+1+1-flavour superfine ensemble — does not seem to support this hypothesis, but we must remember that it is a calculation at a single lattice spacing. No continuum extrapolation has therefore been performed and so we cannot draw reliable conclusions based on this calculation alone. It is also worth noting again that we are not allowing for any sea quark mass dependence in any of these fits, and so studies which take this into account may be able to provide some resolution.

The discrepancies in the cases of the moments and of  $f_\Upsilon$  are different in some key respects. Firstly, it is clear from the plots in Figures 4.12 and 4.13 that discretisation effects are large for the decay constant fit, and it could be that we require a more sophisticated fitting function to fully account for this. This is not obviously true in the case of the moments. In addition, the largest discrepancy in the moments case when calculated using the local operator is only on the order of 3%. The smallest discrepancy in the case of the vector decay constant, by contrast, is around 8%, and so this is the more compelling of the two.

Ultimately these calculations are still computationally expensive, and it is only recently that the ability to perform them to the required accuracy has been developed. The work described in this chapter therefore provides an excellent base from which to develop these methods further.

# Chapter 5

## Radial and Orbital Excitations of Charmonium

The charmonium system consists of mesons formed of a charm quark and its own antiquark. The masses and decay rates of the pseudoscalar ( $J^{PC} = 0^{-+}$ ) and vector ( $J^{PC} = 1^{--}$ ) ground states, as well as numerous radially and orbitally excited states, are well-determined experimentally [4], and we examined the form of the mass spectrum (in tandem with that of bottomonium) at the beginning of chapter 4. Figure 5.1 provides an overview of the current experimental determinations of states in the charmonium system, as well as some of their known relative transitions.

Previous studies of multiple states in the charmonium spectrum have been performed on the lattice — see [83] for a particularly impressive example, with determinations of numerous excited states — but these have typically only been done at one lattice spacing, and frequently also with unphysical masses for light quarks in the sea. With only one lattice spacing, it is not possible to be sure of values in the continuum limit, and so studies at multiple lattice spacings are required.

One previous study performed at multiple lattice spacings is that by the Fermilab Lattice and MILC Collaborations [84], which uses the Wilson clover formulation [18] for valence charm quarks on gauge configurations with 2+1 flavours of asqtad quarks in the sea [15]. However, this produced preliminary results for the spin-averaged 2S – 1S splitting which showed a surprisingly large disagreement with the experimental value. A plot of their results for this quantity is reproduced in Figure 5.2. The HPQCD collaboration has previously performed an accurate calculation of ground-state charmonium masses in [56], and the previous chapter of this thesis builds on many of the methods developed there. In combination, then, this provides a foundation and motivation to study excited states in the charmonium system, and determine whether we also observe a similar discrepancy.

In this chapter we will examine states below the open charm threshold for decay into  $D$  and  $\bar{D}$  mesons, since these can, in principle, be determined accurately via

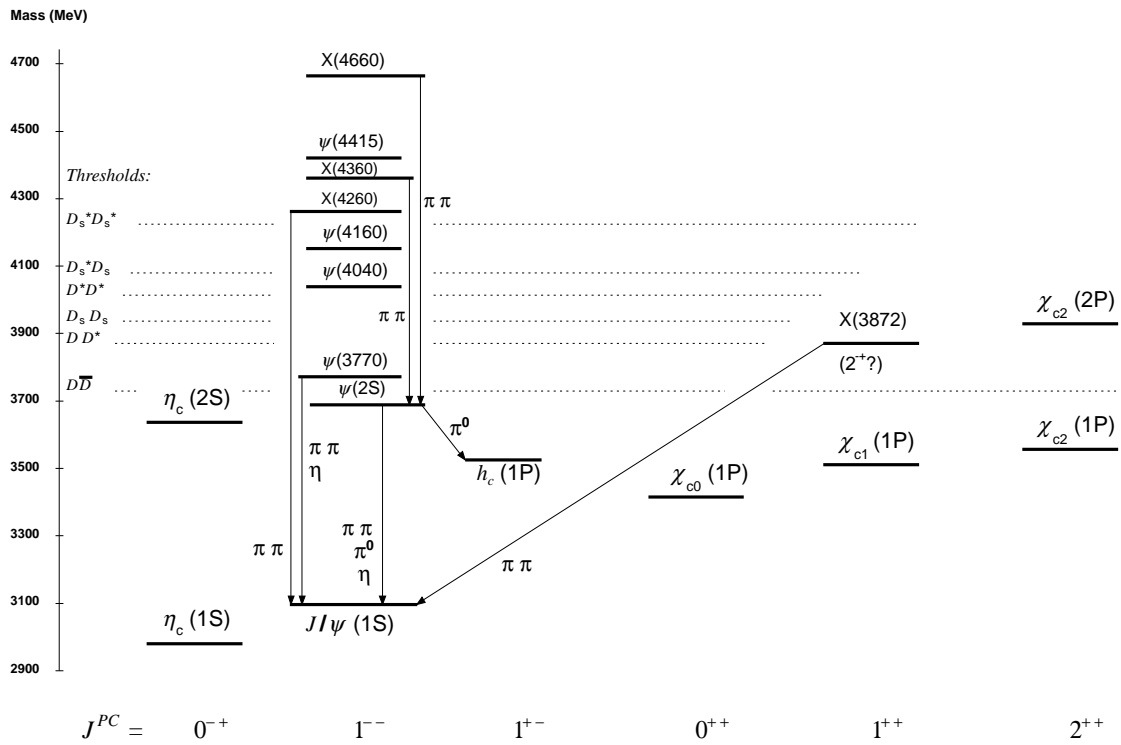


Figure 5.1: An overview of the current experimental understanding of the charmonium spectrum, as presented in [4]. Note the open charm threshold, labelled  $D\bar{D}$ , just above 3700 MeV.

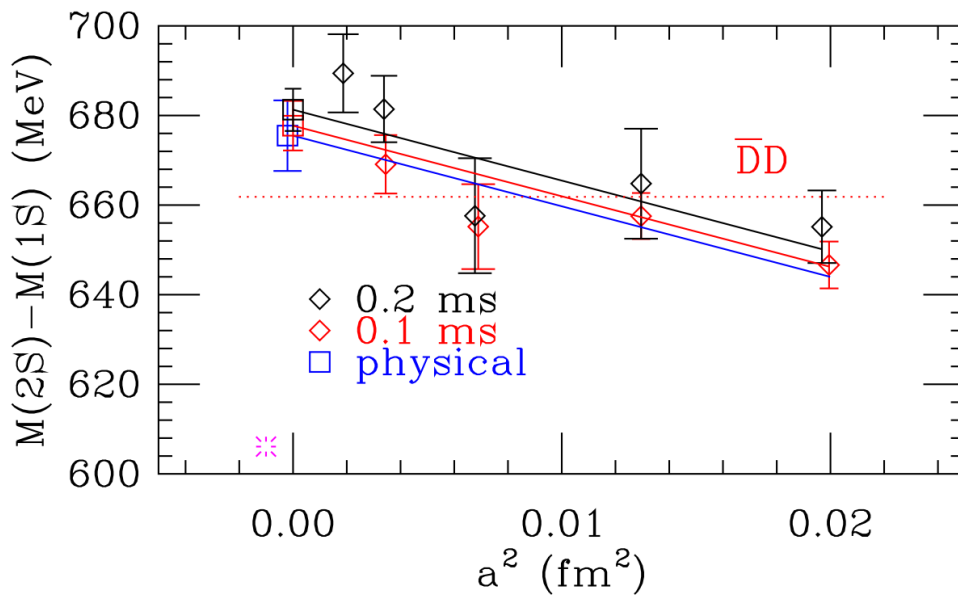


Figure 5.2: The Fermilab/MILC result for the spin-averaged 2S – 1S splitting in charmonium. Note the magenta burst at the lower left which represents the experimental value. This figure is reproduced from [84].

straightforward lattice QCD calculations with single meson operators — that is, we can assume that the impact of hadronic decays and multihadronic scattering is small or negligible. Specifically, we will concentrate on determinations of the  $\eta_c(1S)$ ,  $\eta_c(2S)$ ,  $J/\psi(1S)$ ,  $\psi(2S)$  and  $h_c(1P)$  states, and will additionally make some less detailed determinations of the  $\chi_{c0}(1P)$  and  $\chi_{c1}(1P)$  states. The HISQ action will be used for valence charm quarks to keep discretisation errors small. We will perform calculations on the 2+1+1-flavour gauge configurations [16] detailed in section 2.1.2, which include the effects of light quarks in the sea at their physical masses.

Radially excited states are accessed on the lattice via their contributions to correlation functions at small  $t$ , and we discuss this further when considering our correlator fits. We use Gaussian covariant smearings on our source and sink operators, as discussed in section 2.2.3, to improve overlap with the ground state. This then allows for data on the radially excited states to be extracted more accurately. Data on orbital excitations are obtained by considering the oscillating parts of the correlators, since those that we consider are the parity partners of other states we are calculating.

This is the first time that the HPQCD collaboration has used smeared operators with staggered quarks to obtain continuum results. The overall effects of their inclusion will therefore be evaluated in chapter 6, via comparisons to earlier calculations.

## 5.1 Lattice Calculation

We again perform our lattice calculations using the MILC code [1]. In contrast to most of the heavyonium calculations in the previous chapter, here we use the 2+1+1-flavour ensembles detailed in Table 2.2, and we now determine the lattice spacing  $a$  using the Wilson flow parameter  $w_0$  as described in section 2.1.3. We take its physical value to be  $w_0 = 0.1715(9)$  fm as calculated in [46].

We use ensembles with multiple different lattice spacings, including those where the masses of light quarks in the sea are set to their physical values. As in the previous chapter, we begin by generating a random wall source on a given timeslice of the lattice, and the following procedure is repeated for a number of timeslices  $N_t$  on multiple configurations  $N_{\text{cfg}}$  in each ensemble. The numbers of configurations and time sources that we use on each ensemble are given in Table 5.1.

Bare lattice charm masses are also shown in Table 5.1, and these were tuned by fixing to the mass of the  $\eta_c(1S)$ . We will see later just how well-tuned these actually are. For now, we note that we do not match directly to the experimental average of the  $\eta_c(1S)$  mass, since we make an allowance for annihilation to two gluons. Annihilation effects are not included in our lattice calculation and we must

Label	$m_\ell/m_s$	$am_c$	Naik $\varepsilon$	$N_{\text{cfg}} \times N_t$	Smearing $s_1$		Smearing $s_2$	
					$r$	$n$	$r$	$n$
very coarse	1/5	0.888	-0.3820	$1020 \times 8$	—	—	—	—
	1/10	0.873	-0.3730	$1000 \times 8$	—	—	—	—
	phys.	0.863	-0.3670	$1000 \times 8$	—	—	—	—
coarse	1/5	0.664	-0.2460	$1053 \times 8$	1.5	10	3.0	20
	1/10	0.650	-0.2378	$1000 \times 8$	1.5	10	3.0	20
	phys.	0.643	-0.2336	$1000 \times 8$	1.5	10	3.0	20
fine	1/5	0.450	-0.1250	$300 \times 8$	2.5	20	3.5	30
	1/10	0.439	-0.1197	$300 \times 8$	2.5	20	3.5	30
	phys.	0.433	-0.1167	$565 \times 8$	2.5	20	3.5	30
superfine	1/5	0.274	-0.0491	$1019 \times 8$	2.5	20	4.0	50
ultrafine	1/5	0.188	-0.0235	$100 \times 8$	4.0	50	—	—

Table 5.1: Parameters used on the different ensembles of 2+1+1-flavour MILC configurations in the calculations in this chapter. We list the bare lattice charm mass  $am_c$  and the Naik parameter  $\varepsilon$  on each ensemble, the number of configurations  $N_{\text{cfg}}$  from each ensemble, and the number of time sources  $N_t$  on each configuration that are utilised. The rightmost four columns list the parameters used to define the Gaussian covariant smearings applied to the source and sink operators, as described by equation 2.37. No smearings are used on the very coarse ensembles, and only one smearing is used in the ultrafine case.

therefore shift our target  $\eta_c(1S)$  mass upwards<sup>1</sup>.

Using equation 4.4 from the previous chapter, obtained from a perturbative calculation in [20], we obtain a shift of  $-3.1$  MeV. This shift will have a negligible effect on most of the quantities that we will calculate, being only just over 0.1% of the  $\eta_c$  mass. It could have a relatively large effect when considering the hyperfine splitting, though, and we consider this fully in section 5.2.1.

Table 5.1 also lists the Naik  $\varepsilon$  parameter used in conjunction with each bare lattice charm mass. This is determined by computing the expansion in powers of the charm mass as defined in [20], exactly as we did in chapter 4.

### 5.1.1 Smearings

Since we are using staggered quarks, the source operator is embedded in the random wall source that we generate, and so we apply our Gaussian smearings to this operator by modifying the random wall source. This allows us to retain the statistical advantages of using the random wall source for each smearing that we apply.

We use two different smearing functions on most of the ensembles, with some exceptions: no smearings are used on the very coarse lattices, since we do not expect to be able to extract the excited states here with enough statistical precision, even when smearings are used. Only one smearing is used on the ultrafine configurations to reduce the amount of computer time required, since these configurations have such a large volume ( $L^3 \times T = 64^3 \times 192$ ). Smearings were used on the fine  $m_\ell/m_s = 1/5$  ensemble, but we do not extract excited states from these correlators due to doubts over the thermalisation of the different molecular dynamics streams in the ensemble, which we have entered into correspondence with the MILC Collaboration about.

Values for the smearings we use are listed in Table 5.1. These were determined for the coarse and fine ensembles by Peter Knecht [2], while working with the HPQCD collaboration, by calculating correlators on a small subset of configurations with different preselected values for the smearing parameters  $r$  and  $n$ . In plotting a normalised effective amplitude for these correlators, it becomes clear which smearings cause the correlator to reach a plateau most quickly — these are therefore the smearings with the largest ground-state overlap. The best smearings determined in [2] for the coarse and fine ensembles are those which we have listed in Table 5.1.

Such extensive testing was not performed on the superfine or ultrafine ensem-

---

<sup>1</sup>To be clear, the calculated shift in the  $\eta_c$  mass due to annihilation effects is negative for the perturbative approach that we use, meaning that the mass is reduced by these effects. Our lattice calculations do not include annihilation effects, and so the masses computed by them will be higher than the physical mass. To calculate a mass to match to when rescaling, we therefore apply this shift to the experimental average of the  $\eta_c$  mass, but in the opposite direction — as an increase — to ‘undo’ the effects of annihilation.

bles due to the extra computing power required to perform calculations on these ensembles. Instead, reasonable adjustments were made to the smearings from the next-coarsest lattices, and effective amplitudes for correlators calculated using these smearings were plotted to confirm that they were suitable for use. Plots of the effective amplitude  $A_{\text{eff}}$  for the two smearings used on the superfine ensemble are shown in Figure 5.3, where we define:

$$A_{\text{eff}}(t) = \frac{1}{N} \cdot \frac{\overline{C}_{2\text{pt}}(t)}{e^{-Et} + e^{-E(T-t)}} \quad (5.1)$$

with  $\overline{C}_{2\text{pt}}(t)$  the average correlator,  $E$  the energy of the ground state, and  $T$  the temporal extent of the lattice.  $N$  is a normalisation factor equal to the average value of the correlator's central plateau, and so the effective amplitude will converge to 1 when the plateau is reached.

It is clear for both the smaller and larger smearings in Figure 5.3 that the correlator converges more quickly than when no smearing is applied. In addition, the approximate shape of the smeared effective amplitudes is what we expect from Peter Knecht's work [2], where an example is given of a calculation where the smearing has too small a number of iterations  $n$  to properly approximate a Gaussian shape. Our choice of smearings on the superfine ensemble is discussed further in section 5.5.

### 5.1.2 Matrices of Correlators

We generate a HISQ quark propagator beginning from each of our random wall sources, and tie together each possible combination with an appropriate sink operator to calculate both pseudoscalar and vector correlators. Let us consider these cases separately. The pseudoscalar case is simpler since it does not require the source to be patterned with phases. We may simply use the local  $\gamma_5 \otimes \gamma_5$  operator at the sink, which we will represent by  $\ell$ , or we may also apply one of the smearings in Table 5.1 at the sink:  $s_1$  denotes the smaller smearing, and  $s_2$  the larger.

We may uniquely refer to the different propagators that we generate by specifying the operators applied at their sources and sinks. For example, the propagator denoted by  $\ell.\ell$  has no smearings applied at either end. Combining this local-local propagator with each other propagator then results in the following matrix of correlators being generated:

$$\begin{pmatrix} \ell.\ell & \ell.s_1 & \ell.s_2 \\ s_1.\ell & s_1.s_1 & s_1.s_2 \\ s_2.\ell & s_2.s_1 & s_2.s_2 \end{pmatrix} \quad (5.2)$$

where the same notation now refers to the overall smearing applied at the source and sink of each correlator.

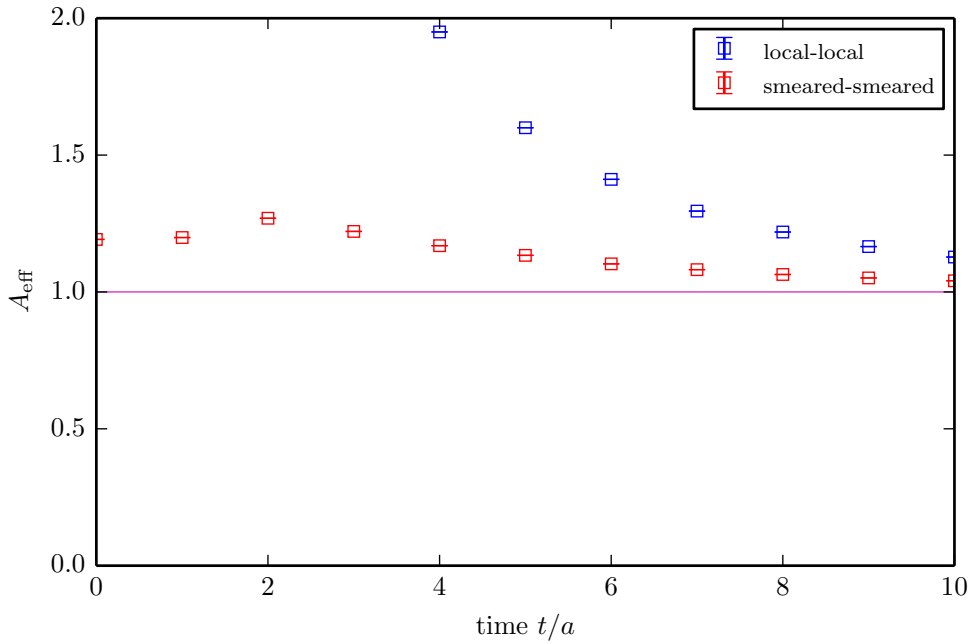
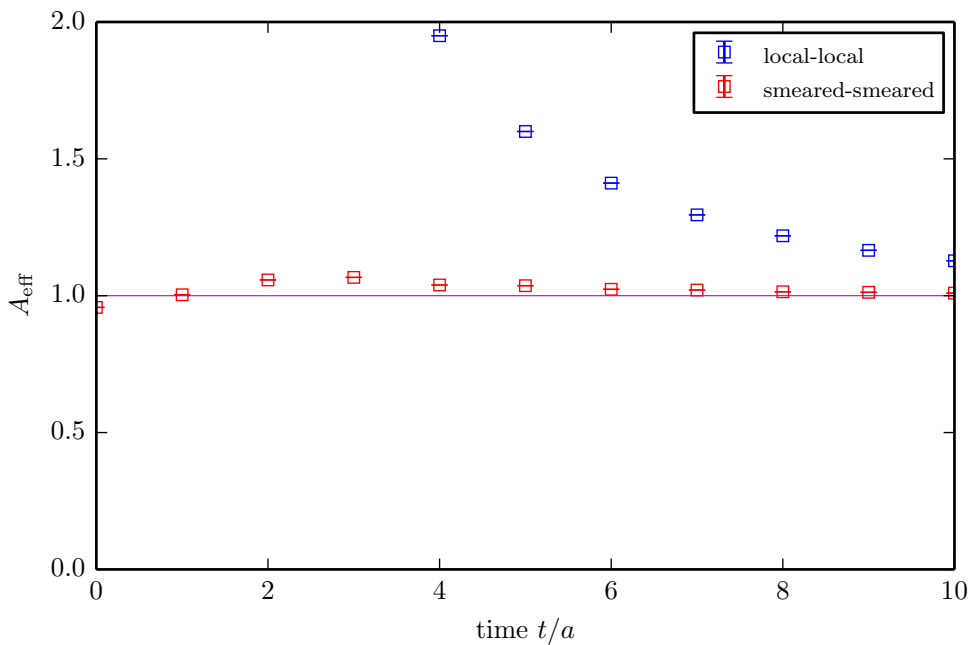
(a) Smaller smearing:  $r = 2.5, n = 20$ (b) Larger smearing:  $r = 4.0, n = 50$ 

Figure 5.3: Plots of the effect of smearings on the convergence of correlators to a plateau. Here we show the effect of two different smearings applied to pseudoscalar charmonium correlators on the superfine  $2+1+1$  ensemble. The blue points are those obtained when no smearing is applied, and the red points show the results with the respective smearing applied to both the source and sink operators. It is clear that in both cases, the smearing causes the correlators to plateau more quickly than they otherwise would.

Because the pseudoscalar is generated from a simple random wall source with no phases applied, we may also combine pairs of propagators which both have a smearing applied to the source or sink, and still produce a pseudoscalar meson of the same taste. This results in another matrix of correlators being obtained:

$$\begin{pmatrix} \ell.\ell & \ell.d_1 & \ell.d_2 \\ d_1.\ell & d_1.d_1 & d_1.d_2 \\ d_2.\ell & d_2.d_1 & d_2.d_2 \end{pmatrix} \quad (5.3)$$

where, for example,  $d_1.\ell$  denotes that the smaller smearing has been applied at the source of both propagators that are being combined, not just one.

Consider now the vector case. Here we must pattern the source with appropriate vector phases, and applying a smearing once this has taken place would destroy the signal that we obtain. We therefore apply the appropriate vector phases to the local source, and only combine the local-local propagator resulting from this patterned source with each of the smeared propagators from the unpatterned source. Using the local vector operator  $\gamma_x \otimes \gamma_x$  (or, in practice, applying the appropriate vector phases) at the sink then results in the production of a vector meson in each case, and we obtain a matrix of correlators with the same form as that in equation 5.2.

Note here that, for efficiency, we only study a single vector polarisation (in this case, in the  $x$  direction, although this is a somewhat arbitrary choice) since the smearing function cannot be applied to a source generated with the subset corner mask.

Correlators are again normalised by dividing by 3 to account for the random colour 3-vectors in the source, and by  $L^3$  to account for the statistics of the random wall source. We also average over time sources and over configurations in each ensemble before performing correlator fits.

Correlators were generated as described above on the coarse  $m_\ell/m_s = 1/5$  ensemble, and on the fine physical ensemble, by Peter Knecht while working with the HPQCD collaboration. We include these two sets of correlators in the fits in the next subsection, along with the correlators on the other ensembles generated by the author.

### 5.1.3 Correlator Fits

Our averaged correlators are fit to the form given in equation 3.9, which allows the specific amplitudes for each smeared operator to take on different values. We again use the fit code described in section 3.1.2, and include oscillating terms for the vector correlators. Opposite-parity terms cancel for the pseudoscalar correlators, and so oscillating terms are not necessary in this case.

Since we are here attempting to fit a matrix of correlators, we can make full use of the EigenBasis method described in section 3.1.3. This will inherently generate priors for our fit parameters — the energy-logarithm and amplitude values — by virtue of its determination of a diagonalised basis. The only exception to this is when studying the  $h_c(1P)$  meson: its associated values are extracted from the oscillating part of the vector correlators, and this is not examined by the diagonalisation. We therefore simply feed the fit a prior of  $\sim 3500 \pm 200$  MeV for the mass of the  $h_c(1P)$ , converted to lattice units.

Values for  $t_{\min}$  and SVD cuts are again altered to find the fit which gives the best  $\chi^2$  and statistical  $Q$ -values. Generally, we find that a  $t_{\min}$  value of about 8 is enough to give a good fit, but that SVD cuts of around  $10^{-4}$  or even  $10^{-3}$  are required to complement this. In each case, we check the impact of binning the correlators before averaging them. This is only implemented if it increases the errors on our ground-state parameters, since this indicates that statistical correlations between neighbouring configurations are being reduced. We find that this is necessary in only a few cases, and the bin sizes we use are never larger than 4.

We perform separate fits to the pseudoscalar and vector data, relying on the EigenBasis method for accuracy. Any correlations between vector and pseudoscalar data are small enough to be negligible — we have performed some (traditional) simultaneous fits to the pseudoscalar and vector correlators, and the results from these agree in all cases with those from the separate fits. We extract values from the fits only once they have stabilised: in each case we include at least  $n_{\text{exp}} = 7$  exponentials in the fit function, and, as explained further in section 5.5, we extend some out as far as  $n_{\text{exp}} = 13$ . All the fits have a stable  $\chi^2$  value of less than 0.98, with some as low as 0.49.

Generally we find that including the matrix of ‘doubly-smeared’ pseudoscalar correlators (e.g.  $d_1.\ell$ ) is not necessary in order to obtain a good fit. When they are included, we are significantly increasing the number of degrees of freedom that the fit must take care of, and this does not result in any notable increase in statistical precision. These correlators are therefore usually neglected in the pseudoscalar fits. This is no great loss since they required very little extra computer time to produce.

For several of the ensembles, we have performed a more traditional fit alongside the fit using the EigenBasis method, and we extract values from the best fit in each pair, preferring the EigenBasis fit if there is only a small difference between the two, since it generally has smaller statistical errors. On the ensembles where no smearings were applied, we do not have a matrix of correlators to fit, and so only a traditional fit is carried out. Priors used in performing traditional fits are the same as those listed in section 3.1.1.

From these numerous fits, we are able to accurately extract the mass and the

amplitude for several states in the charmonium system. We list the masses of these states on each ensemble in Table 5.2, and the corresponding (local) amplitudes in Table 5.3.

Label	$m_\ell/m_s$	$aM_{\eta_c(1S)}$	$aM_{J/\psi(1S)}$	$aM_{\eta_c(2S)}$	$aM_{\psi(2S)}$	$aM_{h_c(1P)}$	
very coarse	1/5	2.331900(70)	2.42000(30)	—	—	—	*
	1/10	2.305350(40)	2.39305(15)	—	—	—	*
	phys.	2.287710(30)	2.37483(14)	—	—	—	*
coarse	1/5	1.876549(44)	1.943562(80)	2.2980(32)	2.3319(66)	2.1965(91)	
	1/10	1.848042(30)	1.914726(54)	2.2529(26)	2.2830(84)	2.1814(68)	
	phys.	1.833954(16)	1.900475(32)	2.2371(15)	2.2726(55)	2.1675(94)	
fine	1/5	1.366850(90)	1.41574(21)	—	—	—	*
	1/10	1.342465(19)	1.391323(34)	1.6413(20)	1.6546(86)	1.5891(27)	
	phys.	1.329308(16)	1.378308(26)	1.6255(18)	1.6420(48)	1.5644(46)	
superfine	1/5	0.896686(23)	0.929906(43)	1.0975(40)	1.1148(97)	1.0549(60)	
ultrafine	1/5	0.652460(50)	0.677810(50)	0.8115(63)	0.8179(39)	0.7787(16)	‡

Table 5.2: Results in lattice units for the rest masses of the  $\eta_c(1S)$ ,  $J/\psi(1S)$ ,  $\eta_c(2S)$ ,  $\psi(2S)$  and  $h_c(1P)$  charmonium mesons as determined on each of the ensembles listed in Table 5.1. The presence of a symbol in the rightmost column indicates that values in that row have been taken from a traditional fit; else, they have been determined via an EigenBasis fit. Rows with a \* had no EigenBasis fit performed to the data, and in the ultrafine row denoted by ‡, the traditional fit was chosen over the EigenBasis fit for all correlators. The ultrafine case is the only one where the traditional fit is better, most likely because of the relatively small data sample on this ensemble.

### Effect of Smearings

It is a simple matter to demonstrate that our smearings have the desired effect on our correlators. Taking the vector correlators on the fine  $m_\ell/m_s = \text{phys}$  ensemble as an example, we can fit only the local ( $\ell.\ell$ ) correlators and compare the results to those from a full matrix fit. Both of the fits described here are traditional fits, and a comparison with the results in Tables 5.2 and 5.3, we can see that the use of an EigenBasis fit has, in most cases, further improved our error estimates.

The full matrix fit on this ensemble has a  $\chi^2$  value per degree of freedom of 0.72 (for an impressive 387 degrees of freedom), and a  $Q$ -value of 1.0. The best fit we can find to just the local correlators has a  $\chi^2$  value per degree of freedom of 0.93 for 43 degrees of freedom, and a  $Q$ -value of 0.59.

Label	$m_\ell/m_s$	$A_{\eta_c(1S)}$	$A_{J/\psi(1S)}$	$A_{\eta_c(2S)}$	$A_{\psi(2S)}$	$A_{h_c(1P)}$	
very coarse	1/5	0.53392(26)	0.4737(17)	—	—	—	*
	1/10	0.52486(14)	0.46306(60)	—	—	—	*
	phys.	0.519001(83)	0.45412(73)	—	—	—	*
coarse	1/5	0.367338(76)	0.28974(13)	0.3768(70)	0.313(14)	0.1033(80)	
	1/10	0.360436(53)	0.28206(10)	0.3461(55)	0.280(17)	0.1134(57)	
	phys.	0.357350(29)	0.278484(62)	0.3413(33)	0.290(12)	0.1134(76)	
fine	1/5	0.22841(18)	0.16313(44)	—	—	—	*
	1/10	0.224696(28)	0.159453(48)	0.1887(58)	0.133(16)	0.0629(19)	
	phys.	0.222803(26)	0.157507(35)	0.1852(62)	0.1337(96)	0.0557(32)	
superfine	1/5	0.128767(32)	0.084147(47)	0.1078(54)	0.074(12)	0.0291(34)	
ultrafine	1/5	0.086034(53)	0.052529(52)	0.0802(69)	0.0517(20)	0.02166(44)	‡

Table 5.3: Results in lattice units for the local amplitudes of the  $\eta_c(1S)$ ,  $J/\psi(1S)$ ,  $\eta_c(2S)$ ,  $\psi(2S)$  and  $h_c(1P)$  charmonium mesons as determined on each of the ensembles listed in Table 5.1. The ‡ and \* symbols mean the same as in Table 5.2.

Moreover, the accuracy with which we are able to determine energies and amplitudes is significantly improved when the smeared correlators are included. The mass of the ground-state  $J/\psi(1S)$  is determined, in lattice units, as 1.378263(40) with an associated amplitude of 0.157480(76) from just the local correlators, or 1.378291(29) with an amplitude of 0.157498(43) from the full fit. The error on the mass is reduced by more than 27%, while the error on the amplitude sees a reduction of over 43%.

This is likely to be a greater reduction in statistical errors than we would expect from simply having greater statistics. Statistical errors scale approximately as  $1/\sqrt{N}$ , with  $N$  the number of data points. The amount of data generated when using a total of three different smearings (including no smearing) is, in principle, 9 times as much as when using no smearings (since this results in a  $3 \times 3$  matrix of correlators instead of the equivalent of a  $1 \times 1$  matrix) so with nine times as much data, errors would be reduced by at most 67%. However, the data with smearings is correlated, and so we cannot expect a full  $1/\sqrt{N}$  reduction in statistical errors in this case. The smearings appear to be further improving our determinations.

The improvement is even more striking for higher excitations. The  $\psi(2S)$  mass from just the local correlators comes out at 1.6488(117) with an amplitude of 0.1470(130), whereas from the full fit we obtain a mass of 1.6463(53) and a corresponding amplitude of 0.1441(69). In this case, the errors on the mass and amplitude have been reduced by approximately 55% and 47% respectively. It is clear that the use of smeared operators is helpful in accurately extracting excited states.

## Parity Partners

Determinations were also made of the rest masses of the  $\chi_{c0}(1P)$  and  $\chi_{c1}(1P)$ . These are less straightforward to access on the lattice than the other five charmonium states in Tables 5.2 and 5.3, and so have correspondingly fewer determinations. We do not utilise the results for these mesons in the following sections, but they are depicted in Figure 5.4, and so we briefly describe them here.

The  $\chi_{c0}(1P)$  is a  $J^{PC} = 0^{++}$  meson, and is the parity partner of the pseudoscalar  $J^{PC} = 0^{-+}$  meson. This is inaccessible when using the local pseudoscalar  $\gamma_5 \otimes \gamma_5$  operator, since the opposite-parity terms cancel and no oscillation is observed in the correlator. To access the  $\chi_{c0}(1P)$ , we therefore use the  $\gamma_0\gamma_5 \otimes \gamma_0\gamma_5$  operator — this also creates a local pseudoscalar, but the opposite-parity term no longer cancels and we can extract the  $\chi_{c0}(1P)$  from the oscillating part. This was calculated by Peter Knecht on the coarse  $m_\ell/m_s = 1/10$  lattices.

The  $\chi_{c1}(1P)$  is a  $J^{PC} = 1^{++}$  meson, and is a parity partner of the vector  $J^{PC} = 1^{--}$  meson. The oscillating partner of the  $J/\psi(1S)$  when created using the  $\gamma_x \otimes \gamma_x$  operator is, as we have noted previously, the  $h_c(1P)$  meson, and so we must again use a different operator to create the vector if we wish to access a different oscillating state. In the case of the  $\chi_{c1}(1P)$ , we use the  $\gamma_x\gamma_0 \otimes \gamma_x\gamma_0$  operator to create the local vector and access it via the oscillation of this correlator. The  $\chi_{c1}(1P)$  was calculated by Peter Knecht on the coarse  $m_\ell/m_s = 1/10$  lattices, and by the author on the superfine  $m_\ell/m_s = 1/5$  lattices.

Peter Knecht's determinations of the rest masses of these mesons on the coarse  $m_\ell/m_s = 1/10$  ensemble were as follows:

$$M_{\chi_{c0}(1P)} = 3416.5(3.1) \text{ MeV} \quad (5.4)$$

$$M_{\chi_{c1}(1P)} = 3518.7(7.3) \text{ MeV} \quad (5.5)$$

and the author's determination on the superfine  $m_\ell/m_s = 1/5$  ensemble was:

$$M_{\chi_{c1}(1P)} = 3524.9(7.8) \text{ MeV} . \quad (5.6)$$

Given that no continuum or chiral extrapolation has been carried out, these are all in reasonable agreement with the experimental values [4], which are:

$$M_{\chi_{c0}(1P)} = 3414.75(31) \text{ MeV} \quad (5.7)$$

$$M_{\chi_{c1}(1P)} = 3510.66(7) \text{ MeV} \quad (5.8)$$

and this provides a further test of the validity of our methods.

## Spectrum Plot

Using the masses determined from our fits displayed in Table 5.2, as well as the handful of results obtained for the  $\chi_{c0}(1P)$  and  $\chi_{c1}(1P)$  listed above, we construct a

plot of the spectrum of charmonium that we have determined. This is displayed in Figure 5.4.

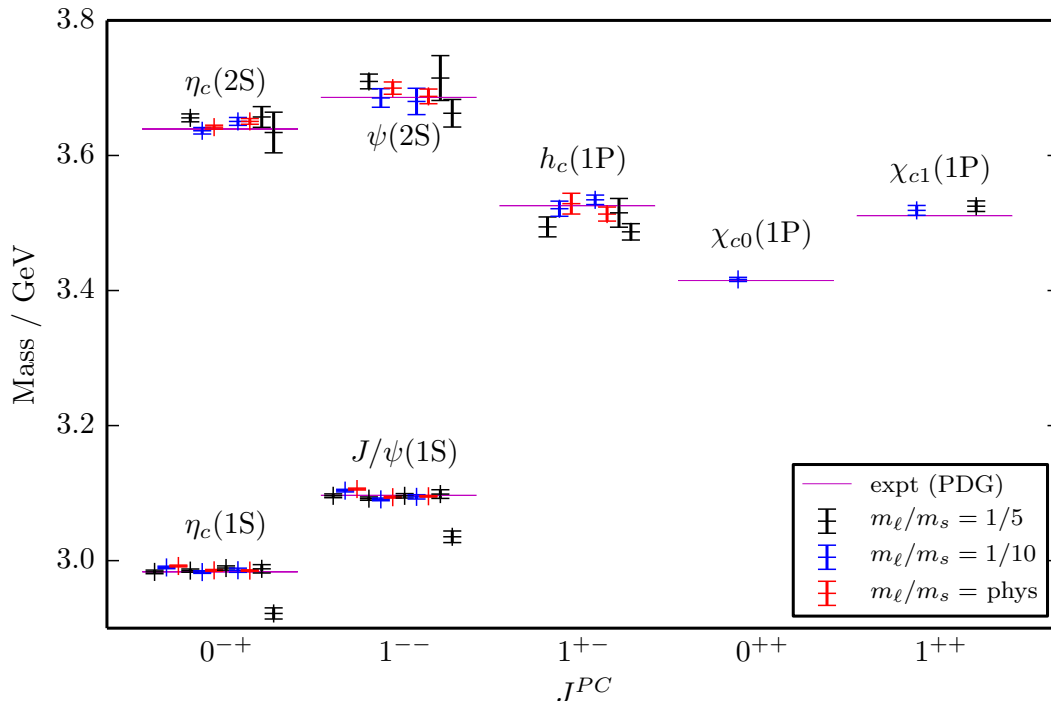


Figure 5.4: The spectrum of low-lying charmonium states as computed on each of the ensembles in Table 5.1. Individual determinations of each mass are plotted in order of decreasing lattice spacing from left to right, atop an indication of their experimental values. The lattice charm quark masses are tuned by fixing to the value of the  $\eta_c(1S)$ , and it is clear from the plot how well-tuned they actually are — excepting, of course, the results on the ultrafine ensemble, which are discussed further in the text. Results for excited states on the superfine ensemble, particularly the 2S states, have an increased error in comparison to their coarser counterparts, and this is also discussed further in the text.

A few items are worthy of note in this plot. Firstly, we have tuned our bare lattice charm masses by fixing to the mass of the  $\eta_c(1S)$ , and generally, we can see that they are all very well-tuned. There is a notable exception, however: the points corresponding to results on the ultrafine lattices are significantly lower than their counterparts on the other ensembles, in the masses of both the  $\eta_c(1S)$  and  $J/\psi(1S)$ . We can therefore conclude that the charm quark mass on the ultrafine ensemble is mistuned, and so we will not use the ultrafine results in the majority of what follows.

The second unusual feature is the relatively large errors on the masses of excited states calculated on the superfine ensemble. It is curious that these results should be less accurate than those from their coarser relatives. We discuss the investigation into these results, and the cause of their increased statistical error, much further in

section 5.5. For now, we note that it is still perfectly possible to attempt continuum fits with a larger error on the superfine results than on the coarse and fine results, and also that the ground states do not seem to be affected to the same extent. We will therefore delay a full discussion until we have examined the results of said continuum fits.

Errors for the  $\eta_c(2S)$  and  $\psi(2S)$  masses are also significant on the ultrafine lattices. This is not a direct concern at the moment, since we will not use these results in any of the fits that follow, but this may be indicative of some problem appearing at finer lattice spacings. It is difficult to be sure without any results at a correctly-tuned charm mass, but this will also be taken into consideration in section 5.5.

## 5.2 Mass Splittings

We will first examine four different mass splittings between the charmonium states that we have calculated. These are the 1S hyperfine splitting  $\Delta M_{\text{hyp}(1S)}$ , the spin-averaged 2S – 1S splitting  $\Delta M_{2S-1S}$ , the 2S hyperfine splitting  $\Delta M_{\text{hyp}(2S)}$ , and the splitting between the axial vector  $h_c(1P)$  and ground-state vector  $J/\psi(1S)$  states,  $\Delta M_{1P-1S}$ . Values calculated for these splittings on each lattice ensemble are given in Table 5.4, and we now look at each in more detail.

### 5.2.1 1S Hyperfine Splitting

Recall that the charmonium 1S hyperfine splitting is the difference between the masses of the ground-state vector  $J/\psi(1S)$  and the ground-state pseudoscalar  $\eta_c(1S)$ . Results for this quantity are displayed in Table 5.4, and we convert to physical units using the inverse lattice spacings  $a^{-1}$  in GeV that are determined from the  $w_0/a$  values on each ensemble. Physical values are plotted in Figure 5.5 using the squared lattice charm mass as a proxy for the lattice spacing, since we expect discretisation errors to depend on  $a^2$  when using the HISQ action.

This set of results is very accurate, due to the fact that it only requires calculation of the ground-state pseudoscalar and vector mesons: our smearings were designed to achieve a large overlap with the ground states, and as before, the ground-state contributions dominate our correlators at large  $t$ -values. This is further evidence of the ability of the HISQ action to accurately simulate charm quarks.

We note that in translating these results to physical units, we have doubled the error on  $w_0/a$  as it appears in Table 2.2. This is necessary when determining the hyperfine splitting due to our use of the  $\eta_c(1S)$  mass to fix the bare lattice charm mass, as outlined in detail in section 4.2.

We also adjust the value of the hyperfine splitting to correct for mistunings of the

Label	$m_\ell/m_s$	$a\Delta M_{\text{hyp}(1S)}$	$a\Delta M_{2S-1S}$	$a\Delta M_{1P-1S}$	$a\Delta M_{\text{hyp}(2S)}$
very coarse	1/5	0.08810(31)	—	—	—
	1/10	0.08770(16)	—	—	—
	phys.	0.08712(14)	—	—	—
coarse	1/5	0.067013(91)	0.3966(50)	0.2529(91)	0.0339(73)
	1/10	0.066684(62)	0.3774(63)	0.2667(68)	0.0301(88)
	phys.	0.066521(36)	0.3799(41)	0.2670(94)	0.0355(57)
fine	1/5	0.04889(23)	—	—	—
	1/10	0.048858(39)	0.2722(65)	0.1978(27)	0.0133(88)
	phys.	0.049000(31)	0.2718(36)	0.1861(46)	0.0165(51)
superfine	1/5	0.033220(49)	0.1889(73)	0.1250(60)	0.0173(105)
ultrafine	1/5	0.025350(71)	0.1448(33)	0.1008(16)	0.0064(74)

Table 5.4: Results in lattice units for selected mass splittings in the charmonium system, as determined on each of the ensembles listed in Table 5.1. The splitting between the vector and pseudoscalar 1S states is known as the 1S hyperfine splitting, and is labelled as  $\Delta M_{\text{hyp}(1S)}$ . Similarly for the vector and pseudoscalar 2S states, we list the 2S hyperfine splitting  $\Delta M_{\text{hyp}(2S)}$ . The spin-averaged 2S – 1S splitting is denoted by  $\Delta M_{2S-1S}$ . The splitting between the axial vector  $h_c(1P)$  and ground-state vector  $J/\psi(1S)$  states is referred to as  $\Delta M_{1P-1S}$ .

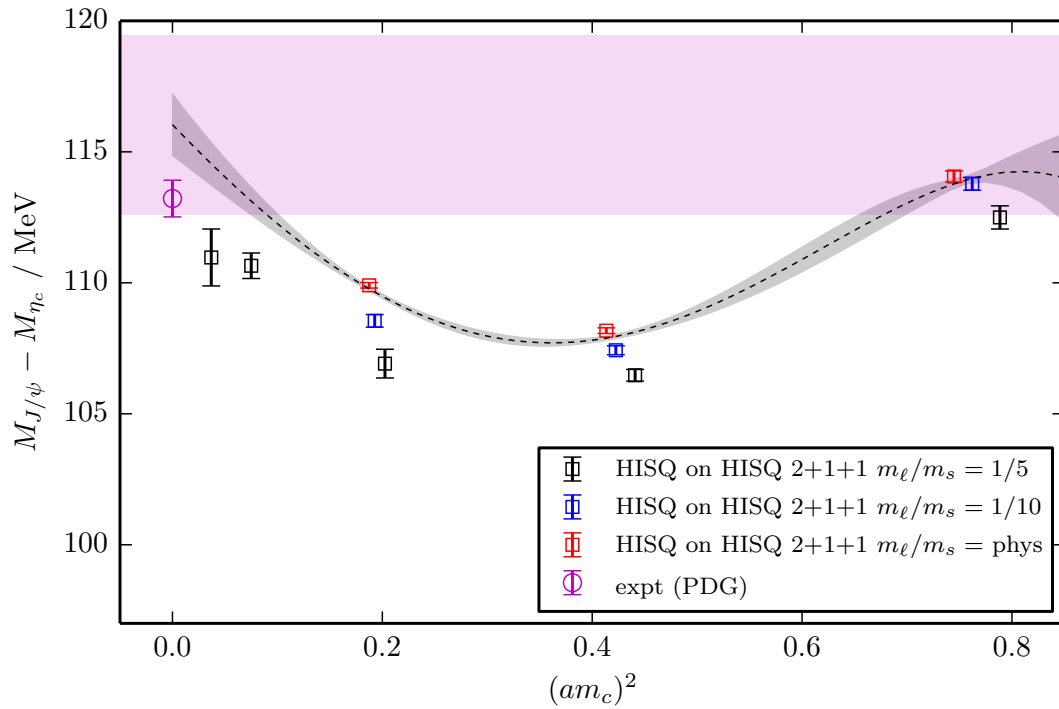


Figure 5.5: The hyperfine splitting of charmonium as determined on a range of ensembles. The groups of points from right to left indicate results on the very coarse, coarse, fine, superfine and ultrafine ensembles respectively, the ultrafine result having been corrected for mistuning with an appropriate uncertainty included. The grey band indicates the fitted curve at the physical light sea quark mass, and the magenta band shows our final result in the continuum limit, including both statistical and systematic errors. This is in excellent agreement with the experimental average [4], shown as the magenta point at zero lattice spacing. Note that the range of the vertical scale is just over 20 MeV, giving an indication of the accuracy of this entire set of results.

charm quark mass. This is done by determining the scaling factor required to match the experimental average of the  $\eta_c(1S)$  mass, appropriately corrected for annihilation effects as in section 5.1. It is then possible to apply the same simple linear scaling to the bare quark mass, to obtain a well-tuned value. The hyperfine splitting is approximately inversely proportional to the bare quark mass — as demonstrated explicitly in section 4.2 — and so we may also apply the inverse of the same scaling factor to our hyperfine splitting results on each ensemble.

In practice this makes very little difference to almost all of our results, since the charm mass is already very well-tuned on all but one of the ensembles we use. Indeed, the adjustment required on all except the ultrafine ensemble is less than 0.2%. The ultrafine result, with its badly-tuned charm mass, requires a shift downwards of approximately 2.2%, and becomes 110.97(70)(83) MeV at a rescaled charm quark mass<sup>2</sup> of 0.1923. The first error on this value is statistical; the second is an estimate of the uncertainty introduced by the rescaling, obtained by applying a percentage error of one-third of the shift required — approximately 0.75%. The values plotted in Figure 5.5 are the rescaled values, and these are also what we include in the fit that follows.

It is worth noting that this is the only quantity for which we include results from the ultrafine ensemble, as the charmonium hyperfine splitting’s relatively simple dependence on the bare quark mass means we can rescale to obtain an estimate of the well-tuned result. This is not the case for the fits we consider in the following sections.

On this wide range of data, we attempt a continuum fit to the form:

$$p \left( 1.0 + A_1 x + A_2 x^2 + A_3 x^3 + A_4 x^4 + A_5 x^5 + \chi_1 \tilde{\delta}_m (1.0 + \chi_{a^2} a^2) + \chi_2 \tilde{\delta}_m^2 \right) \quad (5.9)$$

where the  $A$  and  $\chi$  terms are coefficients to be determined by the fit, along with  $p$ , the physical value of the hyperfine splitting. The fit is a function of  $x = (am_c)^2$ , our chosen proxy for the lattice spacing, and  $\tilde{\delta}_m = \delta_m/10$ , with  $\delta_m$  the mistuning of the sea quark masses as discussed in section 2.1.2.  $\delta_m$  is, of course, very small on the physical point lattices.

It is clear in the above function that taking the continuum limit corresponds to taking  $x \rightarrow 0$ , and the chiral limit corresponds to taking  $\delta_m \rightarrow 0$ . The terms in  $x$  can therefore be thought of as modelling dependence on discretisation errors, and likewise, the terms in  $\delta_m$  as modelling the sea-quark mass dependence. Dependence on sea masses can be clearly seen on the plot in Figure 5.5 by comparing results at similar lattice spacings, but different  $m_\ell/m_s$  values. This arises, at least in part, from the use of  $w_0/a$  to determine the lattice spacing, as discussed in section 2.1.3.

---

<sup>2</sup>We note that this rescaled charm mass is that which we use to calculate the  $\delta_m$  value on the ultrafine ensemble ( $\delta_m = 0.276$ ), as alluded to in section 2.1.2.

We divide  $\delta_m$  by 10 before including it in the fit to allow for a natural choice of priors for the respective coefficients. This arises from chiral perturbation theory: taking  $f_\pi = 0.13$  GeV, we can manipulate the chiral term viz.

$$\frac{m_\pi^2}{(4\pi f_\pi)^2} \approx \frac{m_\pi^2}{5m_{\eta_s}^2} \approx \frac{m_\ell}{5m_s} \quad (5.10)$$

which clearly relates back to our definition of  $\delta_m$ , and would naturally lead us to divide by 5. However, we are here describing sea-quark mass effects, which we expect to be smaller than valence-quark mass effects. Dividing by 10 in the fit is therefore more appropriate, and allows us to assume that  $\chi_1$  and  $\chi_2$  will be of order 1. We take simple priors for them centred on 0.0 with widths of  $\pm 1.0$ .

The fit is carried out using Bayesian methods, and the prior on  $p$  is taken as  $100 \pm 50$  MeV. Priors on the coefficients are generally taken as  $(0.0 \pm 1.0)$ , with two exceptions:  $A_1$  and  $\chi_{a^2}$  are slightly more constrained with priors of  $(0.0 \pm 0.5)$ , since we expect the associated terms to have coefficients of order  $\alpha_s$ .

The fit values at the physical point (i.e. with  $\delta_m$  set to zero) are shown in Figure 5.5 as the grey band, and give a continuum result of

$$M_{J/\psi} - M_{\eta_c} = 116.0(1.2) \text{ MeV} \quad (5.11)$$

with the quoted error purely statistical. The fit here is very good, with a  $\chi^2$  value per degree of freedom of 0.61 for 11 degrees of freedom, and a  $Q$ -value of 0.82.

Following chapter 4, we include a systematic error of  $\pm 3.0$  MeV to account for  $\eta_c$  annihilation effects, while also allowing for uncertainty regarding the sign of the mass shift that these effects induce. Here, however, we must also take account of the error on the physical value of  $w_0$ , which until now has been omitted since it is correlated between points. We therefore also include a systematic error equal to twice the relative error on  $w_0 = 0.1715(9)$  fm — this is small but not negligible at  $\pm(2 \times 0.5\%)$ , and is doubled in this case for the same reason that we double the error on each value of  $w_0/a$  as explained before. Combining these contributions gives a total systematic error of  $\pm 3.2$  MeV.

Overall, then, our result for the physical value of the charmonium hyperfine splitting is:

$$M_{J/\psi} - M_{\eta_c} = 116.0(3.4) \text{ MeV} \quad (5.12)$$

with combined statistical and systematic errors to facilitate comparisons. This is shown in Figure 5.5 as the magenta band, and is clearly dominated by the systematics included to account for annihilation effects.

This result compares very well with numerous others, notably the current experimental average of  $113.2(7)$  MeV [4]. We will perform a detailed comparison of charmonium hyperfine splitting results in chapter 6.

## 5.2.2 Spin-Averaged 2S – 1S Splitting

The spin-averaged 2S – 1S splitting in the charmonium system is

$$\Delta M_{2S-1S} = \frac{1}{4} \left[ (M_{\eta_c(2S)} - M_{\eta_c(1S)}) + 3 (M_{\psi(2S)} - M_{J/\psi(1S)}) \right] \quad (5.13)$$

and this can clearly be calculated from the masses that we have extracted from our fits. Recall that this is the quantity we mentioned at the start of this chapter, which exhibited a significant discrepancy from the experimental value when calculated by the Fermilab Lattice and MILC Collaborations in [84].

We once again use the  $w_0/a$  values from Table 2.2 to determine the lattice spacings required to convert our results to physical units, and these are plotted in Figure 5.6. Doubling the errors on  $w_0/a$ , as we did for the hyperfine splitting, is not appropriate here, since we do not have the same inverse dependence on quark mass seen in the hyperfine case. The squared lattice charm mass is again used as a proxy for the lattice spacing.

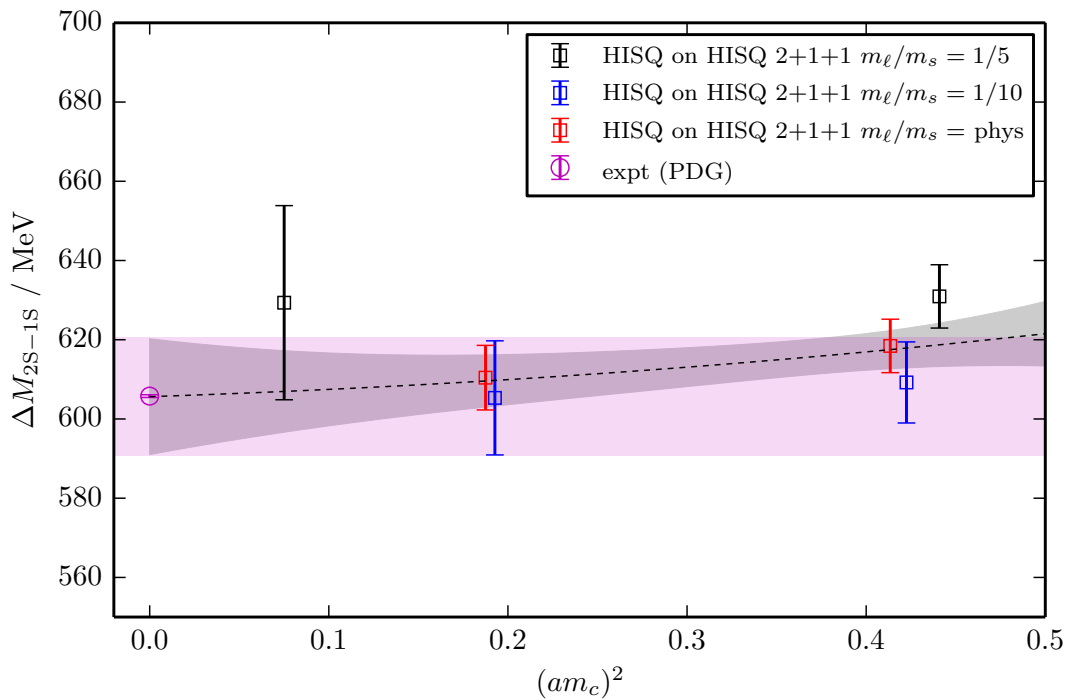


Figure 5.6: The spin-averaged 2S – 1S splitting in charmonium as determined on a range of ensembles — the groups of points from right to left indicate results on the coarse, fine and superfine ensembles respectively. The grey band indicates the fitted curve at the physical light sea quark mass, and the magenta band shows our final result in the continuum limit, including both statistical and systematic errors. This is in good agreement with the experimental average [4], shown as the magenta point at zero lattice spacing.

We perform a continuum and chiral extrapolation by fitting to the function

in equation 5.9, with an important modification. In the hyperfine splitting case, we expect discretisation errors to depend on  $x = (am_c)^2$ , whereas here they will depend on  $(a\Lambda)^2$ , with the QCD scale  $\Lambda \approx 500$  MeV, since the  $2S - 1S$  splitting is — unlike the hyperfine splitting — a result of the spin-independent heavy quark potential discussed at the beginning of chapter 4. We therefore account for this by multiplying each term containing an  $A$  coefficient by  $0.5$  ( $\approx \Lambda/m_c$ ) raised to the appropriate power, and simply take priors on the  $A$  coefficients of  $(0.0 \pm 1.0)$ , or a smaller  $(0.0 \pm 0.5)$  for  $A_1$ , as before. The priors on the  $\chi$  coefficients are the same as those used for the hyperfine splitting:  $(0.0 \pm 1.0)$  except for  $\chi_{a^2}$ , which we constrain as  $(0.0 \pm 0.5)$ .

For the physical value  $p$ , we take a prior of  $600 \pm 100$  MeV, and the fit values at the physical point are shown as the grey band in Figure 5.6. The fit is very good, with a  $\chi^2$  value per degree of freedom of 0.42 and a  $Q$ -value of 0.87. This gives a continuum result of

$$\Delta M_{2S-1S} = 606(15) \text{ MeV} \quad (5.14)$$

with the quoted error purely statistical. Here annihilation effects are not significant in the final result<sup>3</sup>, and we simply need to take account of the error on the physical value of  $w_0$ . This is done by including a systematic error equal to the relative error on  $w_0$  of 0.5%, or  $\pm 3$  MeV.

This systematic error is small enough to be negligible in comparison to the statistical error, so the above is our overall result. This is in good agreement with the current experimental average of  $605.82(37)$  MeV, and we do not seem to observe a similar discrepancy to that in the Fermilab/MILC study [84].

The statistical error on the singular superfine result is somewhat higher than corresponding results on the coarse and fine lattices. Reduction of this error could go some way towards reducing the error on the continuum result, which is just over 2.6%. Unfortunately, the cause of the larger error on the superfine lattices is not clear, and requires further investigation. We discuss this further in section 5.5.

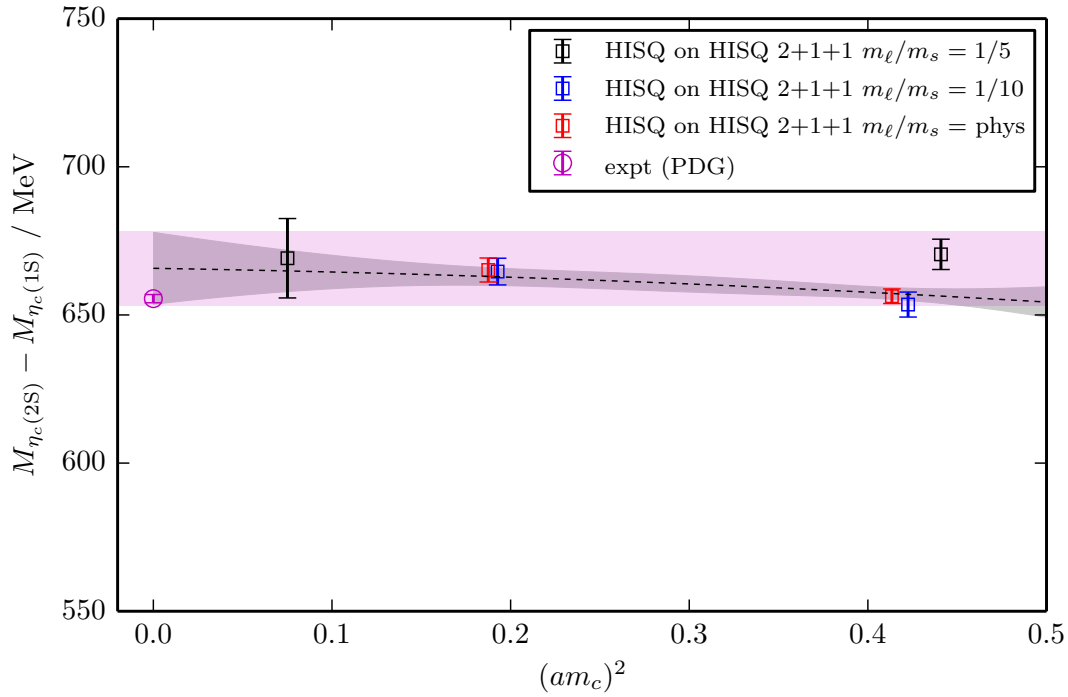
### Separate Fits

For the purpose of obtaining a full spectrum of the states we have determined (see section 6.2.4), we use the same methods as above to perform continuum and chiral extrapolations separately for the  $2S - 1S$  splittings in the pseudoscalar and vector cases. These fits are plotted in Figure 5.7.

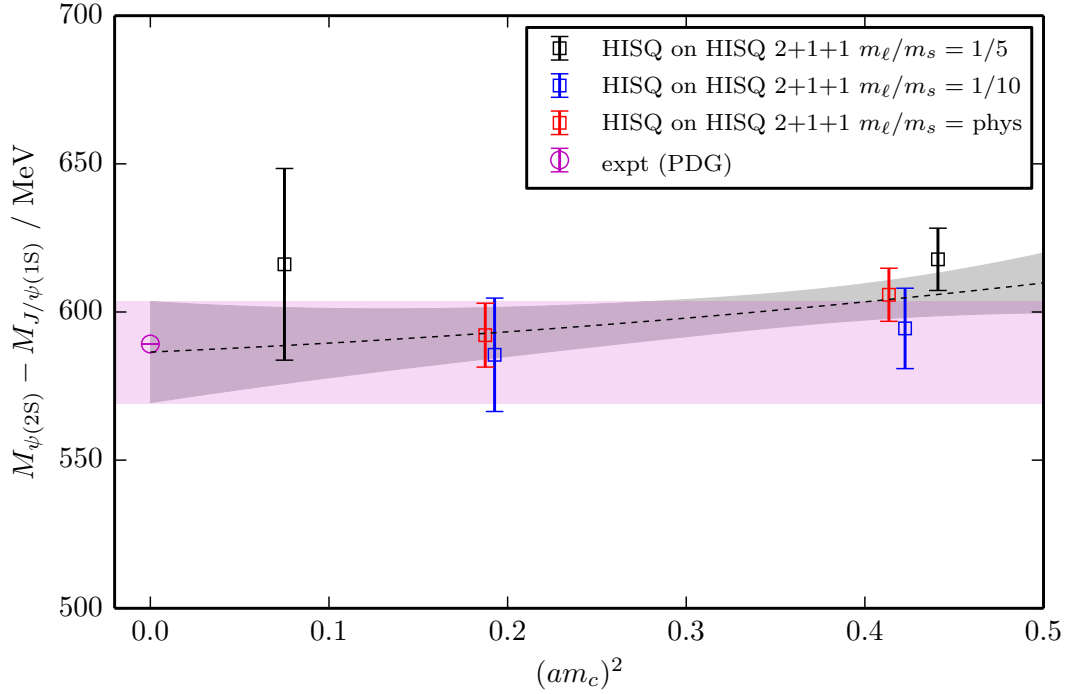
For the pseudoscalar, we fit to the same revised fit function as in the spin-averaged case, with all of the same priors. The fit is good, with a  $\chi^2$  value per

---

<sup>3</sup>Given the different widths of the  $2S$  and  $1S$  states [4], annihilation effects would presumably be of order 1–2 MeV — negligible in comparison to our error estimate.



(a) Pseudoscalar



(b) Vector

Figure 5.7: The 2S – 1S splitting in charmonium pseudoscalar and vector channels, fitted separately rather than being spin-averaged as in Figure 5.6.

degree of freedom of 0.81 and a  $Q$ -value of 0.56. This gives a continuum result of

$$M_{\eta_c(2S)} - M_{\eta_c(1S)} = 666(12) \text{ MeV} \quad (5.15)$$

which agrees well with the difference of the experimental averages for these two masses [4], of 655.7(1.5) MeV. The systematic error here, arising from the uncertainty on the physical value of  $w_0$ , is  $\pm 3$  MeV and adding this to the statistical error in quadrature makes the final physical result 666(13) MeV.

We carry out the same procedure for the vector, obtaining a fit with a  $\chi^2$  value per degree of freedom of 0.34 and a  $Q$ -value of 0.91. This gives a continuum result of

$$M_{\psi(2S)} - M_{J/\psi(1S)} = 586(17) \text{ MeV} \quad (5.16)$$

again with a systematic error of  $\pm 3$  MeV. This is negligible in this case, making the above our final physical result. This result also agrees well with the difference of the experimental averages [4], which is 589.193(18) MeV.

Although it is evident from the above, it is worth noting explicitly that these two results are not the same, nor are they compatible with each other, which we would expect were our methods not sensitive to spin effects — specifically, the difference between the hyperfine splittings in the 1S and 2S energy levels. This leads us neatly to an examination of the said 2S hyperfine splitting.

### 5.2.3 2S Hyperfine Splitting

The charmonium 2S hyperfine splitting is the difference between the masses of the first excited state vector  $\psi(2S)$  and the first excited pseudoscalar  $\eta_c(2S)$ . Much like its 1S-level counterpart, this quantity is listed in Table 5.4, and we plot the physical results in Figure 5.8, using the squared lattice charm mass as a proxy for the lattice spacing. We once again convert to physical units using inverse lattice spacings determined from the  $w_0/a$  values on each ensemble.

Our continuum and chiral fit here is to the same form as for the 1S hyperfine splitting, with discretisation errors dependent on  $am_c$  and identical priors to before, apart from the prior on the physical value  $p$ , which we take as  $50 \pm 25$  MeV. This produces an excellent fit, with a  $\chi^2$  value per degree of freedom of 0.40 and a  $Q$ -value of 0.88, which is plotted as the grey band in Figure 5.8. Our continuum result is then

$$M_{\psi(2S)} - M_{\eta_c(2S)} = 44.3(8.5) \text{ MeV} \quad (5.17)$$

with a purely statistical error quoted. Annihilation effects will again come into play for this quantity, but given the decay width of the  $\eta_c(2S)$  [4], we can reasonably assume that they will be negligible in comparison to our statistical error. Our only

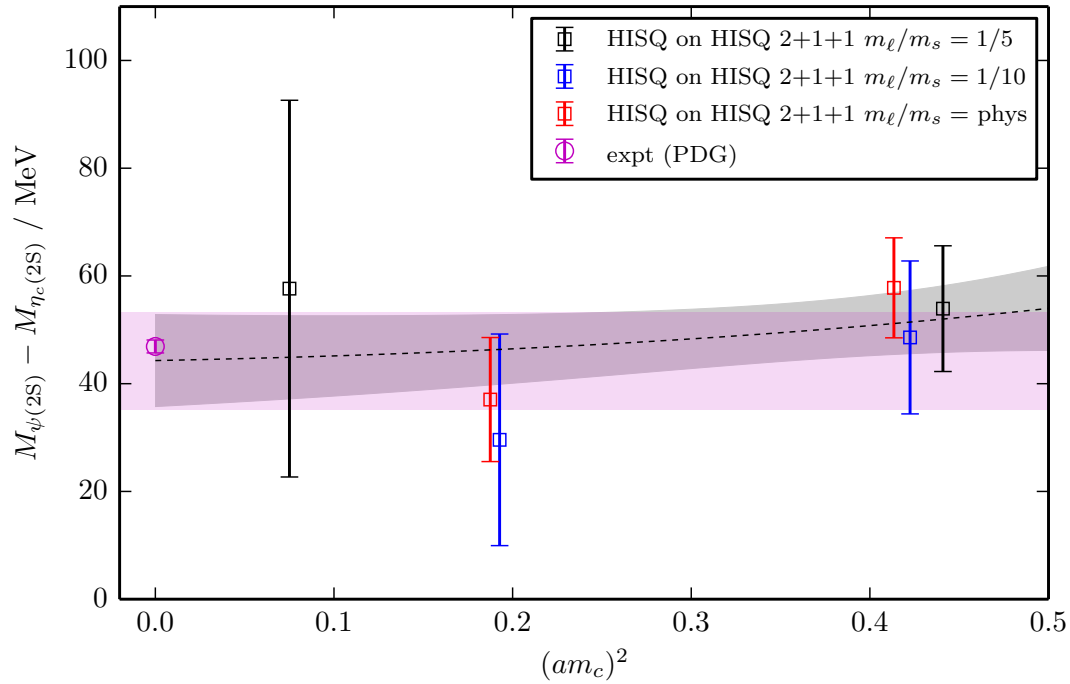


Figure 5.8: The mass splitting between the radially-excited charmonium vector meson  $\psi(2S)$ , and its corresponding pseudoscalar meson, the  $\eta_c(2S)$ , as determined on a range of ensembles. The groups of points from right to left indicate results on the coarse, fine and superfine ensembles respectively. The grey band indicates the fitted curve at the physical light sea quark mass, and the magenta band shows our final result in the continuum limit, including both statistical and systematic errors. This is in good agreement with the experimental average [4], shown as the magenta point at zero lattice spacing.

other systematic error, that arising from the relative error on  $w_0$ , is  $\pm 3$  MeV, and once again has no effect given its relative size.

The above is therefore our final result, more readily quoted as  $44(8)$  MeV, and agrees well with the current experimental average of  $46.9(1.2)$  MeV. It is plain to see that this is a quantity which is far more difficult to determine precisely than its 1S counterpart, both experimentally and on the lattice. We would have been unable to achieve this level of accuracy without the use of smeared operators.

It is notable in Figure 5.8 that the result on the superfine ensemble has a large statistical error associated with it, much like the corresponding results for the 2S–1S splittings, although in this case the effect is magnified since we are dealing with two 2S states and not just one. Again, reduction of this error is likely to be very helpful in improving the accuracy of our continuum determination, but we delay discussion of the underlying issues on the superfine ensemble to section 5.5.

## 5.2.4 Vector–Axial Vector Splitting

Finally, we determine the mass splitting between the ground-state vector meson  $J/\psi(1S)$ , and the orbitally-excited axial vector meson  $h_c(1P)$ . Again this is calculated from the values extracted from our correlator fits, in Table 5.2, and shown in Table 5.4. We convert to physical units via  $w_0/a$ , and the resulting values are plotted against the squared lattice charm mass in Figure 5.9.

We fit to the form of equation 5.9, revised, as before, for discretisation errors dependent on  $(a\Lambda)^2$ , since this is not a spin-dependent splitting. We take the same priors on the  $A$  and  $\chi$  values as for the 2S – 1S splitting, and a prior on  $p$  of  $400 \pm 200$  MeV. This continuum and chiral extrapolation is shown as the grey band in Figure 5.9, and gives a physical result of

$$M_{h_c(1P)} - M_{J/\psi(1S)} = 438(12) \text{ MeV} \quad (5.18)$$

with the quoted error purely statistical. The fit is again satisfactory, with a  $\chi^2$  value per degree of freedom of 1.2 and a  $Q$ -value of 0.28.

Including a systematic error of  $\pm 2$  MeV — derived from the error on the physical value of  $w_0$  — does not affect the error estimate, and the above is our final result. This is in good agreement with the current experimental average of  $428.46(11)$  MeV, but may suffer from the same problem as the 2S – 1S and 2S hyperfine splittings in that the statistical error on the superfine result is significantly larger than the rest. Reducing this error would allow for a more accurate continuum extrapolation, but again we defer to the discussion in section 5.5.

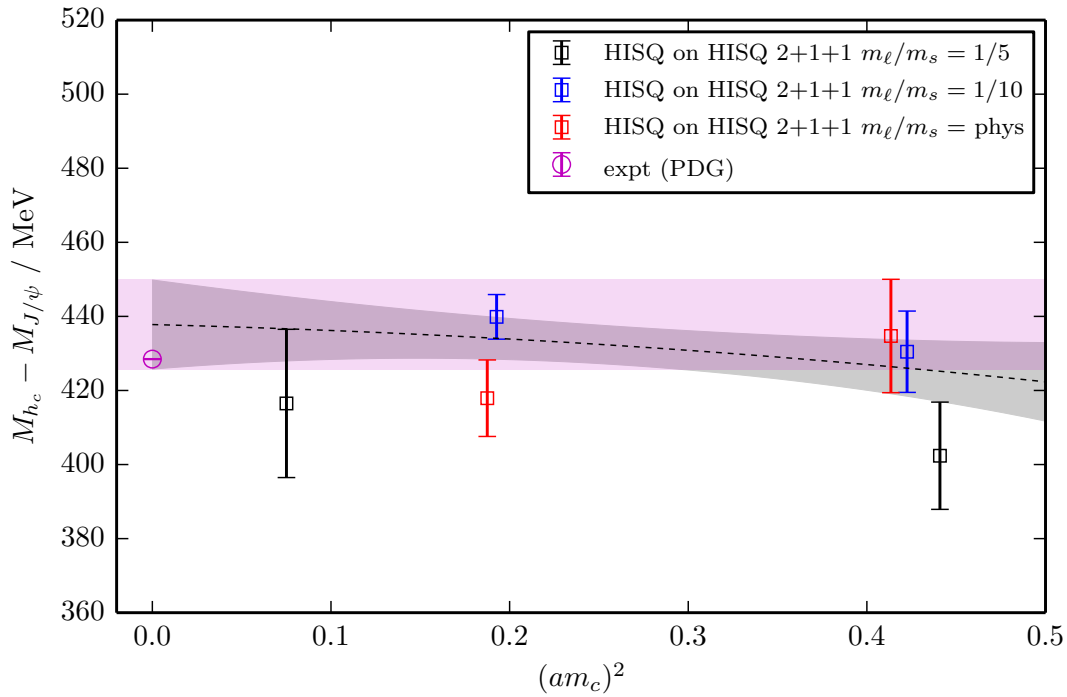


Figure 5.9: The mass splitting between the ground-state charmonium vector meson  $J/\psi(1S)$ , and its parity partner, the orbitally-excited axial vector meson  $h_c(1P)$ , as determined on a range of ensembles. The groups of points from right to left indicate results on the coarse, fine and superfine ensembles respectively. The grey band indicates the fitted curve at the physical light sea quark mass, and the magenta band shows our final result in the continuum limit, including both statistical and systematic errors. This is in good agreement with the experimental average [4], shown as the magenta point at zero lattice spacing.

### 5.3 Moments of the Vector Correlator

Analogously to the calculations in the previous chapter, we can determine the time moments  $G_n^V$  of our local vector correlators, defined as in section 4.3 by:

$$G_n^V = Z^2 C_n^V = Z^2 \sum_{\tilde{t}} \tilde{t}^n \overline{C}_{\ell,\ell}(\tilde{t}). \quad (5.19)$$

This will once again allow us to determine renormalisation factors  $Z$  for each ensemble using the current-current correlator method, and these will be used in the next section to make a physical determination of the  $J/\psi(1S)$  decay constant.

Unrenormalised moments in lattice units, calculated as above and taken to the power  $1/(n-2)$  to reduce them to the same dimension, are displayed in Table 5.5 for each ensemble.

Label	$m_\ell/m_s$	$am_c$	$\left(\frac{G_4^V}{Z^2 a^2}\right)^{1/2}$	$\left(\frac{G_6^V}{Z^2 a^4}\right)^{1/4}$	$\left(\frac{G_8^V}{Z^2 a^6}\right)^{1/6}$	$\left(\frac{G_{10}^V}{Z^2 a^8}\right)^{1/8}$
very coarse	1/5	0.888	0.38967(4)	0.94979(6)	1.41052(8)	1.81550(9)
	1/10	0.873	0.39628(2)	0.96126(3)	1.42550(4)	1.83387(5)
	phys.	0.863	0.40078(2)	0.96905(2)	1.43567(3)	1.84637(3)
coarse	1/5	0.664	0.51119(1)	1.16435(2)	1.70104(3)	2.18470(3)
	1/10	0.650	0.520634(8)	1.18118(1)	1.72431(2)	2.21471(2)
	phys.	0.643	0.525456(5)	1.189780(8)	1.73622(1)	2.23007(1)
fine	1/5	0.450	0.70981(13)	1.53941(20)	2.24688(27)	2.90799(32)
	1/10	0.439	0.72376(1)	1.56612(2)	2.28596(3)	2.95928(4)
	phys.	0.433	0.73149(1)	1.58094(2)	2.30765(2)	2.98772(3)
superfine	1/5	0.274	1.07074(3)	2.27654(6)	3.35547(8)	4.37418(10)
ultrafine	1/5	0.188	1.46556(17)	3.10710(31)	4.59734(43)	6.00058(56)

Table 5.5: Time moments of the charmonium vector correlator on each ensemble, in lattice units and as yet unrenormalised. The  $n^{\text{th}}$  moment is raised to the power  $1/(n-2)$  — this reduces all of the moments to the same dimension.

From here, we divide each result by appropriate powers of the inverse lattice spacing  $a^{-1}$  (determined from  $w_0/a$  on each ensemble) to obtain the moments in physical units, and renormalise them by multiplying by (appropriate powers of)  $Z^2$ . We once again use  $Z_8$ , the value obtained from the 8<sup>th</sup> moment, for this purpose, and the reasoning behind this choice will be explained in section 5.3.1. The physical values of the 4<sup>th</sup>, 6<sup>th</sup>, 8<sup>th</sup> and 10<sup>th</sup> moments are plotted in Figure 5.10.

We perform continuum and chiral extrapolations using the same fit function and priors as for the hyperfine splitting, since the moments are also short-distance quantities with discretisation errors described by  $am_c$ . These fits are plotted as the

grey bands in Figure 5.10, and have  $\chi^2$  values per degree of freedom of 0.077, 0.038, 0.079 and 0.088, for the 4<sup>th</sup>, 6<sup>th</sup>, 8<sup>th</sup> and 10<sup>th</sup> moments respectively. They each have statistical  $Q$ -values of 1.0, indicating four excellent fits.

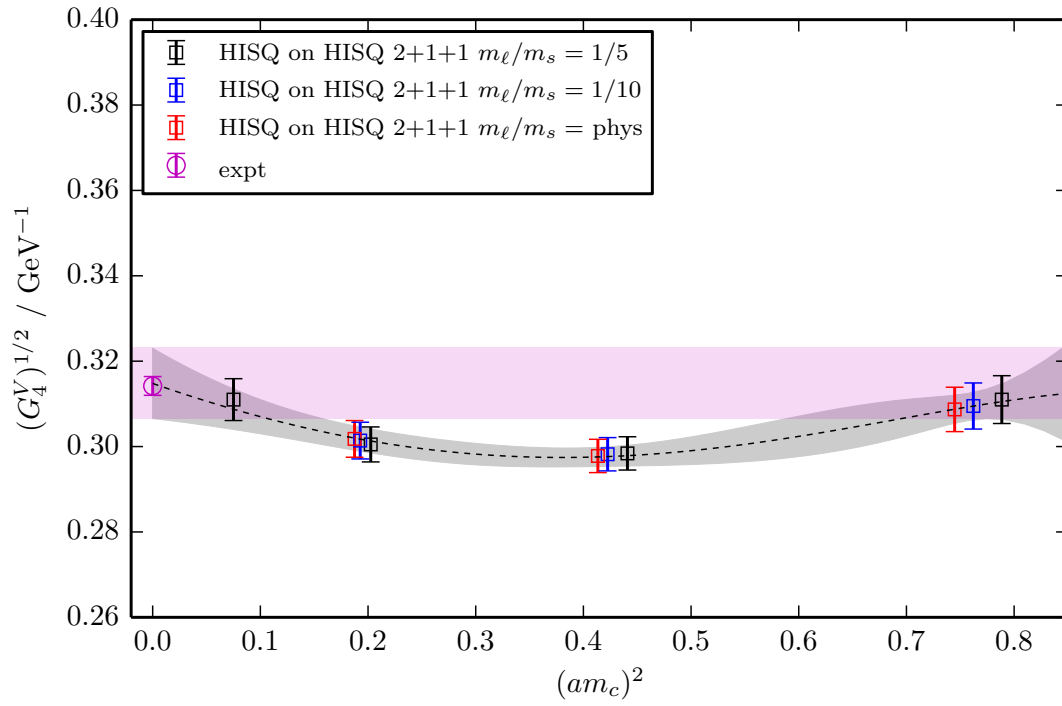
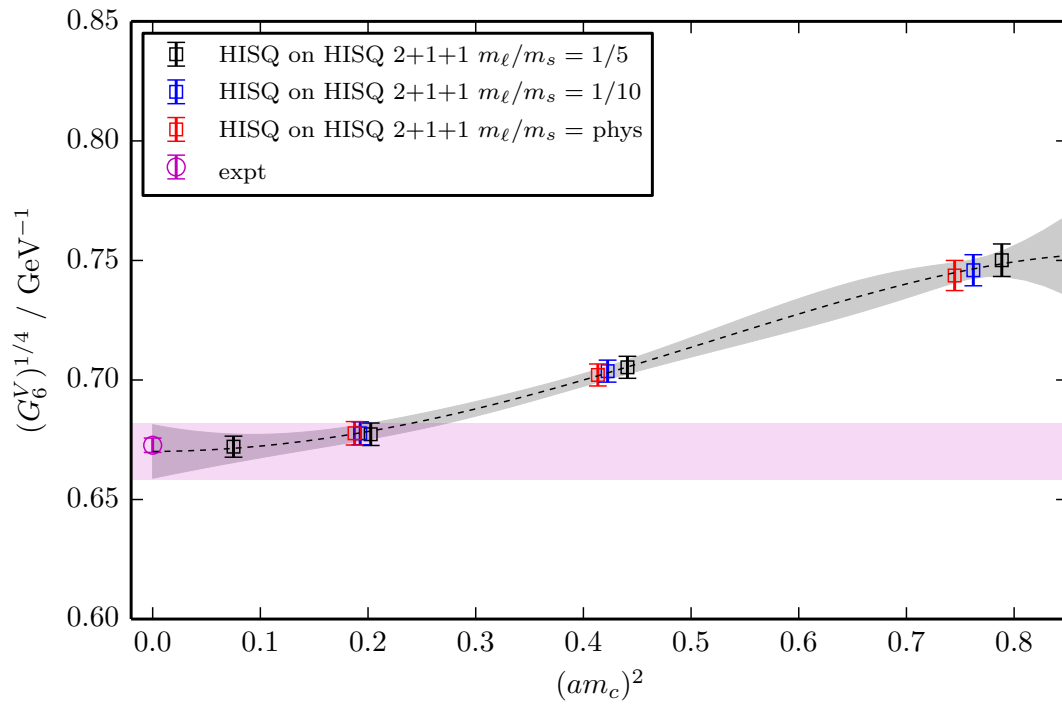
As in the previous chapter, we can compare our continuum determinations of the lattice moments to the  $q^2$ -derivative moments  $\mathcal{M}_k$  of the charm quark vacuum polarisation  $\Pi_c(q^2)$  [78], appropriately normalised as described in section 4.3. The values of  $\mathcal{M}_k^{\text{norm}}$  for the charm quark are listed again in Table 5.6 alongside our continuum values for  $(G_n^V)^{\frac{1}{n-2}}$  from the above fits. The continuum results for the lattice moments are displayed with separate statistical and systematic errors, the systematic arising from the error on the physical value of  $w_0$  which is correlated between the data points. In most cases this is too small in comparison to the statistical error to have a significant effect, but nevertheless, the physical results with the systematic error included are also displayed as the magenta bands in Figure 5.10.

$n$	$(G_n^V)^{\frac{1}{n-2}}/\text{GeV}^{-1}$	$k$	$\mathcal{M}_k^{\text{norm}}/\text{GeV}^{-1}$
4	0.3148(82)(16)	1	0.3142(22)
6	0.6701(112)(34)	2	0.6727(30)
8	0.9962(126)(50)	3	1.0008(34)
10	1.3061(139)(65)	4	1.3088(35)

Table 5.6: Time moments of the charmonium vector correlators. In the left-hand columns, we list the physical results from our continuum fits and their associated index  $n$ . In the right-hand columns, we list the comparable results extracted from experiment in [79] and [80], indexed by  $k$  and appropriately normalised for comparison to our results.

Each of our results in Table 5.6 is in excellent agreement with its respective experimentally-derived value. Errors on the lattice determinations are significantly higher than those on their experimental counterparts, although still on the order of 1% at their highest. This is due to a number of different factors, and we will discuss these further in the sections that follow.

We note that this is one case in which the superfine result does not exhibit a higher statistical error than results on its coarser counterparts, since calculating the moments does not require us to carry out correlator fits. In turn, this gives us much confidence that the raw lattice data from the superfine ensemble is robust and accurate, and that inaccuracies are being introduced only as a result of complications in fitting the correlators. This will be discussed in much more detail in section 5.5.

(a) 4<sup>th</sup> moment(b) 6<sup>th</sup> moment

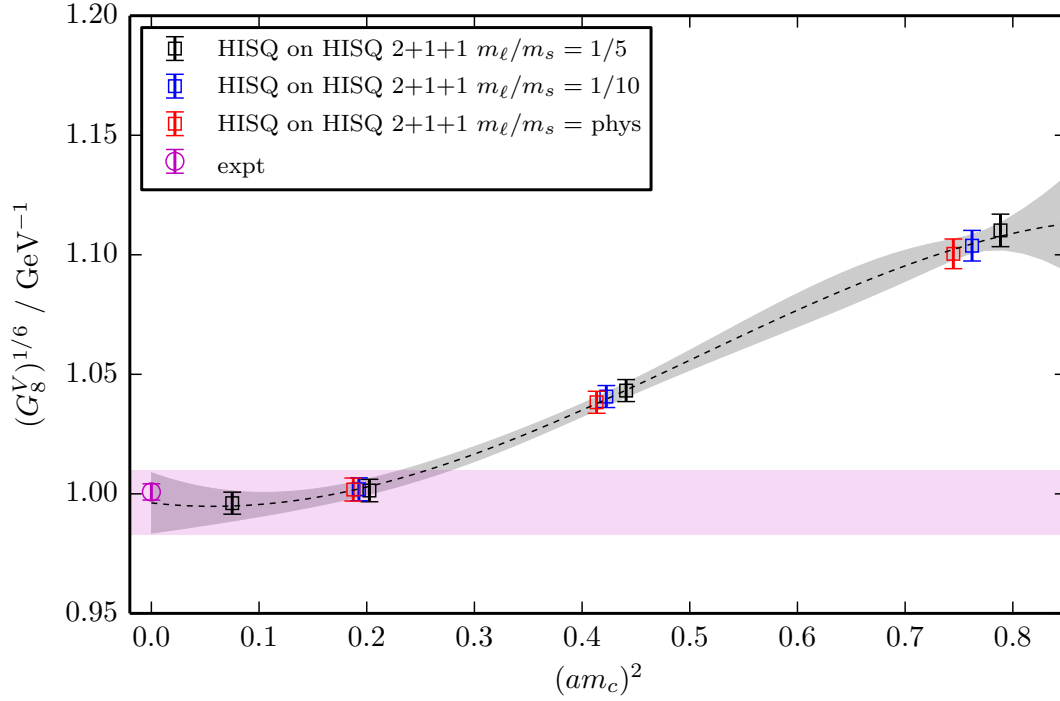
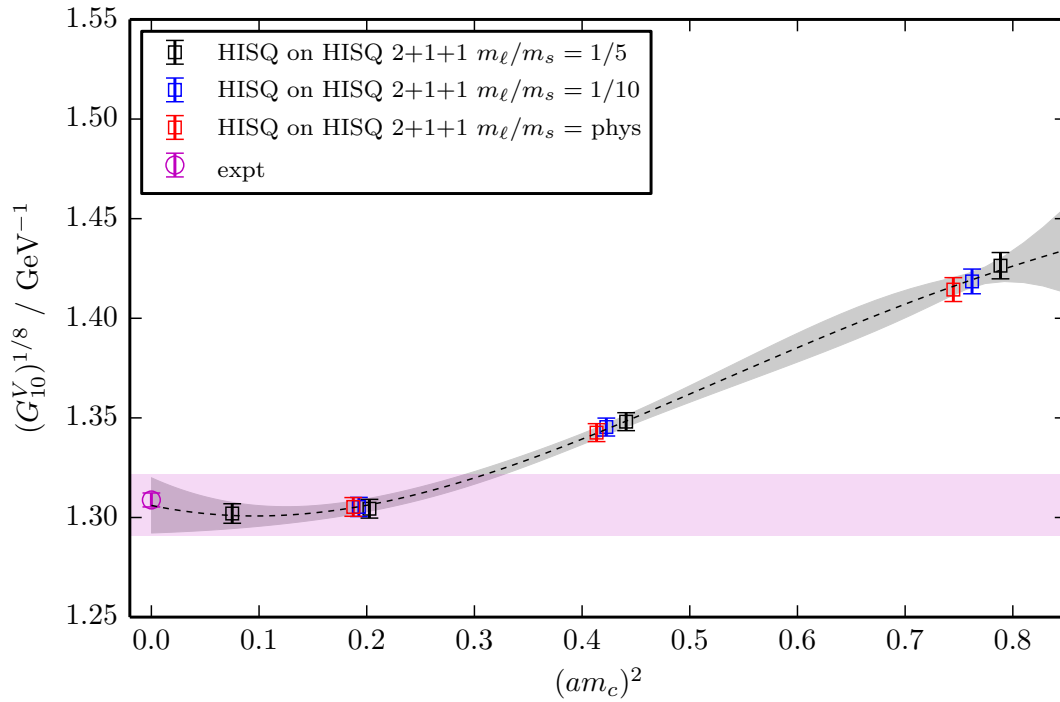
(c) 8<sup>th</sup> moment(d) 10<sup>th</sup> moment

Figure 5.10: Moments of the charmonium vector correlator, determined on a range of lattice ensembles. From right to left, the groups of points indicate results on the very coarse, coarse, fine and superfine lattices. The magenta points are the results derived from experiment, and the grey bands show the fit as described in the text.

### 5.3.1 Current-Current Renormalisation

We determine our renormalisation factors  $Z$  by following the current-current correlator method, as detailed in section 4.3.1, and matching the ratio of pseudoscalar to vector moments on the lattice to that determined from perturbation theory in the continuum:

$$Z_n = \sqrt{\frac{C_{n+2}^P/C_n^V}{c_{n+2}^P/c_n^V}}. \quad (5.20)$$

Our determinations of these  $Z$ -factors on each of our ensembles, using the 4<sup>th</sup>, 6<sup>th</sup> and 8<sup>th</sup> vector moments, are listed in Table 5.7.

Label	$m_\ell/m_s$	$am_c$	$Z_4$	$Z_6$	$Z_8$
very coarse	1/5	0.888	1.2437(25)	1.0736(62)	1.021(18)
	1/10	0.873	1.2321(27)	1.0640(60)	1.013(18)
	phys.	0.863	1.2244(28)	1.0577(58)	1.008(17)
coarse	1/5	0.664	1.0890(82)	0.9557(77)	0.929(12)
	1/10	0.650	1.0811(90)	0.9503(82)	0.925(12)
	phys.	0.643	1.0772(94)	0.9477(85)	0.923(12)
fine	1/5	0.450	1.001(12)	0.926(11)	0.926(13)
	1/10	0.439	0.998(13)	0.926(12)	0.926(13)
	phys.	0.433	0.996(13)	0.926(12)	0.927(13)
superfine	1/5	0.274	0.981(11)	0.960(10)	0.968(12)
ultrafine	1/5	0.188	0.985(11)	0.978(11)	0.984(13)

Table 5.7: Renormalisation factors determined from the current-current correlator method, for each ensemble listed in Table 5.1.  $Z_n$  is the renormalisation factor obtained by matching the  $n^{\text{th}}$  lattice moment to its equivalent continuum value, derived from experimental results.

Following the logic of the previous chapter, we renormalise the vector moments using each of  $Z_4$ ,  $Z_6$  and  $Z_8$ , and determine which of these sets of results gives the best continuum fit. Table 5.8 lists the  $\chi^2$  and statistical  $Q$  values of the fit performed to each calculated moment for each choice of  $Z$ , and, while there is less of a disparity between  $Z$ -factors than in the previous chapter, it is once again clear that using  $Z_8$  results in the minimal  $\chi^2$  value.  $Q$  is the same for all fits, which makes it a less useful discriminator this time round.

Plots of the vector moments renormalised with  $Z_4$  and  $Z_6$  are shown in Figures 5.11 and 5.12 respectively, for comparison to our previous plots using  $Z_8$  in Figure 5.10. As expected, since the lower moments contain higher momentum and are therefore more relativistic, these sets of results both exhibit larger discretisation

$n$	$Z_4$		$Z_6$		$Z_8$	
	$\chi^2$	$Q$	$\chi^2$	$Q$	$\chi^2$	$Q$
4	0.075	1.0	0.12	1.0	0.077	1.0
6	0.14	1.0	0.12	1.0	0.038	1.0
8	0.19	1.0	0.20	1.0	0.079	1.0
10	0.17	1.0	0.18	1.0	0.088	1.0
Sum	0.575	4.0	0.62	4.0	0.282	4.0

Table 5.8:  $\chi^2$  and statistical  $Q$  values for continuum fits to the  $n^{\text{th}}$  moments of the vector correlator, when renormalised using the listed  $Z$ -factors. It is clear that using  $Z_8$  results in the minimal  $\chi^2$  and maximal  $Q$  values.

errors than those renormalised with  $Z_8$ , although the difference in most cases is in fact quite small.

We therefore choose to use  $Z_8$  in renormalising all the required quantities in this chapter, despite noting that it has slightly increased errors in comparison to its lower- $n$  counterparts in Table 5.7.

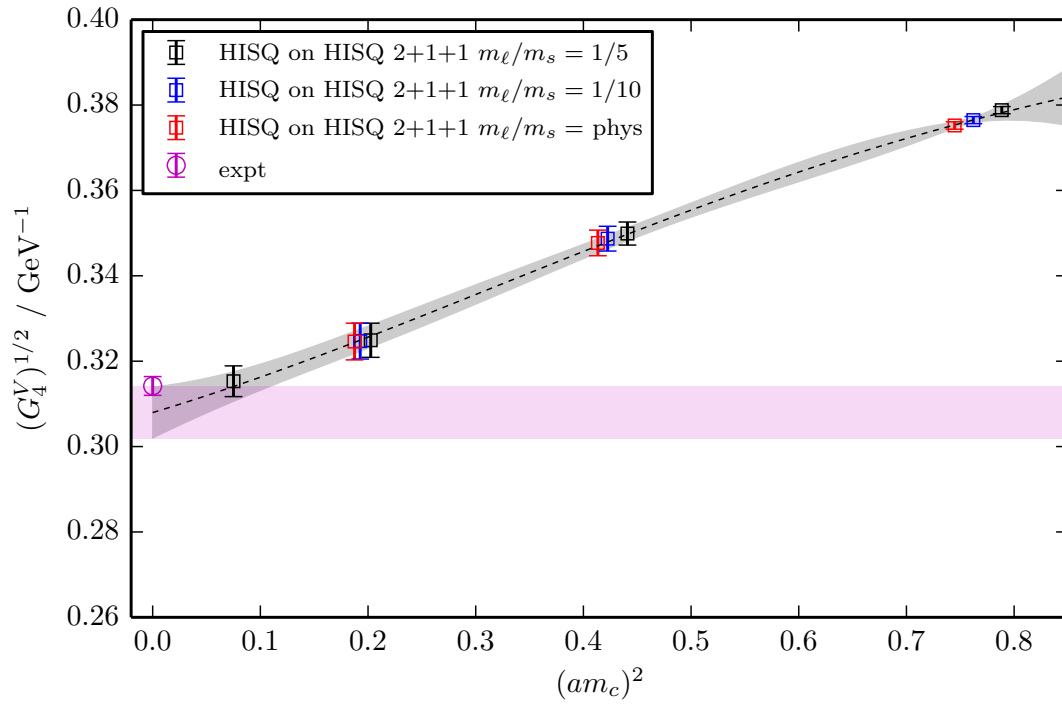
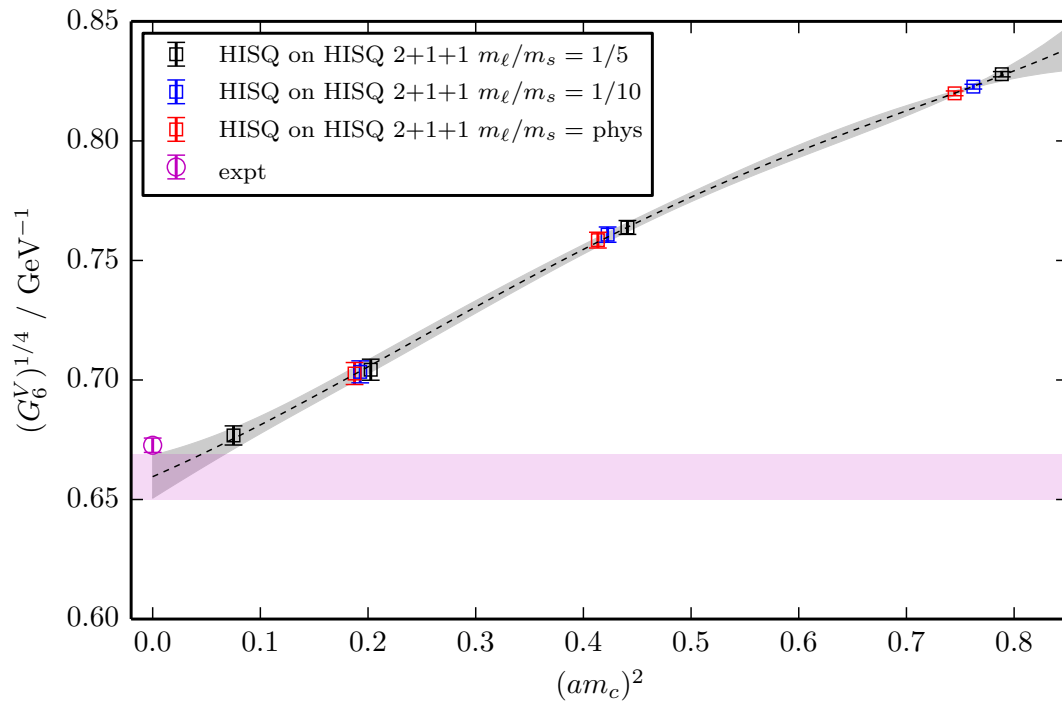
### 5.3.2 Previous Lattice Results

The HPQCD collaboration has previously determined the time moments of vector charmonium on 2+1-flavour lattices, and this calculation is detailed in [56], which is a direct forerunner of this work. Comparing our results to those obtained in the previous calculation, we note that despite using very similar methods for both the lattice calculation and the determination of  $Z$ , our results have statistical errors that are around twice as large.

Let us take the 4<sup>th</sup> moment as a specific example, for reasons which will soon become apparent. Including only statistical errors, we have determined this as  $0.3148(82) \text{ GeV}^{-1}$ , compared to  $0.3152(41) \text{ GeV}^{-1}$  in [56]. Both of these results are in good agreement with the experimental result, but the error estimate on our value is notably larger.

There are two main reasons why this seems to be the case. The first is a difference in the  $Z$ -factor chosen for renormalisation: we use  $Z_8$  whereas the previous work uses  $Z_4$ . The rationale behind this in [56] is to use the  $Z$ -factor with the smallest error estimate, and so naturally this will produce a smaller error on the final result. Quite separately, our reasoning is based on the results which produce the best continuum fit, despite having noted in the previous section that we also observe an error on  $Z_n$  which increases as  $n$  does<sup>4</sup>.

<sup>4</sup>This effect is explained in [56] as arising from errors on the perturbative portion of our calculation of the gluon condensate, which increase faster with  $n$  than discretisation errors fall.

(a) 4<sup>th</sup> moment(b) 6<sup>th</sup> moment

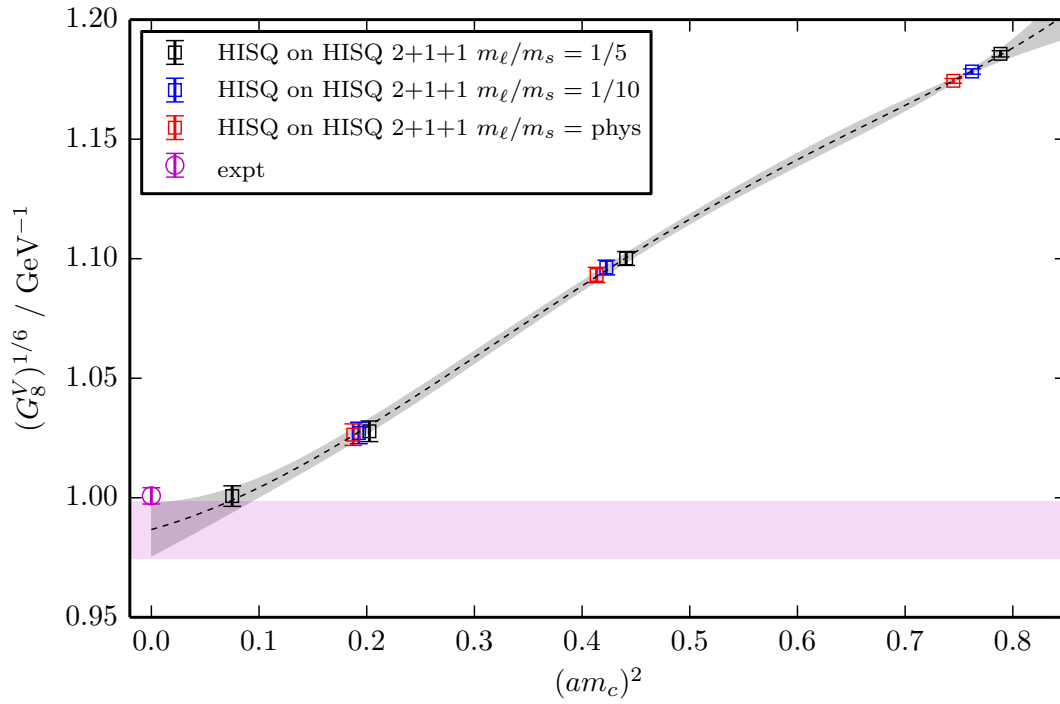
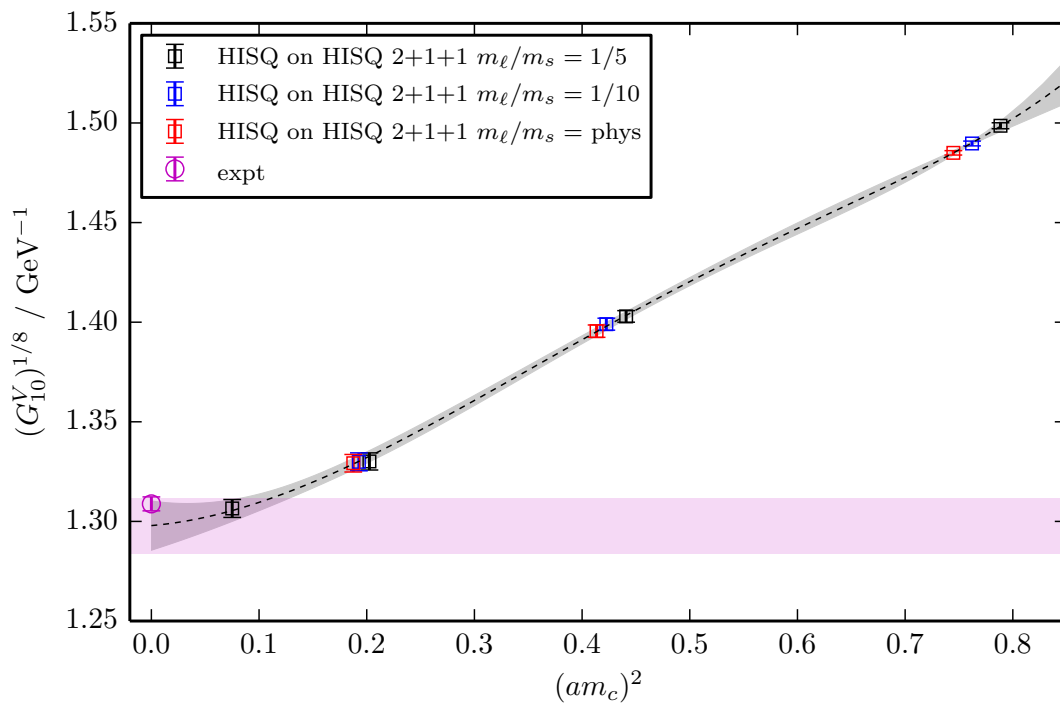
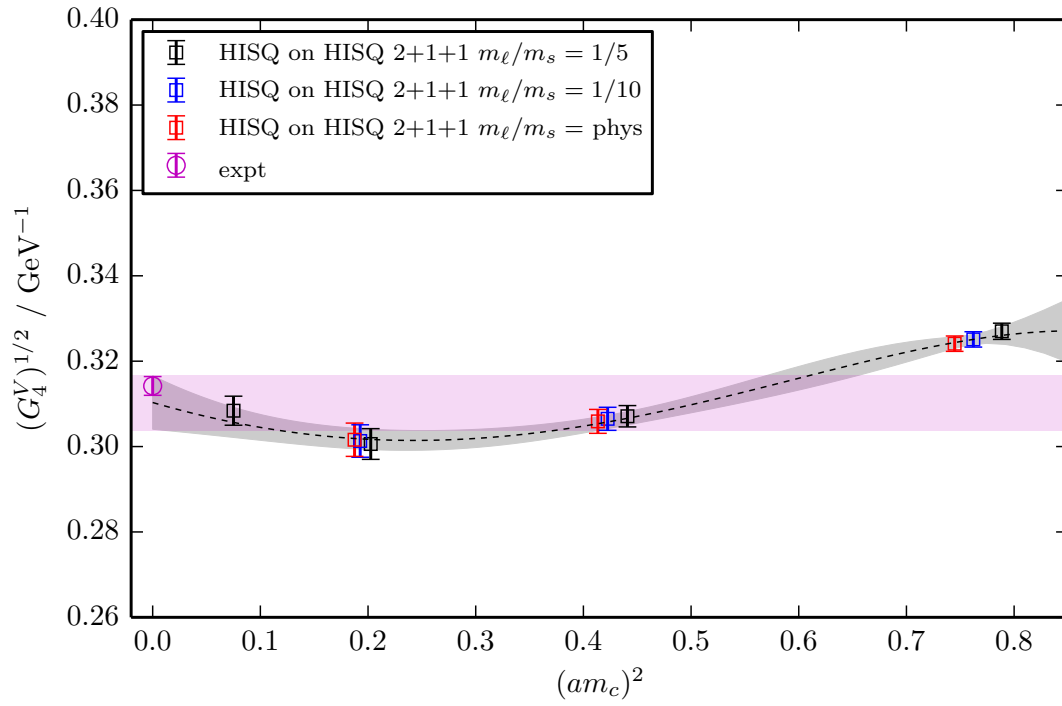
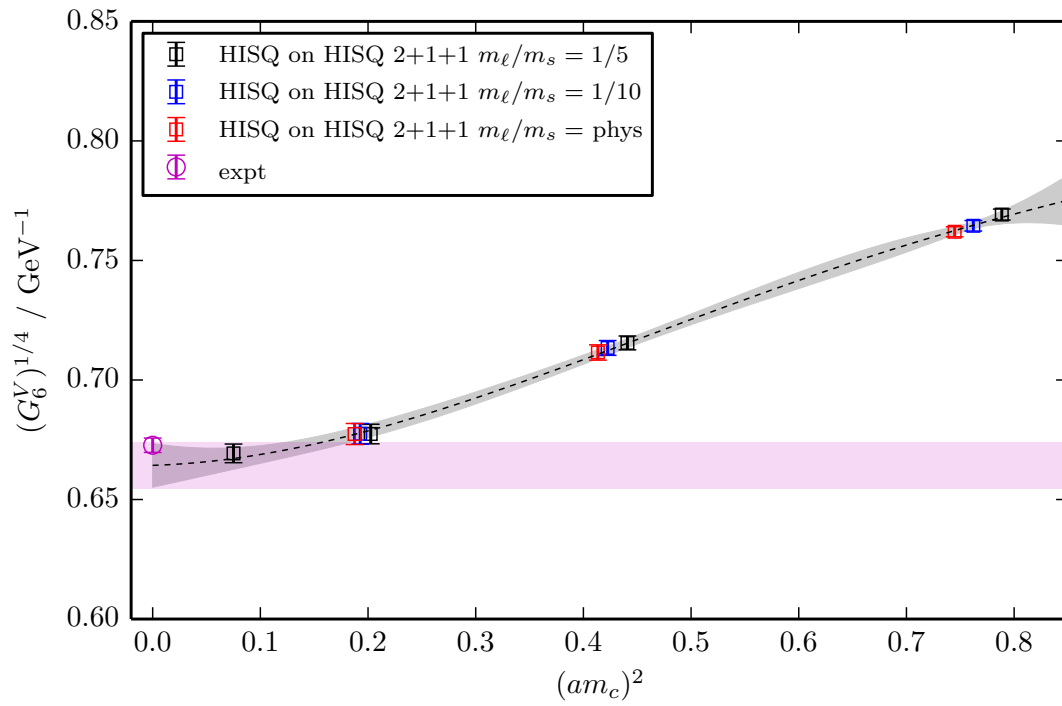
(c) 8<sup>th</sup> moment(d) 10<sup>th</sup> moment

Figure 5.11: Moments of the charmonium vector correlator, as in Figure 5.10, but renormalised using  $Z_4$ , the renormalisation factor obtained from the 4<sup>th</sup> vector moment.

(a) 4<sup>th</sup> moment(b) 6<sup>th</sup> moment

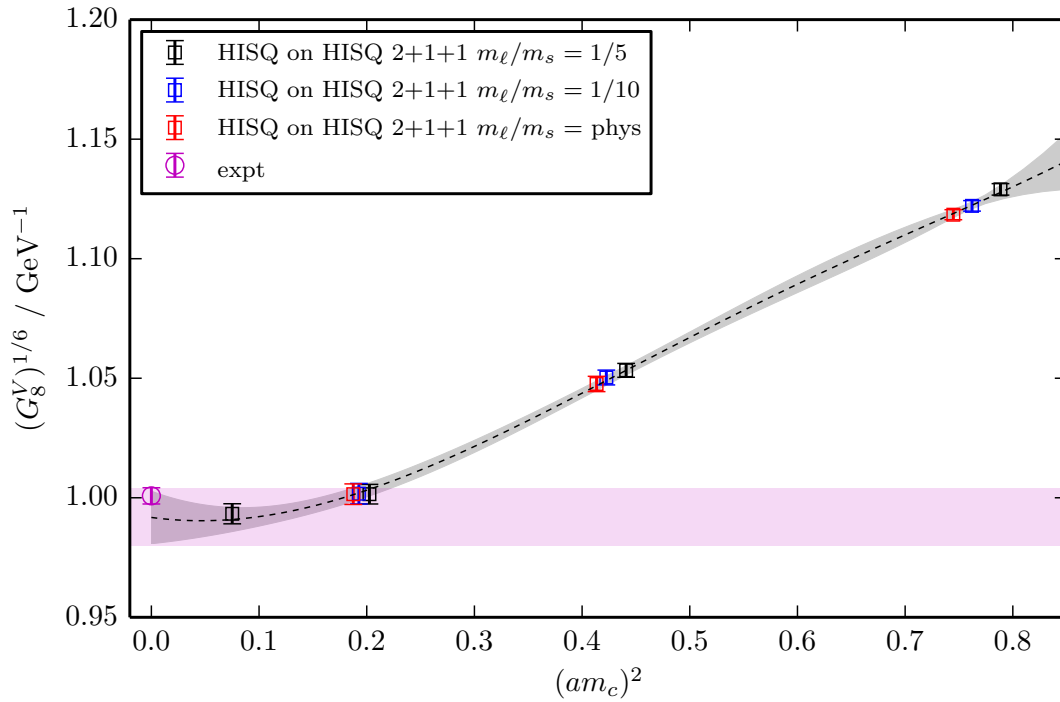
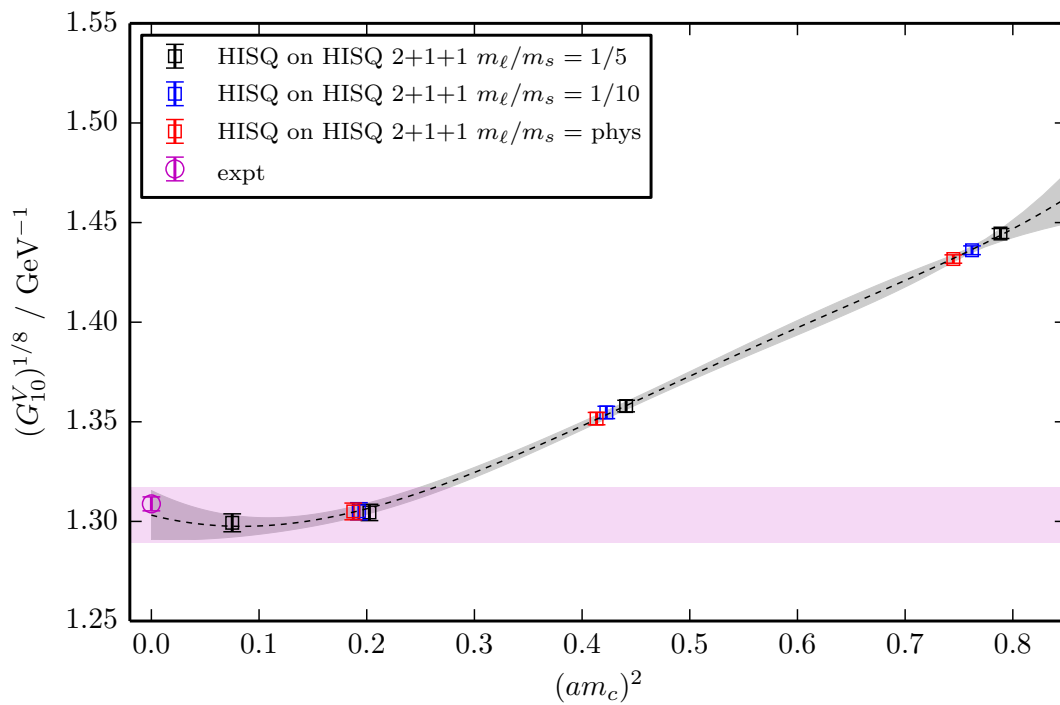
(c) 8<sup>th</sup> moment(d) 10<sup>th</sup> moment

Figure 5.12: Moments of the charmonium vector correlator, as in Figure 5.10, but renormalised using  $Z_6$ , the renormalisation factor obtained from the 6<sup>th</sup> vector moment.

Both sets of reasoning are valid, since the differences between different  $Z_n$  values on the same ensemble are simply a discretisation effect, and so we should obtain the same continuum value no matter which  $Z$  we choose. Indeed we can verify this by comparing Figures 5.10, 5.11 and 5.12. The continuum fits shown in the latter two figures give results for the 4<sup>th</sup> moment of  $0.3080(60) \text{ GeV}^{-1}$  and  $0.3103(63) \text{ GeV}^{-1}$  when using  $Z_4$  and  $Z_6$  respectively — both in agreement with our result using  $Z_8$ , but with smaller errors, and both still in agreement with the experimental point.

The second reason for this difference is that the work in [56] includes a correctly-tuned calculation on the ultrafine 2+1-flavour ensemble. Being closer to the continuum limit, the inclusion of an ultrafine data point will clearly improve the accuracy of the continuum fits. We have omitted our ultrafine results from the fits we perform, since our value for the charm quark mass there is not well-tuned, and the vector moments that we calculate have an explicit dependence on this quantity: as per equation 4.18, the  $n^{\text{th}}$  vector moment varies as  $1/(am_c)^{n-2}$ .

Our 4<sup>th</sup> moment therefore has the lowest-order  $am_c$  dependence, and so it is worthwhile to include our mistuned ultrafine value in a new continuum fit to this quantity, to test how our error estimate then fares. Figure 5.13 shows just this, using data renormalised with  $Z_4$  as a direct comparison to the result from [56] — this result is also plotted in the figure, as the grey point at zero lattice spacing.

The result of this revised continuum fit, performed with the same fit function and priors as the other moments in this chapter, is  $0.3161(44) \text{ GeV}^{-1}$ , in agreement with each of the previous determinations discussed here, as well as the experimentally-derived value. Crucially, though, the statistical error on this estimate is commensurate with that on the previous lattice value of  $0.3152(41) \text{ GeV}^{-1}$ , indicating that our understanding of the errors outlined here seems to be correct.

It is important to note once again that there is still a small  $am_c$  dependence present in the 4<sup>th</sup> moment, and that the higher moments have an even greater  $am_c$  dependence, which is why we have not simply included the ultrafine result in the previous fits. A further calculation at the correctly-tuned charm mass on the ultrafine ensemble would, however, clearly help reduce the error estimates on our continuum extrapolations.

## 5.4 Decay Constants

We turn now to the examination of decay constants for some of the mesons we have been studying. Values calculated for these decay constants (or their ratios) on each lattice ensemble are given in Table 5.9, and we will look more closely at each of them in turn.

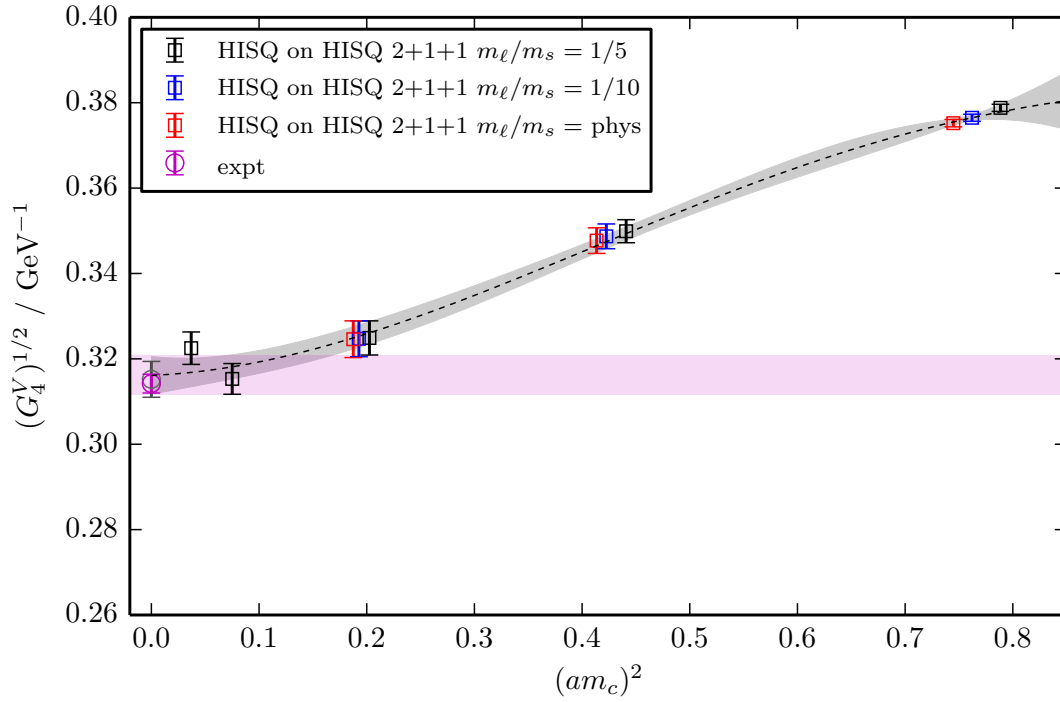


Figure 5.13: The 4<sup>th</sup> moment of the charmonium vector correlator, as determined on a range of ensembles including the ultrafine, and renormalised with  $Z_4$ , plotted on the same scale as Figure 5.10a. The groups of points from right to left indicate results on the very coarse, coarse, fine, superfine and ultrafine ensembles respectively. The grey band indicates the fitted curve at the physical light sea quark mass, and the magenta band shows our final result in the continuum limit. The magenta point is that derived from experimental results, and the grey point at zero lattice spacing is the continuum result from [56].

Label	$m_\ell/m_s$	$af_{\eta_c(1S)}$	$af_{J/\psi(1S)}/Z$	$f_{\eta_c(1S)}/f_{\eta_c(2S)}$	$f_{J/\psi(1S)}/f_{\psi(2S)}$
very coarse	1/5	0.37659(18)	0.4306(16)	—	—
	1/10	0.37025(10)	0.42333(55)	—	—
	phys.	0.366119(59)	0.41674(67)	—	—
coarse	1/5	0.268373(56)	0.29392(13)	1.321(25)	1.014(45)
	1/10	0.263766(39)	0.28827(10)	1.402(22)	1.100(67)
	phys.	0.261678(22)	0.285683(64)	1.411(14)	1.050(43)
fine	1/5	0.18192(15)	0.19389(52)	—	—
	1/10	0.179370(23)	0.191176(58)	1.610(50)	1.31(16)
	phys.	0.178039(21)	0.189732(42)	1.627(55)	1.286(92)
superfine	1/5	0.117528(30)	0.123405(69)	1.617(82)	1.25(20)
ultrafine	1/5	0.086804(54)	0.090232(89)	1.49(13)	1.116(43)

Table 5.9: Results for selected decay constants (or their ratios) in the charmonium system, as determined on each of the ensembles listed in Table 5.1. The ground-state pseudoscalar decay constant  $f_{\eta_c(1S)}$  is absolutely normalised, so we quote a value for it here in lattice units. The decay constants of the vector mesons  $J/\psi(1S)$  and  $\psi(2S)$  require a renormalisation factor to be matched to continuum results (indeed, we quote the ground-state vector decay constant  $f_{J/\psi(1S)}/Z$  before this renormalisation is performed) but this is the same for both mesons on each ensemble, so we can take their ratio to cancel it out. We also determine the ratio of the decay constants of the  $\eta_c(1S)$  and  $\eta_c(2S)$  as a cross-check, since this should be of the same order as the equivalent quantity for the vectors.

### 5.4.1 Ratio of Vector Decay Constants

We extract the decay constant  $f_V$  of a vector meson  $V$  from our fitted amplitudes and masses via:

$$\frac{f_V}{Z} = A_V \sqrt{\frac{2}{M_V}} \quad (5.21)$$

with  $Z$  the required renormalisation factor. This must be determined separately if we wish to normalise our results appropriately for comparison to experimental values. However,  $Z$  will be the same for both the  $J/\psi(1S)$  and  $\psi(2S)$  on each ensemble, and so we can take the ratio of their decay constants such that  $Z$  cancels out.

This ratio can then be compared to a value derived from experimental measurements, using the relation given in equation 4.22. Since we are taking a ratio, the relevant portion of this relation for us to consider is  $f_V \propto (\Gamma_{l,V} M_V)^{1/2}$ , where  $\Gamma_{l,V}$  is the total leptonic width of meson  $V$ . In using the current experimental averages from [4], we find that the value we wish to compare to is  $f_{J/\psi(1S)}/f_{\psi(2S)} = 1.406(32)$ . This is plotted in Figure 5.14 along with each of the points determined on the lattice.

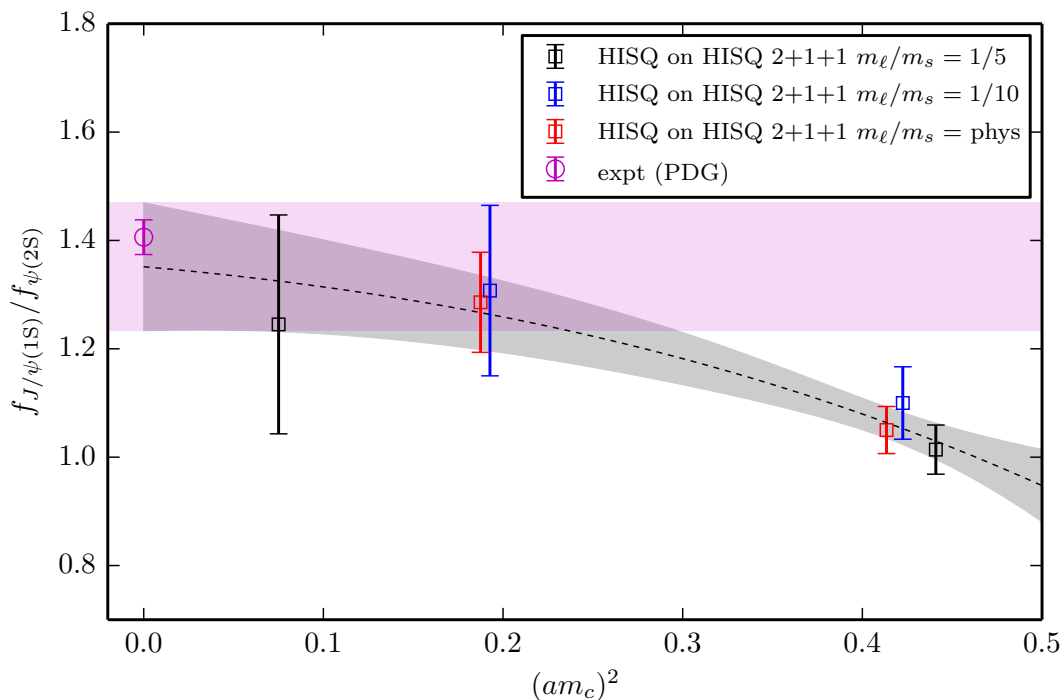


Figure 5.14: The ratio of the decay constants of the vector mesons  $J/\psi(1S)$  and  $\psi(2S)$ , as determined on a range of ensembles. The groups of points from right to left indicate results on the coarse, fine and superfine ensembles respectively. The grey band indicates the fitted curve at the physical light sea quark mass, and the magenta band shows our final result in the continuum limit. The magenta point at zero lattice spacing is derived from experimental results [4] as described in the text.

We perform this fit to the functional form in equation 5.9 — the same as we use for the hyperfine splitting — since we have a large lattice spacing dependence evident in the plot<sup>5</sup>, and so take discretisation errors to be dependent on  $(am_c)^2$ . Priors are also kept the same as in the hyperfine splitting fit, apart from that on the physical value  $p$ , which we take as  $(1.4 \pm 1.4)$ .

The resulting fit is very good, with a  $\chi^2$  value per degree of freedom of 0.27 and a  $Q$ -value of 0.95. This fit is shown as the grey band in Figure 5.14, and gives a continuum result of

$$f_{J/\psi(1S)}/f_{\psi(2S)} = 1.351(118) \quad (5.22)$$

with a purely statistical error. It is not necessary to add a systematic error derived from the uncertainty on  $w_0$ , since this ratio is a dimensionless quantity and we do not therefore fix the lattice spacing in computing it. The continuum result plotted as the magenta band in Figure 5.14 is therefore equal in width to the grey band at zero lattice spacing.

The final result is consistent with our value derived from experiment, although its accuracy could be improved by reducing the error on the (seemingly rather low) result on the superfine ensemble. This will again be discussed in more detail in section 5.5.

## 5.4.2 Ratio of Pseudoscalar Decay Constants

As a cross-check on the vector ratio, we also determine the ratio of the decay constants of the pseudoscalar mesons  $\eta_c(1S)$  and  $\eta_c(2S)$ . We have noted previously that the pseudoscalar decay constant is absolutely normalised when using the HISQ action, and so no renormalisation is required here. Unlike in the vector case, there is no corresponding experimental quantity for comparison, and so this calculation is purely a check that we obtain a result of the same order as that for the vectors.

The decay constant  $f_P$  of a pseudoscalar meson is extracted from our fitted amplitudes and masses via:

$$f_P = 2m_c A_P \sqrt{\frac{2}{M_P^3}} \quad (5.23)$$

with  $m_c$  the charm quark mass. We then simply take the required ratio of quantities in lattice units, since a conversion to physical units would cancel out in any case. Ratios as listed in Table 5.9 are plotted in Figure 5.15.

For a robust comparison, we perform a continuum fit using identical priors to the same fit function as in the vector case, including the prior on the physical value

---

<sup>5</sup>Like the hyperfine splitting, decay constants are short-distance quantities, so one would generally expect sizeable discretisation errors set by  $am_c$ . Of course it is not clear that this is necessarily true for a ratio of decay constants, but it does indeed seem to be the case here for the vectors, and later for the equivalent ratio of pseudoscalar decay constants also.

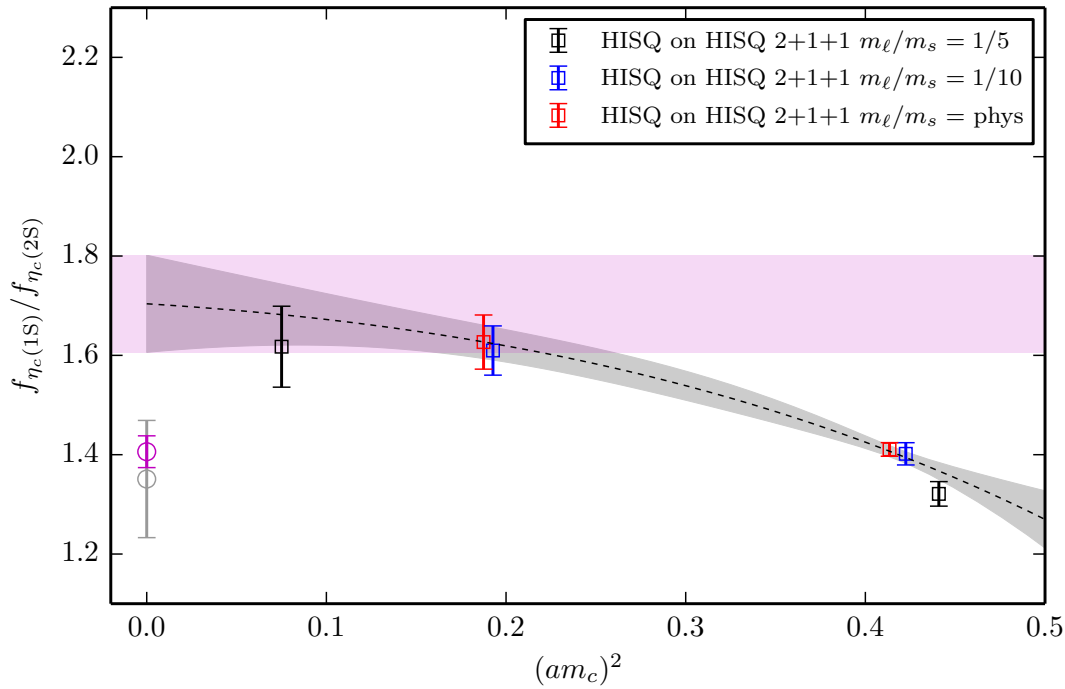


Figure 5.15: The ratio of the decay constants of the pseudoscalar mesons  $\eta_c(1S)$  and  $\eta_c(2S)$ , as determined on a range of ensembles. The groups of points from right to left indicate results on the coarse, fine and superfine ensembles respectively. The grey band indicates the fitted curve at the physical light sea quark mass, and the magenta band shows our final result in the continuum limit. The magenta point at zero lattice spacing is the equivalent ratio of vector decay constants derived from experimental results [4], and the overlapping grey point is our fitted result to the vector ratio from Figure 5.14.

$p$  of  $(1.4 \pm 1.4)$ . The resulting fit is very good, with a  $\chi^2$  value of 0.37 and a  $Q$ -value of 0.9, and is plotted as the grey band in Figure 5.15. This gives a continuum result for the ratio of 1.704(98), which is indeed of the same order as the vector ratio. The experimental vector ratio and our continuum determination of it are also plotted in Figure 5.15 for comparison.

### 5.4.3 $\eta_c$ Decay Constant

The decay constant of the  $\eta_c(1S)$  can be calculated using equation 5.23 in the previous section, and charmonium pseudoscalar correlators are absolutely normalised when using the HISQ action, so no  $Z$ -factor is required here. Unfortunately the  $\eta_c(1S)$  decay constant does not directly correspond to any observable experimental quantity, and so we can only use it to show consistency with other lattice calculations. Here we will compare it to the HPQCD collaboration's previous determination on 2+1-flavour lattices, detailed in [45], of  $f_{\eta_c(1S)} = 394.7(2.4)$  MeV.

The  $\eta_c(1S)$  decay constants listed in Table 5.9 have been calculated from the relevant amplitudes and masses in Tables 5.3 and 5.2, and are plotted in Figure 5.16 after conversion to physical units, along with the fit at the physical light sea quark mass. The fit function and priors are identical to those used for the hyperfine splitting, apart from the continuum value  $p$ , on which we take a prior of  $400 \pm 200$  MeV.

It is clear from Figure 5.16 that there are significant discretisation effects in this quantity, but we are able to take them into account and obtain a very accurate fit thanks to the relevant terms in the fit function: here we have a  $\chi^2$  value per degree of freedom of 0.25 and a  $Q$ -value of 0.99. This gives a continuum result for the  $\eta_c$  decay constant of

$$f_{\eta_c(1S)} = 396.3(2.3) \text{ MeV} \quad (5.24)$$

with a purely statistical error. Adding a systematic error of  $\pm 2.0$  MeV, obtained by applying the relative error of 0.5% on the physical value of  $w_0$ , we have an overall result of

$$f_{\eta_c(1S)} = 396.3(3.0) \text{ MeV} \quad (5.25)$$

with combined errors for ease of comparison. This is in excellent agreement with the HPQCD collaboration's previous value on 2+1-flavour lattices as shown in Figure 5.16, and is also of very similar accuracy ( $< 0.8\%$ ).

### 5.4.4 $J/\psi$ Decay Constant

The decay constant of the  $J/\psi(1S)$  can be calculated using equation 5.21 as we stated for the ratio of vector decay constants, but here we note that we also require

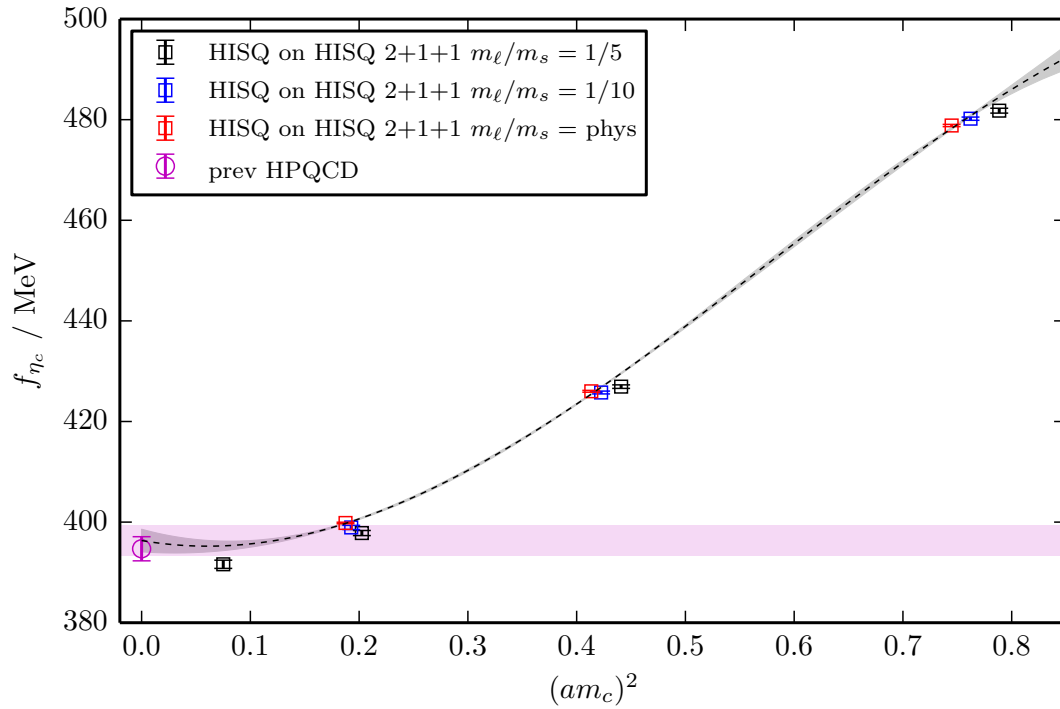


Figure 5.16: The decay constant of the ground-state charmonium pseudoscalar meson  $\eta_c(1S)$ , as determined on a range of ensembles. The groups of points from right to left indicate results on the very coarse, coarse, fine and superfine ensembles respectively. The grey band indicates the fitted curve at the physical light sea quark mass, and the magenta band shows our final result in the continuum limit. This is in very good agreement with the continuum result obtained by the HPQCD collaboration in [45] using HISQ valence quarks on the asqtad configurations, shown as the magenta point at zero lattice spacing.

a renormalisation factor  $Z$ . We have, in fact, calculated these in section 5.3 above, and just as for the moments, we use the  $Z_8$  values from Table 5.7 to renormalise the decay constant.

We convert the  $J/\psi(1S)$  decay constants in Table 5.9 to physical units by multiplying by the inverse lattice spacing, and then renormalise them by multiplying by  $Z_8$ . These physical results are plotted in Figure 5.17, along with a continuum fit to the same fit function and priors as those used for the  $\eta_c(1S)$  decay constant. This is also a short-distance quantity, with discretisation effects expected to depend on  $am_c$ .

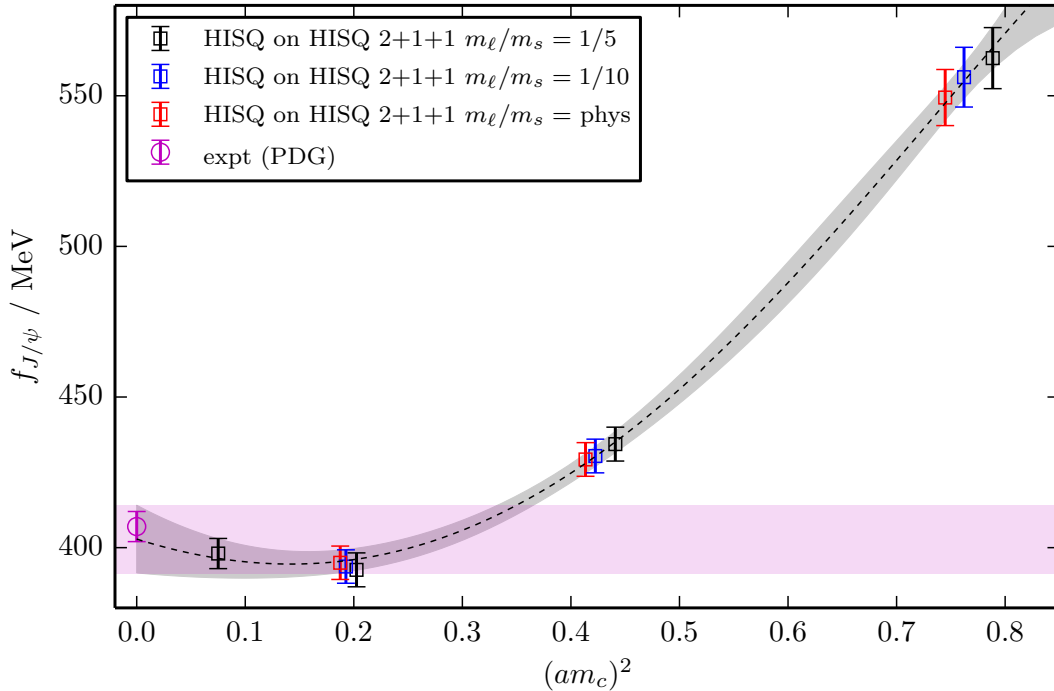


Figure 5.17: The decay constant of the ground-state charmonium vector meson  $J/\psi(1S)$ , as determined on a range of ensembles. The groups of points from right to left indicate results on the very coarse, coarse, fine and superfine ensembles respectively, and the results have been renormalised using  $Z_8$ , determined from the 8<sup>th</sup> moment of the vector correlators. The grey band indicates the fitted curve at the physical light sea quark mass, and the magenta band shows our final result in the continuum limit. This is in good agreement with the experimental result derived from [4], shown as the magenta point at zero lattice spacing.

The fit is very good, with a  $\chi^2$  value per degree of freedom of 0.23 and a  $Q$ -value of 0.99. It yields a continuum result of

$$f_{J/\psi(1S)} = 403(11) \text{ MeV} \quad (5.26)$$

where the error quoted is purely statistical. The systematic error arising from the

physical value of  $w_0$  is  $\pm 2.0$  MeV, which is negligible in comparison to the statistical error, so the above is our final result.

Experimental values are available in [4] for the leptonic width  $\Gamma_l$  of the  $J/\psi(1S)$ , and as noted previously, we can therefore use equation 4.22 to derive an experimental value for the decay constant. This is found to be  $407.0(5.0)$  MeV, in good agreement with our continuum value, and is plotted as the magenta point in Figure 5.17.

## 5.5 Consideration of Superfine Results

We have noted several times in passing now that the results we have obtained on the superfine ensemble are, generally, less accurate than those on the coarser ensembles, particularly in cases involving excited states. This is puzzling, particularly given that we have higher statistics than, for example, on the fine physical ensemble (where 565 configurations were used compared to 1017 on superfine). We therefore investigate the work performed on the superfine ensemble in more detail in this section.

### 5.5.1 Details of Superfine Calculations

Our first superfine run was based on that which we performed to test our heavyonium fits in the previous chapter, although this used a lattice charm mass which was subsequently found to be mistuned. The charm mass was retuned to the correct 0.274, and one smearing added with parameters  $r = 5.25$  and  $n = 45$ , with the reasoning that a larger smearing would be required on the superfine lattice, but that having two smearings would make the calculation too computationally intensive. An initial run with 333 configurations was performed, and this was subsequently extended to 1016 configurations — though as it turns out, this made little difference to the correlator fits.

Selected results from initial analyses of these runs are listed in Table 5.10, and we pay particular attention to the results for the pseudoscalar and vector 2S – 1S splittings. Given that the results for these quantities on coarser lattices were broadly consistent with experimental results, we expect that the superfine results will follow suit, and produce results in lattice units of approximately 0.1968 and 0.1768 in the pseudoscalar and vector cases respectively<sup>6</sup>.

It is clear from the results in the table that in both the pseudoscalar and vector cases, extending the run to 1016 configurations has reduced the statistical error, but neither of these pairs of results are consistent with the experimental values.

---

<sup>6</sup>These rough values are calculated only for comparison purposes, by taking the experimental results from [4] and dividing by the inverse lattice spacing in GeV on the superfine ensemble, derived from  $w_0/a$ .

Calculation	$N_{\text{cfg}}$	Spin	$t_{\text{min}}$	SVD cut	$n_{\text{exp}}$	$\chi^2$	$Q$	$\Delta M_{2\text{S}-1\text{S}}$ (lat. u.)
One smearing	333	ps	10	$1 \times 10^{-4}$	7	0.87	0.94	0.2010(64)
$\gamma_x$ vector		vec	10	$5 \times 10^{-4}$	7	0.94	0.74	0.1950(37)
One smearing	1016	ps	10	$1 \times 10^{-4}$	7	0.83	0.98	0.2042(26)
$\gamma_x$ vector		vec	6	$5 \times 10^{-4}$	7	0.75	1.00	0.1942(30)
Two smearings	1017	ps	10	$1 \times 10^{-4}$	13	0.98	0.62	0.2041(17)
$\gamma_x$ vector		vec	9	$5 \times 10^{-4}$	13	0.84	1.00	0.1908(24)
$\gamma_x \gamma_0$ vector		vec	6	$5 \times 10^{-4}$	13	0.87	0.99	0.1908(17)

Table 5.10: Results of fits to correlators using the EigenBasis fit method, for three different lattice calculations on the superfine ensemble. We denote pseudoscalar results with *ps* and vector results with *vec*. Various input and output parameters of the fits are also listed — in particular, the final column lists the 2S – 1S splitting that is discussed in the text.

However, the smaller errors from the extended run are comparable to the errors obtained on coarser lattices, on the order of 1.4%.

Two further runs were performed to check the effect of certain calculational choices on these results. It was possible that the smearing we chose was not suitable for our purposes, so the calculation was repeated on 1017 configurations, with the two smearings detailed previously in Table 5.1. Correlators produced using these smearings were also plotted to ensure that they were suitable choices, and the plots in Figure 5.3 confirm that they are. Compared to the results in the one-smearing case, statistical errors are again reduced thanks to the extra data from using an extra smearing, but the results for the 2S – 1S splittings remain consistent with those obtained using only the initial single smearing, and inconsistent with the experimental results.

Finally, we perform a third calculation to ensure that this is not an effect related to the taste of our mesons. Our original vector operator was  $\gamma_x \otimes \gamma_x$ , so we repeat the calculation using the  $\gamma_x \gamma_0 \otimes \gamma_x \gamma_0$  operator, thus generating a different taste of vector meson<sup>7</sup>. As is clear from the table, the result obtained is almost identical to that from the original vector, so taste effects are not the cause here. This is, however, clear further evidence of the HISQ action’s very small taste splittings.

<sup>7</sup>Incidentally, this is the calculation which allowed us to extract the parameters of the parity-partner  $\chi_{c1}(1\text{P})$  meson in section 5.1.3.

### 5.5.2 Effects of Different Fit Methods

Satisfied that our smearings are suitable and that what we are observing is not a taste effect, we look now at different fit methods on our highest-statistics set of correlators, that with two smearings on 1017 configurations.

A large number of different fits were performed to this set of data, testing variations in different  $t_{\min}$  and SVD cut values using both traditional and EigenBasis fit methods. The number of exponentials  $n_{\text{exp}}$  used in the fits was also extended out to 13 in many cases, to ensure that fit stability was not an issue. These variations generally produced similar final results, still inconsistent with the experimental values. We keep binning of the correlator data consistent, using a bin size of 4 in each case. Beyond this value, for the fits that we eventually choose, there is no increase in statistical error on the fitted ground state parameters, and we do not vary this so as to prevent it from affecting the other fits. In any case, the binning procedure only affected our error estimates and did not make any significant difference to our central values.

One change to the fit that did seem to affect the result was thinning the correlator data beforehand, meaning that after averaging over time sources, only a subset of the averaged correlator data was fed into the fit. We denote a situation where we keep data from every  $x^{\text{th}}$  lattice  $t$ -value, and discard the rest, by `thin $x$`  in the plots that follow. This procedure helps to eliminate correlations between data at neighbouring lattice times. Thinning should also enable us to use a smaller SVD cut, since eliminating correlations between these data will clearly regulate the eigenvalues of the associated covariance matrix that the SVD cut acts on.

#### Forced Priors

We will shortly discuss results from varying thinned fits in both pseudoscalar and vector cases, but first we examine whether these data are at all compatible with the experimental results. To do so, we force the amplitudes  $A_0$  and  $A_1$  for the vector ground state and first excited state to be close to values which give the correct experimental value for the ratio  $f_{J/\psi(1S)}/f_{\psi(2S)} = 1.406(32)$ , by feeding precise, narrow priors for these quantities into a traditional fit. We repeat the fit with varying, wider priors, and plot the results for the 2S – 1S splitting in Figure 5.18.

It is clear from the plot that in forcing the amplitudes to their physical values, the fit will happily return a value for the 2S – 1S mass splitting close to the experimental value, and with a low error. Widening the priors on the amplitudes blurs this situation, however, increasing the error on the mass splitting and allowing it to deviate from the expected value. We have also checked that this procedure works when reversed: forcing the mass of the  $\psi(2S)$  to its physical value returns ampli-

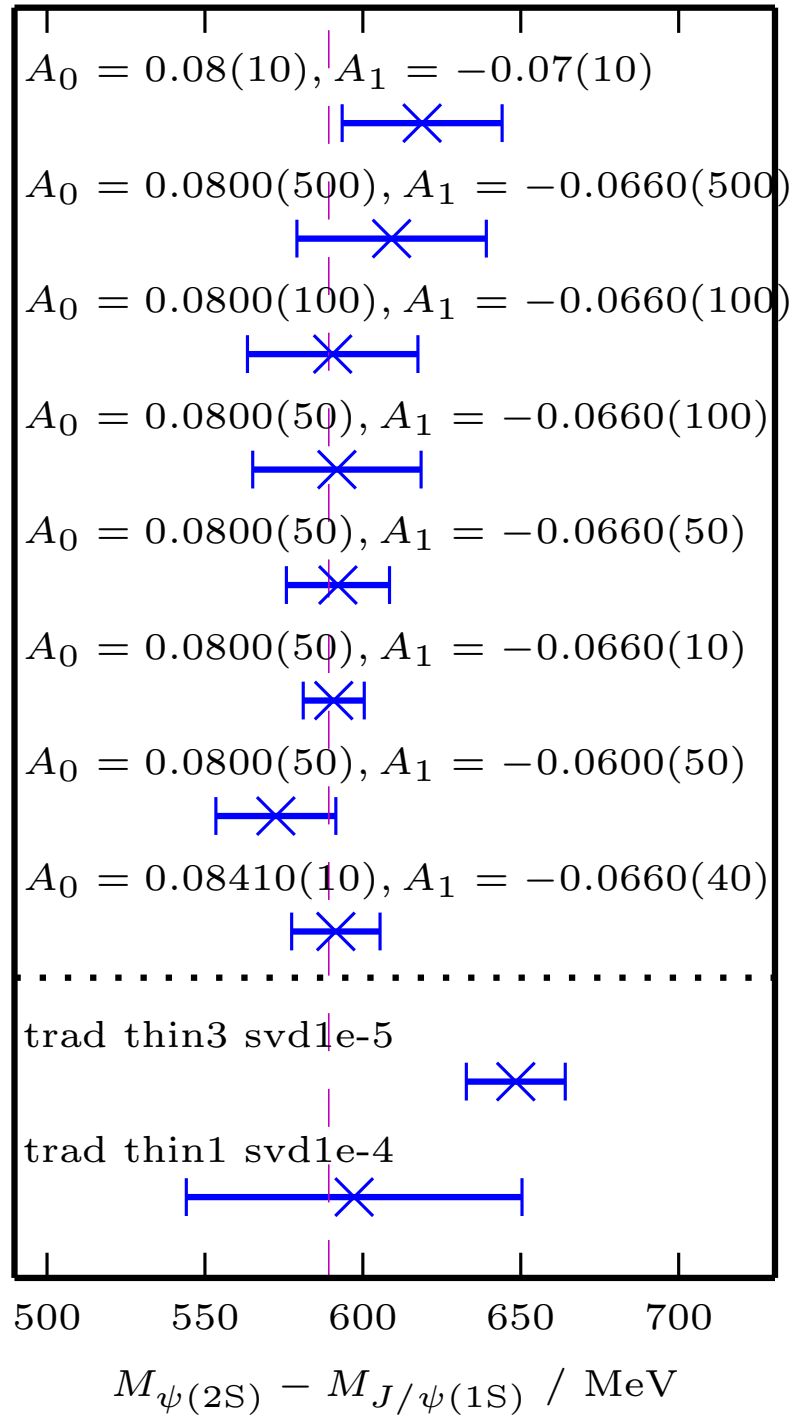


Figure 5.18: Vector channel 2S – 1S mass splitting with varying degrees of forced priors for the associated amplitudes  $A_0$  and  $A_1$ . No thinning of the data is performed on any of the fits above the dotted line. For comparison, the priors used in the bottom two cases are  $A_0 = A_1 = 0.01(1.00)$  and  $A_0 = A_1 = 0.10(20)$ , from the bottom up. As the priors are widened and made less precise, there is a clear drift away from the experimental value [4] (shown as the magenta dotted line) and an accompanying increase in statistical error.

tudes for the ground state and first excited state which are compatible with the experimental value of the ratio of vector decay constants, with a small statistical error, and this too becomes less true as the priors are widened.

We conclude from this that the data are compatible with a result in agreement with experiment, but there are other effects at play here which are suppressed by being very specific about what the fit is permitted to find. We also make a related observation that the vast majority of these fits are compatible with one another — a point that we shall return to momentarily.

### Varying Parameters

It is logical now to compare the results of fits with different parameters, as we have mentioned already. Figure 5.19 shows a comparison of the vector  $2S - 1S$  splitting obtained from three different traditional fits and six different EigenBasis fits, each with varying degrees of thinning, and assorted values used for the SVD cut. It is generally true, as we supposed above, that more extensive thinning of the data allows us to use smaller SVD cuts.

This plot shows that while it is clearly possible to obtain fit results for the vector  $2S - 1S$  splitting that have very small statistical errors, none of the results for which this is true are compatible with the experimental value. Conversely, other results with larger errors do straddle the experimental value, but are also compatible with the more accurate results.

It is possible that contributions from another nearby state are causing higher excitations in the correlator that our fit is not expecting, and it is attempting to take account of these in its determinations of the first excited state. This additional state is unlikely to be a spurious state recognised only by the fit code, since it is not removed by the EigenBasis fits designed to take care of precisely this problem. If contributions from an additional state are truly the problem here, it is a state which is genuinely present in the data.

We have verified that this situation is unique to the superfine ensemble by analysing results for the vector  $2S - 1S$  splitting from a similar set of fits on the coarse and fine ensembles with physical  $m_\ell/m_s$  values in the sea. Separate plots of the results from two different traditional fits and four different EigenBasis fits on the coarse and the fine ensemble are shown in Figures 5.20 and 5.21 respectively. It is clear in both of these cases that the results all have errors of comparable size, while remaining mainly compatible with each other and with the experimental point. On the coarse ensemble, the agreement with experiment is generally not as good, but this is to be expected since discretisation effects will be much more significant on the coarse lattices. Over both ensembles, it seems that using the EigenBasis method produces results which are more closely compatible with the experimental values.

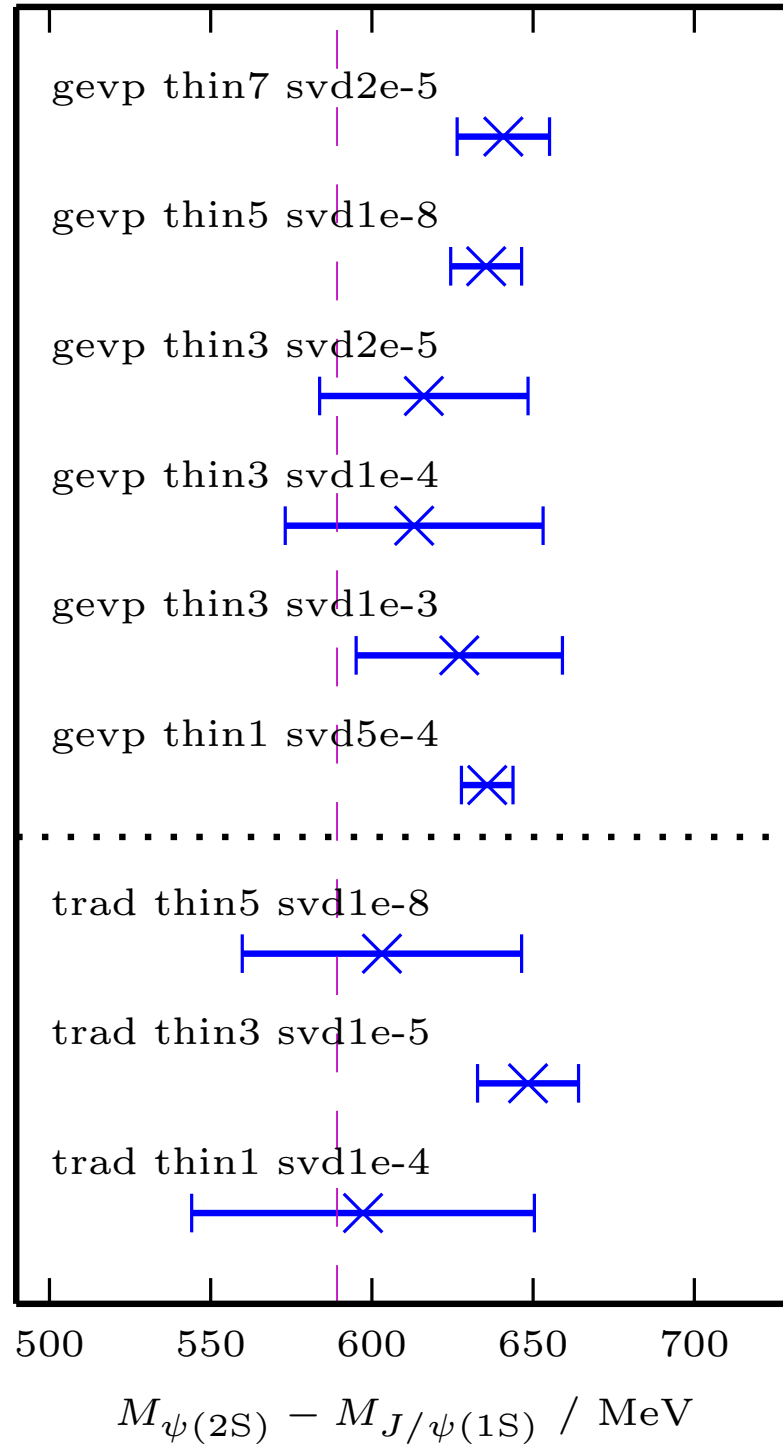


Figure 5.19: The vector channel 2S – 1S splitting from various different traditional (*trad*) and EigenBasis (*gevp*) fits to data from the superfine  $m_\ell/m_s = 1/5$  ensemble. Thinning of the correlator data is denoted by the *thin* parameter, and the applied SVD cut by *svd*. The experimental value [4] is again plotted as the magenta dotted line.

Note that we do not perform such extensive thinning of the data on either of these ensembles: because the lattice spacing is larger and the temporal extent of the lattice is reduced, the same degree of thinning results in fewer data points available to fit to. It could well be true in these cases that thinning to every third data point is too extensive, particularly on the coarse lattice, but we may still make a useful comparison to the superfine results if we bear this in mind.

### Choice of Fits

Without performing a detailed further investigation, it is difficult to conclude exactly what is happening in this situation. To account for the greatest number of possibilities, we conservatively select one of the fits with larger errors to extract results from and use in the continuum fits that we have already detailed in the preceding sections. In the case of the vector fits in Figure 5.19, we use the fit labelled *gevp thin3 svd2e-5*, a thinned EigenBasis fit.

A similar analysis is performed on the pseudoscalar 2S – 1S splitting, as plotted in Figure 5.22, and we find that a similar picture emerges, although these results exhibit a smaller spread, and smaller errors in general. Here we select the fit labelled *gevp thin4 svd1e-8*, a thinned EigenBasis fit. This is a more arbitrary choice than in the vector case, since we have a greater number of suitable fits to choose from here; however, we constrain ourselves to choosing between only the EigenBasis fits so as to maintain consistency with our vector fit selection.

In both the pseudoscalar and vector cases, choosing fits which utilise a small SVD cut allows us to be sure that statistical correlations are small, and that effects due to this are not significant in our final results.

The results from our chosen superfine fits are those quoted in Tables 5.2, 5.3, 5.4 and 5.9. In other words, for the sake of consistency we do not optimise individually for each of the quantities that we are determining, and instead use, for example, the  $\Delta M_{1P-1S}$  value obtained from the selected fits. This has a significant effect on our extrapolations of several quantities, since the 2S state amplitudes calculated on the superfine ensemble have order-of-magnitude larger errors than on the other ensembles, as do the corresponding 2S state energies.

### 5.5.3 Possible Causes

We appear to be observing an unusual effect in correlators on the superfine lattices that is not present (or at least not as pronounced) on coarser ensembles. Fits to these correlators can be forced to produce accurate results which agree with experimental averages, but they are also capable of producing accurate results which are not consistent with experiment. This leads us to use fits which return results with

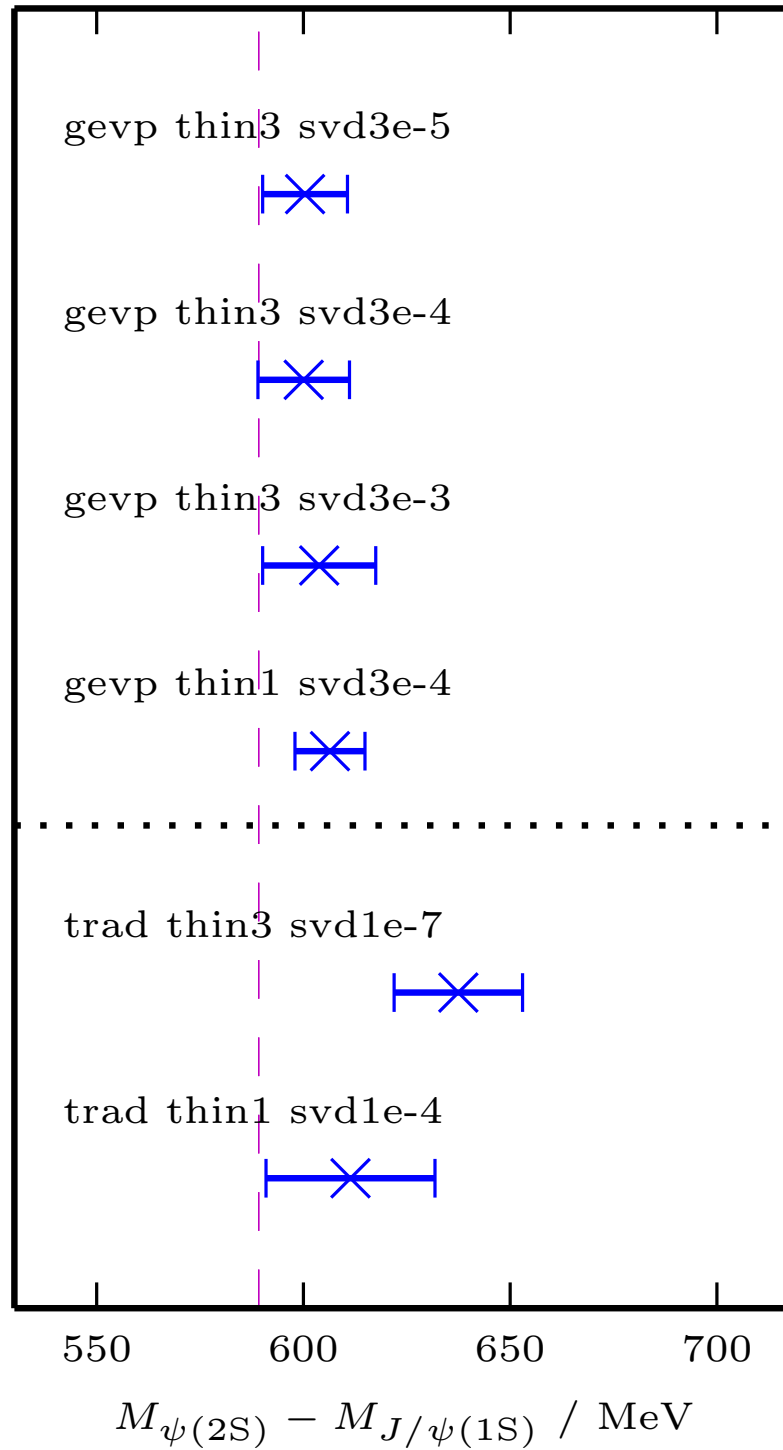


Figure 5.20: The vector channel 2S–1S splitting from different traditional (*trad*) and EigenBasis (*gevp*) fits to data from the coarse  $m_\ell/m_s = \text{phys}$  ensemble. Thinning of the correlator data is denoted by the *thin* parameter, and the applied SVD cut by *svd*. The experimental value [4] is again plotted as the magenta dotted line. This does not display the same erratic behaviour as the corresponding data from the superfine ensemble, displayed in Figure 5.19. We also note here that we do not necessarily expect agreement with the experimental result due to larger discretisation effects on the coarse lattices, and indeed this seems to be the case.

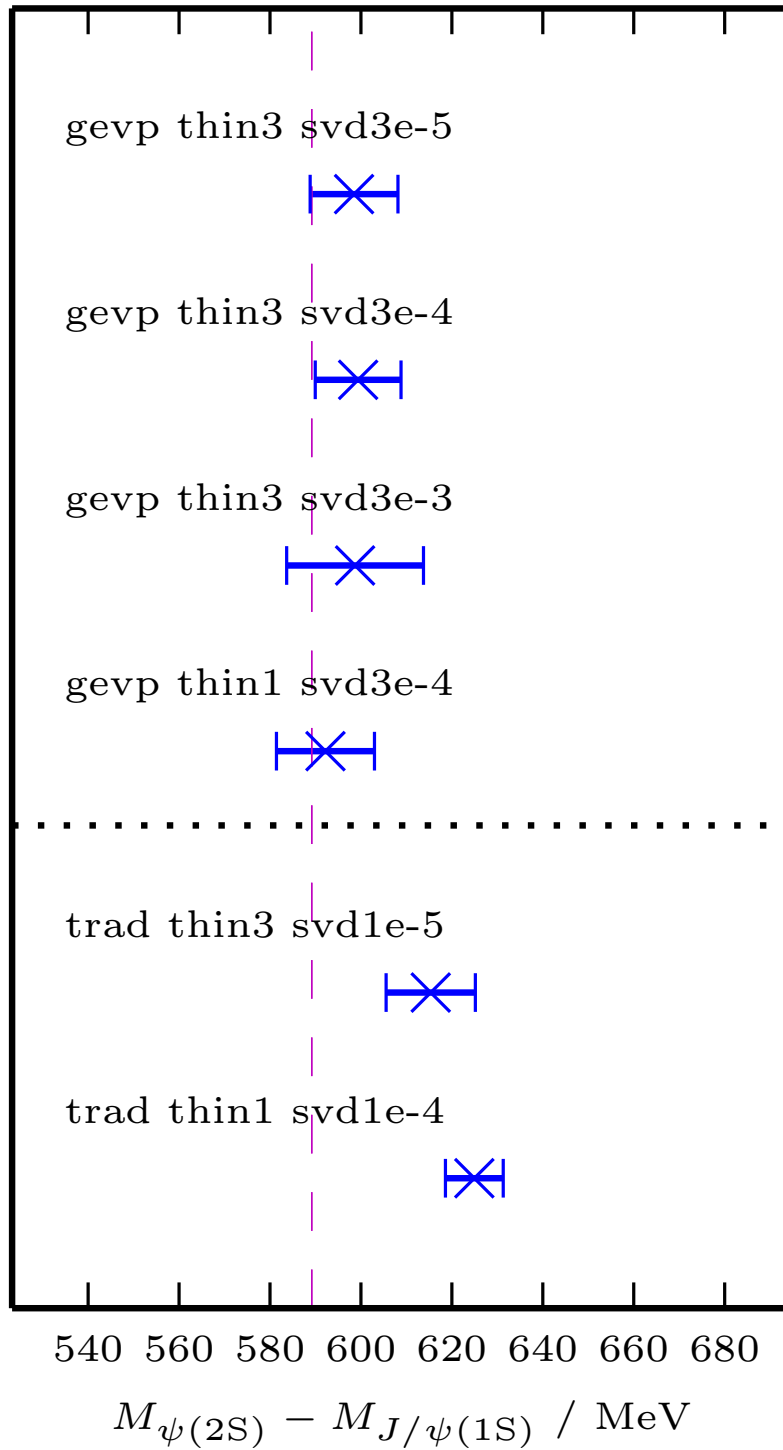


Figure 5.21: The vector channel  $2S - 1S$  splitting from different traditional (*trad*) and EigenBasis (*gevp*) fits to data from the fine  $m_\ell/m_s = \text{phys}$  ensemble. Thinning of the correlator data is denoted by the *thin* parameter, and the applied SVD cut by *svd*. The experimental value [4] is again plotted as the magenta dotted line. This does not display the same erratic behaviour as the corresponding data from the superfine ensemble, displayed in Figure 5.19.

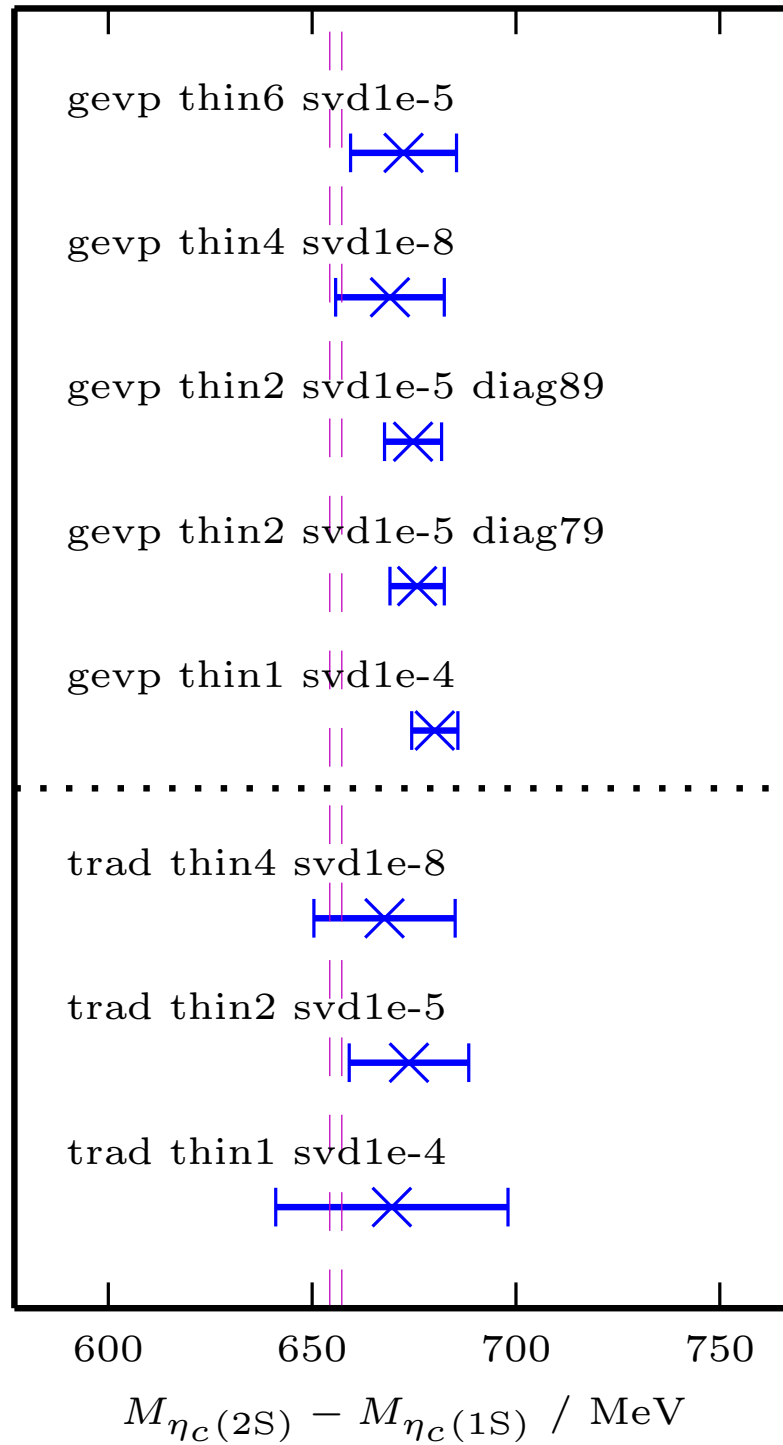


Figure 5.22: The pseudoscalar channel 2S – 1S splitting from various different traditional (*trad*) and EigenBasis (*gevp*) fits to data from the superfine  $m_\ell/m_s = 1/5$  ensemble. Thinning of the correlator data is denoted by the *thin* parameter, and the applied SVD cut by *svd*. The parameter *diag* here represents the pair of  $t$ -values used to diagonalise the matrix of correlators, and as expected for the EigenBasis method [64], this choice has almost no effect on the result. The magenta dotted lines again represent the range of the experimental determination in [4].

significant statistical errors, since we are unable to precisely determine the cause of these effects.

In a sense, we have explicitly chosen to increase the error on our superfine fit results to more accurately reflect the range of values they return for the 2S states. It is not the case that our correlator data is somehow less accurate than those on coarser lattices, as evidenced by our calculations of the time moments of the vector correlators, which do not display evidence of any anomalies in their superfine results. This is, reassuringly, what we would expect, and thankfully, the inclusion of the superfine results in continuum extrapolations does improve the statistical error on the fits.

How are we to explain this behaviour though? It is possible that an additional state (which may or may not be physical) is interfering with the lattice results by contributing to the correlators, and thus ‘stealing’ some amplitude from the states that we expect to see in the fits. This would account for the large errors on, and the relative weakness of, the 2S state amplitudes in Table 5.3, owing to the fact that the fit cannot accurately allocate the different contributions it is examining. It could also be the reason that the vector correlator data are compatible with a relatively wide range of values for the second excited state mass, as seen in Figures 5.18 and 5.19.

We have already seen, at the beginning of this chapter, that the Fermilab/MILC collaborations find a continuum result for the spin-averaged 2S – 1S splitting that is much higher than the experimental value [84]. Our results are not compatible with this prediction in the continuum limit, but qualitatively, we do also observe a 2S – 1S splitting higher than the experimental value, albeit only on the superfine ensemble.

The discussion in [84] speculates that since the 2S states are close to the  $D\bar{D}$  threshold, as illustrated in Figures 5.1 and 5.2, an accurate determination of these states may require the inclusion of effects from open charm decays. This does not seem to be the case for our results, since we obtain an accurate continuum extrapolation which agrees with experiment. However, it is possible that there are open charm effects that manifest themselves in our calculation only for finer lattices like the superfine. One plausible explanation for this is that, when using staggered quarks, there are 16 different taste  $D\bar{D}$  thresholds. On coarser lattices, taste splittings are larger, so some of these taste thresholds will have significantly higher masses than the others, and therefore less impact on any results. On very fine lattices such as the superfine, each taste will be of roughly the same mass, and therefore the effect will be enhanced.

However, of the states we are considering, only the  $\psi(2S)$  can decay to  $D\bar{D}$ , so it is unlikely that this threshold would have any effect on our calculation of

the  $\eta_c(2S)$  mass. We have observed similar effects in both the  $\eta_c(2S)$  and  $\psi(2S)$  cases, suggesting that  $D\bar{D}$  effects are, at best, only a partial explanation for this discrepancy. Additionally, lattice results including  $D\bar{D}$  operators have recently been published in [85], and these do not indicate any dependence of the  $\psi(2S)$  mass — within uncertainties — on the inclusion of these operators.

There is some evidence that this problem appears in other formalisms too. An extensive calculation of charmonium excited states in [86], using twisted-mass fermions, also obtains continuum results for 2S masses which are too high to be in agreement with the experimental average [4]. Discussion in [86] suggests that this could be due to the plateau ranges chosen when fitting the correlators being too short to reliably extract excited states. The systematic uncertainties introduced by the choice of plateau range are investigated in more detail in an extended and improved analysis in [87], which seems to resolve the issues with the  $\psi(2S)$  mass, but produces similar results for the  $\eta_c(2S)$ . This could indicate that this problem is a lattice effect, observed across multiple different fermion actions.

A potentially fruitful avenue of investigation in our case would be a more complete calculation on the ultrafine ensemble. Should it be the case that our fits are being thrown off by the contributions of a state which is, for some reason, only being (at least partially) resolved at small lattice spacings, this should also be true on the ultrafine configurations. The fact that our superfine and ultrafine fits are the only ones in Tables 5.2 and 5.3 where the EigenBasis method does not yield a significantly better fit than the traditional fit method would seem to support this hypothesis: the EigenBasis method works by attempting to align the matrix of correlators with the states that can be resolved from it, so any state for which is difficult to allocate a clear position in the hierarchy will naturally make things more tricky for the EigenBasis fit.

Indeed, the original reason that we undertook our ultrafine calculation was to determine whether we observed similar effects to those we have just discussed on the superfine ensemble. However, the lattice charm mass used in our preliminary ultrafine studies was mistuned, and we deliberately ran on a relatively small number of configurations, with just a single smearing, as a test. A full high-statistics run on the ultrafine ensemble, with a correctly-tuned charm mass, would be computationally expensive, but would almost definitely be able to shed further light on this problem. For now, the fundamental reasons behind it remain unclear.

# Chapter 6

## Conclusions and Comparisons

We have successfully used the HISQ action to accurately simulate heavy valence quarks on multiple sets of gauge configurations with various different lattice spacings. By analysing the correlator data produced through these simulations, and fitting them to particular functional forms, we have calculated a number of different properties of both bottomonium and charmonium. We will now discuss individual results for each of these mesons in turn.

### 6.1 Bottomonium

By calculating two-point correlators for HISQ valence quarks at masses intermediate to the charm quark and bottom quark, on the MILC asqtad gauge configurations, we have been able to successfully extrapolate to, and extract a number of results at, the physical bottomonium mass. It is clear that this extrapolation has introduced some additional uncertainty in our physical results (compared, say, to the equivalent results for charmonium) but this has, in most cases, been well controlled.

#### 6.1.1 Hyperfine Splitting

The result we have obtained for the bottomonium hyperfine splitting is the one which has the most straightforward experimental comparison. In chapter 4, we calculated a value of  $52.9(4.0)$  MeV, and noted that this was more than  $2\sigma$  away from the current experimental world average of  $62.3(3.2)$  MeV [4].

In Figure 6.1, we compare both of these results to a number of others. It is immediately clear, as we claimed in chapter 4, that our calculated value favours the most recent (and most accurate) experimental result included in the world average — that of the Belle Collaboration in 2012 [76], of  $57.9(2.3)$  MeV, which is plotted in blue in the figure.

Our result is also compatible with three other values computed on the lattice,

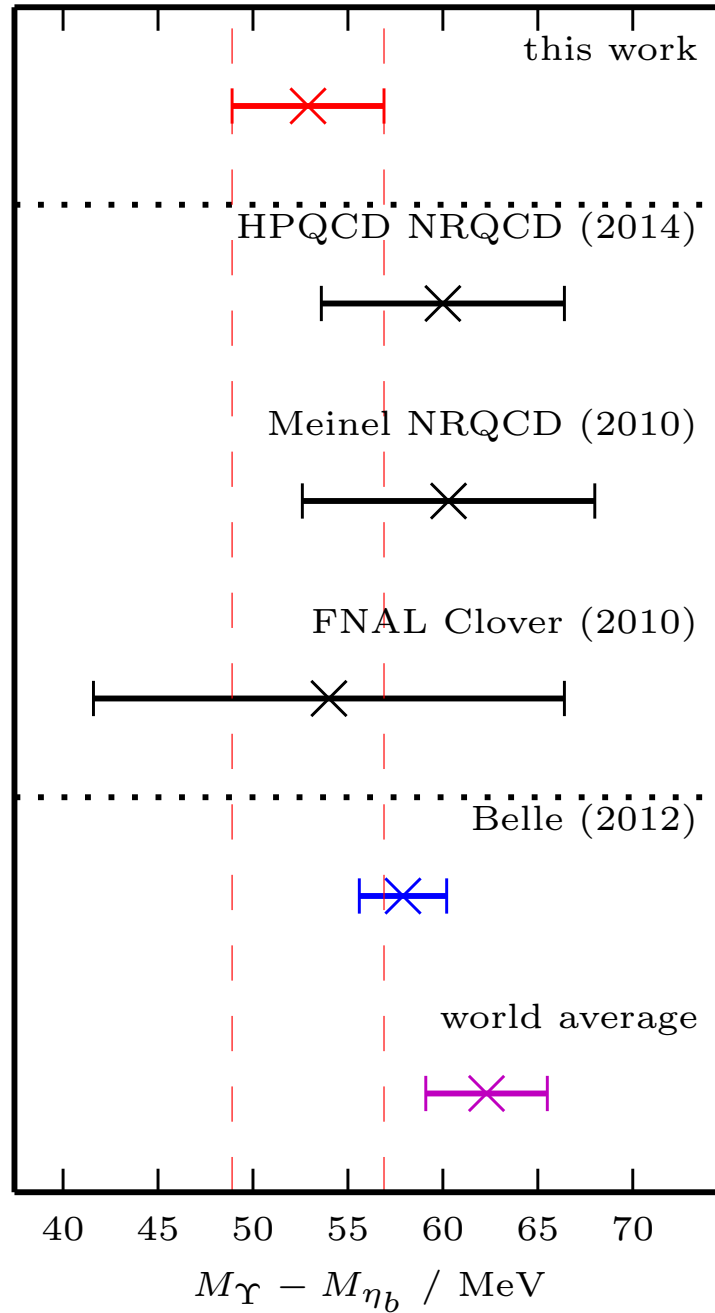


Figure 6.1: A comparison of our continuum-extrapolated result for the bottomonium hyperfine splitting, in red, with two values from experiment, and another three lattice results. In magenta is the world average result from [4], and in blue, the result from the Belle Collaboration [76]. In black are the Fermilab Lattice and MILC Collaborations' Clover result [88], Stefan Meinel's NRQCD result [89], and the HPQCD Collaboration's NRQCD result [73], which each agree well with our value. Although our determination is not incompatible with the experimental average, it clearly favours the recent Belle result.

plotted in black in the figure. The first of these is the Fermilab Lattice and MILC Collaborations' result of  $54.0(12.4)$  MeV from 2010 [88], which utilises the Clover action for valence  $b$  quarks on the same three-flavour MILC configurations that we employ in our calculation. The second is the HPQCD Collaboration's result from 2014 of  $60.0(6.4)$  MeV [73], which used improved NRQCD to simulate the valence  $b$  quarks on the four-flavour MILC gluon field configurations. These improvements included  $\alpha_s$  corrections to the leading spin-magnetic coupling term in the NRQCD action (which is the term that gives rise to the hyperfine splitting). Finally, we include the result of  $60.3(7.7)$  MeV from an NRQCD analysis performed by Stefan Meinel, on gauge configurations generated using the Iwasaki action for the gluons and a domain-wall action for the sea quarks [89].

In addition, a very recent perturbative analysis based on a non-relativistic constituent quark model [90] obtains a result for the bottomonium hyperfine splitting of 47 MeV. Although no estimate of uncertainty is quoted on this figure, it is significantly lower than the experimental average. This solidifies the point that there are still tensions to be resolved in making an accurate determination of this quantity, whether via perturbative or non-perturbative methods, and we therefore contribute our result for consideration in this effort in the future.

The lattice results presented here have errors which have steadily improved over time, and will always benefit from further improvement in this regard. Nevertheless, the good agreement between the lattice results, combined with our result's agreement with the most recent experimental result from Belle, suggest that more sophisticated experimental determinations of bottomonium physics would also be greatly beneficial in resolving this situation.

### 6.1.2 Decay Constants

In chapter 4 we made two determinations of the decay constant of the  $\Upsilon(1S)$ : one using a local vector current, and one using a one-link vector current. These were, respectively,  $616(39)$  MeV and  $636(24)$  MeV — in good agreement with each other. However, both of these results are approximately  $2\sigma$  away from the value of  $689(5)$  MeV derived from experiment. Indeed, the disagreement of the local value was our main motivation for performing the one-link calculation in the first place.

While this is not a huge discrepancy, it is still worthy of further investigation. Given the large discretisation errors evident on both previous plots of this quantity, in Figures 4.12 and 4.13, it may be the case that we are underestimating the errors that need to be included in our heavy-quark extrapolation to the  $b$  mass, particularly since we observe no similar discrepancies for charmonium, where no such extrapolation is required. Correcting this in a quantitative way would require further work

to better understand the specific sources of error for this quantity.

### 6.1.3 Vector Moments

Time moments of the vector correlator were calculated and appropriately normalised for two different vector currents, and are shown in Tables 4.5 (for the local current) and 4.11 (for the one-link current).

We have already mentioned that the one-link current produces results which are in much better agreement with the experimentally-derived values. There is no obvious reason why this should be the case, as the two currents merely probe different tastes of meson, which should have identical properties in the continuum limit. This is an issue worthy of further investigation, particularly given our results for the charmonium moments which we discuss further in the relevant section below.

### 6.1.4 Outlook

We have successfully extended the methods laid out by the HPQCD collaboration in [91] to very fine lattices, and have established a solid base from which to undertake further explorations of bottomonium and  $B$  physics. Notably, this is a fully-relativistic alternative to NRQCD, and one of only a few methods with which we can currently simulate  $b$  quarks on the lattice. It is therefore useful even just as an additional check on NRQCD results.

The extrapolation in the mass of the heavy quark does inherently introduce additional errors, but just as is concluded in [91], these additional errors can, by and large, be kept under control.

Overall, this method will only get better and become more feasible with time, given that the available computing power continues to increase. In the medium term we should be able to dispense with coarser lattices, and in the longer term, simulate directly at the  $b$  quark mass, and therefore test whether the HISQ action performs as well in this regime as it does for charm quarks.

## 6.2 Charmonium

We have calculated several properties of charmonium ground states and excited states using a variety of methods. Ground states were extracted by analysing two-point correlators for HISQ valence quarks on both the MILC 2+1-flavour (asqtad) configurations and the 2+1+1-flavour (HISQ) configurations. We have also, for the first time, applied smearings to our two-point HISQ correlators across multiple lattice spacings, on the 2+1+1-flavour configurations, and used these correlators to calculate properties of charmonium excited states in the continuum limit.

### 6.2.1 Decay Constants

The decay constant of the pseudoscalar  $\eta_c(1S)$  was calculated twice in this work: once on the asqtad configurations in chapter 4 with a result of 391.8(3.7) MeV, and once in chapter 5 on the HISQ configurations, with a result of 396.3(3.0) MeV. As noted previously, there is unfortunately no direct experimental comparison possible for this quantity, so we instead compare it to the HPQCD Collaboration’s previous determination in [45], of 394.7(2.4) MeV. These three values are plotted in Figure 6.2, and are in excellent agreement. The range of the horizontal scale indicates that this is a quantity we have been able to extract very accurately, since it depends only on the ground state parameters extracted from the correlator.

Calculating the decay constant of the vector  $J/\psi(1S)$  requires renormalisation of the vector current used to create it on the lattice, and so we do not expect to be able to determine this quite as accurately as for the  $\eta_c(1S)$ . Nevertheless, we have also obtained a number of values for this quantity: in the 2+1-flavour case, thanks to our attempts to resolve the discrepancies between experimental values and our calculated values of the decay constant for vector bottomonium, we determined the  $J/\psi(1S)$  decay constant once using a local vector current, and again using a one-link vector current. Our calculated values were 407.5(6.8) MeV and 410.8(5.4) MeV respectively, in excellent agreement with each other.

In chapter 5 we also obtained a value of 403(11) MeV on the 2+1+1-flavour lattices. In Figure 6.3, we plot each of these results, as well as two further results for comparison. The first of these is the value of 407(5) MeV derived from experimental measurements, and the second is the value of 405(6) MeV obtained from a precision lattice calculation by the HPQCD collaboration on 2+1-flavour lattices [56]. It is clear that these results all agree very well, and that our lattice results are still very accurate despite the need for renormalisation.

### 6.2.2 Vector Moments

As mentioned for bottomonium, time moments of the vector correlator were calculated and appropriately normalised on the 2+1-flavour lattices for two different vector currents, and are shown in Tables 4.5 (for the local current) and 4.11 (for the one-link current).

Again, much as for the bottomonium case, it is clear that the one-link current produces results which are in much better agreement with the experimentally-derived values. However, in the case of charmonium, we have additional data available for comparison: that from [56], which also agrees with the values from experiment, but only considered the local vector current.

There is no obvious reason why the one-link current should produce results which

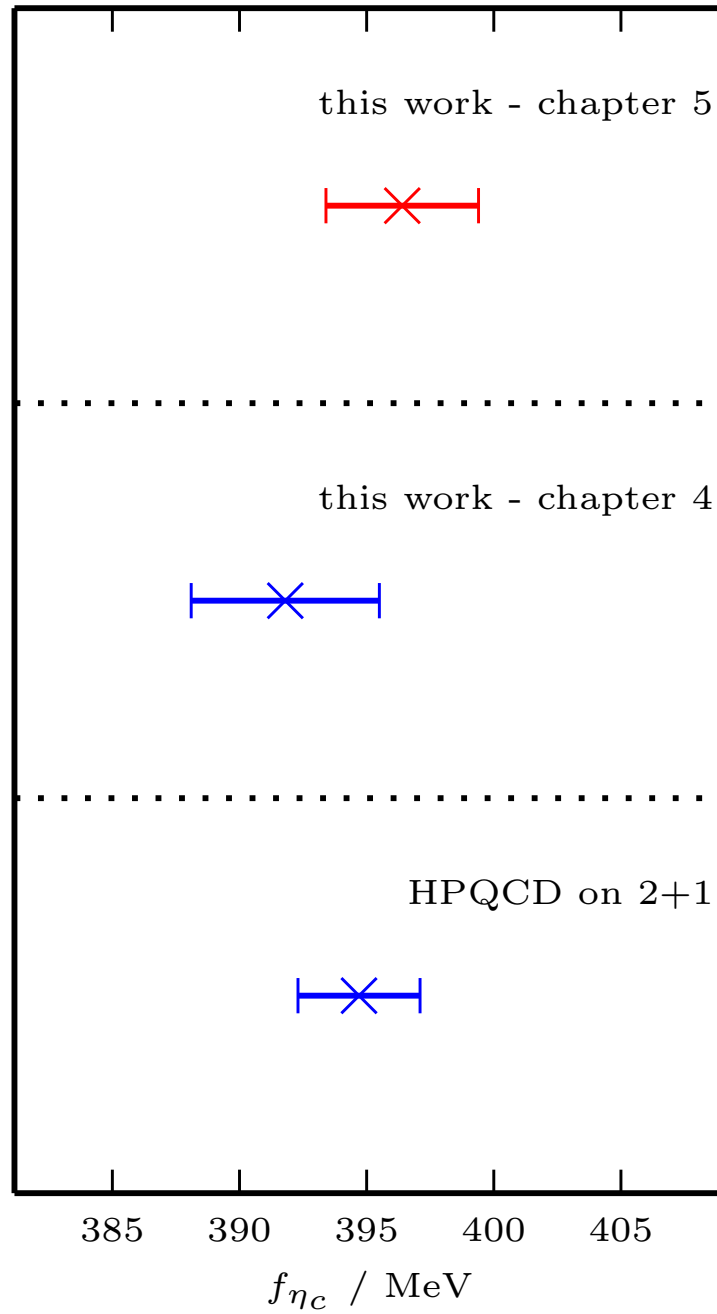


Figure 6.2: A comparison of results for the decay constant of the  $\eta_c(1S)$ . The lower section plots a previous determination by the HPQCD collaboration on 2+1-flavour lattices in [45]. The middle section contains the continuum result on 2+1-flavour lattices from chapter 4 of this thesis, and the top section the continuum result on 2+1+1-flavour lattices from chapter 5 of this thesis.

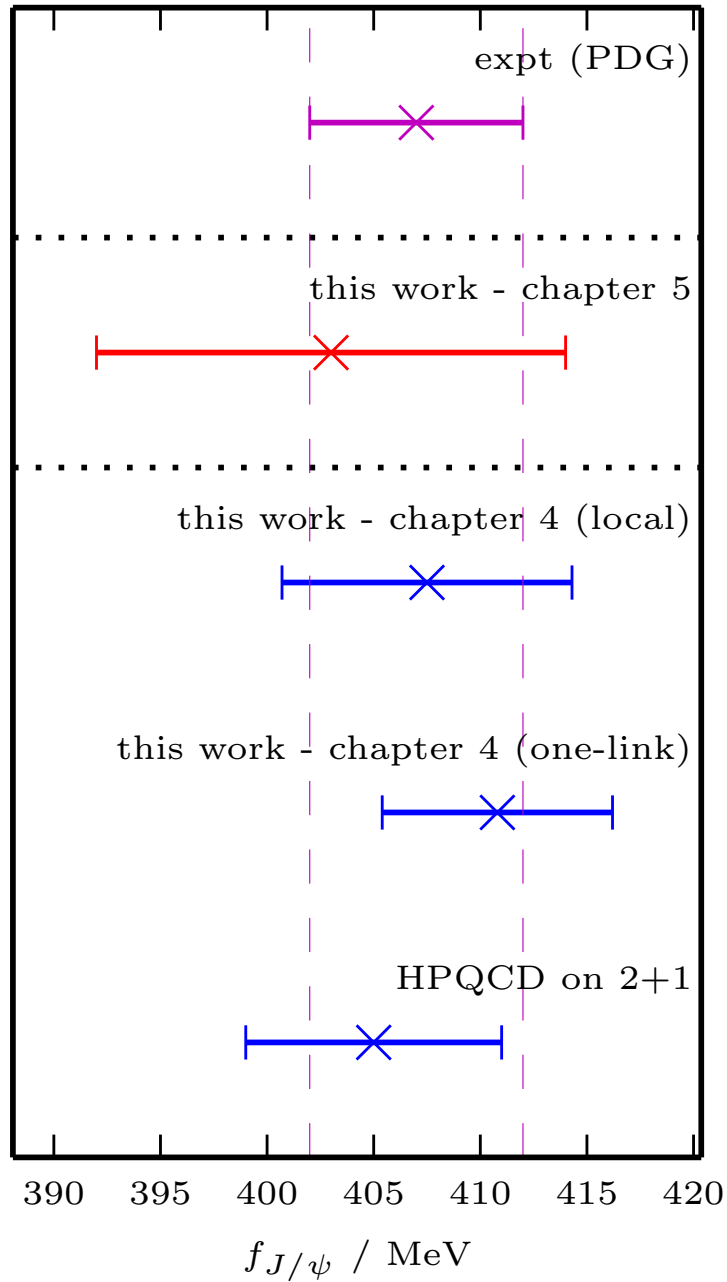


Figure 6.3: A comparison of results for the decay constant of the  $J/\psi(1S)$ . The lower section plots a previous determination by the HPQCD collaboration on 2+1-flavour lattices in [56], and the two continuum results on 2+1-flavour lattices from chapter 4 of this thesis, determined using local and one-link vector currents. The middle section plots the continuum result on 2+1+1-flavour lattices from chapter 5 of this thesis, and the top section contains the result derived from experimental world averages in [4].

differ from those produced with the local current. The deviation between these two sets of results is not large — at most  $2\sigma$  — but this is still a minor open issue which is worthy of further investigation. The main difference between our local-current calculation and that presented in [56] is our extrapolation in the heavy quark mass, and it is possible that this is adversely affecting the results obtained for the charmonium moments.

Further work would be required to claim this conclusively, but it is notable that we also have another set of results which do agree with experimental values. In the process of renormalising the local vector current on the 2+1+1-flavour lattices, we again calculated time moments of the vector correlator using the same method as in the 2+1 case, and as in [56]. Continuum results in this case are presented in Table 5.6, and agree well with both the experimental values and the values calculated in [56]. Our continuum values have larger statistical errors than those in [56], and an understanding of why this is the case, and how to address it if required, was detailed in section 5.3.2.

We have noted several times in chapter 5 that further calculations on superfine and ultrafine lattices would help to increase the accuracy of many of our continuum fits, especially those which incorporate information about excited states. Indeed, this was explicitly shown to be one of the ways to reduce the statistical error on our determination of the 4<sup>th</sup> charmonium moment. Such calculations would also be crucial in resolving the unexpected uncertainties we encountered on the superfine ensemble, as outlined in section 5.5. However, they are also extremely expensive in terms of computer resources, and therefore require careful consideration and planning of their execution, as well as taking a considerable amount of time.

### 6.2.3 Hyperfine Splitting

We have determined the 1S hyperfine splitting of charmonium multiple times in this work. On 2+1-flavour lattices in chapter 4, we obtained 115.0(3.6) MeV from the full fit including heavy quark masses, and 113.9(3.5) MeV from a fit purely to the well-tuned charm quark data.

In chapter 5, we calculated a value of 116.0(3.4) MeV. This was a state-of-the-art calculation, performed on gluon configurations which include the effect of 2+1+1 flavours of HISQ quarks in the sea, at multiple different lattice spacings and multiple different  $u/d$  quark masses, down to and including their physical mass. We were therefore able to perform a very well-controlled continuum and chiral extrapolation, and the error on the final result is dominated by the uncertainty introduced by  $c\bar{c}$  annihilation effects.

In Figure 6.4, we plot these results alongside the current experimental average of

113.2(7) MeV [4], and three further lattice results. The first of these is the HPQCD Collaboration's previous determination on 2+1-flavour lattices, of 116.5(3.2) MeV [56]. The next is the Fermilab Lattice and MILC Collaborations' continuum result, extrapolated from results at multiple lattice spacings, of 116.0(7.5) MeV [88].

Finally, we plot a result from the Hadron Spectrum Collaboration determined at a single lattice spacing, of 80(2) MeV [83]. This result must be interpreted with a caveat in mind: since it is not a continuum determination, we do not necessarily expect it to agree with the experimental value, and indeed the authors also do not claim it is a final result. It is included to illustrate the accuracy of modern lattice results over many different discretised actions, and also, inversely to the previous statement, to reinforce the need for calculations at multiple lattice spacings to obtain continuum results.

It is clear from the plot that the continuum lattice results are all in very good agreement with each other, and with the experimental average. Including errors, all of the results drawn from this work (as well as the previous HPQCD determination) fall entirely within the 10 MeV range from 110–120 MeV, giving an indication of the accuracy with which we have been able to determine this quantity.

## 6.2.4 Continuum Spectrum

To draw together the work on excited charmonium states detailed in chapter 5, we present a plot of the low-lying charmonium spectrum as calculated via the mass splittings that we have determined in the continuum and chiral limit. Starting from the experimental value of the  $\eta_c(1S)$  mass at 2983.6(6) MeV [4], we can add our fitted continuum values for different splittings to obtain the masses of various other states.

Explicitly, we add the hyperfine splitting (116.0(3.4) MeV) to obtain the mass of the  $J/\psi(1S)$ ; the pseudoscalar 2S – 1S splitting (666(12) MeV) to obtain the mass of the  $\eta_c(2S)$ ; the hyperfine splitting and the vector 2S – 1S splitting (586(17) MeV) for the mass of the  $\psi(2S)$ ; and finally, the hyperfine splitting and the vector–axial vector splitting (438(12) MeV) to get the mass of the  $h_c(1P)$ .

The results of these computations are plotted atop the experimental averages for the respective masses in Figure 6.5, and it is clear that we have succeeded in making accurate determinations of them all which match the experimental results. Uncertainties on the excited states are clearly larger than the corresponding error on the ground-state  $J/\psi(1S)$ , but this is to be expected since the excited states are much less straightforward to determine. Nevertheless, the uncertainties are impressively small: the errors on the excited state masses are all less than 0.5%, and the error on the mass of the  $J/\psi(1S)$  comes in at just over 0.1%.

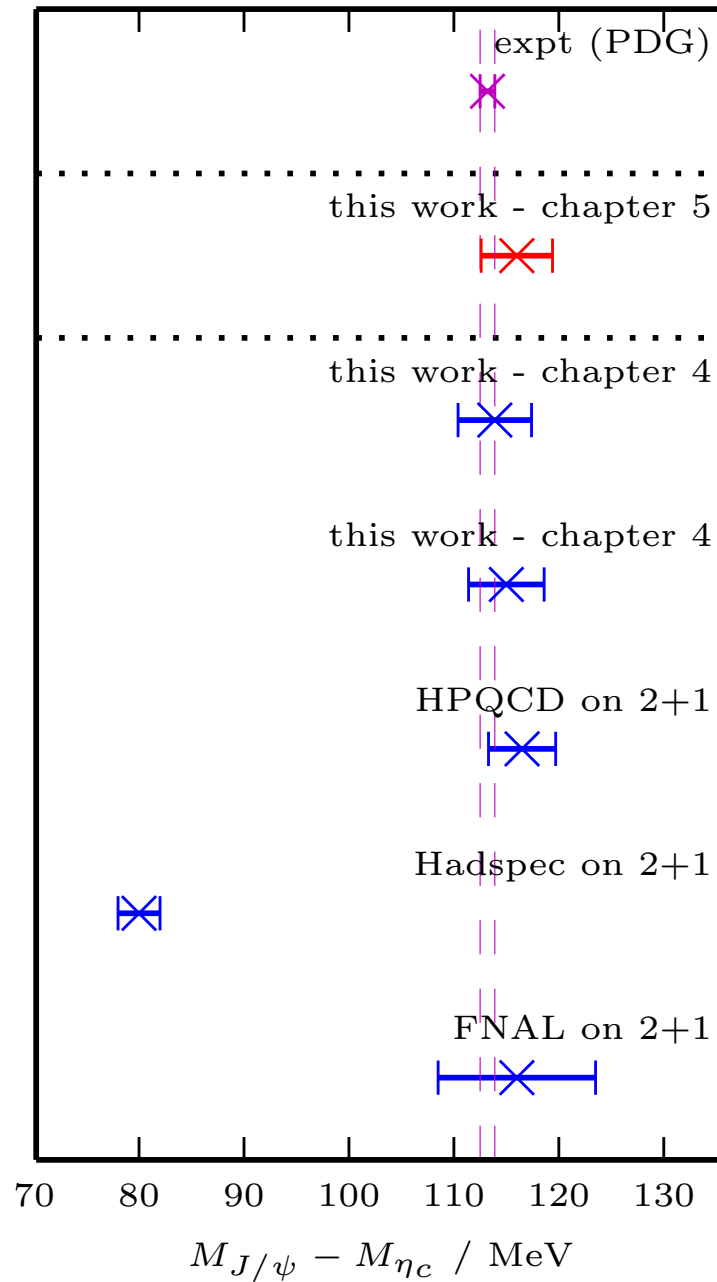


Figure 6.4: A comparison of results for the charmonium hyperfine splitting, as determined in this work and in others. The lower section contains results computed on 2+1-flavour lattices, in blue: two in chapter 4 of this thesis via different continuum fits, and previous determinations by several lattice collaborations [56, 83, 88]. The middle section contains the continuum result on 2+1+1-flavour lattices from chapter 5 of this thesis, in red. In magenta in the top section is the current experimental average from [4].

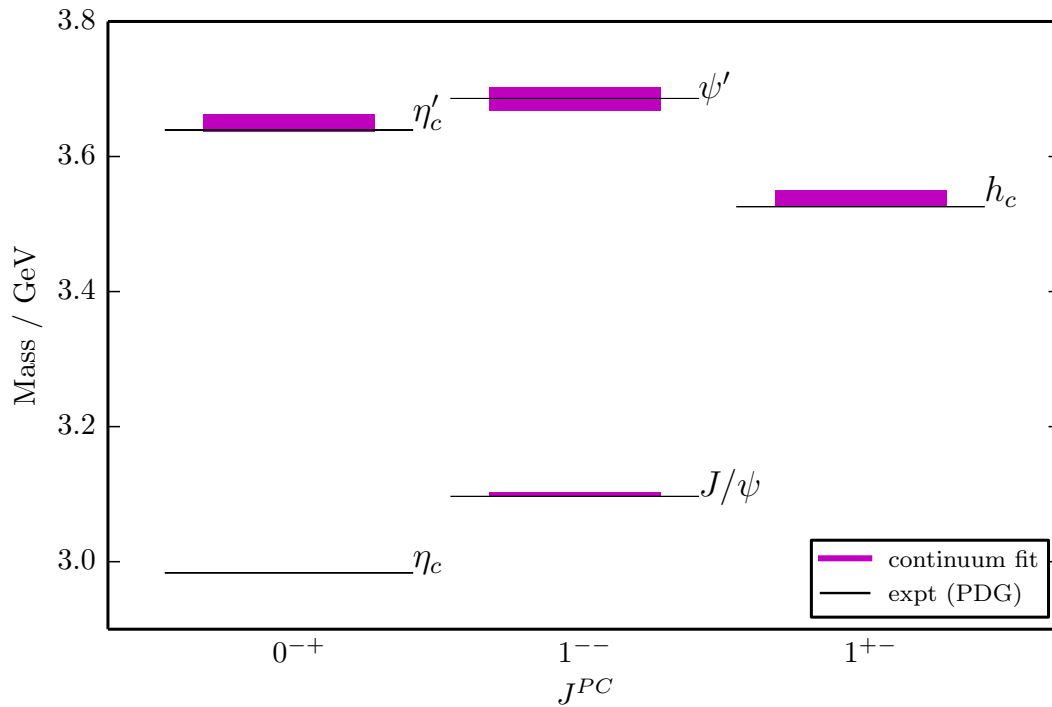


Figure 6.5: The spectrum of low-lying charmonium states computed from the continuum results of fits to the hyperfine splitting, pseudoscalar and vector  $2S - 1S$  splittings, and the vector-axial-vector splitting. The black lines indicate the experimental averages from [4], and the line widths correspond to the (generally very small) uncertainties on these results. The magenta boxes indicate the range of our results from the continuum fits. The baseline here which all the splittings are added to is the mass of the  $\eta_c(1S)$ , which we fix to for tuning our bare lattice charm quark masses, and for which we do not therefore compute a continuum determination.

A key conclusion of this work in relation to the excited charmonium states is that we find a spin-averaged  $2S - 1S$  splitting consistent with experiment ( $606(15)$  MeV compared to  $605.82(37)$  MeV), and do not observe the same discrepancy as the Fermilab/MILC Collaborations in [84]. We have discussed at length the possibility that we are observing a similar effect on the superfine lattices (although fortunately not in the continuum limit) and that this may also be manifesting itself in simulations using other lattice actions [86, 87]. Whether this is actually the case is an open question worthy of further study, perhaps on even finer lattices.

### 6.2.5 Outlook

As has been noted multiple times, in this work and in others [20, 91], the HISQ action is eminently capable of accurately simulating charm quarks on the lattice. This has been demonstrated many times in this thesis by our extremely accurate extraction of the ground states from two-point HISQ correlators — see, for example, Figures 3.1 and 3.2 — and by our accurate extractions of mass splittings and decay constants in the charmonium spectrum, particularly the ground-state hyperfine splitting.

We have also demonstrated, for the first time, the high-precision determination of excited state charmonium masses using HISQ valence charm quarks. This is not solely down to the HISQ action: careful consideration of smeared sources and sinks is required when constructing correlators with the intention of extracting excited states. We have made a significant improvement on rudimentary calculations of excited charmonium states with the HISQ action, as shown, for example, in Figure 7 of [20]. It is also notable that we have been able to perform these calculations on very fine lattices, something that would have been at least infeasible if not downright impossible when the HISQ action was first introduced. This is an important step towards ensuring that future calculations are able to improve upon current levels of precision.

The work presented in this thesis on the charmonium spectrum has deliberately concentrated on relatively low-lying excited states, but has performed calculations at multiple lattice spacings and multiple sea quark masses. In contrast, work such as that presented by the Hadron Spectrum Collaboration in [83] utilises multiple operators to make determinations of many states including exotics, but does not undertake any lattice spacing studies. These are important endeavours with complementary aims.

In concentrating on more conventional excited states, we have laid the groundwork for possible studies of more exotic states like the  $X(3823)$  [92] and  $X(3872)$  [93, 94] which may be undertaken with the HISQ action in the future. These would be extremely challenging calculations by today's standards, and indeed would be

tricky to perform with the HISQ action in general, since they would require non-trivial exotic operators that cannot currently be constructed in the HISQ formalism.

It is, however, clear that our results here represent significant progress in making accurate determinations of more conventional excited states over a wide range of lattices, including state-of-the-art gauge configurations with very fine lattice spacings. These have proven crucial in obtaining small errors when extrapolating to the continuum.



# References

- [1] MILC Collaboration. *The MILC Code Manual*. Version 7.7.11. 29 Dec. 2013. URL: <http://www.physics.utah.edu/~detar/milc/> (cit. on pp. ix, 19, 32, 47, 93).
- [2] Peter Knecht. “Calculation of the masses of the  $\eta'_c$ , the  $\psi'$  and the  $h_c$  mesons in Lattice QCD”. Master’s thesis. School of Physics and Astronomy, University of Glasgow, 2014 (cit. on pp. ix, 95, 96).
- [3] B. A. Galloway et al. “Radial and orbital excitation energies of charmonium”. In: *Proceedings of the 32nd International Symposium on Lattice Field Theory (Lattice 2014)*. Italy: Proceedings of Science, 2014. arXiv: 1411.1318 [hep-lat] (cit. on p. xi).
- [4] K. A. Olive et al. (Particle Data Group). “The Review of Particle Physics”. In: *Chin. Phys. C* 38.090001 (2014). URL: <http://pdg.lbl.gov> (cit. on pp. 1, 2, 21, 43, 45, 47, 54, 55, 84, 91, 92, 102, 106, 108–110, 112, 113, 115, 129, 131, 134, 135, 138, 140, 142–144, 146–148, 153, 155–157).
- [5] M. Agostini et al. (GERDA Collaboration). “ $2\nu\beta\beta$  decay of  $^{76}\text{Ge}$  into excited states with GERDA Phase I”. In: *Journal of Physics G: Nuclear and Particle Physics* 42.11 (Sept. 2015), p. 115201. arXiv: 1506.03120 [hep-ex] (cit. on p. 2).
- [6] Franz Mandl and Graham Shaw. *Quantum Field Theory*. Wiley, 1993 (cit. on p. 2).
- [7] David J. Gross and Frank Wilczek. “Ultraviolet Behavior of Non-Abelian Gauge Theories”. In: *Phys. Rev. Lett.* 30.26 (June 1973), pp. 1343–1346. DOI: 10.1103/PhysRevLett.30.1343 (cit. on p. 3).
- [8] H. David Politzer. “Reliable Perturbative Results for Strong Interactions?” In: *Phys. Rev. Lett.* 30.26 (June 1973), pp. 1346–1349. DOI: 10.1103/PhysRevLett.30.1346 (cit. on p. 3).
- [9] Michael E. Peskin and Daniel V. Schroeder. *An Introduction to Quantum Field Theory*. Westview Press, 1995 (cit. on p. 4).

- [10] G. Peter Lepage. “Redesigning Lattice QCD”. In: *Perturbative and Nonperturbative Aspects of Quantum Field Theory*. Ed. by H. Latal and W. Schweiger. Vol. 479. Lecture Notes in Physics. Springer Berlin Heidelberg, 1997, pp. 1–48. arXiv: hep-lat/9607076 [hep-lat] (cit. on pp. 4, 13, 18, 43).
- [11] Kenneth G. Wilson. “Confinement of Quarks”. In: *Phys. Rev. D* 10.8 (Oct. 1974), pp. 2445–2459. DOI: 10.1103/PhysRevD.10.2445 (cit. on p. 5).
- [12] Thomas DeGrand and Carleton DeTar. *Lattice Methods for Quantum Chromodynamics*. World Scientific, 2006 (cit. on pp. 5, 6, 24, 43).
- [13] K. Symanzik. “Continuum limit and improved action in lattice theories: (I). Principles and  $\phi^4$  theory”. In: *Nucl. Phys. B* 226.1 (1983), pp. 187–204. DOI: 10.1016/0550-3213(83)90468-6 (cit. on p. 6).
- [14] K. Symanzik. “Continuum limit and improved action in lattice theories: (II). O(N) non-linear sigma model in perturbation theory”. In: *Nucl. Phys. B* 226.1 (1983), pp. 205–227. DOI: 10.1016/0550-3213(83)90469-8 (cit. on p. 6).
- [15] A. Bazavov et al. (MILC Collaboration). “Full nonperturbative QCD simulations with 2 + 1 flavors of improved staggered quarks”. In: *Rev. Mod. Phys.* 82 (2 May 2010), pp. 1349–1417. arXiv: 0903.3598 [hep-lat] (cit. on pp. 7, 17, 19, 22, 41, 43, 91).
- [16] A. Bazavov et al. (MILC Collaboration). “Lattice QCD ensembles with four flavors of highly improved staggered quarks”. In: *Phys. Rev. D* 87 (14 Mar. 2013), p. 054505. arXiv: 1212.4768 [hep-lat] (cit. on pp. 7, 20, 21, 41, 43, 78, 93).
- [17] Heinz J. Rothe. *Lattice Gauge Theories: An Introduction*. World Scientific, 2012 (cit. on pp. 8, 9).
- [18] A. X. El-Khadra, A. S. Kronfeld and P. B. Mackenzie. “Massive Fermions in Lattice Gauge Theory”. In: *Phys. Rev. D* 55 (1 Apr. 1997), p. 3933. arXiv: hep-lat/9604004 [hep-lat] (cit. on pp. 9, 91).
- [19] Leonard Susskind. “Lattice Fermions”. In: *Phys. Rev. D* 16.10 (Nov. 1977), pp. 3031–3039. DOI: 10.1103/PhysRevD.16.3031 (cit. on p. 9).
- [20] E. Follana et al. “Highly improved staggered quarks on the lattice with applications to charm physics”. In: *Phys. Rev. D* 75 (14 Mar. 2007), p. 054502. arXiv: hep-lat/0610092 [hep-lat] (cit. on pp. 9, 11, 13, 14, 24, 42, 47, 54, 63, 95, 158).
- [21] Satchidananda Naik. “On-shell improved action for QCD with Susskind fermions and the asymptotic freedom scale”. In: *Nucl. Phys. B* 316.1 (1989), pp. 238–268. DOI: 10.1016/0550-3213(89)90394-5 (cit. on p. 10).

- [22] G. Peter Lepage. “Perturbative improvement for lattice QCD: An update”. In: *Nucl. Phys. B Proc. Suppl.* 60.1–2 (1998), pp. 267–278. arXiv: hep-lat/9707026 [hep-lat] (cit. on p. 11).
- [23] J.-F. Lagaë and D. K. Sinclair. “Improved staggered quark actions with reduced flavor symmetry violations for lattice QCD”. In: *Phys. Rev. D* 59.1 (Dec. 1998), p. 014511. arXiv: hep-lat/9806014 [hep-lat] (cit. on p. 11).
- [24] G. Peter Lepage. “Flavor-symmetry restoration and Symanzik improvement for staggered quarks”. In: *Phys. Rev. D* 59.7 (Feb. 1999), p. 074502. arXiv: hep-lat/9809157 [hep-lat] (cit. on p. 11).
- [25] Kostas Orginos, Doug Toussaint and R. L. Sugar (MILC Collaboration). “Variants of fattening and flavor symmetry restoration”. In: *Phys. Rev. D* 60.5 (July 1999), p. 054503. arXiv: hep-lat/9903032 [hep-lat] (cit. on p. 12).
- [26] G. Peter Lepage and Paul B. Mackenzie. “Viability of lattice perturbation theory”. In: *Phys. Rev. D* 48.5 (Sept. 1993), pp. 2250–2264. arXiv: hep-lat/9209022 [hep-lat] (cit. on p. 12).
- [27] M. Alford et al. “Lattice QCD on small computers”. In: *Phys. Lett. B* 361.1 (Sept. 1995), pp. 87–94. arXiv: hep-lat/9507010 [hep-lat] (cit. on p. 12).
- [28] G. Peter Lepage. “Simulating Heavy Quarks”. In: *Nucl. Phys. B Proc. Suppl.* 26 (1992), pp. 45–56 (cit. on pp. 13, 42).
- [29] A. Bazavov et al. (MILC Collaboration). “Scaling studies of QCD with the dynamical highly improved staggered quark action”. In: *Phys. Rev. D* 82.7 (Oct. 2010), p. 074501. arXiv: 1004.0342 [hep-lat]. Appendix B (cit. on p. 13).
- [30] S. Hashimoto, J. Laiho and S. R. Sharpe. “Lattice Quantum Chromodynamics”. In: *The Review of Particle Physics*. Ed. by K. A. Olive et al. (Particle Data Group). Vol. 38. 090001. Chin. Phys. C, 2014. URL: <http://pdg.lbl.gov/2015/reviews/rpp2014-rev-lattice-qcd.pdf> (cit. on pp. 15–18, 23, 41).
- [31] G. Peter Lepage. “Lattice QCD for Novices”. In: *Strong interactions at low and intermediate energies: Proceedings, 13th Annual Hampton University Graduate Studies (HUGS’98), Newport News, USA*. Ed. by J. L. Goity. Singapore: World Scientific, 1998, pp. 49–90. arXiv: hep-lat/0506036 [hep-lat] (cit. on pp. 16, 40).
- [32] S. Aoki et al. (CP-PACS Collaboration). “Light hadron spectrum and quark masses from quenched lattice QCD”. In: *Phys. Rev. D* 67.3 (Feb. 2003), p. 034503. arXiv: hep-lat/0206009 [hep-lat] (cit. on p. 16).

- [33] C. T. H. Davies et al. (HPQCD and UKQCD Collaborations, MILC Collaboration, and HPQCD and Fermilab Lattice Collaborations). “High-Precision Lattice QCD Confronts Experiment”. In: *Phys. Rev. Lett.* 92.2 (Jan. 2004), p. 022001. arXiv: hep-lat/0304004 [hep-lat] (cit. on p. 16).
- [34] Stephen R. Sharpe. “Rooted staggered fermions: good, bad or ugly?” In: *Proceedings of the 24th International Symposium on Lattice Field Theory (Lattice 2006)*. Italy: Proceedings of Science, 2006. arXiv: hep-lat/0610094 [hep-lat] (cit. on pp. 17, 25).
- [35] Andreas S. Kronfeld. “Lattice gauge theory with staggered fermions: how, where, and why (not)”. In: *Proceedings of the 25th International Symposium on Lattice Field Theory (Lattice 2007)*. Italy: Proceedings of Science, 2007. arXiv: 0711.0699 [hep-lat] (cit. on p. 17).
- [36] Maarten Golterman. “QCD with rooted staggered fermions”. In: *Proceedings of the 8th Conference on Quark Confinement and the Hadron Spectrum (Confinement8)*. Italy: Proceedings of Science, Dec. 2008. arXiv: 0812.3110 [hep-lat] (cit. on p. 17).
- [37] Yigal Shamir. “Locality of the fourth root of the staggered-fermion determinant: Renormalization-group approach”. In: *Phys. Rev. D* 71.3 (Feb. 2005), p. 034509. arXiv: hep-lat/0412014 [hep-lat] (cit. on p. 17).
- [38] Yigal Shamir. “Renormalization-group analysis of the validity of staggered-fermion QCD with the fourth-root recipe”. In: *Phys. Rev. D* 75.5 (Mar. 2007), p. 054503. arXiv: hep-lat/0607007 [hep-lat] (cit. on p. 17).
- [39] Simon Duane et al. “Hybrid Monte Carlo”. In: *Phys. Lett. B* 195.2 (1987), pp. 216–222. DOI: 10.1016/0370-2693(87)91197-X (cit. on p. 17).
- [40] Steven Gottlieb et al. “Hybrid-molecular-dynamics algorithms for the numerical simulation of quantum chromodynamics”. In: *Phys. Rev. D* 35.8 (Apr. 1987), pp. 2531–2542. DOI: 10.1103/PhysRevD.35.2531 (cit. on p. 17).
- [41] M. A. Clark and A. D. Kennedy. “Accelerating staggered-fermion dynamics with the rational hybrid Monte Carlo algorithm”. In: *Phys. Rev. D* 75.1 (Jan. 2007), p. 011502. arXiv: hep-lat/0610047 [hep-lat] (cit. on p. 17).
- [42] M. A. Clark and A. D. Kennedy. “Accelerating Dynamical-Fermion Computations Using the Rational Hybrid Monte Carlo Algorithm with Multiple Pseudofermion Fields”. In: *Phys. Rev. Lett.* 98.5 (Jan. 2007), p. 051601. arXiv: hep-lat/0608015 [hep-lat] (cit. on p. 17).
- [43] Michael Creutz. “Global Monte Carlo algorithms for many-fermion systems”. In: *Phys. Rev. D* 38.4 (Aug. 1988), pp. 1228–1238. DOI: 10.1103/PhysRevD.38.1228 (cit. on p. 18).

- [44] Rajan Gupta, Gregory W. Kilcup and Stephen R. Sharpe. “Tuning the hybrid Monte Carlo algorithm”. In: *Phys. Rev. D* 38.4 (Aug. 1988), pp. 1278–1287. DOI: 10.1103/PhysRevD.38.1278 (cit. on p. 18).
- [45] C. Davies et al. (HPQCD Collaboration). “Update: Precision  $D_s$  decay constant from full lattice QCD using very fine lattices”. In: *Phys. Rev. D* 82 (2010), p. 114504. arXiv: 1008.4018 [hep-lat] (cit. on pp. 19, 47, 88, 89, 132, 133, 151, 152).
- [46] R. J. Dowdall et al. (HPQCD Collaboration). “ $V_{us}$  from  $\pi$  and  $K$  decay constants in full lattice QCD with physical  $u$ ,  $d$ ,  $s$  and  $c$  quarks”. In: *Phys. Rev. D* 88 (Dec. 2013), p. 074504. arXiv: 1303.1670 [hep-lat] (cit. on pp. 20–23, 93).
- [47] B. Chakraborty et al. (HPQCD Collaboration). “High-precision quark masses and QCD coupling from  $n_f = 4$  lattice QCD”. In: *Phys. Rev. D* 91 (5 Mar. 2015), p. 054508. arXiv: 1408.4169 [hep-lat] (cit. on pp. 20, 21, 23).
- [48] R. Sommer. “A New Way to Set the Energy Scale in Lattice Gauge Theories and its Application to the Static Force and  $\alpha_s$  in  $SU(2)$  Yang-Mills Theory”. In: *Nucl. Phys. B* 411.2–3 (1994), pp. 839–854. arXiv: hep-lat/9310022 [hep-lat] (cit. on pp. 21, 22).
- [49] C. Bernard et al. “The static quark potential in three flavor QCD”. In: *Phys. Rev. D* 62 (7 July 2000), p. 034503. arXiv: hep-lat/0002028 [hep-lat] (cit. on p. 21).
- [50] R. J. Dowdall et al. (HPQCD Collaboration). “The Upsilon spectrum and the determination of the lattice spacing from lattice QCD including charm quarks in the sea”. In: *Phys. Rev. D* 85.5 (Mar. 2012), p. 054509. arXiv: 1110.6887 [hep-lat] (cit. on pp. 22, 43).
- [51] Szabolcs Borsányi et al. (Budapest-Marseille-Wuppertal Collaboration). “High-precision scale setting in lattice QCD”. In: *JHEP* 2012.9 (Nov. 2012), p. 10. arXiv: 1203.4469 [hep-lat] (cit. on p. 22).
- [52] C. T. H. Davies et al. (HPQCD Collaboration). “Precise determination of the lattice spacing in full lattice QCD”. In: *Phys. Rev. D* 81.3 (Feb. 2010), p. 034506. arXiv: 0910.1229 [hep-lat] (cit. on pp. 22, 29, 47).
- [53] Q. J. Mason. “High Precision Lattice QCD: Perturbations in a Non-Perturbative World”. PhD thesis. Cornell University, 2004. URL: <http://hdl.handle.net/1813/57> (cit. on p. 24).
- [54] G. Peter Lepage. “Notes on Naive/Staggered Quarks”. Apr. 2005 (cit. on p. 27).

- [55] M. R. Hestenes and E. Stiefel. “Methods of conjugate gradients for solving linear systems”. In: *Journal of Research of the National Bureau of Standards* 49.6 (Dec. 1952), p. 409. DOI: 10.6028/jres.049.044 (cit. on p. 29).
- [56] G. Donald et al. (HPQCD Collaboration). “Precision tests of the  $J/\psi$  from full lattice QCD: Mass, leptonic width, and radiative decay rate to  $\eta_c$ ”. In: *Phys. Rev. D* 86 (2 Nov. 2012), p. 094501. arXiv: 1208.2855 [hep-lat] (cit. on pp. 34, 43, 47, 50, 54, 55, 59, 62, 89–91, 121, 126, 127, 151, 153–156).
- [57] G. P. Lepage et al. “Constrained Curve Fitting”. In: *Nucl. Phys. Proc. Suppl.* 106 (2002), pp. 12–20. arXiv: hep-lat/0110175 [hep-lat]. URL: <https://github.com/gplepage/corrfitter> (cit. on pp. 36, 38).
- [58] C. M. Bouchard et al. “ $B_s \rightarrow K\ell\nu$  form factors from lattice QCD”. In: *Phys. Rev. D* 90.5 (Sept. 2014), p. 054506. arXiv: 1406.2279 [hep-lat]. Appendix A1 (cit. on p. 38).
- [59] G. P. Lepage. *lsqfit Documentation*. Version 5.0. 30 June 2014. URL: <https://github.com/gplepage/lsqfit> (cit. on p. 38).
- [60] K. Hornbostel (HPQCD Collaboration). “Fast fits for lattice QCD correlators”. In: *Phys. Rev. D* 85.3 (Feb. 2012), p. 031504. arXiv: 1111.1363 [hep-lat] (cit. on p. 39).
- [61] C. Michael. “Adjoint sources in lattice gauge theory”. In: *Nucl. Phys. B* 259.1 (1985), pp. 58–76 (cit. on p. 39).
- [62] Martin Lüscher and Ulli Wolff. “How to calculate the elastic scattering matrix in two-dimensional quantum field theories by numerical simulation”. In: *Nucl. Phys. B* 339.1 (1990), pp. 222–252 (cit. on p. 39).
- [63] Benoit Blossier et al. (ALPHA Collaboration). “On the generalized eigenvalue method for energies and matrix elements in lattice field theory”. In: *JHEP* 2009.04 (2009), p. 094. arXiv: 0902.1265 [hep-lat] (cit. on p. 39).
- [64] G. P. Lepage. *corrfitter Documentation*. Version 4.1. 30 June 2014. URL: <https://github.com/gplepage/corrfitter> (cit. on pp. 39, 144).
- [65] Gilberto Colangelo, Stephan Dürr and Christoph Haefeli. “Finite volume effects for meson masses and decay constants”. In: *Nucl. Phys. B* 721 (2005), pp. 136–174. arXiv: hep-lat/0503014 [hep-lat] (cit. on p. 41).
- [66] M. Lüscher. “Volume dependence of the energy spectrum in massive quantum field theories. I. Stable particle states”. In: *Comm. Math. Phys.* 104.2 (1986), pp. 177–206 (cit. on p. 41).

- [67] Craig McNeile. “Heavy Quarks on the Lattice”. In: *Heavy Quark Physics*. Ed. by David Blaschke, Mikhail A. Ivanov and Thomas Mannel. Vol. 647. Lecture Notes in Physics. Springer Berlin Heidelberg, 2004, pp. 100–128. DOI: 10.1007/978-3-540-40975-5\_4 (cit. on pp. 42, 47).
- [68] B. A. Thacker and G. Peter Lepage. “Heavy-quark bound states in lattice QCD”. In: *Phys. Rev. D* 43 (1 1991), pp. 196–208. DOI: 10.1103/PhysRevD.43.196 (cit. on pp. 43, 46).
- [69] Christine Davies. “The Heavy Hadron Spectrum”. In: *Computing Particle Properties: Proceedings of the 36. Internationale Universitätswochen für Kern- und Teilchenphysik, Schladming, Austria, March 1–8, 1997*. Ed. by Helmut Gausterer and Christian B. Lang. Springer Berlin Heidelberg, 1998, pp. 1–64. arXiv: hep-ph/9710394 [hep-ph] (cit. on pp. 45, 46).
- [70] P. A. Rapidis et al. “Observation of a Resonance in  $e^+e^-$  Annihilation Just above Charm Threshold”. In: *Phys. Rev. Lett.* 39.9 (Aug. 1977), pp. 526–529. **Erratum:** *Phys. Rev. Lett.* 39, 974 (1977) (cit. on p. 46).
- [71] Jonathan L. Rosner. “Charmless final states and  $S$ - and  $D$ -wave mixing in the  $\psi''$ ”. In: *Phys. Rev. D* 64.9 (Sept. 2001), p. 094002. arXiv: hep-ph/0105327 [hep-ph] (cit. on p. 46).
- [72] Chris Quigg. “Realizing the Potential of Quarkonium”. In: *AIP Conference Proceedings* 424.1 (1998), pp. 173–188. arXiv: hep-ph/9707493 [hep-ph] (cit. on p. 46).
- [73] R. J. Dowdall et al. (HPQCD Collaboration). “Bottomonium hyperfine splittings from lattice NRQCD including radiative and relativistic corrections”. In: *Phys. Rev. D* 89 (28 Feb. 2014), p. 031502. arXiv: 1309.5797 [hep-lat]. **Erratum:** *Phys. Rev. D* 92, 039904 (2015) (cit. on pp. 47, 55, 148, 149).
- [74] C. McNeile et al. (HPQCD Collaboration). “Heavy meson masses and decay constants from relativistic heavy quarks in full lattice QCD”. In: *Phys. Rev. D* 86 (2012), p. 074503. arXiv: 1207.0994 [hep-lat] (cit. on pp. 47, 53, 88, 89).
- [75] E. Follana et al. (HPQCD and UKQCD Collaborations). “High-Precision Determination of the  $\pi$ ,  $K$ ,  $D$ , and  $D_s$  Decay Constants from Lattice QCD”. In: *Phys. Rev. Lett.* 100.6 (Feb. 2008), p. 062002. arXiv: 0706.1726 [hep-lat] (cit. on p. 53).
- [76] R. Mizuk et al. (Belle Collaboration). “Evidence for the  $\eta_b(2S)$  and Observation of  $h_b(1P) \rightarrow \eta_b(1S)\gamma$  and  $h_b(2P) \rightarrow \eta_b(1S)\gamma$ ”. In: *Phys. Rev. Lett.* 109.23 (Dec. 2012), p. 232002. arXiv: 1205.6351 [hep-ex] (cit. on pp. 54, 55, 147, 148).

- [77] L. Levkova and C. DeTar. “Charm annihilation effects on the hyperfine splitting in charmonium”. In: *Phys. Rev. D* 83.7 (Apr. 2011), p. 074504. arXiv: 1012.1837 [hep-lat] (cit. on p. 54).
- [78] Bahman Dehnadi et al. “Charm mass determination from QCD charmonium sum rules at order  $\alpha_s^3$ ”. In: *Journal of High Energy Physics* 2013.9 (2013), pp. 1–56. arXiv: 1102.2264 [hep-ph] (cit. on pp. 59, 63, 117).
- [79] K. G. Chetyrkin et al. “Charm and Bottom Quark Masses: an Update”. In: *Phys. Rev. D* 80 (14 Oct. 2009), p. 074010. arXiv: 0907.2110 [hep-ph] (cit. on pp. 59, 62, 63, 71, 117).
- [80] Johann H. Kühn, Matthias Steinhauser and Christian Sturm. “Heavy quark masses from sum rules in four-loop approximation”. In: *Nucl. Phys. B* 778.1–2 (2007), pp. 192–215. arXiv: hep-ph/0702103 [hep-ph] (cit. on pp. 59, 62, 71, 117).
- [81] H. Na et al. “ $D$  semi-leptonic decay form factors with HISQ charm and light quarks”. In: *Proceedings of the XXVII International Symposium on Lattice Field Theory - LAT2009*. Italy: Proceedings of Science, 2009. PoS: LAT2009: 247 (cit. on p. 63).
- [82] B. L. Ioffe. “QCD at Low Energies”. In: *Progress in Particle and Nuclear Physics* 56.1 (2006), pp. 232–277. arXiv: hep-ph/0502148 [hep-ph] (cit. on p. 63).
- [83] L. Liu et al. (Hadron Spectrum Collaboration). “Excited and exotic charmonium spectroscopy from lattice QCD”. In: *JHEP* 126.7 (2012). arXiv: 1204.5425 [hep-lat] (cit. on pp. 91, 155, 156, 158).
- [84] C. DeTar et al. (Fermilab Lattice and MILC Collaborations). “Charmonium mass splittings at the physical point”. In: *Proceedings of the 30th International Symposium on Lattice Field Theory (Lattice 2012)*. Italy: Proceedings of Science, 2012. arXiv: 1211.2253 [hep-lat] (cit. on pp. 91, 92, 109, 110, 145, 158).
- [85] C. B. Lang et al. “Vector and scalar charmonium resonances with lattice QCD”. In: *Journal of High Energy Physics* 2015.9 (2015), pp. 1–24. arXiv: 1503.05363 [hep-lat] (cit. on p. 146).
- [86] Krzysztof Cichy, Martin Kalinowski and Marc Wagner. “Mass spectra of mesons containing charm quarks — continuum limit results from twisted mass fermions”. In: *Proceedings of the 33rd International Symposium on Lattice Field Theory (Lattice 2015)*. Italy: Proceedings of Science, Oct. 2015. arXiv: 1510.07862 [hep-lat] (cit. on pp. 146, 158).

- [87] Krzysztof Cichy, Martin Kalinowski and Marc Wagner. “The continuum limit of the  $D$  meson,  $D_s$  meson and charmonium spectrum from  $N_f = 2 + 1 + 1$  twisted mass lattice QCD”. In: *pre-publication* (Mar. 2016). arXiv: 1603.06467 [hep-lat] (cit. on pp. 146, 158).
- [88] T. Burch et al. (Fermilab Lattice and MILC Collaborations). “Quarkonium mass splittings in three-flavor lattice QCD”. In: *Phys. Rev. D* 81.3 (Feb. 2010), p. 034508. arXiv: 0912.2701 [hep-lat] (cit. on pp. 148, 149, 155, 156).
- [89] Stefan Meinel. “Bottomonium spectrum at order  $v^6$  from domain-wall lattice QCD: Precise results for hyperfine splittings”. In: *Phys. Rev. D* 82.11 (Dec. 2010), p. 114502. arXiv: 1007.3966 [hep-lat] (cit. on pp. 148, 149).
- [90] Jorge Segovia et al. “Bottomonium spectrum revisited”. In: *Phys. Rev. D* 93.7 (Apr. 2016), p. 074027. arXiv: 1601.05093 [hep-ph] (cit. on p. 149).
- [91] C. McNeile et al. (HPQCD Collaboration). “Towards precise relativistic  $b$  quarks on the lattice”. In: *Proceedings of the 27th International Symposium on Lattice Field Theory (Lattice 2009)*. Italy: Proceedings of Science, 2009. arXiv: 0910.2921 [hep-lat] (cit. on pp. 150, 158).
- [92] V. Bhardwaj et al. (Belle Collaboration). “Evidence of a New Narrow Resonance Decaying to  $\chi_{c1}\gamma$  in  $B \rightarrow \chi_{c1}\gamma K$ ”. In: *Phys. Rev. Lett.* 111.3 (July 2013), p. 032001. arXiv: 1304.3975 [hep-ex] (cit. on p. 158).
- [93] S.-K. Choi et al. (Belle Collaboration). “Observation of a Narrow Charmoniumlike State in Exclusive  $B^\pm \rightarrow K^\pm \pi^+ \pi^- J/\psi$  Decays”. In: *Phys. Rev. Lett.* 91.26 (Dec. 2003), p. 262001. arXiv: hep-ex/0309032 [hep-ex] (cit. on p. 158).
- [94] R. Aaij et al. (LHCb Collaboration). “Determination of the  $X(3872)$  Meson Quantum Numbers”. In: *Phys. Rev. Lett.* 110.22 (May 2013), p. 222001. arXiv: 1302.6269 [hep-ex] (cit. on p. 158).